UNIVERSITY OF LEEDS

Optical and Radar Satellite Measurement of Volcanic Eruption Impacts on Vegetation

Megan Laura Udy

Submitted in accordance with the requirements for the degree of Doctor of Philosophy

The University of Leeds

Faculty of Environment

School of Earth and Environment

May 2025

Author Contributions and Intellectual Property

The candidate confirms that the work submitted is their own, except where work which has formed part of jointly authored publications has been included. Contributions of the candidate and other authors to this work has been explicitly indicated below and appropriate credit has been given where reference has been made to the work of others.

The work in Chapter 2 is adapted from a publication in the *Journal of Volcanology and Geothermal Research*:

Udy, M.L., Ebmeier, S.K., Watt, S.F.L., Hooper, A. and Paredes, A., 2024. Satellite measurement of forest disturbance, recovery and deposit distribution following explosive volcanic eruptions. Journal of Volcanology and Geothermal Research, 455, p.108204.

As first author, M.L. Udy undertook the data processing, software set up, methodology, investigation, formal analysis, visualisation and writing (original draft and editing). S.K. Ebmeier provided supervision, conceptualisation, methodology and project administration. S.F.L. Watt provided supervision, conceptualisation and validation. A. Hooper provided supervision. A. Paredes provided data collection and validation (field photos and measurements). All co-authors provided comments on the manuscript.

The work in Chapter 3 is being written up as a manuscript to be submitted to *Earth and Planetary Science Letters* as:

Udy, M.L., Ebmeier, S.K., Watt, S.F.L, Hooper, A. (In Prep.) The impact of volcanic SO_2 on vegetation health as captured by satellite data.
As first author, M.L. Udy undertook the conceptualisation, data processing, software set up, methodology, investigation, formal analysis, visualisation and writing (original draft and editing). S.K. Ebmeier provided supervision, conceptualisation, methodology and project administration. S.F.L. Watt provided supervision. A. Hooper provided supervision. All co-authors provided comments on the manuscript.

The work in Chapter 4 is being written up as a manuscript to be submitted in summer 2025 under the title:
Udy, M.L., Ebmeier, S.K., Watt, S.F.L, Hooper, A. (In Prep.) Global patterns of forest disturbance, recovery, and resilience following volcanic eruptions: insights from satellite data across 18 volcanoes since 1984.
As first author, M.L. Udy undertook the conceptualisation, data processing, software set up, methodology, investigation, formal analysis, visualisation and writing (original draft and editing). S.K. Ebmeier provided supervision, conceptualisation, methodology and project administration. S.F.L. Watt provided supervision. A. Hooper provided supervision.All co-authors provided comments on the manuscript.

Acknowledgements

I'd like to start by thanking my supervisors Dr. Susi Ebmeier, Dr. Seb Watt and Prof. Andy Hooper for all of your help and guidance over these last few years. Particularly, thank you to Susi for all of your support throughout my PhD, it was a rough start, and there's certainly been highs and lows, but I got there eventually! From my time in Liverpool, I'd particularly like to thank Pablo, who inspired and cultivated my passion for remote sensing, and Richard, whose support and always-open door helped me become the geophysicist I am today.

I would like to thank the SENSE CDT, not only for funding my PhD and their support throughout, but for all of the training, trips and retreats, Esrin and Firbush were highlights of my PhD! And I'm so grateful for all the friends and colleagues I've made along the way as a result. Thanks to all my fellow IGT PGRs I couldn't have got through these last few years without you (catch breaks definitely helped!). Particularly, thank you to Jess, Rachel and Rosie for offering to, and taking me on coffee breaks, walks, and wines when they were most needed. Thank you to the InStars, our practices and performances were one of the highlights of my time in Leeds.

I'd also like to say thanks to all my friends and family for helping me get to this point. My Geolsquad who got me through undergrad, my best friends Abi, Alice and Claire, thank you for your friendship and your support and I can't wait to celebrate with you now I will (hopefully) be less stressed. Thank you to my parents who have supported me throughout and always told me I could do anything. Thank you to Anthony, I would not have got through these last few months (and years) without your unwavering support,

patience, phone calls and always telling me that I can do this...even when I was adamant I can't. And thanks to the LMU group for always having a spare desk for me and giving me some great discussions about science, I look forward to many more pizza Fridays, hopefully in the not too distant future.

And lastly, a quiet thank you to the version of myself that kept going. There were times when I wanted to give up, when it felt impossibly hard, and with the support of those mentioned above, I chose to persevere, and for that, I'm so proud.

Abstract

Vegetation disturbance caused by volcanic eruptions can span large areas and persist for years, yet remains poorly constrained and underutilised as a tool for understanding eruptive processes. Many volcanoes are located in forested and remote regions, where access is limited and field observations are difficult. In this thesis, I explore how optical and radar satellite remote sensing can be used to detect, quantify, and analyse vegetation disturbance and recovery caused by volcanic eruptions and emissions at volcanoes worldwide, encompassing a range of eruptive styles and environmental settings, to assess the global applicability of these methods.

This thesis is structured around three core investigations. First, in Chapter 2, I analyse vegetation disturbance and regrowth following the 2015 eruption of Calbuco, Chile, using Sentinel-2 NDVI time series and Sentinel-1 radar backscatter and coherence. I use this case study to test different methods and assess the most effective earth observation tools for studying vegetation disturbance at volcanoes. I demonstrate how declines in vegetation health and coverage correlate with deposit type, thickness and distribution, and show that forest recovery times vary with impact type and possibly local topography. These results are used to refine isopach maps and estimate eruption volume based on vegetation damage.

In Chapter 3, I assess the effects of volcanic gas emissions, particularly SO_2, on forest health, using multi-year optical and radar observations at Krakatau, Semeru, Reykjanes Peninsula, Turrialba and Masaya. I show that both short-term eruptive plumes and long-term passive degassing cause measurable impacts to vegetation from satellite data,

with spatial patterns and recovery trajectories linked to gas flux, exposure time, and vegetation type.

Finally, in Chapter 4, I present a global comparison of forest disturbance and recovery across 18 volcanoes, quantifying recovery times by disturbance type and forest biome. Tephra-affected areas recover most rapidly, while PDC and blast zones show much longer recovery times on the order of decades. Tropical forests recover faster than temperate ones, suggesting ecological resilience plays a major role. In general, the majority of impacted areas recover in as little as 30 years but flow deposits can significantly alter the vegetated landscape for hundreds to thousands of years.

Across all chapters, I highlight the value of optical and radar satellite data to monitor ecological impacts of eruptions, particularly when combined or used in conjunction with field campaigns. These methods offer new ways to assess eruption magnitude, map deposit extents, and evaluate ecosystem recovery, particularly in inaccessible regions. The findings also point toward broader applicability to other disturbance types, and show how vegetation change can be a useful proxy for understanding volcanic activity.

Contents

List of Figures

List of Tables

Chapter 1

Introduction

Volcanic eruptions can cause widespread damage to their surrounding environment. Many volcanoes worldwide are situated in forested regions, which can make them inaccessible and difficult to monitor, in turn limiting knowledge of their past activity, a critical factor in assessing the risks to surrounding communities. Previous studies on vegetation damage as a result of volcanic eruptions have predominantly been conducted via field studies (Martin et al. 2009; Wilson, Cole, et al. 2011; Swanson, Jones, et al. 2013; Payne et al. 2019), often limited to key volcanoes and only sampling a handful of sites, due to accessibility issues from steep topography or dense forests (Macorps et al. 2023). By measuring and analysing forest changes (disturbance and regrowth) at volcanoes, we can better understand both the long-term effects of volcanic activity on vegetation and how volcanoes influence the broader ecological landscape.

We are currently experiencing a period of rapid advancement in Earth Observation, with a growing number of satellites offering enhanced acquisition density and resolution (Ustin and Middleton 2021; Zhao et al. 2022). This increase in satellite capabilities has led to an abundance of data, enabling large-scale studies of forest dynamics around volcanoes, particularly in regions where accessibility is limited. This thesis aims to improve our understanding of how volcanic eruptions impact forests and how these effects can be detected using satellite data. This analysis is conducted at a range of volcanoes worldwide,

exhibiting varying eruptive behaviours and located in different environmental settings, to enhance our understanding of forest disturbance and recovery following volcanic activity.

1.1 Volcanic Eruptions and Forest Dynamics

Volcanic eruptions can vary widely in style, resulting in damage to surrounding plant life that differs in severity and occurs across a range of temporal and spatial scales. As volcanic eruptions are often large, sudden and infrequent disturbances they can have unpredictable impacts on surrounding vegetation, with potentially long lasting impacts (Foster et al. 1998). In this section, I outline the various deposits associated with volcanic eruptions, describe how these processes can damage vegetation, and their influence on subsequent vegetation recovery.

1.1.1 Volcanic Eruption Hazards and Their Impacts on Vegetation

Volcanic eruptions can affect the environment through physical, chemical, climatic and biological mechanisms, producing impacts that vary in scale and duration, with the potential for global changes lasting thousands of years (Payne et al. 2019). Eruptions can be effusive or explosive and result in a variety of different hazards which can have direct (primary) or indirect (secondary) affects on surrounding vegetation (Dale, Delgado-Acevedo, et al. 2008). The direct damage caused by large explosive eruptions can be extensive, reaching thousands of square kilometres (Carey and Sigurdsson 1989; Self 2006). Table 1.1 summarises the primary impacts from volcanic eruptions, with expected spatial scale, damage intensity and influence on recovery.

Temperature, chemical characteristics and volume of ejected material all affect the degree of damage or destruction of vegetation (Dale, Delgado-Acevedo, et al. 2008). Hot pyroclastic density currents (PDCs) may not only destroy vegetation they come into contact with, but can also singe adjacent areas of vegetation up to hundreds of metres away from the flow deposit (Charbonnier et al. 2013). In contrast, tephra fall causes less intensive damage over a much greater area, spreading to regions many hundreds or thousands of kilometres away (Wilson, Stewart, et al. 2013; Wilson, Jenkins, et al. 2015;

Table 1.1: Summary of primary volcanic eruption hazards and their impact on vegetation

Eruption impact	**Spatial scale of impact**	**Intensity (how strong the effect on vegetation is)**	**Vegetation recovery**	**Estimated vegetation recovery time**
Blast	Affects immediate vicinity and adjacent areas	Medium – Will blow down vegetation, but unlikely to fully destroy, residuals left.	Likely to leave some residuals, land surface left usually suitable for regrowth	Years to decades
Pyroclastic Density Current	Affects immediate vicinity, usually localised to channels	High – buries, burns, and destroys vegetation in path, and damages on outskirts.	May leave no residuals, affecting vegetation. May lead to change in vegetation if some species left residuals	Decades to centuries
Lava flows	Affects immediate vicinity but can spread further, may follow channels or be wider reaching	High – destroys everything in path, buries, and burns it.	Unlikely to have residuals left, new land is extremely hard to recolonise, affecting vegetation recovery dramatically.	Centuries
Lahars	Affects areas further reaching from volcano, likely to stay in channels/follow rivers	Low-medium – can knock over, destroy, and bury vegetation but may not bury deep enough to destroy or flow past some areas.	May clear vegetation but likely to leave residuals	Years
Volcanic Landslides	Can affect large areas in local vicinity	Medium-high – can clear vegetation and bury it.	May have residuals, but could transport vegetation types leading to a change in vegetation distribution if recovery is possible.	Decades to centuries
Ash/Tephra	Likely to be most far-reaching impact, spreading 1000s of km	Low-medium – covers vegetation, in some places may be enough to prevent growth or remove leaves and bark.	May affect vegetation health and so which species survive, but this would be in extreme cases	Years to decades
Volcanic Gas	Can spread very far, but likely to only have sever impact on vegetation more locally where concentrations are higher	Low – can have potential to kill trees in small patches.	Possible to affect vegetation health in small areas but not drastically in terms of vegetation type or quantity over a large area.	Years

Arnalds 2013), damaging vegetation through abrasion, which can impair photosynthesis, and in areas of thick tephra deposit, cause complete burial of vegetation (Wilson, Cole, et al. 2011; Turner et al. 1997). The presence of chlorine in volcanic gas can cause chemical toxicity in vegetation, it can also make volcanic ash more acidic, contributing to vegetation loss (Swanson, Jones, et al. 2013; Lowenstern et al. 2012).

These primary hazards can also trigger secondary hazards, often occurring after the eruption, which may cause additional vegetation damage (Dale, Delgado-Acevedo, et al. 2008; Dale, Swanson, et al. 2005). Volcanic gases can result in vegetation damage both during an eruption or by passive emission and can directly or indirectly damage vegetation. Indirect methods include altering soil conditions or contributing to acid rain, in comparison to direct methods such as gases entering the plant through the leaves and causing plant death (Lowenstern et al. 2012; Smith 1981; Delmelle 2003). These secondary impacts, while important in vegetation damage and recovery, are difficult to detect and monitor, particularly using satellite data. Therefore, I focus on the direct impacts of volcanic eruptions on vegetation.

1.1.2 Vegetation Recovery and Resilience

In any setting, vegetation interacts with its surrounding environment, any rapid changes to the environment will likely change the vegetation dynamics (Tang et al. 2021). The degree of damage and how long it takes to recover is primarily linked to plant matter survival, which can be influenced by both volcanic characteristics and local environmental setting. The duration of exposure to eruption impacts, the patterns of damage, distance from eruption centre, size/age of vegetation, location of plants and even time of year can affect the amount of surviving plant matter and in turn how quickly it can recover (Foster et al. 1998; Dale, Delgado-Acevedo, et al. 2008).

Vegetation recovery relies on plant survival, legacies, plant recruitment and the time to maturity (Dale, Delgado-Acevedo, et al. 2008). Plant survival will depend on the level of damage and the type of eruption deposit it has been affected by. Surviving plants aid recovery, and distance to surviving plant matter directly impacts recovery

time (Dale, Swanson, et al. 2005). Legacies can be divided into two categories: physical (e.g. topography and landscape changes, soil alterations) and biological (e.g surviving plant matter, animals, seeds or spores) (Dale, Delgado-Acevedo, et al. 2008). In areas of no surviving plants, if there are remaining biological legacies this can aid recovery and regrowth of vegetation in this area. Plant recruitment is the establishment of new plants in an area. When this occurs for the first time on a previously uninhabited surface, it is termed primary succession; when it occurs on a previously vegetated surface, it is secondary succession (Dale, Swanson, et al. 2005; Crisafulli et al. 2015). Environmental factors such as distance to seed sources, wind and water transport, dispersal agents, and elevation or topography can influence recruitment (Dale, Delgado-Acevedo, et al. 2008). Time to maturity also influences recovery, if this period of time is shorter vegetation will become more resilient more quickly, potentially enabling it to withstand future disturbances. This is due to mature plants often having more resilience, due to factors like size and cuticle thickness (Rankenberg et al. 2021; Han et al. 2022; Hintz et al. 2021; Dominguez et al. 2017). Ecological resilience was first introduced by Holling in 1973, and is defined as the ability of an ecosystem to withstand disturbance without structural or state changes (Holling 1973). Other definitions refer to resilience as the return time to a stable state or equilibrium after disturbance (Gunderson 2000). In this study, resilience is defined as the ability of vegetation to withstand volcanic disturbances and return to its pre-eruption state, as observed through satellite measurements such as vegetation indices. It is important to acknowledge that while remote sensing can effectively detect patterns of change and recovery, it may not capture smaller scale ecological processes, such as species or composition changes which may also reflect longer term changes in the ecosystem and its resilience.

Volcanic deposits that are more destructive and likely to destroy all plant matter, or produce a new surface requiring primary succession (e.g. lava flows, PDCs), will result in longer recovery times than deposits that leave remnant plant matter (e.g. tephra deposits, lahars, volcanic blasts). The typical pattern of disturbance from a deposit will also affect recovery (Foster et al. 1998). Tephra deposits or blasts typically produce

sectoral (or isodiametric) patterns with an epicentre of disturbance, while lavas, lahars, and channelised PDCs have a linear impact pattern, with any vegetation in surrounding drainage channels likely to be destroyed (Foster et al. 1998). As a result, linear flows are often closer to surviving plant matter or seed sources as they are narrower, and this could reduce recovery time. However, these linear deposits are also the most damaging, making the relationship complex.

The amount of surviving plant matter, or how quickly it recovers can also be influenced by the type of vegetation and the environmental setting. Plant species may have more inherent resilience, by being taller or having a thicker cuticle, and so be above the level of impact or able to withstand environmental stressors resulting from eruptions (Dominguez et al. 2017; Gillman et al. 2015). Forest type will also likely influence survival and recovery as tropical forests have faster growth rates (so quicker times to maturity) as well as more variation which is required for resilience (Gillman et al. 2015; Smith, Traxl, et al. 2022). Older trees will likely be more resilient, so even in a given setting older plants may survive even if juvenile plants do not (Rankenberg et al. 2021). Seasonality can significantly impact plant survival, depending on whether it occurs during the growing season. Environmental factors, such as the time of year, snow cover, and topography, can also play a crucial role in determining plant survival and recovery (Dale, Delgado-Acevedo, et al. 2008; Dale, Crisafulli, et al. 2005).

Although factors influencing recovery and resilience can be separated into those defined by the volcano and those related to vegetation and environmental conditions, these factors are interconnected and can influence one another. For instance, the type of volcanic deposit, particularly its shape, affects the distance to surviving vegetation, a critical factor in the vegetation's ability to recover. As a result, the interplay between these factors and their impact on recovery times is likely to be complex.

1.2 Satellite Detection of Forest Properties

Satellite data provides global insights into the spatial and temporal changes of variables indicating the condition of vegetation (Dorigo et al. 2007). Since the launch of Landsat 1 in 1972, it has been demonstrated how image-based remote sensing can be used to monitor vegetation through crop identification, estimation of canopy properties and forecasting crop production (Dorigo et al. 2007; Moran et al. 1997). While characteristics used to indicate forest health and growth rates, such as tree height, tree diameter, and wood density, are not directly measurable from satellite data, there are well established relationships between satellite-derived metrics and forest-derived physical characteristics (Brown et al. 1989). Optical data dominates the field, as the relationship between the optical reflectance spectrum and vegetation is well understood in comparison to the relationship between satellite radar data and vegetation. However, it is limited by cloud cover and time of day. As radar satellite data becomes ever more widely available, its advantages over optical data make it an asset for studying vegetation (Kim et al. 2012). Unlike optical data, radar is not hindered by time of day or cloud cover and can return information about the various layers of vegetation, as longer wavelengths can penetrate through the forest canopy (Treuhaft et al. 1996; Balzter 2001).

Earth Observation techniques have been used to monitor forest change and damage from a range of environmental disturbances including wildfires, flooding and drought (Zhu et al. 2012; Coppin et al. 1994; Masek et al. 2008; Michener et al. 1997; Gouveia, Trigo, et al. 2009). Fires, and the impact they have on vegetation, have been studied using both optical and radar earth observation methods to monitor fire extent and map areas of burn severity (White et al. 1996; Ban et al. 2020). Vegetation changes due to flooding have been detected using high resolution optical data (Michener et al. 1997). Similarly, drought impacts on vegetation have been studied through optical indices, such as the Normalised Difference Vegetation Index (NDVI) and soil moisture index to investigate drought extent, duration and severity (Gouveia, Trigo, et al. 2009). A restriction of using satellite data to study forest disturbance is the size of the disturbed area, which must be within the resolution range of the sensor in order for it to be detectable (White

et al. 1996), smaller areas of disturbance could be missed as a result.

1.2.1 Optical Remote Sensing

Optical remote sensing is a passive form of remote sensing, utilising the visual, infrared and thermal bands of the electromagnetic spectrum between 400-15,000 nm. The optical properties of a canopy largely depend on the characteristics of the leaves, including leaf structure, leaf area, chlorophyll content, and indirectly on soil moisture through its effect on vegetation health (Jiang et al. 2008). These properties provide a direct indication of plant health from optical reflectance data (Jacquemoud et al. 1990). However, optical data has limitations, as it can only be retrieved during daylight hours, due to it requiring sunlight as its energy source (passive remote sensing). Data acquisition can also be blocked by cloud cover, this can be particularly difficult for studying volcanoes, as many, particularly those in inaccessible regions where remote sensing would be most beneficial, are in tropical regions with extensive cloud cover.

Vegetation Indices

Optical satellite images can provide valuable information, as they are relatively easy to interpret and can be used to monitor land cover or detect changes by simply comparing images. But often, spectral indices are used to highlight features in the data, such as water, urban areas, or vegetation, providing a more detailed view of land cover and changes. Vegetation health and coverage is often ascertained by using vegetation indices, using wavelength combinations that highlight areas of high or low vegetation coverage. There are countless vegetation indices to highlight different aspects of the vegetation spectra, the three most commonly used to monitor vegetation health, coverage or disturbance are the Normalised Difference Vegetation Index (NDVI), the Enhanced Vegetation Index (EVI) and the Normalised Burn Ratio (NBR).

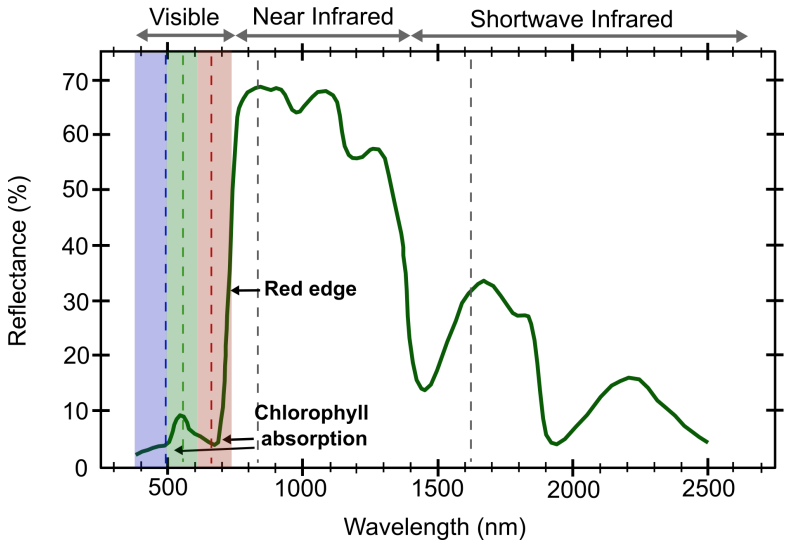

Figure 1.1: Spectral reflectance curve of green vegetation modified from Clark (1999). The visible, near infrared and short wave infrared parts of the EM spectrum are highlighted, along with the blue, green and red sections of the visible spectrum. The dashed lines represent the wavelengths of the respective bands from Sentinel-2.

To understand the different indices it is important to understand the reflectance spectra of vegetation (Figure 1.1). The reflectance spectra of healthy, green vegetation is characterised by low reflectance in the blue, green and red bands, with the lowest reflectance at ∼690 nm due to chlorophyll absorption, followed by a sharp increase in reflectance between the red band and the near infrared (NIR) band (Figure 1.2) (Myneni et al. 1995; Clark 1999; Agilandeeswari et al. 2022). The high reflectance in the NIR is due to the internal leaf structure, with the mesophyll cells scattering NIR wavelengths (Slaton et al. 2001). This sharp transition from maximum absorption to maximum reflectance is called the red edge and is very distinctive for healthy vegetation (Horler et al. 1983). As such, most vegetation indices rely on this sharp transition to indicate vegetation health. If a plant loses chlorophyll the absorption will be reduced, or if there are changes to the internal leaf structure, due to damage, the reflection maximum will be reduced, changing the steepness of this red edge transition.

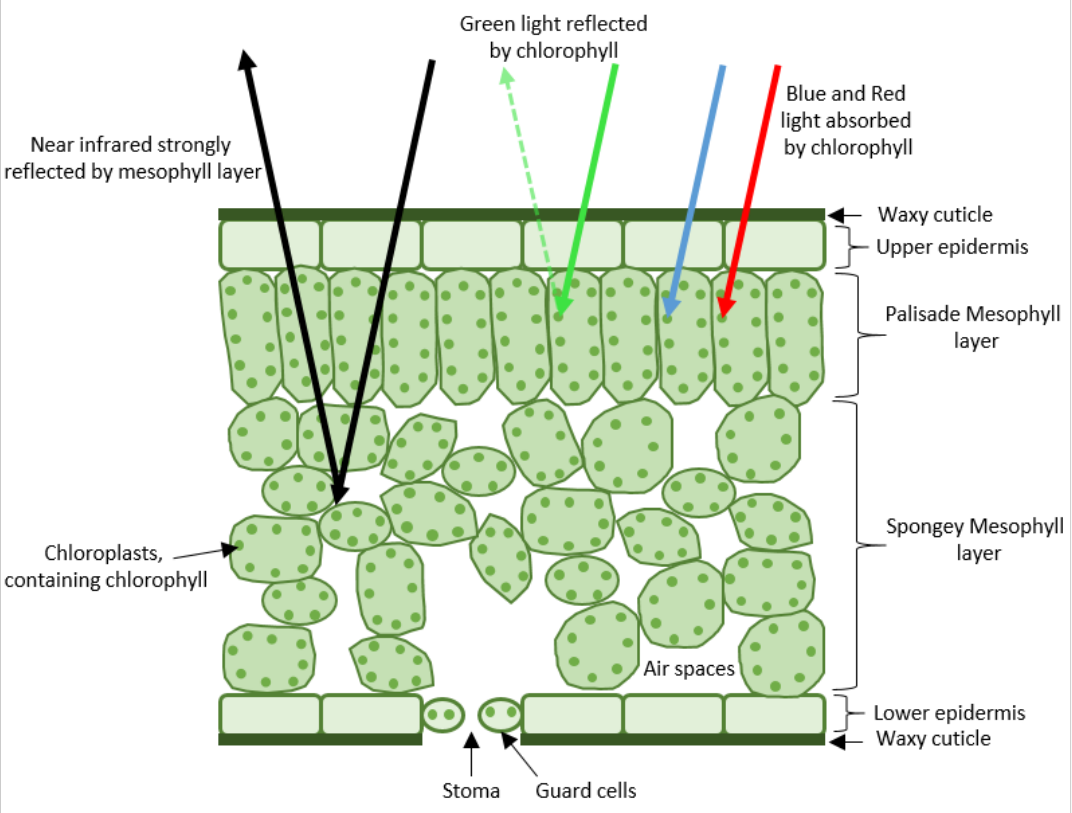

Figure 1.2: A diagram of the internal structure of a leaf, and how it affects the absorption/reflection of the optical and near-infrared wavelengths, modified from (Ustin and Jacquemoud 2020).

Normalised Difference Vegetation Index

The Normalised Difference Vegetation index (NDVI) is one such index that takes advantage of this red edge to assess vegetation quantity and health (Myneni et al. 1995), as shown in the equation below.

$$NDVI = \frac{NIR - R}{NIR + R} \tag{1.1}$$

This is one of the most widely used vegetation indices, due to its simplicity and ability to be used with any multispectral sensor (Huang et al. 2021). NDVI values range from -1 to 1, vegetation is indicated by strong positive values, due to the red edge, values that are close to zero or negative indicate non-vegetated areas, as the red edge is not

present. NDVI has been used to monitor vegetation coverage and health, and has been shown to be effective at capturing gradual changes in vegetation as well as more abrupt disturbances (Goetz et al. 2006; Bai et al. 2008; Tian et al. 2015). Consequently, it should be a useful tool for detecting the change in vegetation following a volcanic eruption and the subsequent recovery.

Enhanced Vegetation Index

The Enhanced Vegetation Index (EVI) similarly utilises the NIR and red bands and the characteristic red edge, as shown in the equation below (Jiang et al. 2008).

$$EVI = G\frac{NIR - R}{NIR + C_1R - C_2B + L} \tag{1.2}$$

It was intended to improve sensitivity in higher biomass areas and reduce atmospheric noise. G is a gain factor, C_1 and C_2 are the atmospheric correction coefficients and L is the soil-adjustment factor (Jiang et al. 2008). These values were empirically estimated through simulations and analysis of MODIS data across a range of vegetation types and atmospheric conditions, with a focus on minimising aerosol-related errors and improving vegetation signal sensitivity (Jiang et al. 2008; Huete et al. 2002; Liu et al. 1995). The standard values are used for MODIS, Landsat and Sentinel-2 instruments but can be adjusted for specific applications or ecosystems (Morais et al. 2021). The EVI has been shown effective in land cover and change detections and is particularly effective over cropland to differentiate different growing signals, in comparison to the NDVI (Jiang et al. 2008). However, EVI is more sensitive to topographic changes, a factor that will be important to consider as I will be comparing volcanoes with varying topography (Matsushita et al. 2007).

Normalised Burn Ratio

The Normalised Burn Ratio, unlike the previous indices, does not utilise the red edge. Instead it uses the near infrared and short-wave infrared (SWIR) bands to detect and

map burnt areas and burn severity (Picotte et al. 2011; Roy, Boschetti, et al. 2006).

$$NBR = \frac{NIR - SWIR}{NIR + SWIR} \tag{1.3}$$

Given the likely similarities between the damage caused by fire and that caused by volcanic eruptions, this could prove to be a valuable index. However, it may struggle to detect volcanic deposits that do not burn vegetation (e.g. tephra, volcanic blast) and it may struggle to differentiate between levels of damage to vegetation as it does not use the red edge. In Sentinel-2 the spatial resolution of the SWIR band is lower than the NIR and R band (20 m compared to 10 m), an important consideration particularly for looking at impacts over smaller areas.

1.2.2 Radar Remote Sensing

Radar is an active form of remote sensing, emitting its own signal which interacts with the ground surface and is then recorded back at the sensor. This has benefits over passive sensors as it is not limited by time of day or cloud cover, however, it is more complex to process and interpret. I use synthetic aperture radar data, which takes advantage of the Doppler effect of the moving satellite to simulate a larger antenna, providing higher resolution images (Balzter 2001; Hanssen 2001). In SAR imaging, data are acquired in radar geometry, defined by two principal directions: azimuth and range. The azimuth direction is the along-track direction, following the direction of travel of the satellite. The range direction is oriented perpendicular to the azimuth, and increases from the near-range to the far-range (Woodhouse 2017). For SAR, the spatial resolution describes the ability to distinguish objects in both the range and azimuth directions. Range resolution depends on the systems bandwidth and incidence angle, while azimuth resolution is achieved through the aperture synthesis concept, using the Doppler effect to simulate a much larger antenna. It is of note that the spatial resolution of a SAR image is different to its pixel spacing (Woodhouse et al. 2011). For example, a Sentinel-1 L1 single look complex (SLC) has a spatial resolution of 2.7-3.5x22m (slant range x azimuth)

but a pixel spacing of 2.3x17.4 m (ESA 2013). The ground range resolution varies due to the side-looking geometry of SAR, increasing from the near to the far field with increasing incidence angle. Radar waves can be vertically or horizontally polarised (1.3), both in terms of the outgoing wave and the recorded polarisation of the incoming wave. Most common is a VV polarised wave (vertical emitted, vertical received), but cross-polarised radar is better for detecting vegetation properties as vegetation is a volume scatterer (Imperatore et al. 2017), meaning the radar signal penetrates the canopy and interacts with internal structures like leaves and stems, producing complex backscatter from multiple scattering effects.

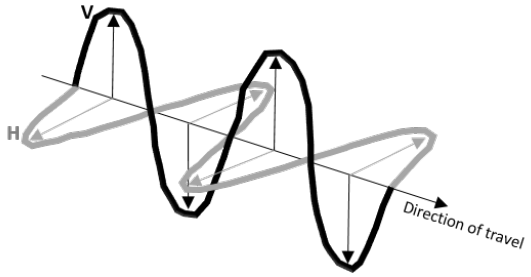

Figure 1.3: A diagram of vertical and horizontal radar polarisations.

Different radar wavelengths interact with different sized scatterers and reach different depths of the canopy (Figure 1.4). Generally, within a forest canopy, the smaller scatterers (e.g. leaves and twigs) are near the top, and larger scatterers (branches and trunk) are near the bottom. As a result, increasingly longer wavelengths are able to penetrate through the canopy, down to the forest floor (Woodhouse 2017). Radar techniques to monitor vegetation include the use of backscatter, coherence and polarimetry, which can provide information on vegetation coverage, layer depth, tree height and Above Ground Biomass (AGB) (Treuhaft et al. 1996; Askne et al. 1997; Evans et al. 1988). Of these derived second order values, most common for vegetation is the AGB, which is the dry mass of all plant material above the soil surface, typically expressed in Mg ha^{-1} (Mitchard et al. 2009; Lewis et al. 2013; Kumar et al. 2017). AGB can be estimated a number of ways from first order values. Backscatter is one such way, as there is a strong positive relationship between backscatter and AGB calculated from field studies (Mitchard

et al. 2009), particularly for long wavelengths and cross polarisation, although shorter wavelengths and co-polarisation can also provide useful estimates (Mitchard et al. 2009; Woodhouse 2017)

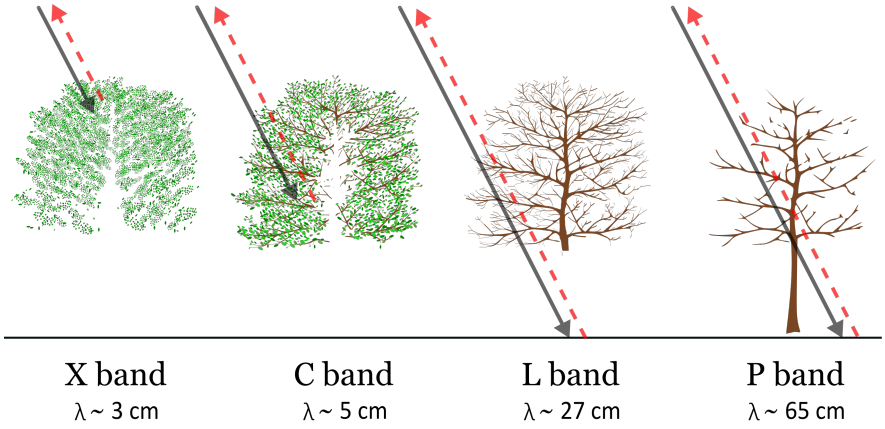

Figure 1.4: A diagram of different radar wavelengths and the dominant scattering elements they interact with in a forest context.

Backscatter

Radar sensors emit an electromagnetic pulse and record the returning signal which has been directed back from the surface (backscatter). Radar backscatter can be used to make estimates of forest biomass, due to the inferred relationship that as biomass increases backscatter also increases. This is particularly true at longer wavelengths (P-band) as the backscatter values continue to increase with increasing biomass, compared to shorter wavelengths where the backscatter return saturates at lower biomass values (Woodhouse 2017; Mitchard et al. 2009).

The backscatter coefficient, also known as the normalised radar cross section (σ_0), is defined as the energy scattered back from the ground surface at a given distance (R), normalised by the area illuminated (A) by the satellite where ρ_T and ρ_R are the intensities of the incident and received waves, respectively (Equation 1.4) (Woodhouse 2017; Dualeh et al. 2021).

$$\sigma_0 = \frac{4\pi R^2 \rho_R}{\rho_T A} \tag{1.4}$$

The backscatter coefficient is sensitive to satellite parameters like the incidence angle, wavelength and polarisation as well as scattering properties on the ground which change with surface roughness, slope, and dielectric properties (Dualeh et al. 2021). Vegetation, being a volume scatterer, typically has higher backscatter than bare ground, as the multiple deflections within the canopy result in a higher proportion of the incoming signal being returned to the sensor. Backscatter has been used to monitor vegetation (Treuhaft et al. 1996; Askne et al. 1997; Thiel et al. 2016), vegetation changes as a result of natural hazards like wildfires (Ban et al. 2020; Imperatore et al. 2017) and to study volcanic deposits (Dualeh et al. 2021; Babu et al. 2019). Hence, vegetation changes caused by volcanic eruptions, such as defoliation, or complete vegetation removal, should be detectable through changes in radar backscatter, as these disturbances alter the volume scattering behaviour by reducing or eliminating internal canopy structures that contribute to the signal.

Coherence

The phase coherence is used to show how similar two waves, or acquisitions are. Two waves are considered to be coherent if their difference in phase remains the same with time. Coherence is defined as the complex cross correlation between two waves E_1 and E_2, which gives a value between 0 and 1, with 0 being completely incoherent and 1 being completely coherent (Woodhouse 2017; Dualeh 2022; Babu et al. 2019).

$$\Gamma = \frac{\Sigma_N E_1 E_2}{\sqrt{\Sigma_N \mid E_1 \mid^2 \Sigma_N \mid E_2 \mid^2}} \tag{1.5}$$

Surfaces that do not change between acquisition, like bare ground, have higher coherence than those that do, like vegetation. Vegetation is a volume scatterer, with the incoming radar being scattered multiple times within the canopy. These canopy elements will move between acquisitions and will also have changing roughness and dielectric properties, meaning it has very low coherence. Coherence will vary with wavelength, shorter

Table 1.2: Summary of the satellites used in this thesis including key characteristics (Torres et al. 2012; Drusch et al. 2012; Irons et al. 2012)

Satellite	**Type**	**Mission length**	**Bands**	**Spatial resolution**	**Repeat time**
Sentinel-1	Radar (C-band)	April 2014 - present	VV,VH,HH,HV	2.7-3.5x22m (IW mode)	12-day (6-day combined)
Sentinel-2	Optical/IR	June 2015 - present	13 spectral bands	10m	10-day (5-day combined)
Landsat 8	Optical/IR	February 2013 - present	11 spectral bands	30m	16-day
Landsat 7	Optical/IR	April 1999 - April 2022	8 spectral bands	30m	16-day
Landsat 5	Optical/IR	March 1984 - May 2012	7 spectral bands	30m	16-day
Landsat 4	Optical/IR	July 1982 - December 1993	7 spectral bands	30m	16-day

wavelengths will result in lower coherence, as these smaller scatterers are often the least stable. Longer wavelengths, that interact with larger elements like branches, trunks and penetrate to the ground surface will be more coherent as these elements are more stable (Balzter 2001). Absolute coherence values can be used to indicate ground surface properties, with thresholds set to identify areas of low coherence, possible due to vegetation (Burrows et al. 2019; Refice et al. 2014). Alternatively, double difference coherence can identify areas of coherence change and has previously been used to monitor and detect natural hazards such as landslides and wildfires, as increases in coherence demonstrate areas of vegetation loss (Yun et al. 2015; Burrows et al. 2019; Liew et al. 1999)

A summary of the optical and radar satellite instruments used throughout this thesis can be found in Table 1.2. The spatial resolution varies by band for Sentinel-2 and Landsat 8, the resolutions stated refer to the bands used in this study.

1.3 Thesis Aims

This thesis aims to use satellite data to monitor vegetation damage at volcanoes worldwide, as a novel proxy to measure eruption deposits, distribution, duration and magni-

tude. I will use optical and radar satellite data to quantify the damage caused to forests as a result of volcanic eruptions to improve deposit maps, monitoring and understanding of forest disturbance caused by volcanic eruptions. My key aims for the thesis are as follows:

1. Investigate which optical and radar satellite methods are best suited for capturing vegetation changes caused by volcanic eruptions.
2. Study the different impacts explosive and effusive eruptions can have on forests, and the subsequent satellite signature.
3. Explore forest changes at a range of global volcanoes to better understand how the impact varies with eruption style and ecological setting.

1.3.1 Thesis Structure

In this thesis I will use optical and radar satellite data to identify and measure the impacts of volcanic eruptions on forests.

In Chapter 2, I use the 2015 eruption of Calbuco to identify and introduce the most suitable data and methods to detect forest disturbance due to an explosive volcanic eruption. I use NDVI, radar backscatter and phase coherence to study changes in vegetation coverage due to the eruption. I use k-means cluster analysis to spatially group damaged areas as a novel proxy for deposit mapping in intensely damaged zones. This chapter has been published in *Journal of Volcanology and Geothermal Research* (Udy et al. 2024).

In Chapter 3, I investigate the impacts of volcanic gases on vegetation and the scale (both temporal and spatial) over which damage and recovery can be measured from optical and radar satellite data. I do this at 5 case studies in different environmental settings and with gas emission at different scales. This chapter has been written up as a paper to be submitted to *Earth and Planetary Science Letters*.

In Chapter 4, I use NDVI and k-means cluster analysis to analyse forest disturbance, recovery and resilience following eruptions at 18 volcanoes worldwide. I quantify vegetation damage and recovery across different eruption types, magnitude, durations and

forest biomes, to identify patterns linking recovery times to volcanic processes and environmental settings.

In Chapters 2-4, I use plural pronouns (e.g. we, us, our etc.) as these chapters are from joint-author work that is either published or is currently being prepared for publication, the co-author contributions have been explicitly stated on pages iii-iv.

Chapter 2

Satellite Measurement of Forest Disturbance from Volcanic Eruptions

Abstract

The characteristics and extent of forest damage, and the subsequent patterns of recovery, reflect the intensity of an explosive volcanic eruption and have the potential to be a novel proxy for eruption magnitude and impact. Using satellite measurements of vegetation damage and recovery patterns, following the 2015 explosive eruption of Calbuco, Chile, we assess the impact on surrounding temperate forests and how areas impacted by different deposit types recover post-eruption. The Calbuco eruption resulted in tephra deposition over hundreds of square kilometres, pyroclastic flows extending 6 km and lahars extending 15 km. We explore NDVI derived from optical imagery (June 2013 - May 2023) as well as radar backscatter and phase coherence (October 2014 - June 2023) through time series analysis, clustering and estimation of recovery timescales to find patterns in forest disturbance and recovery. We find that forest damage and recovery correspond primarily with deposit type, thickness and dispersal directions. The thickest

tephra deposits (> 40 cm) correlate with the most vegetation loss, so our vegetation impact maps allow us to refine the spatial mapping of tephra fall-deposit isopachs to give a revised eruption volume of 0.28 km^3. Vegetation recovery rates relate to initial impact type and intensity, but also local topography, aspect and altitude. Our results demonstrate a novel application of optical and radar satellite remote sensing to determine eruption extents and magnitudes through vegetation disturbance. We show that measuring vegetation disturbance, particularly in remote and densely vegetated environments, can help refine field-based analyses in inaccessible or intensely damaged zones.

2.1 Introduction

Explosive volcanic eruptions can cause widespread impacts on their surrounding environment, ranging from total destruction and burial of vegetated landscapes through to minor and temporary damage (Dale, Swanson, et al. 2005; Grilli, Tappin, et al. 2019; Major and Lara 2013). The extent and style of damage reflects the intensity and mechanism of the driving volcanic process. Timescales and patterns of regrowth potentially reflect both the nature of initial impacts and local floral, climatic, and environmental parameters (Foster et al. 1998; Swanson and Major 2005). Vegetation damage therefore holds potential as a novel proxy for the magnitude and nature of volcanic eruptions, enabling evaluation of the long-term environmental consequences of volcanic events. If we can calibrate the scale of vegetation damage to the nature of the driving process, this is a potential route to estimating eruption magnitudes and deposit volumes, particularly in remote volcanic environments.

Freely available, global-coverage satellite data, provides an opportunity to systematically study relationships between volcanic eruptions and vegetation. By mapping forest recovery after a sudden disturbance event, we can gather data on the timescales and patterns of vegetation succession and ecosystem recovery. This allows us to test if, and how the post-disturbance recovery is controlled by the initial impacts (Dale, Delgado-Acevedo, et al. 2008; Moral et al. 1993). If recovery timescales can be better understood, such methods hold the prospect of evaluating the impacts and magnitude of unobserved

eruptions.

Here, we use the 2015 eruption of Calbuco volcano, Chile, to develop a satellite-based analysis of the impact of explosive volcanic eruptions on forest environments. This eruption is an ideal case to develop our approach, given that it occurred during an era of frequent high-resolution satellite coverage, and in a densely vegetated proximal environment that was affected by tephra fall deposition, lahar deposits and pyroclastic density currents. We map the extent and timescale of vegetation damage and recovery detected from satellite imagery, and identify the extent of the impacts from different eruption mechanisms, using this to categorise the damaged vegetation. We calibrate our results using ground-based observations to better map out the dispersal pattern of erupted material.

2.1.1 Impact of Volcanic Eruptions on Forests

The nature and timescale of volcanic impacts on vegetation are dependent on the volcanic process and its magnitude, alongside regional and local ecologies. The damage caused by large explosive eruptions can be particularly extensive, reaching thousands of square kilometres (Carey and Sigurdsson 1989; Self 2006). Pyroclastic density currents (PDCs) generated during explosive eruptions generally have topographically controlled distributions, destroying vegetation with which they come into contact through burning, erosion, abrasion or burial, and can singe areas adjacent to the flow deposit (Charbonnier et al. 2013). In contrast, tephra fall deposits cause less intensive damage but cover a much greater area, without topographic controls. Impacts from tephra fall deposition range from burial and branch breakage for intense and thick fallout, through to abrasion damage and defoliation for thinner and finer ash deposition (Wilson, Stewart, et al. 2013; Wilson, Jenkins, et al. 2015; Wilson, Cole, et al. 2011; Turner et al. 1997). Lahars, which occur during or after an eruption through the mixing of volcanic particles with water, are highly erosive flows that damage vegetation through channel-wall erosion and, downstream, by inundation and burial of adjacent landscapes beyond the outer flanks of volcanoes (Castruccio and Clavero 2015).

Eruption rate, transport mechanism, deposit thickness and volume, and grain coarseness may all also affect the degree of damage or destruction of vegetation (Dale, Delgado-Acevedo, et al. 2008; Ayris et al. 2012; Swanson, Jones, et al. 2013; Zobel et al. 1997). The temperature of deposit emplacement (for example, high temperature PDCs versus cold lahars) may be significant in controlling the style and extent of damage (Charbonnier et al. 2013). Chemical characteristics, including volatile species, soluble salts or mobile trace elements, may influence vegetation impacts and the longevity of environmental damage. For example, the presence of chlorine in volcanic gas can cause chemical toxicity in vegetation and acidification through ash deposition, contributing to vegetation loss (Swanson, Jones, et al. 2013; Lowenstern et al. 2012; Dale, Delgado-Acevedo, et al. 2008). Volcanic deposits can influence vegetation patterns by affecting soil structure and composition (Ayris et al. 2012; Dale, Delgado-Acevedo, et al. 2008). In forested environments, the degree of damage is dependent on the duration and/or frequency of exposure to eruption impacts, with sustained exposure likely to impede recovery (Foster et al. 1998), as well as the mechanisms involved and their relative magnitude. Recovery timescales are influenced by local climatic and environmental conditions, the extent of environmental degradation (e.g. hydrographic changes, soil burial) caused directly by the eruption, and the nature of the local forest ecosystem. For example, regrowth and succession timescales in tropical forests can be very rapid in comparison to high-latitude environments (Moral et al. 1993; Foster et al. 1998; Gillman et al. 2015). Patterns of damage can also vary between eruption processes. Tephra fall deposits or blasts typically produce sectoral patterns decaying away from the eruption site. In contrast, lava flows, lahars and PDCs have a more linear impact pattern, mainly influenced by topography, with similar degrees of damage along the main transport pathway (Foster et al. 1998). Volcanic gases contribute to vegetation damage, both during an eruption or via passive emission, and either indirectly (e.g. soil alteration or acid rain) or directly (e.g. direct gas exposure leading to plant death) (Lowenstern et al. 2012; Smith 1981; Delmelle 2003; Gerlach et al. 2001).

The disturbance pattern has an influence on the post-eruption recovery of vegetation

(Foster et al. 1998). Linear disturbances from lahars, lava flows and PDCs, may be adjacent to healthy, relatively undisturbed and mature vegetation, with a sharp boundary. This influences recovery and succession at the margins of damaged areas, with nearby seed sources promoting regrowth within narrow damage zones (Foster et al. 1998). Conversely, sectoral patterns of disturbance from blasts or tephra fall are characterised by gradational damage patterns. The most intensely damaged parts of these regions may be slow to recover due to their distance from undamaged vegetation and the severity of damage (Dale, Delgado-Acevedo, et al. 2008), while marginal zones may recover rapidly. Surviving plant matter is key to recovery as it is essential to instigate regrowth (Franklin et al. 2000; Franklin 1990; Dale, Crisafulli, et al. 2005). Post-disturbance vegetation recovery rates can vary, and may be exponential or linear depending on vegetation type, the stage of regrowth and how the recovery is measured (Viedma et al. 1997; Jong et al. 2012; Buitenwerf et al. 2018; Bonesmo et al. 1999; Bastos et al. 2011).

2.1.2 Estimation of Forest Properties from Satellite Data

Satellite data provides global information about the state of vegetation (Dorigo et al. 2007). Forest characteristics used to assess health and growth rate, such as tree height, tree diameter and wood density, are not directly measurable from satellite imagery (Brown et al. 1989). However, there are well established relationships between many satellite-derived metrics and forest-derived physical characteristics (Mitchard et al. 2009; Santin-Janin et al. 2009). The relationship between the optical reflectance spectrum (between 400-15,000 nm wavelength, containing the visual, infrared and thermal bands) and vegetation is relatively well understood. The reflectance of a forest largely depends on characteristics of leaves and soil, including leaf structure, chlorophyll content and soil moisture, giving a direct indication of plant health (Jacquemoud et al. 1990). However, the application of optical data is limited by cloud cover or regions of high biomass where the signal saturates (Song 2013).

Satellite radar, dominantly Synthetic Aperture Radar (SAR), ($\sim$ 3-100 cm wavelength) is not limited by time of day or cloud cover (Kim et al. 2012). Radar can also return

information about vegetation heights due to its longer wavelength, allowing it to penetrate through the top vegetation layer (Treuhaft et al. 1996; Balzter 2001). Different radar wavelengths interact with different sized scatterers and reach different depths of the canopy. Generally, smaller scatterers are near the top and larger scatterers near the bottom of the canopy, and increasingly longer wavelengths are therefore able to penetrate through the canopy down to the forest floor (Woodhouse 2017). Vegetation can be monitored using radar backscatter, phase coherence and polarimetry (Treuhaft et al. 1996; Askne et al. 1997; Evans et al. 1988). Backscatter in particular, is used to estimate forest biomass, on the basis of empirical relationships (Woodhouse 2017; Mitchard et al. 2009) that are strongest at longer wavelengths (Woodhouse 2017; Mitchard et al. 2009).

2.1.3 Volcanic Eruption Impacts on Forests

The impact of explosive eruptions on vegetation has been investigated in detail at a handful of historical eruption sites (e.g. Mt St Helens, USA, 1980; Unzen, Japan, 1990-1995; Chaitén, Chile, 2008; Cordón Caulle, Chile, 2011)(Moral et al. 1993; Dale, Swanson, et al. 2005; Martin et al. 2009; Lai et al. 2022; Swanson, Jones, et al. 2013; Biass et al. 2022; Easdale et al. 2018; Smathers et al. 1972). There have also been regional investigations of ecosystem structures in eruption-impacted regions (e.g. (Grishin et al. 1996)) and global studies of specific impact types (e.g. tephra fall; (Biass et al. 2022; De Schutter et al. 2015; Easdale et al. 2018)). Studies that rely on field measurements, such as ash thicknesses or vegetation samples, tend to capture only one or a few points in time after an eruption (Martin et al. 2009; Swanson, Jones, et al. 2013). A subset of studies use tree ring data to understand the impact of volcanic eruptions on forests, demonstrating at a number of volcanoes (including Parictuin, Colima and Tacana) that ashfall inhibits growth of trees during eruption periods (Biondi et al. 2003; Carlón Allende, Macías, Mendoza, and Villanueva Díaz 2020; Carlón Allende, Macías, Mendoza, and Díaz 2022). Tree rings have also been used to identify lahar activity and pre-eruption enhanced growth through measurement of stable oxygen isotopes in tree rings (Franco-Ramos et al. 2016; Seiler et al. 2021).

Satellite studies rely primarily on metrics derived from optical imagery (Li et al. 2018; De Schutter et al. 2015; Easdale et al. 2018; Lai et al. 2022; Teltscher et al. 2018; Biass et al. 2022; Balzter 2001). While satellite radar data are widely used to investigate effusive and explosive volcanic deposits (Dualeh et al. 2021; Ebmeier et al. 2012; Jung et al. 2016; Babu et al. 2019), the focus is primarily on volcanic flow deposits (Head et al. 2012; Macorps et al. 2023) and studies can avoid vegetated areas, as they are a source of phase decorrelation (Zebker et al. 1992).

2.1.4 The 2015 Eruption of Calbuco

Calbuco is an andesitic arc stratovolcano located in the Southern Chilean Andes at 41.3° South. The land to the west is agricultural, but the flanks of the volcano and the land to the east and south are densely forested, and relatively undisturbed by human activity (Figure 2.1). The volcano has an elevation of 1974 m and is in a temperate broadleaf and mixed forest, characterised by high species diversity and high endemism (Olson et al. 2001; Echeverria et al. 2006). The climate at Calbuco is temperate oceanic, resulting in heavy rainfall throughout the year but with relatively warmer and drier summers (Peel et al. 2007). In the 100 years prior to the VEI 4 2015 eruption, Calbuco experienced explosive eruptions in 1972, 1961, 1945, 1932, 1929, 1927, and 1917; all of these had lower estimated magnitudes (VEI 3 or lower) than the 2015 eruption (Global Volcanism Programme 2015; Romero, Morgavi, et al. 2016). Historical eruptions have involved tephra fall deposition, lava flows, lahars and PDCs (Global Volcanism Programme 2015). Although these previous eruptions have impacted the forested flanks of Calbuco, their lower magnitude means that their footprint was likely smaller than the 2015 event, and the 43 year hiatus in activity since the previous eruption has provided a long recovery period. There are detailed independent observations of the 2015 eruption, with some mention of specific damage to vegetation (Castruccio, Clavero, et al. 2016; Romero, Morgavi, et al. 2016; Van Eaton et al. 2016).

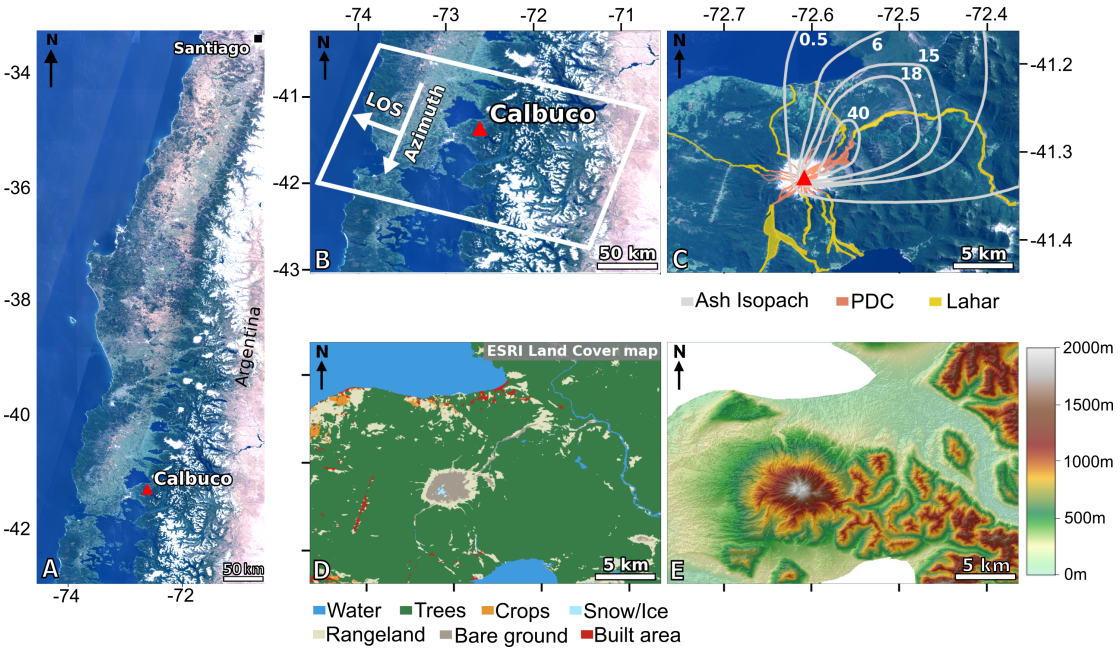

Figure 2.1: A) Sentinel-2 optical satellite image showing the location of Calbuco within Chile, and in relation to the capital of Santiago B) Sentinel-2 optical satellite image showing the location of Calbuco with the Sentinel-1 tile used, with the line of sight and azimuth direction shown. C) Sentinel-2 optical satellite image showing the location of PDC, lahar and tephra deposits from a combination of Hayes et al. (2019), Mella et al. (2015), Castruccio, Clavero, et al. (2016), and Romero, Morgavi, et al. (2016) and our own mapping. D) ESRI land cover map of Calbuco in 2022. E) A TanDEM-X digital elevation Model of Calbuco. The geographic extents of panel D and E are the same as panel C. Where necessary the keys required are below their relevant panel.

The 2015 eruption of Calbuco began on the evening of the 22nd of April and involved two main explosive pulses. The initial pulse began soon after the start of the eruption and lasted ∼90 minutes, generating a 15 km high plume dispersed on an azimuth of 48°. A second, more intensive pulse followed on 23rd April, lasting six hours and generating a >15 km high plume, dispersed on an azimuth of 55° (Romero, Morgavi, et al. 2016). Umbrella cloud expansion patterns suggest slightly different dispersal axes, of ∼35° for the first pulse, alongside a more northerly component, and ∼50° for the second pulse (Van Eaton et al. 2016), broadly consistent with the dispersal axes constructed from tephra deposits in Castruccio, Clavero, et al. (2016). Continued venting, with columns <2 km high, occurred over several days, with a further pulse and 4 km high column on 30th April (Romero, Morgavi, et al. 2016). The eruption caused tephra

fall to the NE of the volcano, as shown by the isopachs in Figure 2.1 from Romero, Morgavi, et al. (2016). Romero, Morgavi, et al. (2016) identify four units in the tephra fall deposits, interpreting the two larger-volume central layers as corresponding to the two main eruption pulses, with the bounding layers representing activity leading into and out of these phases. Dispersal patterns of the two thickest layers are consistent with the satellite-observed dispersal directions, although constraints on very proximal depositional patterns are limited due to inaccessibility on the flanks of Calbuco. The total tephra fall deposit volume was estimated at 0.27 km^3 (Romero, Morgavi, et al. 2016) (a separate estimate of 0.34 km^3 is given by Castruccio, Clavero, et al. (2016)), with ∼38% of the volume erupted from the first pulse, and ∼46% from the second pulse (the remaining volume being erupted by subsequent activity) (Romero, Morgavi, et al. 2016). Pyroclastic flows, channelised within radial valleys, occurred on the N, NE, W and S flanks of the volcano, as seen in Figure 2.1 (based on previous channel deposit maps and our own satellite observations), reaching up to 8 km from the vent and with a total bulk volume of ∼0.07 km^3 (Global Volcanism Programme 2015; Castruccio, Clavero, et al. 2016; Romero, Swanson, et al. 2023). Concentrated PDCs were generally channelised along river valleys, with more extensive impacts to a distance of 4 km NE of the vent. Within areas impacted by concentrated PDCs, deposits reached several metres in thickness, and vegetation death occurred through toppling, burial, and charring, with flow temperatures estimated at ∼500°C. Marginal zones, scorched by dilute PDCs, did not experience total death of vegetation, with surviving trees subsequently re-sprouting (Romero, Swanson, et al. 2023). Syn-eruptive lahars extended down river channels beyond the limits of PDC deposits, extending to coastal or lake outflows to the N, S and E (Global Volcanism Programme 2015; Castruccio, Clavero, et al. 2016). Following the final explosive eruption episode on the 30^{th} of April, low level activity continued throughout May until the eruption was deemed to be over on the 26^{th} of May (Global Volcanism Programme 2015).

2.2 Methods

2.2.1 Data

Optical Imagery

We extracted surface reflectance data from Sentinel-2 and Landsat 8 through Google Earth Engine. Sentinel-2, comprising Sentinel-2a and Sentinel-2b, has a 5 day repeat time with spatial resolution of 10 m and Landsat 8 has a 16 day repeat time with 30 m spatial resolution. The level 2 data used in this work have been atmospherically corrected (Main-Knorn et al. 2017; Vermote et al. 2016). We then used Google Earth Engine to remove any acquisitions with more than 40% cloud cover. A cloud mask using the pixel Quality Assurance band (Foga et al. 2017; Main-Knorn et al. 2017) was applied to the remaining dataset, and any images that still contain clouds were removed manually. This resulted in a dataset of 79 Landsat-8 images and 162 Sentinel-2 images spanning from June 2013 to May 2023.

Radar Imagery

We used radar images obtained from Sentinel-1 (from descending track 83), a satellite constellation that consisted of Sentinel-1a and Sentinel-1b (until Sentinel-1b failed on the 23rd of December 2021). Sentinel-1 uses a C band (6 cm) synthetic aperture radar (SAR), with a revisit time of 6 days (when 1a and 1b are combined) and a geometric resolution of 5 m x 20 m in interferometric wide swath (IW) mode, which is the default mode over land (Torres et al. 2012). We used 201 Single Look Complex (SLC) images from October 2014 until June 2023, accessed through the Nasa ASF data portal. We limited our analysis to single polarisation (VV), as dual polarisation was not available for all acquisitions. The SLCs are geo-referenced, focused SAR images in slant range geometry.

Study Areas

Throughout this article, we use five sites around Calbuco (Figure 2.2) to illustrate the impact of different volcanic deposits on vegetation and recovery rates. We selected three areas impacted by tephra fall, one impacted by channelised PDC deposition and one area not directly impacted by the eruption material. The study sites have been selected to only contain pixels impacted by the specified deposit type, and the mean pixel value is then taken for each study area. The style of initial impact was independently verified using reported post-eruption observations (Global Volcanism Programme 2015; Hayes et al. 2019; Van Eaton et al. 2016; Romero, Morgavi, et al. 2016). A detailed description of these study areas is provided in Section A2 in the appendix.

2.2.2 Optical Remote Sensing

We used the optical imagery to calculate Normalised Difference Vegetation Index (NDVI), a widely used index that utilises the relationship between chlorophyll reflectance in the infrared and red spectral bands to assess quantity and health of vegetation (Santin-Janin et al. 2009; Myneni et al. 1995; Veloso et al. 2017; Goetz et al. 2006; Bai et al. 2008; Tian et al. 2015). We chose this index over alternatives such as the normalised burn ratio or enhanced vegetation index because it is a traditional vegetation index that has been proven to be effective in showing vegetation disturbance and recovery, particularly for characterising post-fire recovery (Veraverbeke et al. 2012; Chen, Vogelmann, et al. 2011; De Schutter et al. 2015). We expect it will perform better at differentiating volcanic impact types, and assessing vegetation health, rather than just structural changes, as it is chlorophyll sensitive and better suited to areas of changing topography (Roy, Boschetti, et al. 2006; Matsushita et al. 2007; Lai et al. 2022).

NDVI values range from -1 to 1; dense, healthy vegetation is indicated by strong positive values, due to high near infrared reflectance and low red reflectance associated with chlorophyll containing cells, while values close to zero or negative indicate non-vegetated areas. We generated time series of NDVI to highlight areas of significant change and to

capture the footprint of volcanic deposits (De Schutter et al. 2015; Gouveia, DaCamara, et al. 2010; Marzen et al. 2011; Gouveia, Trigo, et al. 2009; Michener et al. 1997; Lu et al. 2012; Chou et al. 2009; Easdale et al. 2018).

2.2.3 Satellite Radar Backscatter and Coherence

SAR sensors emit an electromagnetic pulse and measure the returned signal that is directed back from the ground (backscatter). We estimated backscatter from the Sentinel-1 dataset using the GAMMA remote sensing software (Werner, Schmid, et al. 2018) following the processing steps outlined by Werner, Wegmüller, et al. (2000) including terrain correction and radiometric calibration, summarised by Figure A.1. We limited our analysis to five bursts (2-6, middle swath, descending track 83). The SLC was deramped to account for the Doppler centroid generated by the TOPS ScanSAR mode (Yagüe-Martínez et al. 2016), and the 5 bursts were mosaicked together and co-registered to a common date (23/10/2014). We multi-looked over a window size of 10×2 in the range and azimuth direction respectively to produce a multi-look intensity image (MLI) (Lee, Grunes, et al. 1994). We performed terrain corrections and radiometric calibrations using the TanDEM-X digital elevation model to mitigate for the impact of topography on backscatter, remove geometric and radiometric image distortions and decrease sensitivity to fluctuations in incidence angle (Dualeh et al. 2021; Meyer et al. 2015; Small 2011). We geocoded the images using the same DEM to produce 201 backscatter images. We then produced time series of backscatter for the 5 study areas by averaging the pixel values. We produced backscatter difference maps to view the changes associated with the eruption impacts and post-eruption regrowth.

We constructed interferograms for the sequential 24-day pairs within our dataset and estimated phase coherence for each pair using a 5×5 sliding window (Hanssen 2001). We chose 24-day coherence due to the temporal resolution of our dataset, in order to maximise the number of coherence images we could use for cluster analysis. Interferometric phase coherence is commonly characterised by estimating the complex correlation

coefficient between two SAR images and ranges from 0 (completely incoherent) to 1 (completely coherent) (Just et al. 1994). Rapidly changing surfaces, like vegetation, will have low coherence (values close to 0) compared to more stable scattering surfaces, like bare ground, which have high coherence (values closer to 1) (Zebker et al. 1992; Babu et al. 2019; Dualeh et al. 2021). Damage to the vegetation due to volcanic deposits should be detected by changes in coherence, with vegetation loss resulting in a more stable surface and higher values of coherence. We produced time series of coherence, and use the convention of plotting coherence for each interval as the first date in the pair.

2.2.4 Cluster Analysis

We generated a time series for each of the pixels in the NDVI, backscatter and coherence datasets and used k-means clustering (Likas et al. 2003) to group the pixels sharing common trends. Before clustering we downsampled the images by a factor of 2 in both the azimuth and range directions, and removed acquisitions that have more than 10% NaNs. We removed any remaining NaNs by 2D linear interpolation, followed by zero-padding any regions unable to be interpolated. We found the optimal number of clusters for each dataset through experimentation and iterative refinement. For each dataset the k-means algorithm was run 10 times with different centroid seeds.

2.3 Results

2.3.1 NDVI

We show the changes in NDVI with time in Figure 2.2, for five selected study sites representing different initial impacts. Areas impacted by tephra fall deposition (Figure 2.2 panels A and B) all show an immediate decrease in NDVI of up to 85%, followed by a relatively rapid initial recovery until around 2018, when the rate of recovery slows but continues to increase steadily towards pre-eruption values. The magnitude of the co-eruptive decrease in NDVI correlates with the thickness of ash deposition (and the distance from the vent), as expected. However, the initial rate of recovery is highest for the region closest to the volcano. By early 2017, this region has higher NDVI values than

the other two tephra-impacted areas, by around 15%. This is in contrast to what would be expected if recovery rate were simply proportional to tephra thickness. The PDC-impacted area shows a different trend: immediately after the eruption, NDVI decreases by 99%. Compared to the tephra-fall areas, there is little recovery in NDVI until 2019, after which it increases linearly. By 2023, the NDVI in channels affected by PDCs is still well below pre-eruption values.

NDVI change is shown in panels E-G for three periods spanning the eruption. Panel E shows the change in NDVI from a year pre-eruption (26/02/2014) to 6 months post-eruption (27/10/2015). The change here is likely to be dominated by co-eruptive impacts, and NDVI change is negative for all areas impacted by the eruption. This decrease is most intense in the vicinity of the volcano and towards the north-east, correlating closely with the area of thickest (and coarsest) tephra fall deposition (Romero, Morgavi, et al. 2016). This gradation in NDVI (plotted in increments of 0.15) corresponds well to previous tephra-fall deposit isopach maps (Romero, Morgavi, et al. 2016; Hayes et al. 2019), but highlights finer scale spatial variation than is evident in field-based ash-thickness reconstructions (which are extrapolated from a small number of point measurements). Panel F shows the post-eruption recovery in NDVI over a period of 7 years and 4 months (until 17/02/2023). Over this time, NDVI increases with a magnitude corresponding closely to the initial decrease in Panel E. There are some differences at a finer scale, implying that recovery may also be influenced by local factors, such as topography, slope aspect, altitude or soil conditions. Despite greater initial impacts, the forests affected by the thickest tephra fall deposits have recovered to similar NDVI values as those areas affected by thinner deposits over the 7 year timescale. Panel G shows the total change in NDVI from a year pre-eruption (26/02/2014) until almost 8 years post-eruption (17/02/2023). The overall change throughout the image is close to zero, but isolated patches to the north east of the volcano still show the imprint of tephra-fall. We note that these remaining patches of lower NDVI are discontinuous and do not simply correspond to the extent of initial NDVI reduction. The strongest residual impact on vegetation is in the channels affected by both PDC and lahar deposition.

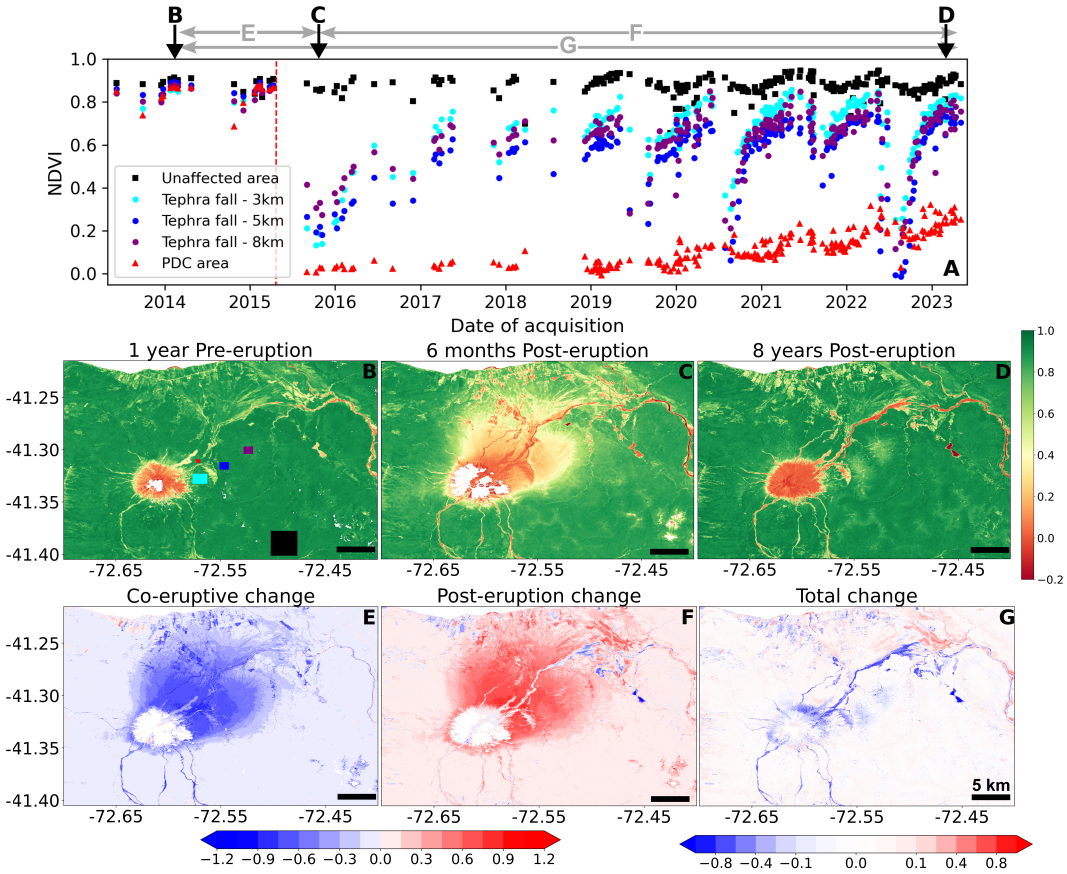

Figure 2.2: A) NDVI time series of 1 unaffected area (black), 3 tephra impacted areas (at 3, 5 and 8 km from the vent) in light blue, dark blue and purple respectively and 1 PDC affected area (red). Time of eruption is indicated by the red dotted line. We generate time series by calculating the average NDVI value within the defined study area. For a given acquisition, if any study area has >10% of pixel values (likely due to clouds) it was removed from the analysis. B) Pre-eruption NDVI image (26/02/2014) highlighting the location of the 5 study areas, C) Post-eruption NDVI image (27/10/2015), D) post-recovery NDVI image (02/02/2023), E) NDVI difference image demonstrating co-eruptive change (26/02/2014 - 27/10/2015), F) NDVI difference image demonstrating post-eruption change (27/10/2015 - 17/02/2023) G) NDVI difference image demonstrating total change in NDVI (26/02/2014 - 17/02/2023).

Figure 2.3 illustrates the relationship between tephra-fall deposition and NDVI, and shows 8 areas at increasing distances along a line of approximately 60°azimuth, chosen to align with the dispersal axis of tephra deposited from the most intense phase of the eruption (Romero, Swanson, et al. 2023). With increasing distance, the co-eruptive decrease in NDVI gets smaller until around 16 km, beyond which there is no clearly

detectable eruption impact in the NDVI. Based on post-event mapped isopachs, this distance equates to around 15 cm of ash deposition (Hayes et al. 2019; Romero, Morgavi, et al. 2016). Within this 16 km transect, the post-eruption recovery of NDVI is slowest in the most proximal areas, but follows a similar recovery trend at all sites, of a rapid initial increase followed by a steady, slower increase back towards pre-eruption values. Locations beyond 10 km return to pre-eruption values within 2 years following the eruption. The three locations closest to the volcano take substantially longer and are yet to fully recover to pre-eruption values. The impacts of tephra fall within a distance corresponding to the ∼20 cm isopach are more substantial and persistent than zones beyond this thickness, with an average NDVI decrease of 0.58 and minimum recovery time of 5 years. Within distances of 10 km, there is a strong seasonal signal evident in the NDVI recovery period, particularly from 2020 onwards. This seasonality signal appears to strengthen as the forest recovers (but we note that winter data gaps in the earlier recovery period may obscure seasonality signals from 2015-2020). We speculate that this could relate to a stronger seasonal growth signal from early successional vegetation on the forest floor, following canopy damage, rather than a tree-dominated mature forest signal from the relatively less damaged region beyond 10 km.

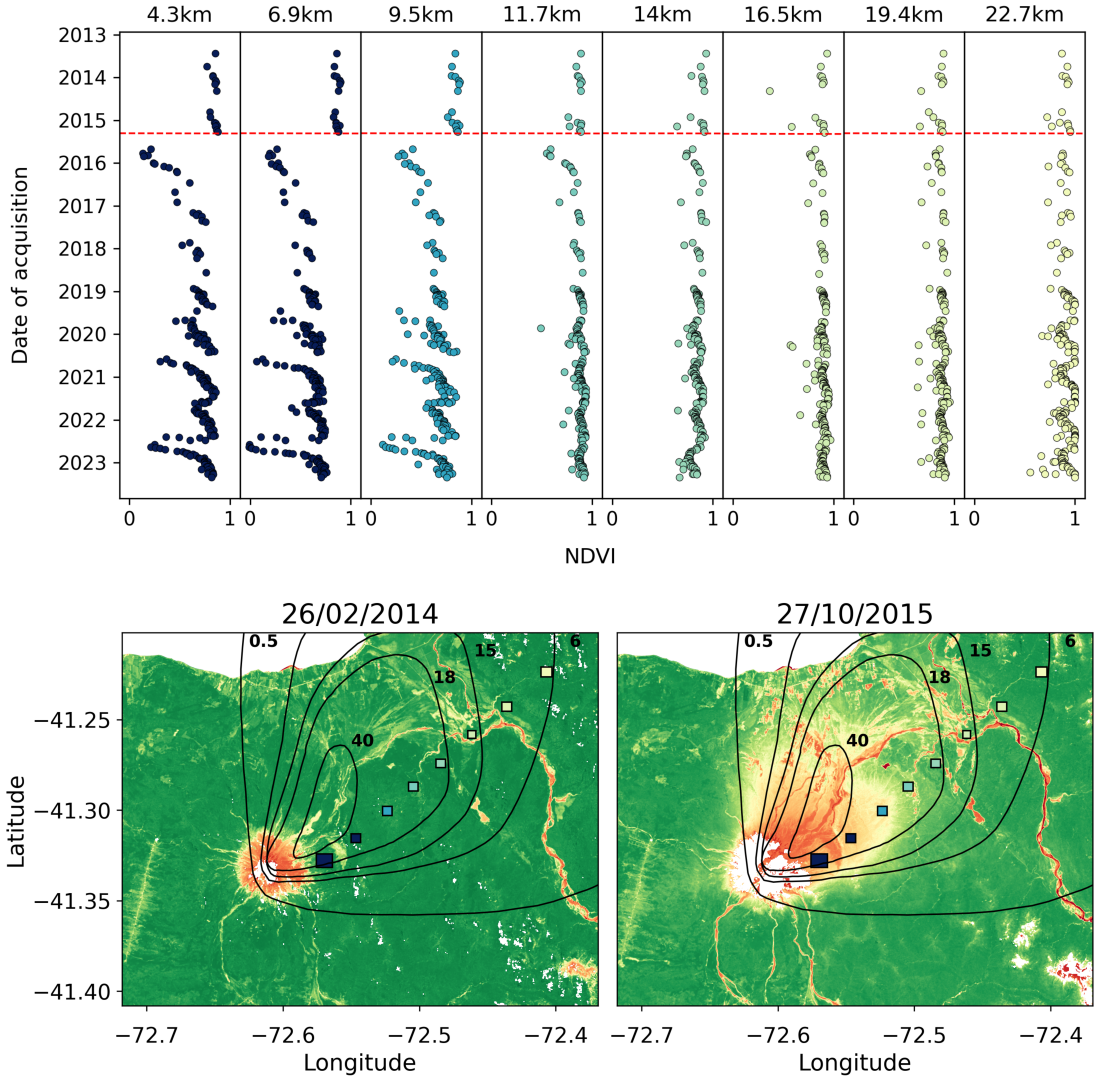

Figure 2.3: A) Time series of NDVI at 8 locations of increasing distance from Calbuco, the eruption marked by a red dotted line, B) pre-eruption NDVI image (26/02/2014) with the 8 locations indicated and the ash isopachs from Romero, Morgavi, et al. (2016), C) post-eruption NDVI image (27/10/2015) showing the locations and ash isopachs.

2.3.2 Backscatter

The backscatter data has been referenced to an average background value of the mean backscatter for all pixels excluding the volcano and the areas to the north and east (the directly impacted areas). Radar backscatter is most strongly affected where there is a change from volumetric to surface scattering (e.g., due to forest canopy loss or changes to local slope). Immediately following the eruption, there is a sharp increase in backscatter

wherever vegetation was damaged (Figure 2.4), with the greatest increase in the most proximal areas, affected by tephra fall deposition. Following this, all affected locations show a decline in backscatter, which had not returned to pre-eruption values consistently by 26/06/2023. The variation in the backscatter values after the eruption onset is greater than before the eruption. The variance decreases with recovery, but does not reach pre-eruption values (Appendix Figure A.2). Panel E in Figure 2.4 shows an increase in backscatter around the vent and a slight increase towards the north east, broadly corresponding to the area affected by thickest tephra fall deposition (isopachs of >30 cm), but without the clear gradation evident in NDVI. The negative backscatter difference to the NE of the vent (panel F) correlates with the initial positive increase, again showing a less gradational pattern to that observed in NDVI. Recovery trends are less evident in the backscatter, but some increase is evident in PDC channels and proximal tephra zones, but with no discernible difference between these two impact types in terms of backscatter recovery rates. This is likely due to the loss of vegetation or changes to its structure, which lead to minor alterations to the scattering pathway, resulting in backscatter changes in areas affected by both tephra fall and PDC deposits. The overall change in average backscatter is minimal, with the strongest changes occurring close to the volcano. These changes show an offset concentric pattern, which may be due to structural changes at the vent or long-term changes in snow and ice cover.

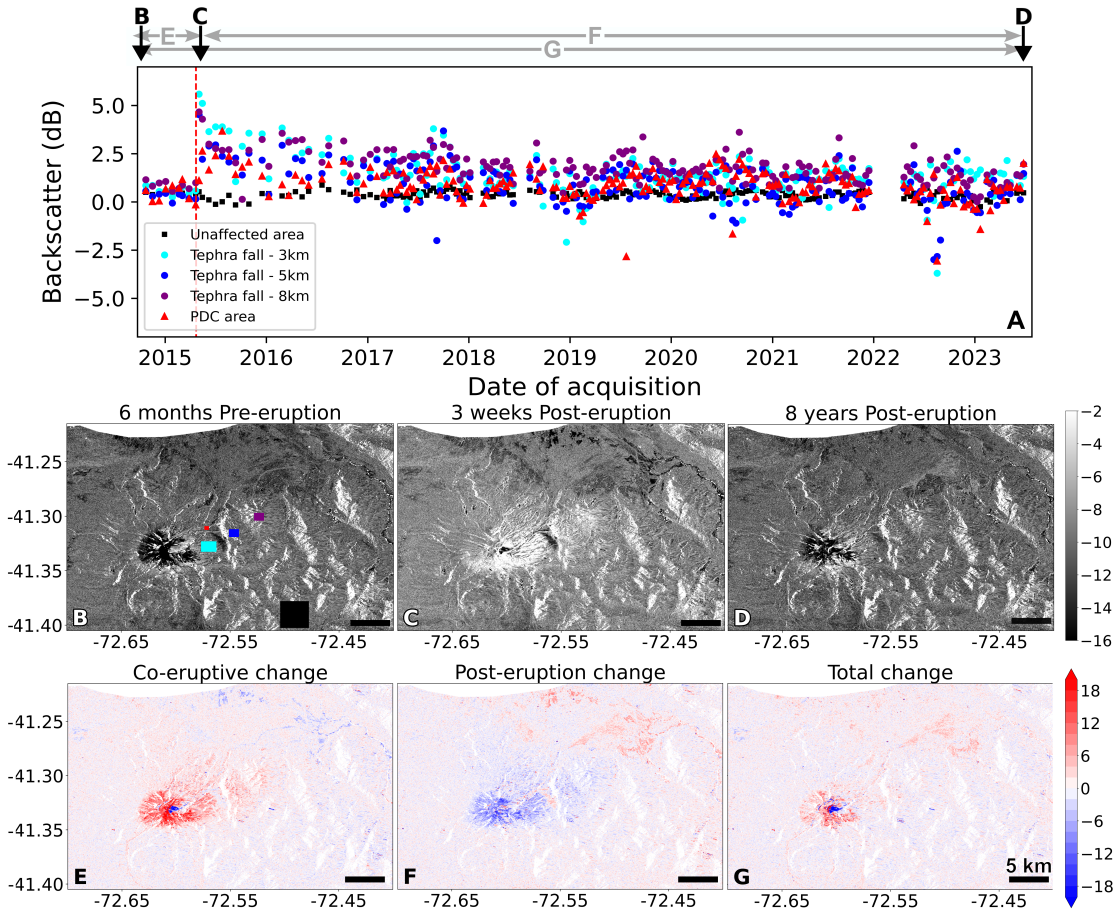

Figure 2.4: A) Backscatter time series for 5 areas around Calbuco, the backscatter is referenced to the average value of the image with the volcano and directly impacted areas removed. If any box in a given acquisition has values for >10% of the pixels it was removed from the analysis. B) pre-eruption backscatter (23/10/2014) image showing the study area locations, C) post-eruption backscatter (15/05/2015) image, D) Post-recovery backscatter (02/06/2023), E) Backscatter difference showing co-eruptive change (23/10/2014 - 15/05/2015), F) backscatter difference showing post-eruption change (15/05/2015 - 02/06/2023), G) total change backscatter (23/10/2014 - 02/06/2023).

2.3.3 Coherence

Changes in phase coherence for a 24-day temporal baseline are shown in Figure 2.5, plotted at the time of the first image in the pair, for the same study areas assessed using NDVI and backscatter (Panel B). The pre-eruption correlation values are very low (<0.3) over the undisturbed forest. At the time of the eruption (red dotted line) they decrease to 0-0.1, due to the phase changes associated with the eruption deposits, before increasing steadily to 0.4 by early 2016, due to vegetation loss and an increase in exposed ground

surfaces. From mid-2016 onwards the coherence values in the channels where PDCs and lahars have removed all vegetation are generally higher than those areas affected by tephra fall deposition. In areas affected by tephra fall, there is a decrease in coherence values lasting several years, returning to pre-eruption values by 2022. This contrasts with the NDVI, where tephra fall impacted areas generally reached pre-eruption values after 5 years. Within the channels, coherence values remain high but very variable.

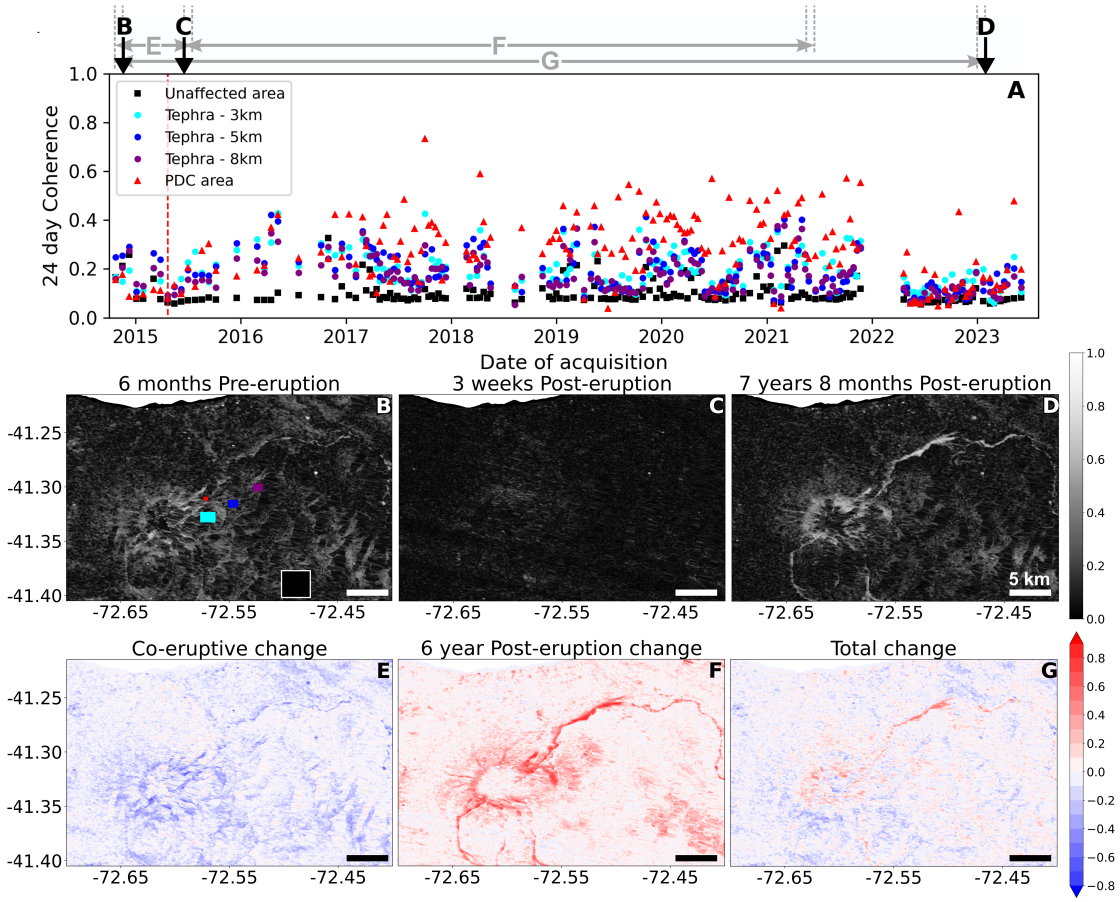

Figure 2.5: A) Time series of 24-day coherence at 5 locations around Calbuco, the date is taken as that of the first image in the coherence pair B) pre-eruption (23/10/2014 - 16/11/2014) coherence image showing the study area locations C) post-eruption coherence image (15/05/2015 - 08/06/2015) D) a post-recovery coherence image (28/12/2022-21/01/2023) E) Co-eruptive coherence change formed by a pre-eruption coherence image (23/10/2014 - 16/11/2014) and a post-eruption coherence image (15/05/2015 - 08/06/2015) F) post-eruption coherence change from a post-eruption coherence image (15/05/2015 - 08/06/2015) and a 6 year post-eruption coherence image (01/05/2021 - 25/05/2021) G) Total coherence change from pre-eruption (23/10/2014 - 16/11/2014) to 8 years post-eruption (28/12/2022 - 21/01/2023).

We generate coherence difference maps (Figure 2.5 panels E-G) to highlight changes in coherence throughout the eruption and recovery process, and to show how coherence evolved from pre-eruption to 8 years post-eruption. The eruption of Calbuco caused an immediate drop in coherence in most areas around the volcano (Figure 2.5 panel E), but also in areas known not to have been affected by the eruption (e.g., to the south), such that the eruption-affected area is not clearly delineated. However, during the six-year post-eruption period (Figure 2.5 panel F) there are strong increases in coherence, particularly in channels around the volcano and some patches to the N and E. These patches match those areas affected most strongly by tephra fall in the NDVI data, but other patches are also present to the SE, which were less discernible in the NDVI data. The total change in coherence from pre-eruption to post-eruption is around zero in most of the surrounding forest, with increases in coherence limited to a concentric zone around the volcano summit, within channels, and within a small proximal zone towards the NE (Figure 2.5 panel G) where damage to the forest was most severe.

2.3.4 Classification of Impact Zones

We perform k-means cluster analysis for all pixels in our NDVI and 24-day phase coherence datasets, grouping pixels with similar time series to produce clusters. We found that our backscatter time series were too noisy to identify meaningful clusters (Appendix Figure A.3). During the period spanning the eruption (26/02/2014 - 09/02/2016), NDVI forms 8 clusters with similar impact trajectories that strongly delineate a radiating sectoral damage pattern similar to known tephra fall deposit patterns in Figure 2.6 (panels A and B). During the post-eruption recovery period (12/03/2016 - 13/04/2023), the cluster analysis also forms 8 clusters, but reveals a different spatial distribution. Cluster distribution is dominated by channels and higher topographic areas, rather than a sectoral pattern (Figure 2.6 panels C and D). We cluster the coherence time series spanning the post-eruption period from 27/02/2016 to 12/01/2019, due to a loss of coherence over the co-eruptive period, forming 6 clusters (Figure 2.6 panels E and F). This outlines an impact pattern NE of the volcano that is consistent with the NDVI clustering but less spatially extensive, and emphasises channels. Linear changes to the west of Calbuco,

grouped within the same clusters, are due to forest clearing that occurred during the eruption and recovery period. One cluster of the coherence time series (labelled 'tephra zone c/topography') does not correspond to any spatial pattern of deposits but aligns with areas of higher elevation (see Figure 2.1 panel E). Local environmental factors related to altitude, topography or variations in vegetation type, could explain this cluster in the coherence data.

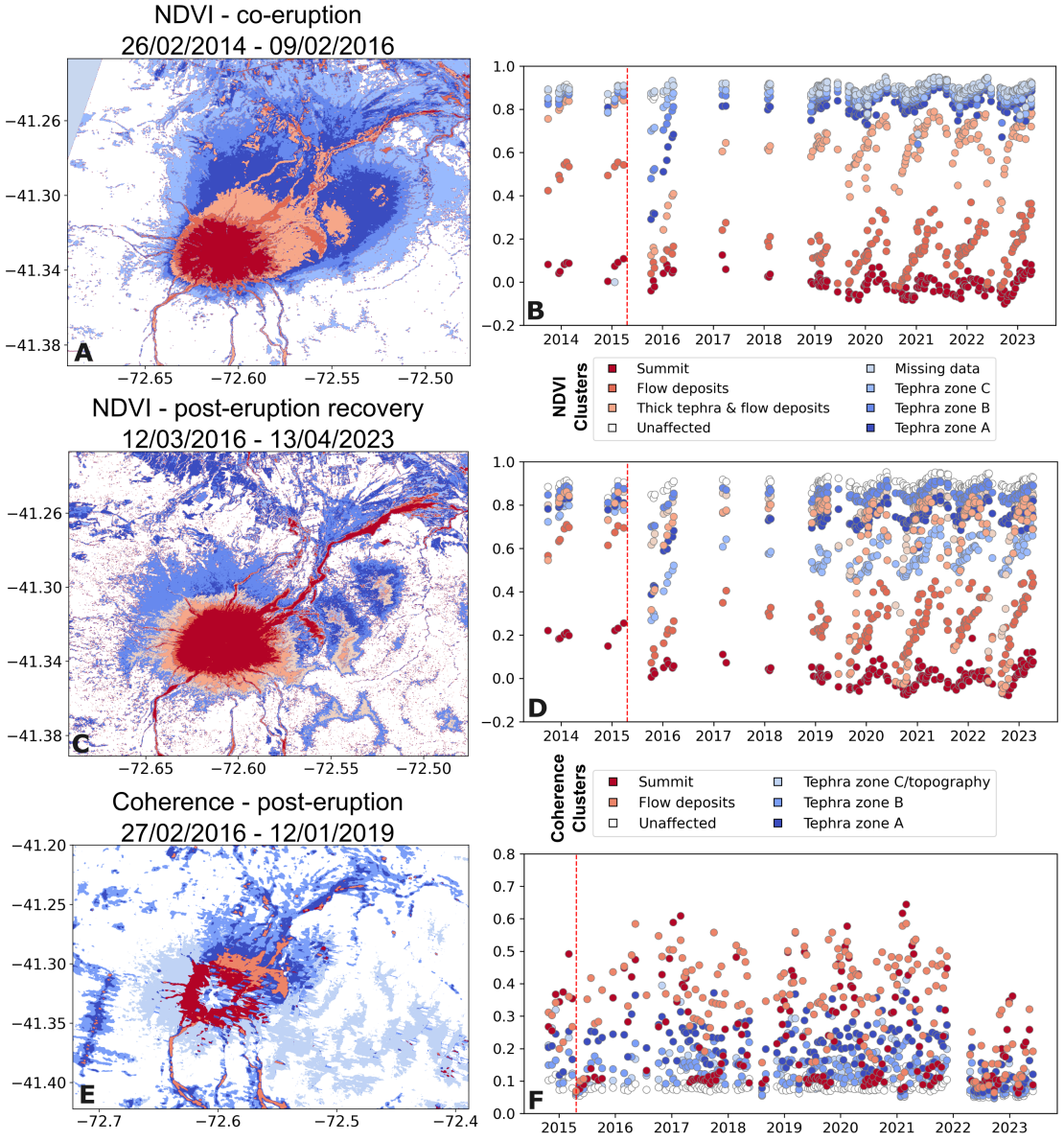

Figure 2.6: A) NDVI clustering over the eruptive period (26/02/2014 - 09/02/2016), producing 8 clusters, B) time series for the median pixel value of the 8 NDVI clusters, c) NDVI clustering over the post-eruption recovery period (12/03/2016 - 13/04/2023) D) time series for the median pixel of the 8 recovery clusters E) coherence clustering over the post-eruptive period (27/02/2016 - 12/01/2019) F) time series for the median pixel for the 6 coherence clusters.

2.4 Discussion

2.4.1 The Impact of the 2015 Calbuco Eruption on Vegetation

Different aspects of the Calbuco 2015 eruption and recovery of the surrounding forests are captured by optical and radar imagery. The immediate eruption impacts are clearest in a sudden NDVI decrease over all areas affected by PDCs, lahars and tephra fall up to approximately 15 cm deposit thickness (Figure 2.2 F, Appendix Figure A.4). While the decrease in NDVI effectively shows gradational changes corresponding to eruption impact intensity, backscatter values only pick out high magnitude change within a few kilometres of Calbuco's summit. Part of this backscatter increase, perhaps related to slope changes close to the vent, remains 8 years post-eruption. Some backscatter increase in channels is also evident due to vegetation loss or structural changes (Figure 2.4 E, F, G, Appendix Figure A.4). The increase in backscatter variance from pre-eruption to post-eruption may be due to structural changes to the vegetation, and would be consistent with the vegetation coverage becoming less homogeneous, a change that may not be apparent in the NDVI or the coherence. The forests around Calbuco typically have relatively high backscatter and very low coherence values. As such, the loss of vegetation, resulting in the creation of temporarily stable surfaces in the channels affected by both PDCs and lahars, is strongly highlighted by a post-eruption increase in coherence, which is also evident in NDVI. Similar coherence mapping also identifies the areas of thickest tephra deposition, but without the fine gradation evident in the NDVI dataset. While the optical data provides a detailed view of vegetation health changes, the radar imagery complements this by highlighting structural changes and areas of high magnitude impact. As such, using and comparing multiple datasets provides insight and flexibility, especially in cases where one type of data may be limited (e.g. cloud coverage limiting optical image acquisitions).

2.4.2 Post-Eruption Forest Recovery

Vegetation recovery trends, observable in both the optical and radar datasets, can be linked to the intensity of the eruption impacts and to the type of vegetation damage.

Areas affected by tephra fall began their recovery within 6 months of the eruption, with rapid increases in NDVI occurring in the first few years. This is indicative of vegetation damage rather than death, decreasing with distance from the volcano up to around 20 km, along a gradient defined both by decreasing tephra thickness and coarseness. The lack of extensive zones of increased phase coherence, away from the eroded channels, indicates that trees were not damaged to the extent that the signal became dominated by the more stably scattering forest floor. In contrast, the PDC impacted channels experienced a larger immediate decrease in NDVI and also a much slower recovery rate, with little evidence for any regrowth in the 5 years immediately post-eruption. This is also clear in the higher phase coherence values in channels over this time. This is consistent with total vegetation loss and burial within these channels (Romero, Swanson, et al. 2023) and with high levels of channel activation (e.g. lahars) and instability persisting for several years, preventing any vegetation recovery. After 2019, the gradual onset of NDVI recovery suggests channel stabilisation and the growth of a sparse successional assemblage, which then exhibits a linear rate of recovery. This period also corresponds to an increase in post-eruption NDVI at the perimeters of the channels (Figure 2.7 panel E), showing that initial stages of vegetation recovery develop from channel margins, likely due to the proximity of healthy vegetation and potentially to less extensive initial damage or ongoing rates of erosion. A field campaign undertaken in December 2023 confirmed the regrowth pattern of vegetation at the edges of these channels (Figure 2.7). We use NDVI as a way to map channel evolution during and following the eruption. Where channels are marked by vegetation at their edges, satellite NDVI measurements capture initial flow width (including bank erosion and overtopping) and then the gradual narrowing of this damaged region as vegetation recovers post-eruption. Figure 2.7 shows a clear decrease in NDVI at the time of eruption across all studied channel transects. In locations also affected by tephra fall, the specific channel impacts are hard to discern, because the NDVI is initially low across the whole transect (Figure 2.7 transects 1,2,3), but where there was no tephra deposition (channel 4) the initial impact and recovery patterns are clearly constrained. These transects also highlight changes in active channel patterns driven by the eruption, including a new channel in transect 2 and widening of channels

in 1 and 3.

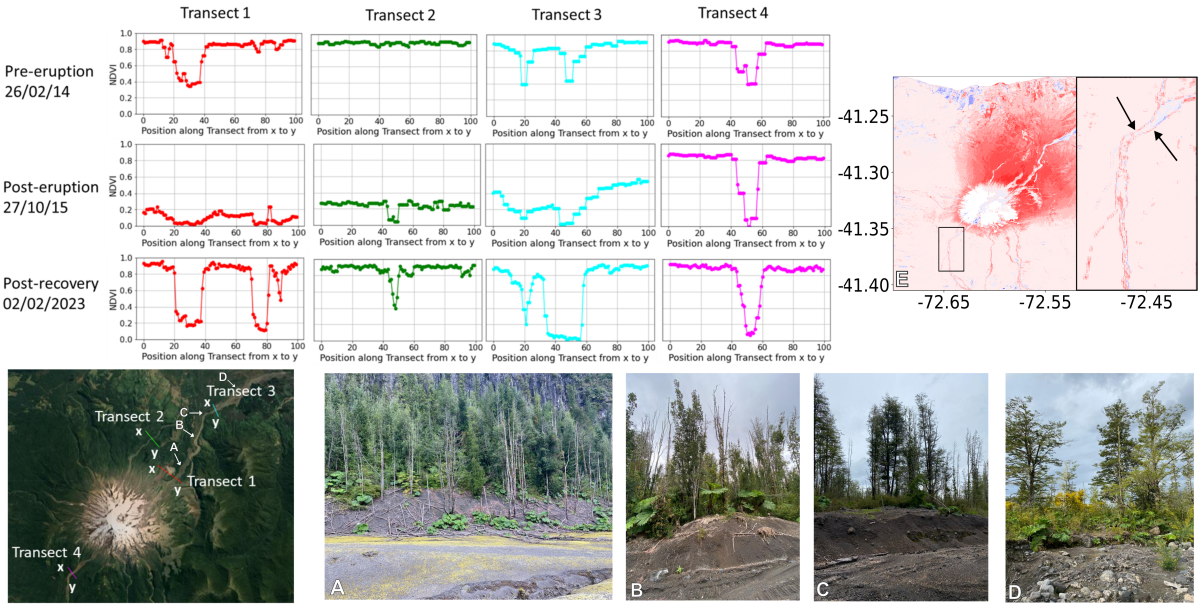

Figure 2.7: NDVI transects at different channel locations around Calbuco show the impact of flow deposits on vegetation and how they recover post eruption. Transects 1-4 (locations shown on the Sentinel-2 image) show the changes in NDVI from pre-eruption, 6 months post-eruption and almost 8 years post-eruption. Images A-D show the vegetation at the edges of channels from a field campaign in December 2023. E) Post-eruption NDVI change highlighting the pattern of NDVI increase on the channel perimeters.

2.4.3 Vegetation Damage as a Proxy for Tephra Thickness

Cluster analysis is advantageous for the classification of vegetation impact and recovery as it utilises the full trajectory of damage and recovery to differentiate between processes (Figure 2.6). Clusters of the time series highlight structure in the proximal impact zone and in the PDC affected channels (Figure 2.6) that are harder to discern in the maps of NDVI or coherence change alone. Several of the clusters from the NDVI co-eruption cluster analysis form a concentric sectoral pattern, which we infer to reflect the true shape of tephra-fall deposit isopachs close to the volcano. Although our cluster boundaries are not strictly quantitative indicators of tephra deposit thickness (and the number of boundaries is dependent on our selected discretisation), they mark zones of similar initial damage and similar recovery rate, which we expect to correlate closely with tephra

thickness. This interpretation is supported by the very clear spatial correspondence between the axes of the cluster-defined pattern and the observed distribution directions of the two main eruption pulses: the cluster analysis picks out two discrete transport trajectories (at approximately 40° and 65°), with the sector along the southerly axis extending slightly further from the vent, consistent with the larger volume and column height of the second eruptive pulse. This pattern is most clearly evident in the NDVI cluster analysis, on which we base our re-defined isopach distribution, but is also evident in the coherence cluster analysis (Figure 2.6 panel E). The spatial pattern of the cluster analysis thus closely corresponds to the expected tephra fall dispersal patterns, and picks out spatial relationships and the impacts of discrete eruptive phases that would simply be unobservable based on the resolution of point-based field measurements. The challenges with producing accurate proximal isopachs based on field measurements is evident in Figure 2.8, with a substantial discrepancy between two published proximal isopach patterns, neither of which constrains the spatial form evident in our NDVI cluster analysis. Using our NDVI clusters we re-estimate the tephra deposition isopachs. We calibrate our NDVI cluster-based boundaries against the nearest ground based measurements from Romero, Morgavi, et al. (2016), thus assigning an estimated numerical value to each boundary and using this to define revised proximal isopachs. The thinning pattern is consistent for all prior ground based measurements but one (24 cm), which we consider may be an erroneous measurement as it is an outlier in terms of expected thinning trends. Although there is some uncertainty in our approach, the isopach areas that we redefine in this way show a clear exponential thinning rate, as expected in tephra-fall deposits. This further validates our use of the cluster boundaries as a proxy for fall deposit thickness. By combining our newly defined proximal isopach shapes (15 cm and above) with previous mapping of more distal isopachs, shown in Supplementary Figure A.6 (less than 15 cm thickness; from Romero, Morgavi, et al. (2016)), we re-estimate the volume of the eruption. Using the method from Pyle (1989) and Pyle (1995), based on two exponential segments, we obtain a re-estimated eruption volume of 0.28 km^3, a slightly higher value than the estimate of Romero, Morgavi, et al. (2016) of 0.27 km^3.

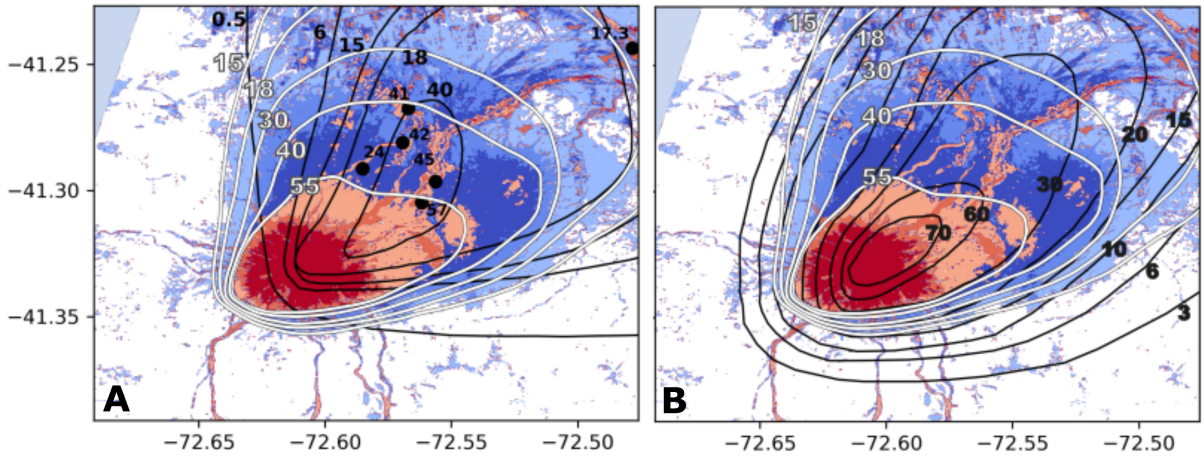

Figure 2.8: NDVI clustered eruption impacts overlain with previous eruption isopachs in black and our re-estimated isopachs, from the cluster analysis of NDVI, in white. A) Comparing our re-estimated isopachs with the ash isopachs and field measurements of tephra thickness from Romero, Morgavi, et al. (2016) B) Comparing our re-estimated isopachs with isopachs from Hayes et al. (2019))

Using NDVI change as a proxy for tephra thickness seems to be effective at Calbuco only for deposits exceeding 15 cm, because thinner tephra deposition did not produce measurable changes in NDVI. The thickness of tephra deposits that produce measurable NDVI changes may vary between eruptions and likely has some dependence on tephra density, grain size and vegetation type. It may also differ substantially between dry and wet tephra deposition. Our observations imply that our method is most useful in the proximal regions of larger magnitude eruptions with extensive tephra deposition. This is nevertheless valuable, because these regions are often forest covered, inaccessible, and may show the most complex depositional and damage patterns. A significant proportion of deposit volume lies within these proximal regions, and our approach has strong potential for revealing the complexities in eruption impacts in high-damage zones, to complement field-based observations that can be more easily made in distal locations.

Cluster analysis can also provide insights into post-eruption vegetation recovery and how this may be affected by local conditions. Clustering over different time windows, reveals different spatial distributions of NDVI change (Figure 2.6 panel C and D), demonstrating that recovery is not only dictated by the initial damage. This is apparent in some regions closer to the vent, where zones impacted by thicker tephra deposits recover to

pre-eruption NDVI values more rapidly than regions at a greater distance, with thinner tephra deposits (Figure 2.9 Panel A). The areas of slower recovery align with areas of elevated topography (>1000 m) (Figure 2.9 and Figure 2.1 panel D), suggesting that altitude and slope gradient may be factors that delay forest recovery. It has been shown in previous studies how environmental factors influence vegetation recovery after damage (Crk et al. 2009; Johnstone et al. 2010; Decker et al. 2003; Ireland et al. 2015).

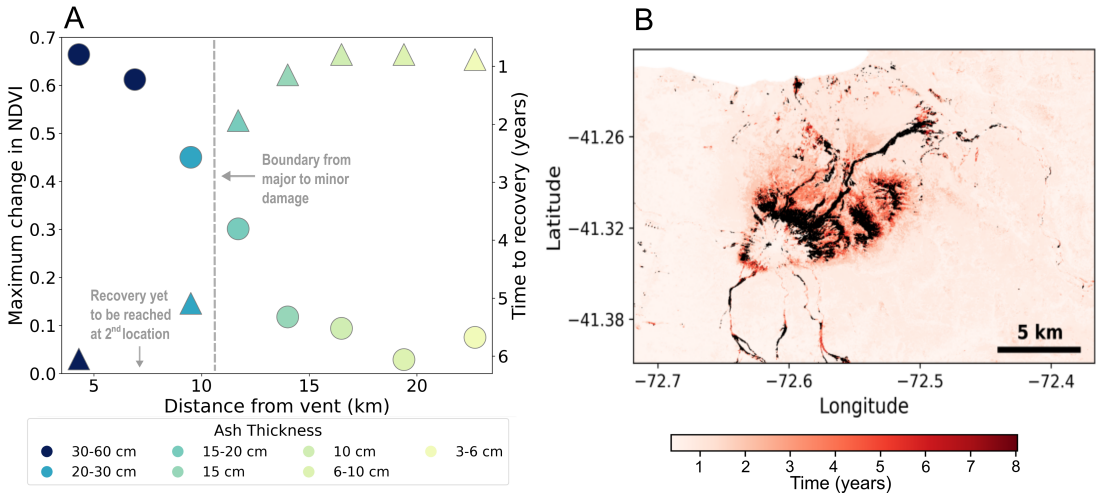

Figure 2.9: A) A comparison of vegetation damage vs recovery at increasing distance (decreasing ash thickness), circles show maximum NDVI decrease immediately post-eruption, triangles shows the time to recovery in years for the same areas in Figure 2.3. B) The recovery time of NDVI, recovery is defined as being within 1% of the pre-eruption median value and is calculated on a pixel basis, with darker red being more time to recovery and black pixels being yet to reach the pre-eruption value.

2.4.4 Link Between Impact and Recovery Time

The time taken for vegetation to recover is related to the intensity of the eruption's initial impact. Panel A in Figure 2.9 shows maximum NDVI change against recovery time according to distance from the vent and tephra thickness (colour scale). The recovery time is defined as the time when the NDVI value reaches within 1% of the pre-eruption median. At just over 10 km distance (equal to around 20 cm tephra thickness) the initial change in NDVI is approximately 0.3 and the time to recover is <3 years. Inside this distance, loss of green vegetation is generally greater and recovery times are longer, with some patches of forest that are yet to recover to previous NDVI levels. In addition to local

factors, the characteristics of the tephra itself may affect total recovery time. A previous study on the impact of tephra fall on tree ring thickness showed varying amounts of growth loss, possibly due to differing tephra thickness or characteristics (Carlón Allende, Macías, Mendoza, and Villanueva Díaz 2020). This relationship is not necessarily simple and warrants further exploration. Although thicker tephra deposits at Calbuco clearly show a correlation with increased initial damage, this doesn't necessarily impede recovery. Coarse tephra deposits (lapilli) are likely to form a permeable layer that protects the underlying soil and allows water penetration and retention, plausibly benefiting tree recovery. In contrast, finer and thinner ash deposits may be less permeable and promote enhanced runoff and erosion. For the Calbuco eruption, initial damage nevertheless shows a clear correlation with distance and tephra dispersal patterns, suggesting that increased grain size and increased intensity of tephra fallout both led to greater damage. Post-eruption photographs, including a field survey in 2023 (Figure 2.7), show that trees throughout the region affected by intense tephra fall remained standing and generally retained their branched form (away from the more intensely damaged zones adjacent to channels). This suggests that initial damage likely involved a combination of tree defoliation and the burial of ground vegetation, perhaps coupled with minor branch breakage, but not extensive branch damage or tree felling. Field observations suggest this was the case even in the areas of highest tephra fallout. This explains the very rapid recovery of areas affected by tephra fall, with mature trees remaining in place and able to re-sprout. Although this may appear surprising, given deposit thicknesses up to half a metre or more, low density pumice lapilli may fall through canopies with relatively limited damage. Had this deposition been wet, or accompanied by rainfall, the impacts and recovery rate may have been quite different, especially in areas affected by finer-grained (ash) deposition. As was observed from extensive mud-rain following the Krakatau eruption in 1883 (Simkin 1983), wet ash can rapidly coat and load branches, causing extensive breakage and damage at much lower fall deposit thicknesses than occurred at Calbuco. Such processes are likely to strongly influence forest recovery rates and successional patterns, given the impacts on canopy structure.

2.5 Conclusion

We investigate the use of NDVI, backscatter and coherence to identify forest disturbance and recovery after the 2015 eruption of Calbuco. We analyse time series from all three methods, which show the co-eruptive change and post-eruption recovery. NDVI drops sharply post-eruption due to vegetation loss or damage. The pattern of NDVI loss and recovery shows a bilobate shape that corresponds closely with observed eruption plume dispersal and the intensity of the two main eruption phases, indicating that NDVI can be used as a proxy for tephra distribution. NDVI can also be used to map changes to vegetation at channel boundaries, and therefore their changing extent during and post-eruption. Backscatter increases with the emplacement of eruptive material, and subsequently decreases, although not to pre-eruption values in the most severely impacted areas. The variance in backscatter is significantly larger post-eruption, possibly consistent with a now less homogeneous vegetation cover due to eruption damage. Coherence is lost with the emplacement of material at the eruption onset, but then increases with the loss of vegetation, particularly in channels and to the north east of the volcano (in the zone most heavily impacted by tephra fall deposition). Both the NDVI and coherence show areas that have not yet fully recovered from the eruption. The detailed pattern of changes in NDVI and coherence can effectively be demonstrated using k-means clustering of multiple acquisitions. Cluster analysis groups pixels with similar time series, and therefore with similar levels of both initial damage and recovery. In NDVI this highlights the tephra fall deposit dispersal patterns in detail, and cluster boundaries can be used as a proxy for tephra isopach distribution (although only in regions of observable NDVI damage, which in this case corresponds to deposit thicknesses over 15 cm). These refined isopachs allow us to re-estimate the eruptive volume at 0.28 km^3. This method has strong potential to reveal depositional complexities and eruptive impacts, and to determine eruption volumes, in proximal regions with high levels of damage following large explosive eruptions, and is complementary to more distal field-based datasets. Vegetation recovery rates differ between impact type, based on the initial intensity of the damage. Vegetation recovery occurs mostly in the 3 years following

the eruption, but areas with the greatest damage (thickest tephra and channel deposits) take 7 or 8 years to recover, and in some locations are yet to recover, particularly at high elevations and in major channels impacted by PDCs and lahars. We demonstrate that optical and radar satellite data can be used to observe forest disturbance and recovery to understand eruption processes, providing high resolution and quantifiable insights into damage characteristics, deposit distributions and environmental change. This is likely to be of particular value following large explosive eruptions with complex disturbance patterns, and provides a route to determining eruption impacts in vegetated volcanic regions globally.

Chapter 3

Satellite Measurement of Volcanic SO_2 Impact on Vegetation

Abstract

Volcanic gases, particularly SO_2, can significantly impact the health, growth and characteristics of exposed vegetation. This study investigates the effects of both short term SO_2-rich eruption plumes and long term passive degassing on surrounding forests and plant life. Using optical and radar satellite data, we assess vegetation damage at Krakatau (2020), Semeru (2019 and 2023), Reykjanes Peninsula (from 2018-2024), Turrialba (from 2000-2024) and Masaya (from 1985 - 2024). We observe a range of impacts consistent with photosynthesis inhibition, chlorosis, defoliation and plant death. These different damage mechanisms vary in duration, from months to years, and in the magnitude of the measurable change, with NDVI decreases in the range of 0.1-0.8. Based on these observations, we present criteria for identifying unusually high SO_2 fluxes and differentiating SO_2 induced damage from tephra effects. This study also captures patterns of long-term vegetation recovery after sustained SO_2 emissions, as well as evidence for the the development of plant resilience to SO_2 exposure. For example, at Turrialba and Masaya, vegetation shows signs of resilience, with regrowth initiating at the peripheries of the damaged areas during periods of reduced flux. Our findings advance understanding

of vegetation responses to volcanic gas exposure over areas up to 100s km^2 and temporal scales of months to decades. This work establishes a new baseline for monitoring the impacts of volcanic gases on surrounding ecosystems, and demonstrates how satellite based detection can be a valuable, global tool for environmental and hazard assessment.

3.1 Introduction

Volcanic gas emission ranges from a diffuse soil flux of CO_2, potentially extending over 100s of km, to focused SO_2-rich plumes which can also contain a variety of environmentally harmful volatile species (Hansell et al. 2004). Gas emission may continue in between eruptions and persist over years to decades (Oppenheimer et al. 2003; Stoiber et al. 1986; Symonds et al. 1994), ascend into the stratosphere in highly explosive plumes (Symonds et al. 1994; Carey and Bursik 2015) or remain in the troposphere impacting the atmosphere and local environment (Mather, Pyle, and Oppenheimer 2003). Volcanic gases have impacts on atmospheric chemistry and radiative forcing (Smith, Pitcher, et al. 2001; Carn et al. 2017), as well as crops, livestock and human health (Hansell et al. 2004; Mather 2015).

SO_2 emissions from passive degassing or effusive eruptions have particular potential to impact surrounding ecosystems because (1) sulphur species can persist in a tropospheric plume for days following emission, (2) impacts on vegetation are strongest when gas is emitted at ground level or when a plume grounds after emission and (3) both SO_2/SO_4^{2+} in the plume and their reactive products can impact vegetation (Mather 2015; Tomsche et al. 2022; Beirle et al. 2014; Delmelle et al. 2002).

Sulphur dioxide is released from volcanoes in a range of styles as a result of volatile exsolution and the development of magma permeability or fragmentation, leading to gas release (Carey and Bursik 2015). Isolating the impact of volcanic gases on vegetation is challenging for a number of reasons. Emissions can be dispersed on a global scale following large-magnitude explosive eruptions injecting volatiles into the stratosphere, while tropospheric emission, from both lower-magnitude explosive eruptions and effusive

activity, is more localised and can cause serious damage to vegetation (Mather, Pyle, and Oppenheimer 2003). Degassing rates fluctuate, resulting in damage that can range from transient to permanent. Volcanic gases can damage vegetation through a variety of mechanisms, such as chlorosis, leaf death and soil changes. Identifying the satellite signature of vegetation damage due to volcanic SO_2 is therefore challenging.

Characterising the signature of volcanic gas emission is important as volcanic gases are thought to have played a critical role in the development of Earth's atmosphere (Kasting 1993; Holland 2002; Kump et al. 2007; Mather, Pyle, and Allen 2004; Mather 2008) and are known to have large scale, regional impacts on ecosystems (Robock 2000; Seiler et al. 2021; Biondi et al. 2003; Briffa et al. 1998). Over longer timescales, exceptional degassing events have also been shown to have global impacts on climate and vegetation (Thordarson et al. 2003; Stothers 1996; Sigurdsson 1982; Oppenheimer et al. 2003). However, the current extent to which volcanic gases affect surrounding vegetation at a baseline level remains largely uncharacterised.

Here, we take a systematic approach using satellite data over years-decades to capture the impact of a range of degassing volcanoes: Krakatau, Turrialba, Masaya, Semeru and Reykjanes Peninsula. We investigate the range of satellite-detectable impacts and the causing damage mechanisms by analysing the scale and rates of impact and subsequent recovery time to characterise the impact of volcanic gases on vegetation.

3.1.1 The Impacts of Volcanic Gases on Vegetation

The most abundant volcanic volatiles are H_2O, N_2 and CO_2, but their atmospheric concentrations are so high that the impact of any single eruption is difficult to assess and relatively insignificant compared to background levels (Robock 2000). As such, SO_2 is the key volcanic gas responsible for not only environmental and vegetation damage, but also health and climate impacts (Mather, Pyle, and Oppenheimer 2003; Carn et al. 2017; Hansell et al. 2004). Previous studies on vegetation impacted by SO_2 have primarily focused on industrial SO_2 and the resulting acid rain, particularly in North America and Europe, with emissions peaking in the 1970's (Cape et al. 2003). The direct

effects of SO_2 on vegetation are observable close to the pollution sources, with plants in urban areas impacted by inhibition of photosynthesis, reduced growth rate and visible damage (Lee, Khaine, et al. 2017; Han et al. 2022), as well as the secondary effect of acid rain on more distal vegetation (Knabe 1976). Acid rain is rain water with very low pH, often associated with pollution from anthropogenic sources but can also be formed when rain passes through a volcanic plume (Likens et al. 1979; Cape 1993; Mather 2015). Acid rain primarily damages vegetation indirectly through the soil, while gaseous SO_2 enters the plants though the leaves, causing direct damage to the cellular structure, which in turn disturbs and can inhibit the photosynthetic process (Cape et al. 2003; Beekley et al. 1981; Han et al. 2022). Photosynthesis, the chemical reaction by which plants convert light energy to chemical energy, occurs through a series of interconnected reactions summarised by equation 1 (Covshoff 2018; Blankenship 2021).

$$6CO_2 + 6H_2O \xrightarrow{\text{light}} 6O_2 + C_6H_{12}O_6 \tag{3.1}$$

The most common form of photosynthesis, and the one most relevant to this study, is chlorophyll based photosynthesis, which uses light driven electron transfer (Blankenship 2021). In the majority of plants, the main phases of photosynthesis occur in the chloroplast, which contains the chlorophyll pigments, and exists within a middle layer of the leaf called the mesophyll (3.1) (Clark et al. 2018). The movement of gases, including SO_2, occurs through openings on the epidermis of the leaf called stomata, typically located on the underside of the leaf. Opening of the cells is controlled by guard cells that respond to environmental changes (Clark et al. 2018; Knabe 1976). Once inside the leaf, SO_2 spreads into intercellular spaces and is dissolved into the cell walls, disrupting the mesophyll structure of the cell and particularly damaging the chloroplasts (Knabe 1976; Han et al. 2022). It can also infiltrate the guard cells, rendering them unable to close the stomatal opening, increasing the infiltration of SO_2 into the leaf. This is summarised in Figure 3.1.

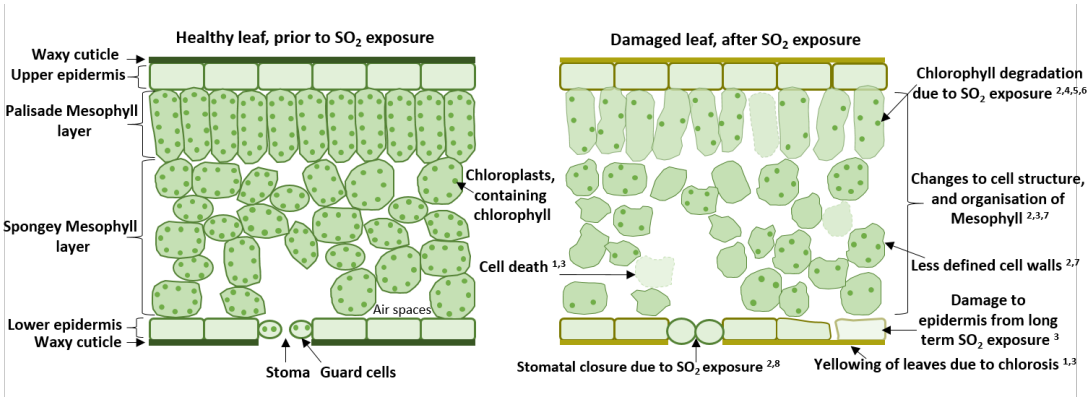

Figure 3.1: A diagram of the internal leaf structure and changes that may occur due to SO_2 exposure, such as chloroplast degradation, changes to the cell structure, cell death and colour change. [1] Brychkova et al. 2007, [2] Makbul et al. 2011, [3] Han et al. 2022, [4] Rudorff et al. 1995, [5] Shimazaki et al. 1980, [6] Zhang et al. 2010, [7] Knabe 1976, [8] Clark et al. 2018

SO_2 exposure damages, or even totally destroys, the internal cell structure from within the chloroplast cells, destroying chlorophyll pigments. This results in substantial decreases in the photosynthetic process, colour changes within the leaves known as chlorosis (as the chlorophyll is what produces the green colour in plants) and can result in the death of leaf cells or the whole leaf (necrosis) (Shimazaki et al. 1980; Beekley et al. 1981; Knabe 1976; Han et al. 2022). Laboratory experiments show chlorophyll destruction in as little as 2-3 hours of SO_2 exposure, resulting in discolouration. In the case of spinach leaves, as little as 2-3 hours of exposure led to leaves turning red-brown; extended exposure over 10-15 hours resulted in leaves turning white (Shimazaki et al. 1980).

While there have been laboratory based studies and research focusing on SO_2 impacts on plants from anthropogenic sources (Lee, Khaine, et al. 2017; Shimazaki et al. 1980; Hüve et al. 2000; Han et al. 2022), there are only a few locations where the vegetation damage due to volcanic SO_2 has been the focus of study (Weiser et al. 2022; Tortini et al. 2017; Delmelle et al. 2002). The 2021 Tajogaite eruption in La Palma is one example: it produced large quantities of SO_2, with surrounding pine forests exposed to over 1 Tg SO_2 during the course of the eruption (Shatto et al. 2024). This resulted in chlorosis and defoliation in a 7 km radius of the volcano (Weiser et al. 2022; Shatto et al. 2024), with distance from the eruption site being the most predictive factor for vegetation damage.

3.1.2 Factors Influencing Vegetation Response to SO_2 Exposure

The extent of damage caused by SO_2 exposure to vegetation depends on environmental conditions such as time of day and temperature, as well as plant-specific traits such as plant age or leaf characteristics (Han et al. 2022). These factors can influence stomata, which usually close in response to pollutants, but may remain open due to these external factors, increasing SO_2 infiltration and resulting in damage (Knabe 1976). It has been shown that for the same duration and concentration of exposure chlorophyll was damaged in daylight but not damaged in darkness (Shimazaki et al. 1980), likely due to stomatal closure in darkness resulting in reduced entry of gas into the leaf cells (Shimazaki et al. 1980). Wind conditions can also influence gas uptake, as wind abraded leaves have been shown to result in open stomata and increased gas uptake (Hoad et al. 1992). Higher temperatures and humidity can also promote stomatal opening and increase SO_2 infiltration (Driesen et al. 2020). Rainfall can also influence gas uptake as wet conditions may wash SO_2 deposits off of plant surfaces and dilute the impacts on soil (Winner and Atkinson 1986; Yoo et al. 2014). Compared to drier conditions allowing more SO_2 accumulation on plant surfaces and so more uptake. However, rain can also provide a transport mechanism for SO_2 as it can cause acid rain (Knabe 1976). SO_2 damage is therefore expected to be higher in summer due to weather conditions, increased light, temperature and relative humidity (Han et al. 2022; Yamaguchi et al. 2012).

Infiltration levels of SO_2 are sensitive to leaf size, structure and age. In general, larger leaf size (e.g. broadleaf vs needles) means increased surface area and increased stomatal opening resulting in greater SO_2 infiltration. However, while more mature leaves are often larger, they show greater resistance to SO_2 exposure, as demonstrated by Han et al. 2022 in broadleaf forests. Mature leaves are more likely to have a thicker cuticle, reducing infiltration by gases and providing higher resilience to environmental stresses and disease in general (Han et al. 2022; Dominguez et al. 2017). As a result, different tree types show different levels of sensitivity to SO_2 exposure with herbaceous plants more

sensitive than woody plants, coniferous tress more so than broad-leaf trees and deciduous broad-leaf more sensitive than evergreens (Han et al. 2022). Beekley et al. 1981 showed that SO_2 fumigation of lichen did not damage the chlorophyll content or absorption, yet still reduced photosynthesis, so damage must have been by other mechanisms. Mosses have also been shown to accumulate SO_2 and have been used as bioindicators of air pollution as a result, but damage may be harder to detect compared to trees as colour change is less likely (Winner and Bewley 1978; Gautason et al. 2015).

3.1.3 Satellite Measurement of SO_2 Impacts on Vegetation

The Normalised Difference Vegetation Index (NDVI) is often used to monitor vegetation health, coverage and damage due to volcanic or other natural disturbances (Hawryło et al. 2018; Jepsen et al. 2009; Kharuk et al. 2009; Marx et al. 2017; Spruce et al. 2011; Santin-Janin et al. 2009; Goetz et al. 2006; Bai et al. 2008; Myneni et al. 1995; Shatto et al. 2024; Udy et al. 2024). It has also been effective in studying SO_2 exposure in urban environments and on crops (Rudorff et al. 1995; Rana et al. 2023; Zhang et al. 2010). We expect NDVI to capture impacts of volcanic gases on vegetation as SO_2 exposure will cause a decline in chlorophyll concentration and changes to the internal cell structure (Shimazaki et al. 1980; Rudorff et al. 1995; Han et al. 2022; Knabe 1976). In turn, this results in an increase in red reflectance and a decrease in near infrared reflectance, reducing the red edge effect that the NDVI detects (Supplementary Figure B.2) (Zhang et al. 2010). There is less change in the green band so, unlike other studies using the green normalised difference vegetation index (GNDVI), we believe the NDVI will be more effective (Supplementary Figure B.1). Another potential index is the MERIS Terrestrial Chlorophyll Index (MTCI), which would detect the changes in the red edge bands. However, it is only possible to use with Sentinel-2 not Landsat 8, and has been shown to be less correlated with SO_2 concentrations in comparison to NDVI (Zhang et al. 2010). The effectiveness of different vegetation indices for detecting SO_2 damage is likely to change between case sites and vegetation type, but NDVI is likely the most broadly suitable (Silva et al. 2013). NDVI has previously detected SO_2 damage in vegetation (Han et al. 2022), including from volcanic eruptions where chlorosis occurred, demonstrated at La

Palma and Turrialba (Shatto et al. 2024; Tortini et al. 2017; Weiser et al. 2022).

Radar, specifically backscatter, has not been used extensively to detect SO_2 damage, however, has been used to assess vegetation health and coverage (Mitchard et al. 2009; Askne et al. 1997; Wegmuller et al. 1997; Imperatore et al. 2017). Dense, healthy forest canopy has higher backscatter values than bare ground, particularly for Sentinel-1 C-band radar, due to volume scattering from the canopy (Balzter 2001). We would expect any defoliation or changes in the canopy structure due to disturbance to result in backscatter changes (Imperatore et al. 2017; Wegmuller et al. 1997; Askne et al. 1997). Backscatter is important to determine the mechanism of SO_2 damage e.g. through necrosis, resulting in defoliation or chlorosis, resulting in leaf damage and colour change. If the damage results in reduced photosynthesis or bleaching due to chlorosis, but limited leaf loss, then the structure of the canopy and its scattering properties will remain mostly intact, meaning there will be limited backscatter change, but it should be detected by NDVI. If there is defoliation as a result of SO_2 exposure, which is extensive enough to cause changes to the canopy structure and scattering properties, this should be detectable in backscatter, and if reduction in photosynthesis and chlorophyll content is limited there will be less change in NDVI (Figure 3.2).

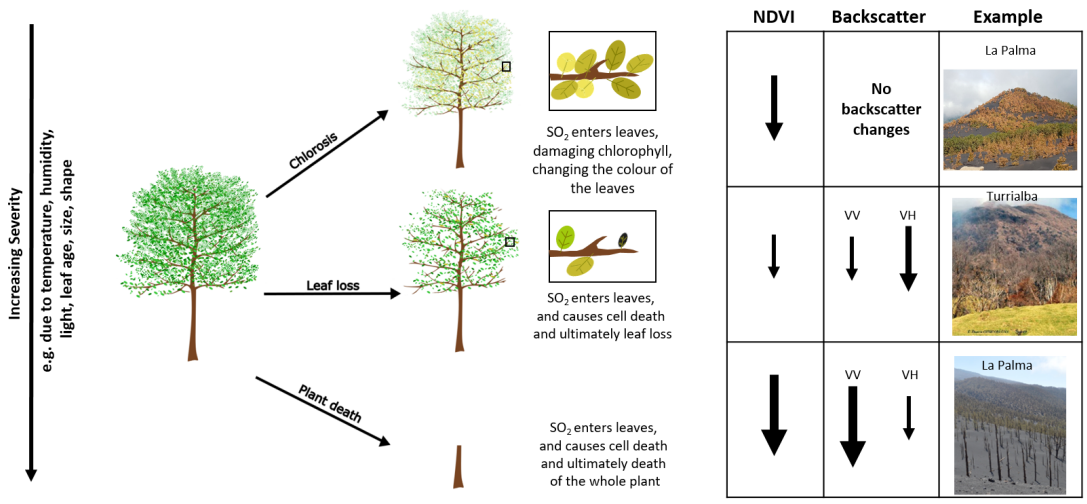

Figure 3.2: A cartoon demonstrating the types of damage expected from volcanic SO_2 emission on vegetation, the expected subsequent change in satellite NDVI or backscatter and demonstrations of those changes at La Palma (Weiser et al. 2022) and Turrialba (Tortini et al. 2017)

Table 3.1: Summary of case studies presented in this study with location (Global Volcanism Program 2025), environmental setting (Peel et al. 2007; Olson et al. 2001) and satellite data used.

Volcano	**Coordinates**	**Elevation**	**Climate type**	**Ecoregion**	**Satellite data**
Krakatau, Indonesia	6.1S, 105.4E	285m	tropical rainforest	tropical and subtropical moist broadleaf	Sentinel-1, Sentinel-2, Landsat 8
Semeru, Indonesia	8.1S, 112.9E	3,657m	tropical rainforest	tropical and subtropical moist broadleaf	Sentinel-1, Sentinel-2, Landsat 8
Reykjanes, Iceland	63.8N, 22.3W	140m	oceanic subpolar	boreal forest and tundra	Sentinel-2, Landsat 8, Landsat 7, Landsat 5
Turrialba, Costa Rica	10N, 83.8W	3,340m	tropical rainforest	tropical and subtropical moist broadleaf	Sentinel-1, Sentinel-2, Landsat 8, Landsat 7
Masaya, Nicaragua	11.9N, 86.2W	594m	tropical monsoon	tropical and subtropical moist broadleaf	Sentinel-1, Sentinel-2, Landsat 8, Landsat 7, Landsat 5, Landsat 4

3.1.4 Case Studies

We select 5 case studies to investigate SO_2, summarised in Table 3.1. These case studies were selected based on high SO_2 emissions, previous studies on vegetation impacts due to SO_2, or due to preliminary observations indicating possible SO_2 impacts. Well known degassing volcanoes like Kilauea, Ambrym, and Etna were not included, either due to limited satellite coverage or vegetation density in close proximity to the vent. Instead, we focused on sites such as Turrialba and Masaya, where SO_2 impacts are both well documented and observable in our analysis.

Krakatau, Indonesia

The islands of Krakatau are made up of the central Anak Krakatau, Sertung to the North West, Panjang to the North East and Rakata to the South East (labelled in Figure 3.3).

The central island of Anak Krakatau is the site of current activity. It had eruptions in 2017, 2014, 2013, 2010, 2009, 2007 (all with VEI 2 or less) before a VEI 3 eruption began in June 2018 consisting of explosions, tephra fall and lava flows, culminating in a lateral collapse in December 2018 resulting in a tsunami. Anak Krakatau is completely unvegetated, since the December 2018 flank collapse, prior to which there was some vegetated areas to the East of the island. The peripheral islands are all densely vegetated, although often impacted by the deposits of the eruptions. The 1883 VEI 6 eruption of Krakatau resulted in the complete loss of vegetation from the Krakatau islands and, since regrowth, volcanic activity has mostly affected Sertung and Panjang islands to the NW and NE of Anak Krakatau, affecting the vegetation succession (Whittaker et al. 1989).

For this study, we focus on unusual eruptive activity for Krakatau from 10^{th}-11^{th} April 2020. This activity consisted of a sulphur-rich, ash-poor plume on the 11^{th} April extending up to 14.3 km. This sulphur rich plume was later noted at 11.3 km high and drifting W and NW, the following days saw continued plumes of mostly sulphur dioxide, with limited ash content, up to elevations of 3 km (Global Volcanism Program 2020). There was also possible mixing of the plumes with meteorological storm clouds(Global Volcanism Program 2020). This period of activity resulted in new lava flows at Anak Krakatau, extending the islands coastline to the West (Global Volcanism Program 2020). We compare the impact of this event to the eruptive period in December 2018 where plumes were more ash rich and at lower altitudes.

Semeru, Indonesia

From April 2014, Semeru has had near continuous eruptive activity with two periods of eruption from 1^{st} April 2014 - 9^{th} January 2017, followed closely by a period of ongoing eruptive activity which began on 6^{th} June 2017. Semeru exhibits a range of deposit types including lava flows, pyroclastic flows, lahars and tephra deposits. To the North of Semeru is Bromo volcano, and combined they have one of the largest volcanic SO_2 fluxes in the 21^{st} century (Carn et al. 2017). However, due to their close proximity they are often treated as one emitter and it is hard to separate out their individual SO_2 fluxes.

We focus on small scale (both temporally and spatially) vegetation damage at Semeru through optical and radar remote sensing to see if any changes can be detected from 2014 onwards, with the onset of near continuous eruptive activity.

Reykjanes Peninsula, Iceland

The Reykjanes Peninsula in Iceland has experienced 3 new fissure eruptions since 2021. Starting with an eruption at Fagradalsfjall from 19th March - 18th September 2018, a second eruption occurred in August 2022 (from 3rd - 21st) before a third eruption period from the 10th July 2023 until 5th August 2023. In December 2023 there was another eruption on the peninsula, to the West of the previous eruption site, at the Sundhnúkur crater (Global Volcanism Program 2025). These eruptions all produced lava flows, igniting wildfires and burning the vegetation adjacent to the lava flows. The limited vegetation cover on the peninsula has been shaped by previous volcanic activity and is dominated by low level moss, shrub and grass like vegetation (Hadač 1972). The eruptions emitted large amounts of SO_2, the 2021 eruption alone emitted 970 $\pm$ 540 kt of SO_2 (Pfeffer et al. 2024). We aim to detect changes in the vegetation, primarily due to SO_2, from optical satellite data. It is known that mosses are very susceptible to environmental pollutants, due to their lack of a cuticle, and have previously been used as a way to sample pollutant concentrations and as a bioindicator for air quality (Gautason et al. 2015).

Turrialba, Costa Rica

Turrialba has had 10 confirmed eruptive periods in the 21st century, the first of which began on the 5th of January 2010, prior to which there had been no eruptions since 1866 (Global Volcanism Program 2025). This 2010 eruption followed increases in SO_2 flux from 2001, reaching 116 kt in 2009 before a significant increase in flux to 741 kt for 2010, with large SO_2 fluxes continuing until 2020 (Xi et al. 2016). Due to these large SO_2 fluxes, the vegetation at Turrialba has been severely damaged, resulting in a kill zone to the west of the vents in line with the strong prevailing wind direction (Tortini et al. 2017). While this vegetation damage and the growth of this kill zone has previously been

captured by NDVI (Tortini et al. 2017), we expand on this knowledge by using radar backscatter as a tool to assess the structural changes in vegetation at Turrialba. We investigate the whole time period from 2000 - 2024, to not only capture the vegetation damage and resulting kill zone, but also the period when SO_2 emissions decline, allowing for recovery of the vegetation around Turrialba.

Masaya, Nicaragua

Masaya has been degassing as far back as the 1500's and has regular cycles of degassing with gas crises in 1852-59, 1902-1906, 1919-1924, 1979-1984 and 1993 (the current degassing period, with fluxes peaking in the late 1990's) (Whitty et al. 2022; Mather, Pyle, Tsanev, et al. 2006). It has one of the largest non-eruptive SO_2 fluxes at 867 (t/d) (Carn et al. 2017), with a high level of variation in the flux, demonstrating changes of 50-75% within hours (Stoiber et al. 1986). It is currently in an ongoing eruptive period which began in October 2015, which saw increases in the SO_2 flux. Masaya's low topography means the plume can ground more easily, affecting the nearby vegetation. This combined with the high SO_2 flux has resulted in an area of 500 km^2 downwind of Masaya being damaged, including nearby coffee farms (Whitty et al. 2022; Stoiber et al. 1986; McBirney 1956). Damage has been noted in the form of leaf injury (both chlorosis and necrosis), particularly on the wind ward side of plants, the predominant wind direction being from the North East (Figure 3.8, panel B inset) with vegetation damage noted as far as 32 km South-west of Masaya (Delmelle et al. 2002). In this study we focus on the long term recovery of the vegetation at Masaya, since the peak of SO_2 degassing in the late 1990's. We also look at shorter term, more proximal vegetation changes as SO_2 fluxes increase following the eruptive activity beginning in October 2015.

3.2 Data and Methods

3.2.1 Optical Imagery

We use atmospherically corrected Level 2 surface reflectance data from Sentinel-2 and Landsat obtained from Google Earth Engine (Main-Knorn et al. 2017; Vermote et al.

2016). Sentinel-2 has a 5 day repeat time (when combining Sentinel-2a and Sentinel-2b) and 10 m spatial resolution. All Landsat data has a 16 day repeat time with 30 m spatial resolution. In Google Earth Engine we remove any acquisitions with cloud cover greater than 40% before applying a cloud mask using the pixel Quality Assurance band (Foga et al. 2017; Main-Knorn et al. 2017) to the remaining dataset. We then manually remove any remaining cloud contaminated images identified through visual inspection. We apply a water mask at Krakatau, Masaya, Semeru and Reykjanes using the Normalised Difference Water Index (NDWI) to identify, and subsequently mask areas of water (Xu 2006).

We use this optical imagery to calculate the Normalised Difference Vegetation Index from the near infrared and red bands of Sentinel-2 and Landsat 8. NDVI values range from -1 to 1, with dense, healthy vegetation indicated by strong positive values. Different vegetation indices may be suited to different environment types and different types of damage, in this study the NDVI showed most effective in detecting the changes at Krakatau following the event in April 2020, and was able to differentiate it from cloud cover (Figure B.1). We believe the NDVI is the best choice due to its chlorophyll sensitivity and its suitability for areas of varying topography (Roy, Boschetti, et al. 2006; Matsushita et al. 2007; Lai et al. 2022; Zhang et al. 2010). We generate time series of NDVI at selected locations shown in Figures 3.3 - 3.8 to assess the changes in vegetation over time and how this changes with eruption behaviour and SO_2 fluctuations.

3.2.2 Radar Imagery

We use Sentinel-1 backscatter imagery to assess changes to the vegetation scattering properties at Krakatau, Masaya, Turrialba and Semeru. Sentinel-1 is a satellite constellation consisting of Sentinel-1a, Sentinel-1b (until failure on the 23rd of December 2021) and now Sentinel-1c (launched in December 2024). Sentinel-1 uses a C-band (6 cm) synthetic aperture radar (SAR) with a minimum revisit time of 6 days and a geometric resolution of 5 m x 20 m in interferometric wide swath mode (Torres et al. 2012). We use Single Look Complex (SLC) images accessed from the NASA ASF data portal from

2017 onwards due to VH polarisation availability. We use the GAMMA remote sensing software (Werner, Wegmüller, et al. 2000) and limit our analysis to the bursts covering the study sites. We deramp the SLCs to account for the Doppler centroid generated by the TOPS ScanSAR mode (Yagüe-Martínez et al. 2016) and mosaic the bursts together before co-registering to a common date (the first acquisition for each site). We generate multi-looked intensity images (MLIs) over a window size of 10 in the range direction and 2 in the azimuth direction giving a pixel size of 50 m by 40 m (Lee, Grunes, et al. 1994). We perform terrain corrections and radiometric calibrations using the Copernicus GLO-30 Digital Elevation Model (DEM) (OpenTopography 2021) to mitigate for the impact of topography on backscatter, remove geometric and radiometric image distortions and decrease sensitivity to fluctuations in incidence angle (Dualeh et al. 2021; Meyer et al. 2015; Small 2011). We geocode the images using this DEM and produce backscatter images at Krakatau, Masaya, Turrialba and Semeru.

SAR sensors emit an electromagnetic pulse and the proportion of this pulse that is returned back to the satellite from the ground in either the vertical (VV) or horizontal (VH) orientation is known as the backscatter (Woodhouse 2017; Dualeh et al. 2021). We use the backscatter to assess the changes to the surface scattering properties, which we expect to be dominated by defoliation due to SO_2 exposure. We do not use backscatter at the Reykjanes Peninsula as the type of vegetation (low level moss, grass and shrub) does not produce significantly different backscatter compared to bare ground, unlike our other studies with forest vegetation. Forest canopies are volume scatterers, meaning there are multiple scattering elements present that interact with the incident radar, and can be represented by the water cloud model (Woodhouse 2017; Chen, Li, et al. 2014). Areas of volume scattering produce higher backscatter compared to areas of bare ground or less dense vegetation (Balzter 2001; Treuhaft et al. 1996). We expect to see backscatter changes from leaf death resulting in canopy loss, or plant death as a whole as this will change the scattering properties (Figure 3.2), particularly for VH backscatter, which is more sensitive to volume scattering from vegetation (Patel et al. 2006). We anticipate any vegetation recovery in the form of increased canopy density, leaf area or

plant regrowth to result in changes in backscatter, most likely detected as an increase in VH polarised backscatter. We also expect to see backscatter changes if there is tephra deposition, which may result in an increase or decrease in backscatter depending on if the deposition has resulted in a smoother or rougher surface (Arnold et al. 2018; Dualeh et al. 2021; Udy et al. 2024). As such we can use this as a way to determine if damage has been primarily from SO_2, or if ash could be present and contributing to vegetation damage.

3.2.3 SO_2 Data

Where available (at Krakatau, Turrialba, Masaya and Semeru) we have used the Multi-Satellite Air Quality Sulfur Dioxide Database (MSAQSO2L4) to assess SO_2 emissions at these sites. This level 4 product combines satellite data from the Ozone Monitoring Instrument (OMI), the Ozone Mapping and Profiler SUite (OMPS) and the TROPOspheric Monitoring Instrument (TROPOMI) to produce a global catalogue of the largest SO_2 emission sources (Fioletov et al. 2025). For Masaya and Iceland, there are limited ground based SO_2 measurements available. At Masaya, we use data from 1980 - 2023, collated from Whitty et al. 2022; Stoiber et al. 1986; Burton et al. 2000; Delmelle et al. 2002; Williams-Jones et al. 2003; Galle et al. 2003; Duffell et al. 2003; Mather, McCabe, et al. 2006; Nadeau et al. 2009; Aiuppa et al. 2018; Global Volcanism Program 2023. In Iceland, on the Reykjanes Peninsula there is an SO_2 monitoring station at the Hellisheiði power plant with, we access this data from the Icelandic Environment Agency online air quality portal, which provides data from 2021-2024.

3.2.4 Wind Speed and Directions

We estimate wind speeds and directions using ERA5 data from the Copernicus Climate Change Services (C3S), accessed through the Climate Data Store (CDS) for all of our case studies (C3S 2018). We use the reanalysis dataset which has an hourly temporal resolution and 31 km spatial resolution. We take 10 m wind data and downsample daily resolution, as this improves processing times and is sufficient for our analysis. We note that the spatial resolution is large for the given size of our study areas, but should be

sufficient to estimate wind speed and direction, but should be regarded with caution as local fluctuations could occur due to topography or other environmental factors.

3.3 Results

We present our observations of transient to long-term impacts at Krakatau, Semeru, Reykjanes Peninsula, Turrialba and Masaya using NDVI and radar backscatter. The detected impacts vary from case to case, both in terms of spatial and temporal scale as well as mechanism of damage and therefore resulting recovery rate. We then detect the range of impacts and assess the mechanism of SO_2 damage and how this can be measured using satellite remote sensing.

3.3.1 Krakatau

Following increased eruptive activity, including reports of a large sulphur-rich, ash-poor plume and new lava flows on the 10^{th}-11^{th} of April 2020, there is a major drop in NDVI on Sertung (Figure 3.3 panel B). The North-East of the island has the largest decrease, of up to 0.8 (Figure 3.3 panel E). A small area of NDVI decrease can also be seen at the northern tip of Panjang island (Figure 3.3 panel B). The wind rose (Figure 3.3 panel B inset) confirms prevailing wind direction to the NW, consistent with the directions of significant decrease in NDVI on Sertung and the observed plume directions for the 10-11^{th} April activity. This significant drop recovers within $\sim$ 4 months. There is limited backscatter change on Sertung coinciding with the large decrease in NDVI (Figure 3.3 panels C and D).

We compare these changes in NDVI and backscatter following this April 2020 event to an eruptive event in December 2018, which resulted in a flank collapse and ash-rich plumes primarily to the East (Figure 3.4). There are large decreases in NDVI of $\sim$0.8 across the whole of Panjang island, as well as minor changes on Sertung and Rakata (Figure 3.4 panel B and E). This corresponds to the prevailing wind direction and reported plume directions resulting in thick ash deposits and widespread forest damage were observed on Panjang (Cutler, Watt, et al. 2022) (Figure 3.4 panel B inset). Compared to the

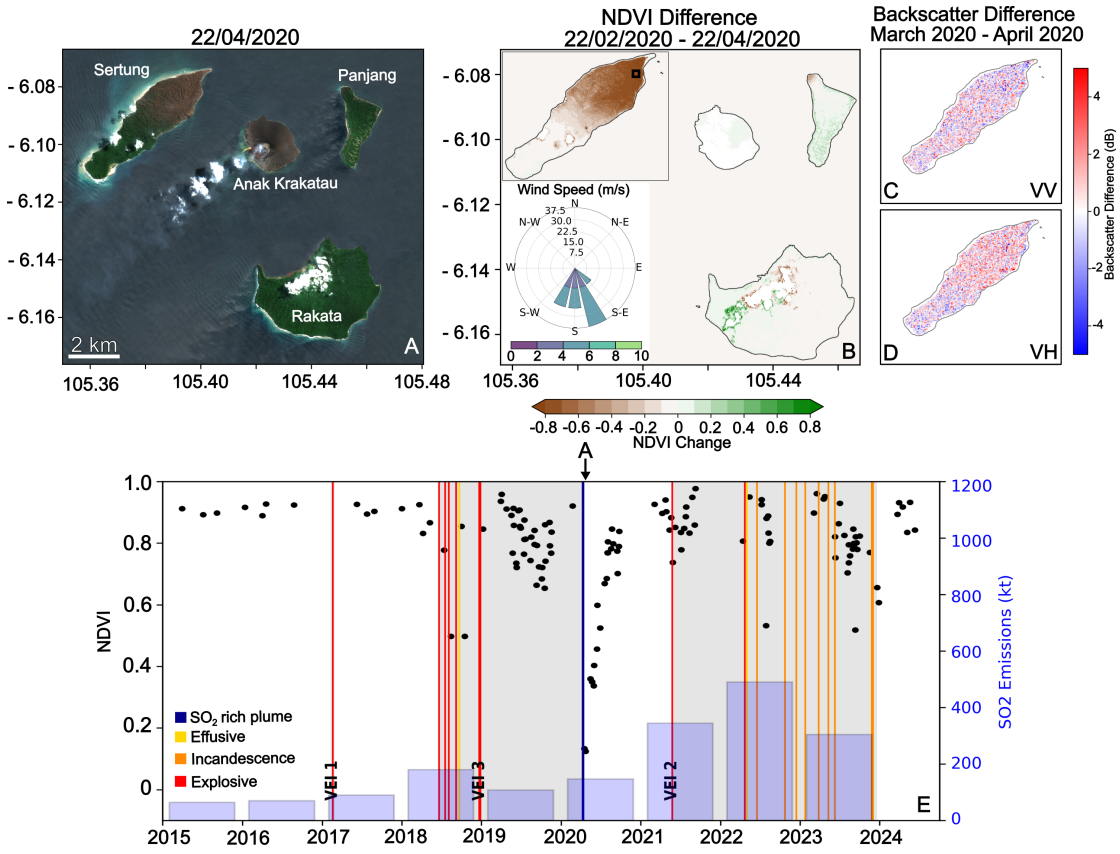

Figure 3.3: A) Sentinel-2 image of the Krakatau islands from 22nd April 2020. B) NDVI difference image showing the change in NDVI (from the 22nd of February until 17th of April), including an inset of a windrose showing the prevalent wind direction and speed over the period 1st April – 20th April. C) Sentinel-1 VV backscatter difference images over Sertung between March and April 2020. D) Sentinel-1 VH backscatter difference images over Sertung between March and April 2020. The difference is between a monthly backscatter composite for March which is subtracted from an April monthly backscatter composite to generate the difference map. E) NDVI time series for region to the North East of Sertung island (location shown by black box in panel B) the grey blocks indicate eruption periods with notable events marked, along with recorded VEI. Annual SO_2 emissions are shown in blue.

2020 event, it takes much longer for the NDVI on Panjang to return to pre-eruption values (just over 2 years), despite similar magnitude of decrease in NDVI (Figure 3.4 panel E). The recovery trajectory following the December 2018 event is consistent with previous studies on ash impacts on vegetation following an eruption (Udy et al. 2024). There is some detectable increase in backscatter on Panjang, most prominently in VV backscatter.

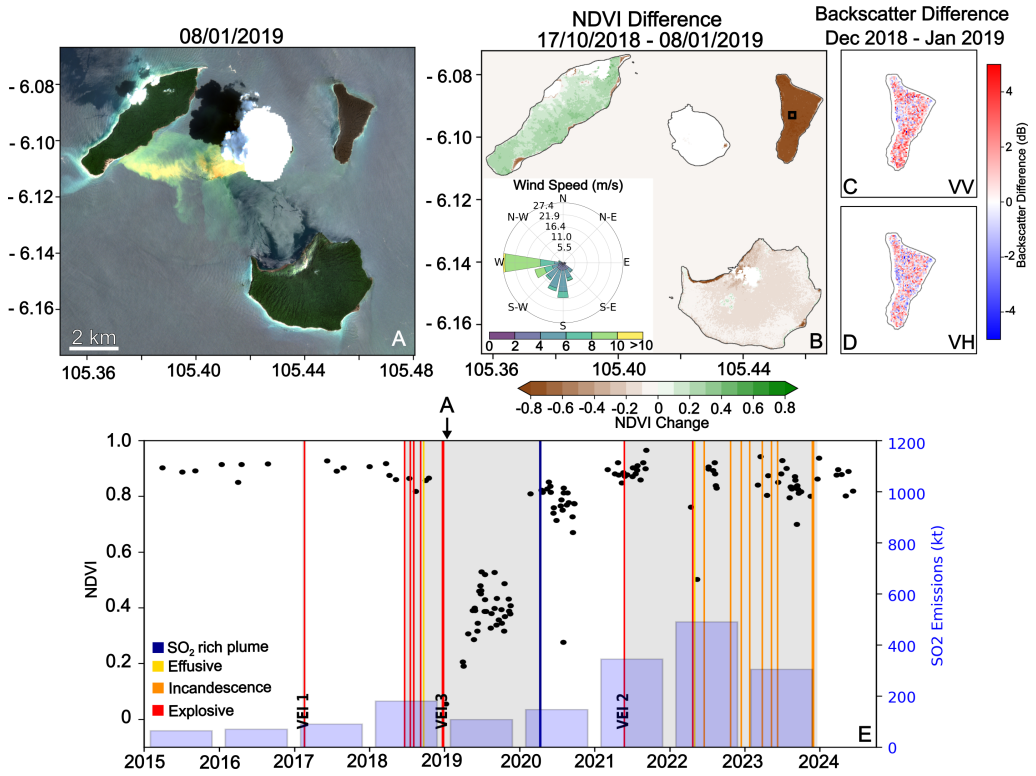

Figure 3.4: A) Sentinel-2 image of the Krakatau islands from 08/01/2019. B) NDVI difference image showing the change in NDVI (from 17/10/2018 until 08/01/2019). Including an inset of a windrose showing wind direction and speed for December 2019. C) Sentinel-1 VV polarisation backscatter difference image over Panjang between December 2018 and January 2019. D) Sentinel-1 VV polarisation backscatter difference image over Panjang between December 2018 and January 2019. The difference is between a monthly backscatter composite for December 2018 which is subtracted from a January 2019 monthly backscatter composite to generate the difference map. E) NDVI time series for a central region of Panjang island to the east of Anak Krakatau (location shown by black box in panel B with time of panel A noted).

3.3.2 Semeru

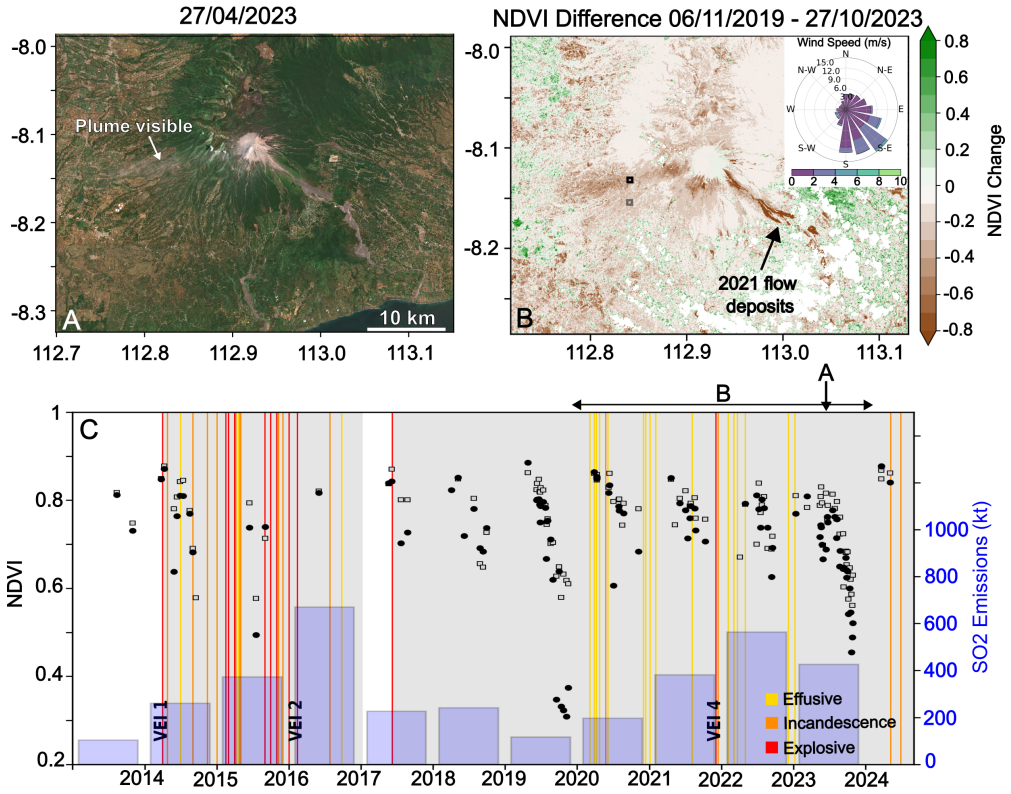

Figure 3.5: A) Sentinel-2 image of Semeru from 27/04/2023. B) NDVI difference image from 06/11/2019 until 27/10/2023 with an inset of a wind rose for 2019-2023 C) NDVI time series for an area SW of Semeru (location shown by black box in panel B) the grey blocks indicate eruption periods with notable events marked, along with recorded VEI. Annual SO_2 emissions are shown in blue for the Tengger Caldera (the combined emissions of Bromo and Semeru volcanoes).

The biggest magnitude decrease in NDVI is to the South East of Semeru, and is associated with flow deposits from the 2021 VEI4 eruption (Figure 3.5 panel B). There is also an area of NDVI decrease to the West/South west, in a similar direction to the plume visible in panel A. This decrease can be identified through the NDVI time series, and appears to be recurring and particularly defined in 2019 and 2023, towards the end of the year (Figure 3.5 panel C). While this area of NDVI decrease to the SW doesn't correspond to the most prominent wind direction (figure 3.5 panel B), wind does travel in this direction and at slower speeds. This trend in wind travelling in this direction at slower speeds occurs from May-December, corresponding to the decreases in the later parts of the year (Supplementary Figure B.7). These slower speeds could be the cause of

NDVI decrease aligning with seasonal patterns, as slower speeds could allow the plume to ground, causing vegetation damage. The occurrence of the minimum NDVI values, as well as corresponding to seasonal wind variations may also be influenced by other seasonal changes such as light, temperature or humidity, factors known to influence SO_2 damage. The SO_2 flux for Tengger caldera (Semeru and Bromo, its neighbouring volcano to the North), over this period doesn't strongly correspond to the largest decreases in NDVI. However, it is hard to know the true SO_2 flux from Semeru alone as it is jointly measured with Bromo. There are some backscatter decreases detected to the SW, more defined in VH polarisation so possibly linked to changes in volume scattering due to changes in the forest canopy, but it is hard to clearly define the region of damage or to differentiate from agriculture (Figure B.6).

3.3.3 Reykjanes

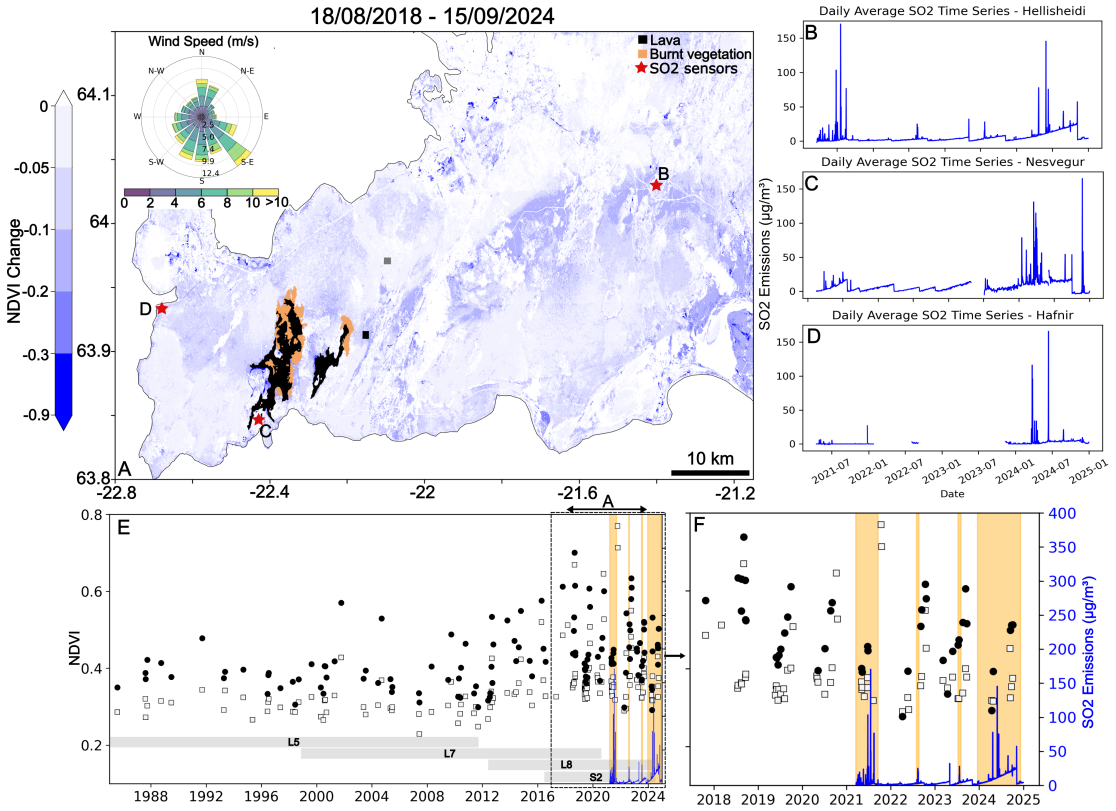

Figure 3.6: A) NDVI difference map for 18/08/2018 – 15/09/2024 showing decreases in NDVI. The lava flows and subsequent burnt vegetation from the 2021-2024 eruptions are shown in black (lavas) and yellow (fires). An inset of a wind rose is included for the period of the 2021 eruption (March – September). B) Daily average SO_2 measurements from Hellisheidi power station, location shown in panel A. C) Daily average SO_2 measurements from Nesvegur near Grindavik, location shown in panel A. D) Daily average SO_2 measurements from Hafnir, location shown in panel A. SO_2 data is taken from airquality.is and is downsampled to be a daily average in $\mu g/m^3$. E) NDVI time series for 2 locations near the eruption sites, 1 showing a more evident NDVI decrease (black) and 1 for reference (grey) shown in panel A, along with SO_2 measurements from Hellisheidi power station. F) NDVI time series using Sentinel-2 only from the end of 2017 - the end of 2024.

On the Reykjanes peninsula there is an area of NDVI decrease in a NE direction from the sites of the 2021-2024 eruptions (Figure 3.6 panel A). The sites of the eruptions are shown by the outline of lava flows (black) and subsequent burnt vegetation (yellow). NDVI time series at locations within this area of decrease (black square), compared with an area outside (grey square), show a decline in NDVI in this region from ∼2019/2020,

along with a decrease in NDVI with the onset of the Fagradalsfjall eruption in March 2021 (Figure 3.6 panel E). This is preceded by a gradual increase in NDVI from 2012 until ∼2019/2020. Lower NDVI values in the black coincide with the periods of elevated SO_2 emissions measured at Hellisheiði power plant (red star in panel A), particularly for longer duration emissions (Figure 3.6 panel F). On the contrary, the grey time series shows less fluctuation, despite starting at a similar NDVI value and showing similar increases from 2012-2019, there is then less decrease with the onset of the eruption. There is very little wind from the NE but occasional wind towards it and at slower speeds, possibly allowing plume grounding in comparison to other directions with higher wind speeds (Figure 3.6 panel A). There is elevated SO_2 emissions recorded at Hellisheidi compared to the other stations, corresponding with the direction of NDVI decline seen in panel A. As such, this decrease could correspond to changes in vegetation due to SO_2 from the eruption and also from the subsequent burning of vegetation from the lava flows (burnt area shown in yellow in Figure 3.6 panel A, covering an area of ∼230 ha).

3.3.4 Turrialba

Degassing started at Turrialba around 1996, increasing in 2001 and drastically increasing in SO_2 emission in late 2009 (Xi et al. 2016; Martini et al. 2010). Due to persistent, prevailing winds from the NE a kill zone has formed extending 2.5 km W/SW of the summit (Figure 3.7 panels A, B and D). In the centre of this area the forest has been completely killed, with decreases in NDVI of over 0.5 (Figure 3.7 panel B), with zones of necrosis on the edge. The kill zone expands during periods of increased SO_2 emission and eruptive activity, and then recovers in periods of decreased activity, with recovery starting at the edges of the kill zone. From 2000-2012 there were increases in SO_2 emission that created the kill zone (panels C and F), followed by a decline in emission rates and some recovery on the outskirts of this damage zone (panels C and G). From the end of 2014-2020 there is an increase in SO_2 emissions and an increase in eruptive activity, further developing the kill zone and decreasing NDVI and VH backscatter at the edge of the kill zone (panels C, H and J). From 2020, SO_2 emission drastically reduce to below 100 kt/y, and NDVI increased by ∼0.5, with greater NDVI increase at the edges of the

kill zone and some structural regrowth indicated by increases in VH backscatter (panels C, I, K). Changes in vegetation at the edges of the kill zone may also be reflected in changes to the variance in backscatter values (Figure B.3). After 2020, at the edge of the kill zone, the backscatter variance decreases and backscatter values start to increase slightly, possibly due to to structural recovery of the vegetation, resulting in a more homogeneous, higher backscatter surface (Udy et al. 2024). In general, the kill zone has increased in size from 2000-2020 and then began to recover from 2020 onwards (panels D and E).

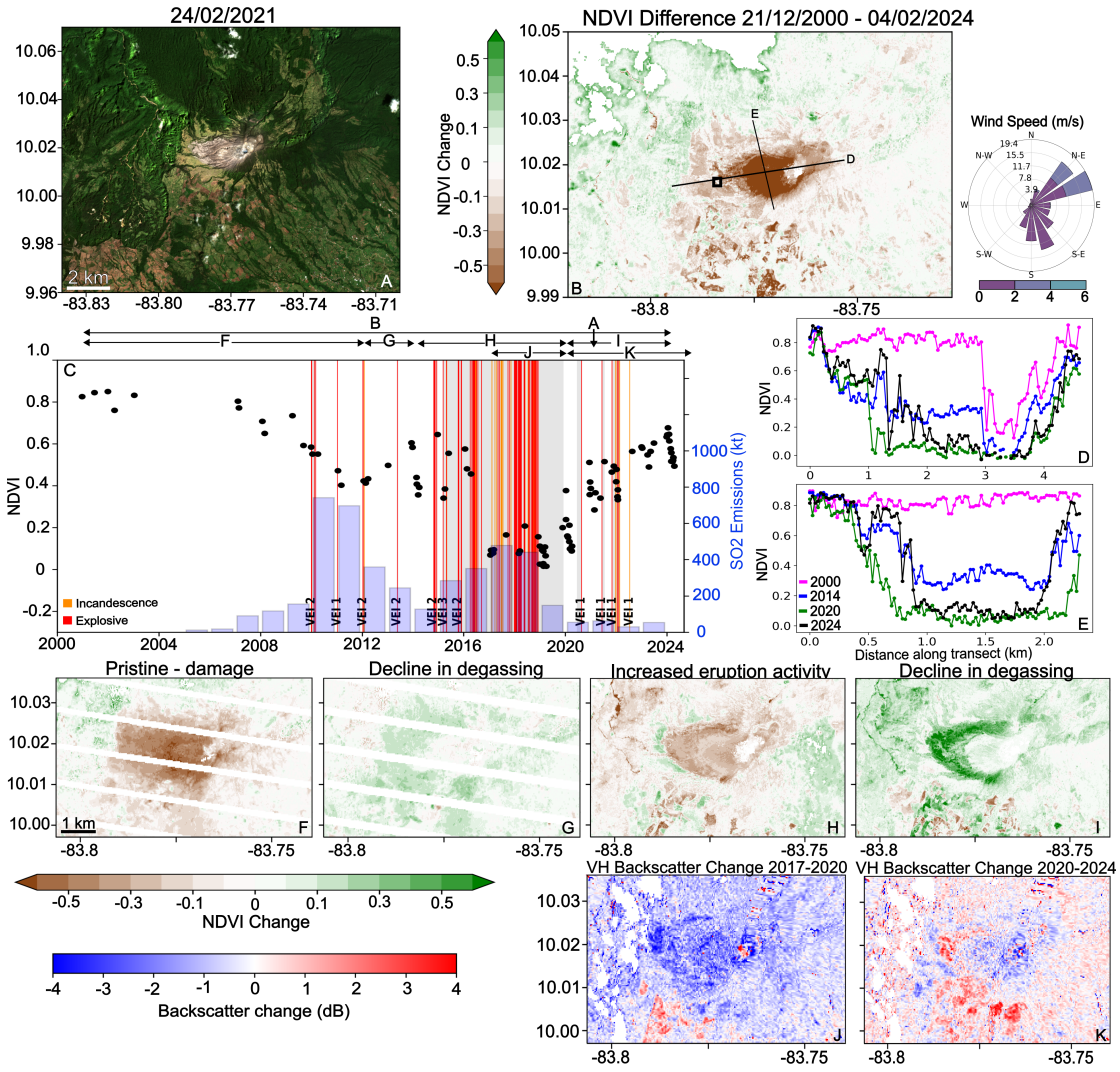

Figure 3.7: A) Sentinel-2 image of Turrialba from 24/02/2021. B) NDVI difference image from 21/12/2000 until 04/02/2024, showing the locations of the transects in panels D and E, with an inset of a wind rose for the period 2000-2024. C) NDVI time series for an area downwind, W/SW of Masaya (location shown by black box in panel B) the grey blocks indicate eruption periods with notable events marked, along with recorded VEI. Annual SO_2 emissions are shown in blue. D) Transect of NDVI values from W-E across the kill zone in 2000 (magenta), 2014 (blue), 2020 (green), 2024 (black). E) transect of NDVI values from N-S across the kill zone in 2000 (magenta), 2014 (blue), 2020 (green), 2024 (black). Panels F-I show NDVI difference maps, with the time period covered noted at the top of panel C. J) VH backscatter difference from 2017 – 2020. K) VH backscatter difference from 2020 – 2024. Each backscatter change map is made from 2 annual composites for the years, with the first subtracted from the second.

3.3.5 Masaya

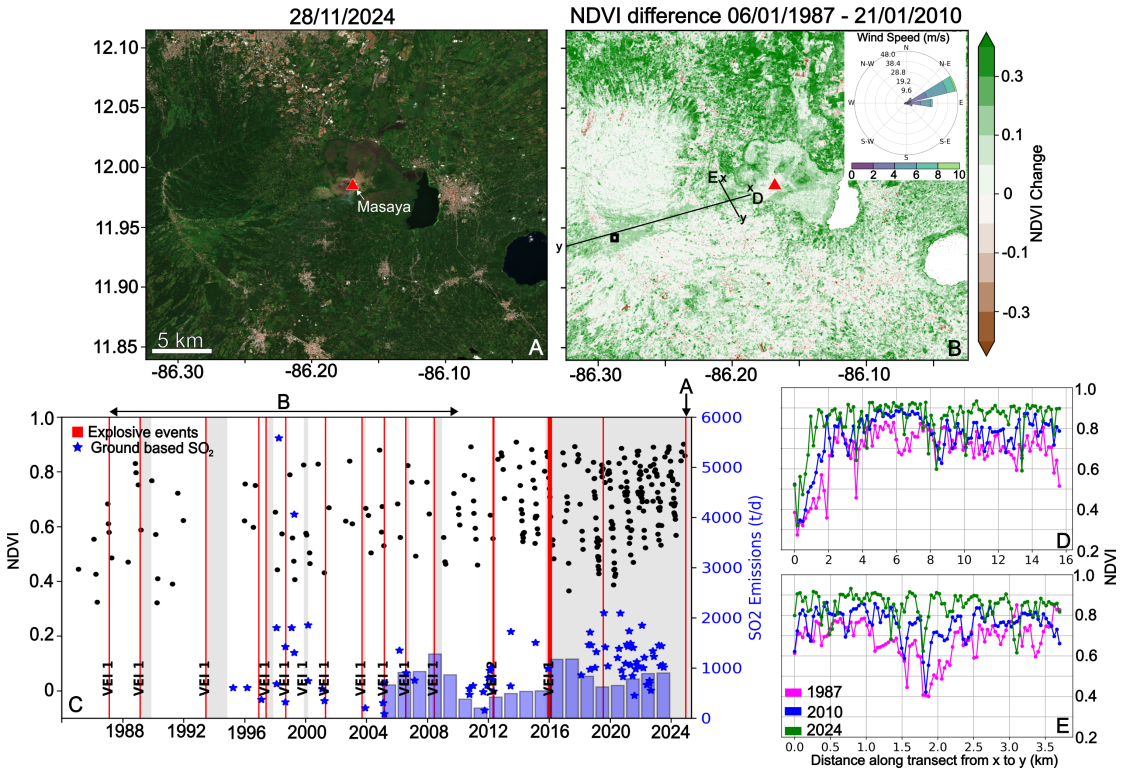

Figure 3.8: A) Sentinel-2 image of Masaya (red triangle) from 28/11/2024. B) NDVI difference image from 06/01/1987 until 21/01/2010 with an inset of a wind rose for the period 1986-2024 C) NDVI time series for an area downwind, SW of Masaya (location shown by black box in panel B) the grey blocks indicate eruption periods with notable events marked, along with recorded VEI. Annual SO_2 emissions are shown in blue, convert from kt/y to t/d to be comparable with the ground based SO_2 measurements,shown as blue stars. D) NDVI transect downwind of Masaya. E)An NDVI transect for the most damaged region close to the summit

Masaya demonstrates long term changes due to volcanic degassing, with a long recovery captured from 1986 - 2024 following the end of the previous gas crises from 1979-84 and the current crises starting in 1993 before peaking in the late 1990s (Figure 3.8 panel C) (Mather, Pyle, Tsanev, et al. 2006). Masaya has a very strong prevailing wind direction from the NE, resulting in areas downwind being damaged from SO_2, which is detectable in optical imagery, NDVI and using cluster analysis (Figure 3.8 panels A and C and Figure B.5). This region has lower NDVI values which have increased as the SO_2 flux has decreased and the vegetation has recovered (Figure 3.8). Masaya has a large variation in SO_2 flux, seen in the variation of measurements taken over short time

periods (Figure 3.8 panel C). There is a general increasing trend in NDVI from 1987 to the end of 2015 when an eruption occurs. The onset of this eruption brings an increased SO_2 flux (annual flux rate shown in blue) in 2016-2017 (Figure 3.8 panel C), resulting in a decrease in NDVI and backscatter until 2020 (Figure 3.9 panels A and C), after which NDVI increases from 2020-2024 (Figure 3.9 panels B and D). These shorter duration changes are most evident closer to the vent, but longer term changes can be seen further downwind, with a general increasing trend in NDVI as the vegetation recovers (Figure 3.8 panels D and E and Figure B.4).

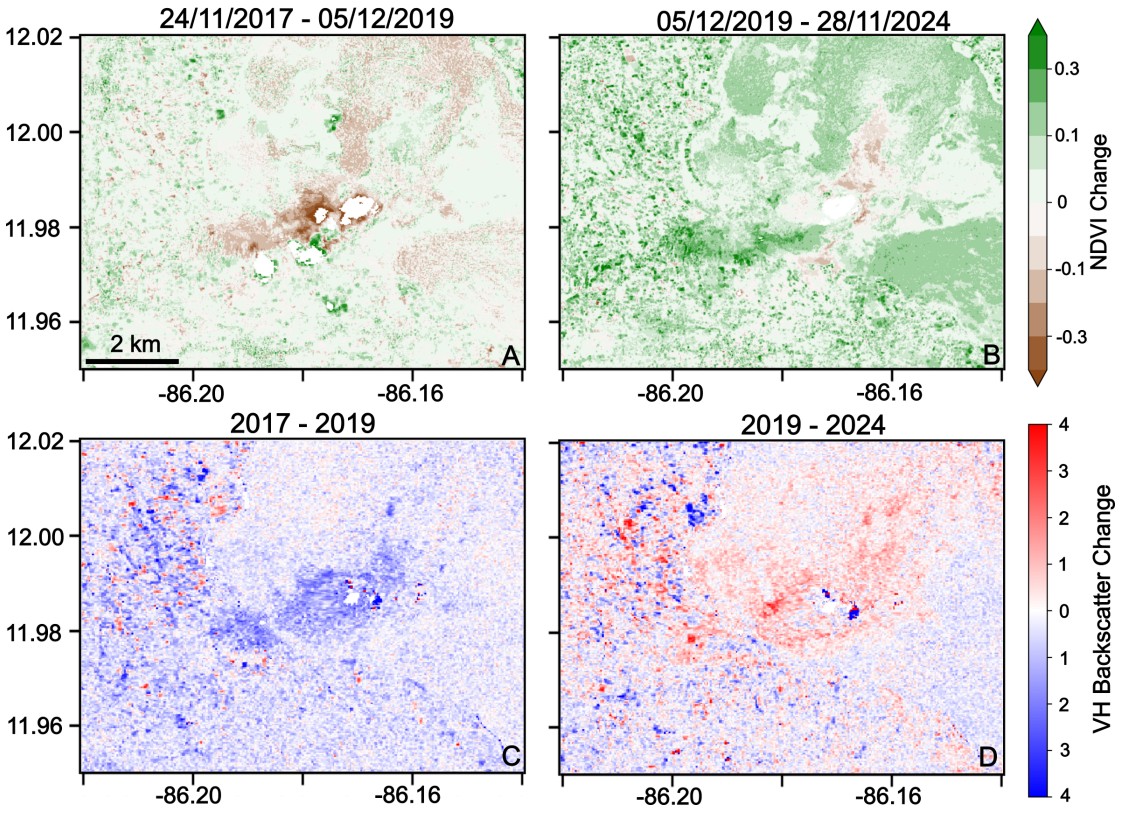

Figure 3.9: A) NDVI Difference map over Masaya for 24/11/2017 – 05/12/2019. B) NDVI Difference map over Masaya for 05/12/2019 -28/11/2024. C) Sentinel-1 VH backscatter difference map from 2017 - 2019. D) Sentinel-1 VH backscatter difference map from 2019 - 2024. The backscatter difference maps are calculated from annual backscatter composites for the years stated.

3.4 Discussion

3.4.1 Satellite Detection of SO_2 Damage on Vegetation

We present 5 examples of volcanic gases, dominantly SO_2, damaging surrounding forests up to 15 km away, with damage and recovery ranging from months to decades. Anak Krakatau exhibits the shortest of these damage durations with recovery within 4 months following the drop in NDVI in April 2020. The following lines of evidence are suggestive of this transient drop in NDVI being due to SO_2 emissions: (1) The signal of rapid NDVI decrease and subsequent recovery corresponds to reports of a plume from Anak Krakatau with high SO_2 concentrations, alongside the emplacement of new lava flows. (2) The large NDVI decrease but rapid recovery is inconsistent with previously detected ash signals (Udy et al. 2024) or from the December 2018 impacts on Panjang Island. (3) There is little to no backscatter change, which would be expected from other volcanic deposits that cause such a large magnitude NDVI change, but not from damage due to SO_2, which could cause chlorosis with limited structural damage.

In order to produce a drop in NDVI of up to 0.8 (Figure 3.3 panel C), we expect that a substantial amount of ash would need to be present (likely $\geq$15 cm (Udy et al. 2024)). This was the case in 2018, when NDVI also decreased by around 0.8, but we expect damage from this thickness of tephra deposition would take significantly longer than four months to recover. Previous studies, and the recovery following the 2018 event, shows timescales closer to 2-3 years (Udy et al. 2024). Where recovery following tephra deposition does occur within a few months, the NDVI drop is significantly lower (Udy et al. 2024). Additionally, the decrease in NDVI after the 2018 event coincided with increases in backscatter in both the VV and VH polarisations (more so in VV polarisation). This is consistent with tephra fall being the primary mechanism of damage as the tephra deposition will increase surface roughness, increasing the backscatter (Figure 3.4 panels C and D). However, there were no backscatter changes of this scale (particularly in VV) detected on Sertung in April 2020. Considering the limited change in backscatter, coupled with the significant decrease in NDVI and the reports of sulphur-rich, ash-poor

plumes and possible further degassing from the new lavas, we believe the NDVI decrease is predominantly caused by SO_2. The damage would likely be chlorosis, and photosynthesis inhabitation, causing low values in NDVI, but limited structural changes to the canopy, hence limited backscatter change. This would also explain the rapid recovery time, as the leaves would not require regrowth. While the reported plume was ash-poor, ash could still have contributed to the damage by abrading the leaves, increasing SO_2 infiltration and subsequent damage. Previous studies have shown that increased leaf abrasion, caused by wind, results in increased pollutant uptake. Abrasion causes damage to the cuticle and stomatal openings of a leaf, and can result in an up to 30 fold increase in pollutant uptake (Hoad et al. 1992). The possible presence of ash is likely to have increased the damage inflicted from SO_2 exposure, but could not have been the sole cause, due to the limited backscatter change and rapid recovery.

Semeru exhibits changes that coincide with seasonal trends in wind and precipitation, rather than coincide with large changes in SO_2 flux. Semeru combined with the neighbouring Bromo volcano make up the Tengger caldera, which has a history of large SO_2 emissions and was ranked the 20th largest volcanic SO_2 source by Carn et al. 2017 from 2005-2015. There are seasonal variations in wind speed and direction at Semeru, with slower speeds, particularly to the south west, in the later parts of the year. We suggest these seasonal changes in wind are allowing the plume to ground, resulting in damage to vegetation. The more significant decreases in NDVI in 2019 and 2023 also coincide with decreases in backscatter to the SW. This suggests some structural changes to the vegetation, reducing the backscatter, possibly leaf loss due to SO_2 exposure. These decreases occur either side of increased eruptive activity from 2020-2023, with this more explosive activity possibly resulting in higher, more energetic plumes meaning it is not affecting proximal vegetation. It is also possible that other seasonal factors are affecting the levels of SO_2 damage. The decreases in NDVI and backscatter seem to coincide with the dry season (June - September) when temperatures are warmer, this could encourage stomatal opening and increase SO_2 infiltration, causing the damage to appear in line with the seasons (Driesen et al. 2020).

The Reykjanes Peninsula shows lower magnitude, longer duration, changes in NDVI, partly due to the vegetation type having low NDVI values initially. The decrease in NDVI, to the north east of the lava flows, is over a much larger area than seen in the other case studies. The area impacted had a slightly higher NDVI value prior to the decrease in NDVI, possibly due to a higher vegetation density or different structure. This may partially be why the decrease was detected here, there needs to be sufficient vegetation, or high enough NDVI values to measure the decline. The type of vegetation likely plays a role as to why the decrease is seen over such a large area, with mosses being particularly sensitive to air pollutants like SO_2. The limited decrease suggests changes in the greenness or health of the vegetation to the north east of the lava flows, possibly due to the SO_2 emissions from the eruptions. As well as the longer term trends of increasing NDVI prior to the eruption, and decreasing from ∼2019-2020, there also appears to be shorter term decreases linked to increases in SO_2 flux. However, it is hard to robustly detect these changes due to limited optical satellite acquisitions due to cloud and snow cover, and the vegetation type not being appropriate to study with radar backscatter.

Similarly to the Reykjanes Peninsula, Turrialba shows both long term and short term NDVI changes in response to changes in SO_2 flux. In the longer term, there is an increase in SO_2 flux, creating a kill zone down wind, which then begins to shrink as it recovers from the exterior, in response to decreasing SO_2 flux. In the shorter term are periods of both increased damage and periods of recovery in response to flux change. Distance downwind controls the severity of damage, the most proximal region (<2 km to the west) has lost all vegetation and exhibits the largest decreases in NDVI and backscatter as a result. The edges of the damage zone (2.5-3 km) show large decrease in NDVI and minor decreases in backscatter, suggesting the main mechanism of damage is chlorosis and some leaf loss, without significant plant death or structural changes. This allows the periods of recovery as total regrowth isn't required.

Masaya also shows longer term trends, with much slower rates of change, likely due to the long durations and high concentrations of SO_2 exposure resulting in significant damage and decimation of vegetation downwind at Masaya, with the most significant damage

linked to areas of highest SO_2 concentration at 4 km and 15 km downwind (Delmelle et al. 2002). Vegetation at Masaya is particularly susceptible to damage due to the volcanos low topography, the plume can regularly ground directly on the vegetation (Whitty et al. 2022). The area of damage highlighted by previous studies is successfully detected through NDVI, and shown as NDVI increase in Figure 3.8 panel B. It is also successfully detected through k-means cluster analysis of the NDVI time series, and is separated as a cluster showing the area downwind of Masaya Figure B.5.

3.4.2 Factors Affecting Damage Severity

Vegetation damage due to SO_2 can result in a range of damage severity and duration, particularly in comparison to other volcanic impacts (Udy et al. 2024). SO_2 flux and duration of exposure are the most significant factors determining damage severity and duration. Lower fluxes over shorter durations will lead to less significant damage, as seen at Krakatau in April 2020 (Shimazaki et al. 1980; Thomas et al. 1935). The exact SO_2 flux in this case is unknown, but the volcano is not normally a large emitter. This, coupled with the short duration of increased activity (2 days) and the plume height, likely resulted in only short periods of grounding on Sertung and so lower flux. We cannot be certain of the exact mechanism of damage here due to the lack of observations. The sulphur-rich plume could have directly come into contact with the vegetation, if there were periods when it had a lower altitude. Degassing from the new lava flows could also have damaged the vegetation, as this would have been at sea level. There were reports of the sulphur-rich plume interacting with meteorological clouds, which would have produced acid rain damaging the vegetation. Or it could be a combination of these processes leading to damage. As such it is likely the flux and duration were low, and as a result, the primary damage mechanism was chlorosis and photosynthesis inhibition, rather than leaf loss and plant death. In comparison, large fluxes, over longer durations cause more severe damage in the form of necrosis and even total plant death. This can be seen at Turrialba from 2000-2016, with the kill zone forming downwind. It is also evident that at a greater distance from this downwind trajectory (at the edge of the kill zone) the damage is less severe, likely due to shorter durations of exposure and

lower SO_2 concentrations. Masaya also shows severe damage, due to large fluxes over a long duration, and we observe the subsequent recovery from 1988 onwards. Closest to the summit there are areas of complete vegetation loss, and downwind there is an area which is sill recovering after the previous gas crises caused very high SO_2 flux. The long duration of SO_2 flux will have contributed to the high levels of damage resulting in plant death.

As well as the SO_2 flux and duration, external factors influence the severity of damage. These factors influence the absorption of SO_2, even if flux and duration are the same the level of damage changes as a result of of external factors (Thomas et al. 1935). Seasonality can affect damage severity as it will affecting daylight, temperature, humidity and wind conditions, all of which will influence SO_2 absorption (Hüve et al. 2000; Driesen et al. 2020; Hoad et al. 1992). This is demonstrated at Semeru as decreases in NDVI and backscatter coincide with the seasons. In this case, it is likely dominated by seasonal wind changes, allowing the sulphur containing plume to ground and deposit on the vegetation, but it is also likely that other seasonal factors, such as precipitation and humidity, may play a role as the damage is coincident with the summer months. The vegetation type itself will also play a role, as plant age, structure, leaf shape and cuticle thickness will affect SO_2 absorption (Han et al. 2022; Knabe 1976; Rankenberg et al. 2021). And as such some plant types are simply more resilient to external stressors such as SO_2 exposure, an important factor in our ability to detect damage due to SO_2 on the Reykjanes Peninsula. The vegetation type being lichen, moss and grassland, means it is sensitive to SO_2 exposure, demonstrating a reduction in photosynthesis, but without significant visible or structural damage that may be shown from other plant types (Beekley et al. 1981; Winner and Bewley 1978). As such, changes due to SO_2 are subtle, particularly as the vegetation begins with lower NDVI values and backscatter is not sensitive to changes in mosses.

Other volcanic activity influences damage severity due to SO_2 exposure. For instance, ash deposition can exacerbate leaf injury by abrading surfaces and damaging stomata, increasing SO_2 absorption (Hoad et al. 1992). This may help explain the damage severity

observed at Krakatau in April 2020, where ash was likely present in the plume, even if not the primary cause of damage. Turrialba also exhibited other volcanic activity from March 2015 - December 2019, including ash deposition and pyroclastic density currents in the areas most proximal to the volcano. This period of increased activity not only increased SO_2 flux beginning in 2015 and peaking in 2017, coinciding with NDVI decrease, but was likely responsible for additional damage due to other deposits. Conversely, increased activity at Semeru from 2020 - 2023 coincided with decreased damage that we attribute to SO_2. This activity likely resulted in more energetic, higher altitude plumes (Global Volcanism Program 2025), and so not directly impacting the adjacent vegetation, and reducing the measurable damage during that period of activity.

These factors control the absorption of SO_2 and the severity of damage, and subsequently the time it takes to recover. Increased flux, duration of exposure, environmental setting or other volcanic deposits lead to more absorption and severe damage such as leaf loss and total plant death. This more severe damage subsequently takes longer to recover, as whole plant elements require regrowth. This is demonstrated at Krakatau, where there was limited structural damage to the vegetation, primarily damage through chlorosis and photosynthesis inhabitation, and so recovery was as little as 4 months, in comparison to the more severe damage at Turrialba and Masaya which takes years-decades to recovery. Environmental setting will play a role in recovery time, similarly to how it plays a role in SO_2 absorption, with light, humidity and temperature as influences in recovery time (Hüve et al. 2000). Distance to disturbance centre, previous disturbances, elevation, slope and forest stand height can also contribute to recovery rate (Shatto et al. 2024; Weiser et al. 2022; Mora et al. 2016). The plant species and maturity level will impact recovery time, as well as the ecoregion, with more tropical regions exhibiting quicker regrowth rates (Gillman et al. 2015; Han et al. 2022; Rankenberg et al. 2021). The volcanic activity and continued SO_2 flux rate will also affect the duration of damage and how long it takes to recover. If there is eruption activity or further periods of increased flux this will prevent recovery, as seen at Turrialba.

3.4.3 Vegetation Resilience in Response to Repeated Disturbance

By investigating SO_2 damage at a range of case studies and timescales we can gain an insight into vegetation resilience at these sites in the presence of SO_2 exposure. Vegetation resilience is defined as the ability to withstand disturbance and recover to its previous state (Holling 1973). The case studies of Turrialba and Masaya are particularly key as we can see long term trends. At Turrialba, despite the high SO_2 flux and years long exposure, when there is a decrease in flux there is vegetation recovery e.g. in 2014 and 2020. The vegetation withstands the disturbance and begins recovery once the disturbance stops. At Masaya this is also evident as we see the long term recovery of the vegetation despite continued SO_2 emission. These cases are possible examples of gained resilience resulting from prolonged exposure to environmental stressors. Such exposure may promote adaptive traits, shifts in species composition, dominance of better adapted species or more diverse assemblages, all of which can contribute to increased resilience (Gunderson 2000; Holling 1973; Han et al. 2022).

Resilience can be inherent to the vegetation type, rather than gained due to increased exposure. For example, the vegetation at Krakatau may be resilient as it is successional vegetation following the 1883 eruption which removed all vegetation. In response to this disturbance, what regrew may be species and assemblages which are more resilient, either due to specific species having physiological advantages or a more varied assemblage (Han et al. 2022; Madamanchi et al. 1991; Olszyk et al. 1984). In recent years Sertung has not experienced excessive periods of disturbance and so vegetation was likely healthy, and these factors combined could have made it more resilient to the SO_2 emission, contributing to the less severe damage and quicker recovery times.

Repeated exposure may contribute to increased resilience, though this effect is likely offset when damage is too severe and recovery time is insufficient. This idea was explored at La Palma following the 2021 Tajogaite eruption which resulted in chlorosis and defoliation in a 7 km radius of the volcano (Weiser et al. 2022; Shatto et al. 2024). Distance was the most controlling factor of vegetation damage, with vegetation at an intermediate distance having a faster recovery rate than vegetation closest or furthest

from the volcano (Shatto et al. 2024). Shatto et al. 2024 hypothesise that vegetation at an intermediate distance would show the most rapid recovery, as it has resilience due to more exposure to disturbance, coupled with less severe damage. In contrast, more proximal vegetation may be too heavily damaged to recover quickly, while distal vegetation, although less affected, may be less resilient due to less exposure to prior disturbances. However, they also demonstrated that forest stands affected by the 2016 wildfires and then subsequent 2021 volcanic eruption are actually recovering faster than stands just impacted only by the eruption, possibly showing that compounding disturbances don't necessarily decrease recovery rates as they initially expected, but increase resilience and so recovery rates. This is likely a factor at Turrialba, as vegetation rapidly recovers despite the repeated disturbance. At Turrialba, whilst looking at the recovery of NDVI shows the edges of the kill zone recovering faster, the VH backscatter difference map from 2020-2024 (Figure 3.7 panel K) shows an area of increased backscatter not quite at the edge of the kill zone and vegetation at a greater distance which shows a decrease in backscatter. This could be structural recovery of the vegetation at this distance as it has been previously exposed to disturbance so could be more resilient and able to recover quicker.

Environmental setting, while likely affecting SO_2 exposure, as discussed previously, also plays a role in the resilience, and as such the subsequent recovery rate of the vegetation. Tropical forests are inherently more resilient, due to being more varied, water availability and species types (Smith, Traxl, et al. 2022; Smith and Boers 2023; Han et al. 2022). Certain species can have inherent resilience due to their structure, as well as becoming more resilient with maturity (Rankenberg et al. 2021; Shatto et al. 2024; Han et al. 2022). This is important in volcanic settings as if large disturbances result in younger, less varied plant communities this could decrease resilience. Alternatively, disturbance could produce successional plant communities which are more varied and resilient, particularly if they reach maturity before the next volcanic disturbance.

3.5 Conclusion

In conclusion, satellite data enables the detection of vegetation damage from SO_2 exposure, revealing a range of damage severities and recovery times linked to different damage mechanisms such as chlorosis, leaf loss and plant death. Shorter term, less severe impacts are typically associated with lower SO_2 fluxes over days, resulting in sharp decreases in NDVI of up to 0.8 with minimal backscatter changes suggesting photosynthesis inhibition, limited structural damage and as such full recovery within months. In contrast, more severe damage caused by higher fluxes over longer durations can result in long-term vegetation loss across several km^2, with both NDVI and backscatter signatures significantly altered, requiring years to decades for full recovery. The degree of damage is primarily driven by SO_2 flux and duration, but is also influenced by environmental conditions, vegetation type and additional volcanic activity. Forest type, species composition, plant maturity, and seasonal factors such as light and wind patterns all play roles in determining resilience and recovery. Notably, sites like Turrialba and Masaya show that resilience may be both intrinsic and developed through repeated exposure. This study contributes to a deeper understanding of how SO_2 emissions impact ecosystems and highlights the potential of remote sensing to monitor such effects. These insights can aid in identifying SO_2-rich plumes and support efforts in plume tracking, environmental monitoring, and hazard assessment.

Chapter 4

Forest Disturbance, Recovery and Resilience at Volcanoes World Wide

Abstract

Volcanic eruptions drive major disturbances to forest landscapes, yet the controls on vegetation damage and recovery remain poorly quantified. This study analyses forest damage and post-eruption recovery across 18 volcanoes worldwide, spanning different climatic zones, forest types, and eruption styles. Using optical satellite time series of NDVI, combined with time series cluster analysis, we quantify the temporal and spatial scales of damage and recovery trajectories associated with tephra fallout, pyroclastic density current (PDCs), lava flows and volcanic blasts. We find recovery is strongly influenced by disturbance type, eruption magnitude (VEI), eruption duration, and forest biome. On average, tephra-affected areas recover to pre-eruption NDVI values in approximately 2.8 years, followed by blast-affected areas in 12.5 years, while forests impacted by pyroclastic density currents (PDCs) take longer, averaging around 22 years. Tropical forests have faster recovery times than temperate forests, likely due to higher resilience and faster regrowth rates. Longer duration and multi-deposit impacts are associated with greater damage and extended recovery times, but may also influence long-term resilience. Our results provide a quantitative framework for predicting forest recovery after volcanic dis-

turbance, identifying the key volcano-environmental parameters (eruption size, duration, deposit type and forest biome) that govern the magnitude, duration and style of satellite detectable ecological impact. These findings enhance our ability to interpret ecosystem development and reconstruct past eruptive activity from forest structure using remote sensing.

4.1 Introduction

Volcanic eruptions cause disturbance to surrounding forests, at a variety of spatial and temporal scales from transient, local impacts to damage that lasts decades over 100s km^2 (Dale, Swanson, et al. 2005; Major and Lara 2013; Grilli, Tappin, et al. 2019). However, the current impact of active volcanism on ecosystems, and how quickly they can recover is not well quantified, particularly with the use of systematic, global scale satellite data. The type of eruption (deposits present, scale, duration and explosivity) and the environmental setting will strongly influence the scale (both spatial and temporal) of disturbance (Foster et al. 1998; Swanson and Major 2005). The duration of detectable disturbance is controlled by vegetation recovery and resilience, which are expected to vary globally with environmental conditions, but may also be influenced by site-specific or eruption-specific factors (Smith and Boers 2023). This is key to understanding how long these signatures may be detected and how far back we can identify previous volcanic activity through assessment of forest disturbance. It has been hypothesised that volcanoes influence surrounding ecosystems on large scales, up to continental scales for the largest eruptions (Briffa et al. 1998; Thordarson et al. 2003). Here, we test the measurable impact of major eruptions on surrounding forests using optical satellite data over the past 40 years. Satellite data provides systematic coverage at a global scale, allowing uniform analysis of multiple volcanoes in different environmental settings. We focus on explosive eruption impacts, with significant enough damage to be detectable in satellite imagery (larger than 10 m pixel size) due to changes in the vegetation properties (i.e. health or coverage).

4.1.1 Impacts of Volcanic Eruptions on Surrounding Vegetation

Forest disturbance is becoming an ever more important topic as climate change increases the severity and frequency of weather related natural hazards such as wildfires, droughts and floods as well as anthropogenic disturbance from pollution. Of these forest disturbance events, wildfires likely cause the most similar style of damage to volcanic deposits. The severity of damage, and subsequent recovery following wildfire is predominantly controlled by the type of vegetation, temperatures reached and tree survival (Gouveia, DaCamara, et al. 2010; Bastos et al. 2011). The most rapid recovery is seen within the first 2 years after the fire disturbance (Trabaud 1987; Inbar et al. 1998; Gouveia, DaCamara, et al. 2010). Optical satellite imagery, and more specifically the Normalised Difference Vegetation Index (NDVI), has been successfully used to monitor fire damage, recovery rates and regrowth dynamics (White et al. 1996; Goetz et al. 2006; Gouveia, DaCamara, et al. 2010; Ireland et al. 2015).

Volcanoes differ from other natural hazards impacting vegetation, such as seasonal events like fire and drought, in the extreme diversity of the character and extent of damage (Zobel et al. 1997). The damage caused by large explosive eruptions can be particularly extensive, reaching thousands of square kilometres (Carey and Sigurdsson 1989; Self 2006). Hot pyroclastic density currents (PDCs) not only destroy vegetation they come into contact with, but can also singe adjacent areas of vegetation up to hundreds of metres away from the flow deposit (Charbonnier et al. 2013). In contrast, tephra fall causes less intensive damage over a much greater area, spreading to regions many hundreds of kilometres away (Wilson, Stewart, et al. 2013; Wilson, Jenkins, et al. 2015). Tephra damages vegetation through abrasion, which can impair photosynthesis, and in areas of thick tephra deposit, cause complete burial of vegetation (Wilson, Cole, et al. 2011; Turner et al. 1997). This variation in damage levels results in a variety of vegetation recovery stages and therefore durations of damage.

The pattern of disturbance also influences the post eruption recovery time of vegetation (Foster et al. 1998). Linear disturbance patterns from flow deposits like PDCs, lava flows and lahars are some of the most intense forms of damage, but due to the linear shape,

will have healthy vegetation adjacent to the damaged vegetation. This will influence the recovery, as healthy vegetation can spread more easily to damaged areas through natural mechanisms such as wind, water or animal dispersal, promoting regrowth. Conversely, sectoral (or isodiamteric) patterns of disturbance such as blast or tephra fall may be slower to recover as the closest surviving vegetation will be further away from the central area of damage (Dale, Delgado-Acevedo, et al. 2008).

Mount St Helens is a seminal study site in understanding forest disturbance dynamics and regrowth patterns following volcanic eruptions. It has improved understanding in the factors influencing forest disturbance and recovery. Surviving plant matter (biological legacies) is key to recovery as it is essential to instigate regrowth. Damage that results in greater numbers of legacies, either due to damage being minor or over smaller areas, will recover faster due to the surviving plant matter. The type of volcanic deposit or the timing of deposits can play a key role in numbers of legacies (Foster et al. 1998). This is evident following the 1980 eruption of Mount St Helens, where the combination of disturbances resulted in a high proportion of surviving plant matter (Franklin et al. 2000). The trees felled in the initial volcanic blast protected underlying vegetation from subsequent impacts, resulting in higher numbers of legacies compared to the regions not impacts by the blast, but impacted by other subsequent deposits. This contributed to quicker recovery rates in certain areas of the blast zone (Dale, Crisafulli, et al. 2005; Dale, Delgado-Acevedo, et al. 2008; Franklin et al. 2000). Some plant species may also be better equipped to survive volcanic eruption damage. For example, plants with underground components (seeds and buds) may survive eruptions and be able to regrow (Dale, Delgado-Acevedo, et al. 2008). Some plant species may have a thicker outer layer on their leaves (cuticle) making them more resilient to environmental stressors. A thicker cuticle also develops in many species with maturity, so that plant age can be a factor in surviving stressors (Rankenberg et al. 2021). This can be a factor in forests where more mature trees may be taller and sit above the height of the potentially damaging volcanic deposit, or protect underlying vegetation from tephra fall, possibly increasing the number of biological legacies. As well as the eruption and vegetation characteristics,

external factors can influence plant matter survival. The time of year can play a role, with plant elements underground at certain parts of the year, or winter snow cover protecting plant matter from eruption deposits (Dale, Delgado-Acevedo, et al. 2008; Dale, Crisafulli, et al. 2005). This was a factor in the high level of biological legacies at Mount St Helens, as the spring time eruption meant some of the temperate species had underground elements protected, along with remnants of the winter snow pack that protected underlying vegetation from the blast and tephra deposits.

This combination of contributing factors from the eruption, vegetation, environmental setting and external factors are likely to mean there is a complex relationship affecting plant matter survival and subsequent recovery rates. Generally, we expect the most damage to be from flow deposits, with eruptions over large areas and long durations to have slower recovery rates. Environmental setting will play a role with tropical regions likely recovering faster than temperate, but this could be complicated by the seasonal timing of deposits, as demonstrated at Mount St Helens. We intend to expand on previous work, that has focussed on only a handful of key sites, using optical satellite data across different environmental settings and different explosive eruptions to better understand and quantify what influence environmental settings and eruption styles have on vegetation damage and subsequent recovery and resilience.

4.1.2 Climate Types

There are 5 main classifications of climate, from the Koppen-geiger classification: Tropical, Arid, Temperate, Cold and Polar, each classification then has further sub classifications dependent on temperature and precipitation, and how they vary throughout the year (Peel et al. 2007). Our 18 target volcanoes span 6 climate types within 2 main classifications: Tropical (Tropical rainforest, Tropical savannah and Tropical monsoon) and Temperate (Humid subtropical, Temperate oceanic, warm summer Mediterranean). A tropical climate is defined by the temperature of the coldest month being greater than 18°C. A temperate climate is classified by the temperature of the hottest month being greater than 10°C and the coldest month between 0-18°C. Vegetation resilience and re-

growth is expected to be greater in tropical regions and is affected by water availability and variability, with regions with more inter-annual precipitation variability being less resilient (Smith and Boers 2023). Although some temperate species may be less susceptible to damage, and some species may be protected in dormant (winter) phases (Dale, Delgado-Acevedo, et al. 2008; Dale, Crisafulli, et al. 2005).

4.1.3 Forest Types

Ecoregions are defined as relatively large units of land containing a distinct assemblage of natural communities and species, with boundaries that approximate the original extent of natural communities prior to major land-use change (Olson et al. 2001). They are therefore a better reflection of the global distribution of species and communities than models derived from, for example, rainfall and temperature (Olson et al. 2001). In the classification scheme by Olson et al. (2001) there are 14 biomes and 8 biogeographic realms. Our target volcanoes are situated within 4 biomes: Tropical and subtropical moist broadleaf forest, Tropical and subtropical dry broadleaf forest, Temperate broadleaf and mixed forest, and Temperate coniferous forest. Tropical and subtropical moist broadleaf forest are characterised by high species variability, low temperature variability and high rainfall levels. Tropical and subtropical dry broadleaf forest share similar characteristics but have dry seasons. Temperate broadleaf and mixed forest have a combination of coniferous and broadleaf tree species. Temperate coniferous forests are characterised by larger temperature variability compared to tropical forests (warm summers, cool winters) with either needle leaf or broadleaf evergreen species dominating (Olson et al. 2001). Forest type is likely to influence vegetation recovery and resilience similarly to climate, with tropical vegetation expected to be more inherently resilient to environmental stressors and disturbances. But variations in dominant species type and density will influence recovery and resilience (Wright 2002; Smith, Traxl, et al. 2022).

4.1.4 Selection of Target Volcanoes

We select target eruptions and volcanoes that we expect have had a measurable impact on surrounding forests during the satellite era. The criteria for inclusion are as follows:

eruptions with VEI 5 after 1970, eruptions with VEI 4 after 1990 and eruptions with VEI 3 after 2014 (Smithsonian Institution's Global Volcanism program (Global Volcanism Program 2025)). These categories are designed to include eruptions with good satellite data coverage and eruptions large enough to produce measurable impacts in satellite imagery. We then filter the list further to remove any eruptions at volcanoes that weren't sufficiently vegetated (either due to being bare rock, dominated by agriculture or directly adjacent to urban areas), or where optical imagery was dominated by cloud cover or snow/ice cover. For example, volcanoes on the Aleutian islands, like Cleveland and Shishaldin, both fit our date and eruption criteria but are not sufficiently vegetated and have snow/ice cover affecting satellite acquisitions. This results in a refined list of 18 target volcanoes, shown in Figure 4.1.

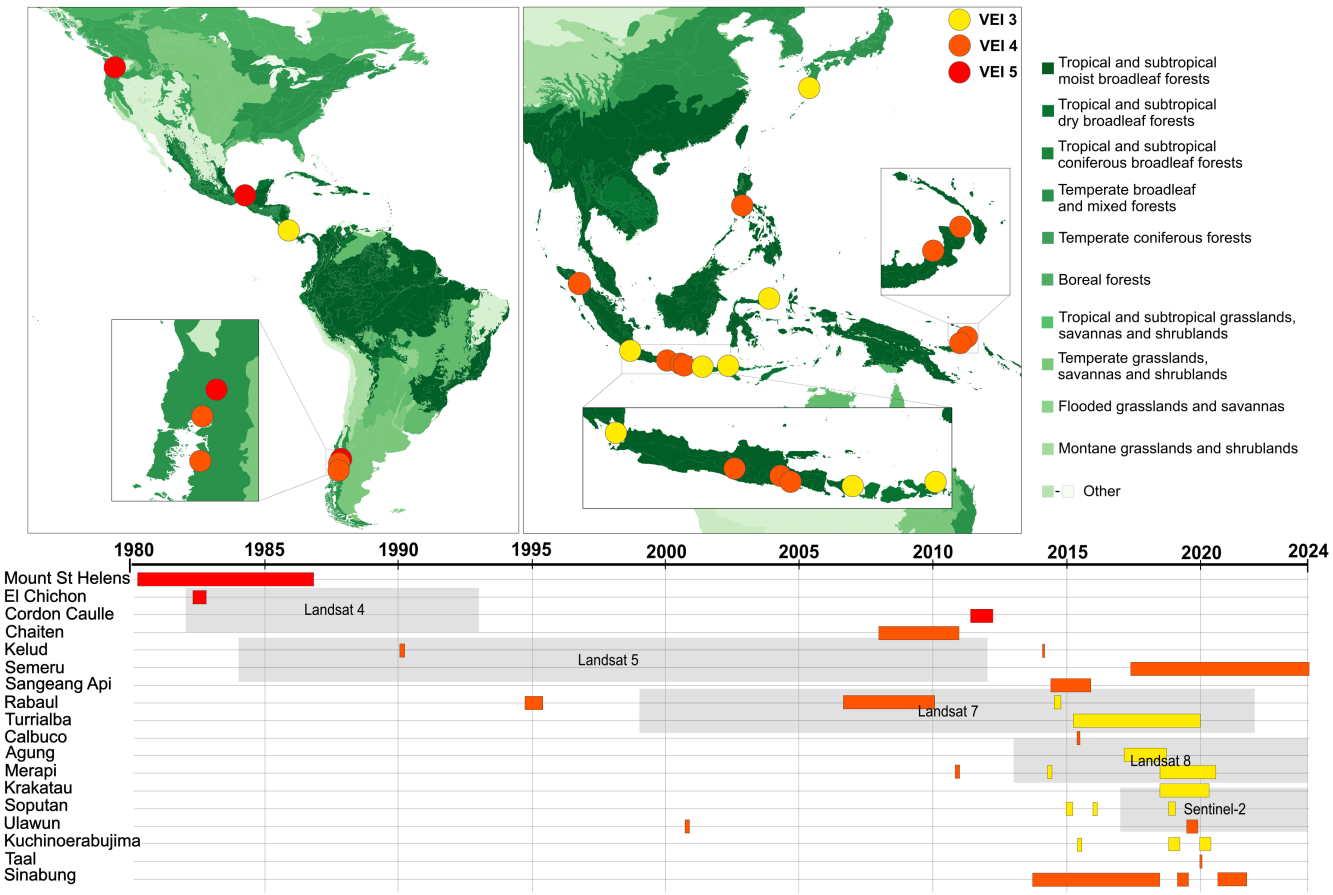

Figure 4.1: A map of the ecoregions of the world (Olson et al. 2001) with the locations of our case studies in circles coloured by the VEI of the eruption studied. Below the map is a timeline of when the eruptions occurred for each site, along with the timespan of the different satellite missions used.

Our target volcanoes are predominantly in tropical and subtropical moist broadleaf forest, with case studies in Indonesia (Sinabung, Soputan, Krakatau, Merapi, Semeru, Kelud), the Philippines (Taal), Papua New Guinea (Ulawun, Rabaul), Costa Rica (Turrialba) and Mexico (El Chichón). In tropical and subtropical dry broadleaf forest is Sangeang Api volcano in Indonesia. In Temperate broadleaf and mixed forest we study Kuchinorabujima in Japan and Calbuco, Chaitén and Puyehue-Cordón Caulle in Chile. And finally, we include Mount St Helens in Washington in a Temperate coniferous forest. Our case studies range from 10 years of data to 40 years of data, depending on the date of eruption we are studying. A summary of our target volcanoes and key information can be found in Table 4.1 with additional details in the supplementary information.

4.2 Methods

4.2.1 Optical Imagery

We combine Landsat 4–8 and Sentinel-2 data (accessed through the Google Earth Engine collections). All case studies use Landsat-8 and Sentinel-2 imagery, with older case studies using Landsat 7, Landsat 5 and Landsat 4, depending on the start date of the eruption. We use imagery starting from Landsat 4 for Mount St Helens and El Chichón, starting from Landsat 5 for Kelud and starting from Landsat 7 for Puyehue-Cordón Caulle, Chaitén, Rabaul (there is no Landsat 5 coverage for Rabaul) and Merapi. The Landsat satellites all have a spatial resolution of 30 m and a repeat time of 16 days. Sentinel-2 has a spatial resolution of 10 m with a combined revisit time of 5 days. We use level 2 data which has been atmospherically corrected (Main-Knorn et al. 2017; Vermote et al. 2016) and remove any images from our analysis with more than 40% cloud cover within the vicinity of the volcano, before applying a cloud mask using the pixel quality assurance band (Foga et al. 2017; Main-Knorn et al. 2017) and finally manually removing any images with remaining cloud cover that obstructs the area of interest. We mask out bodies of water using the normalised difference water index (NDWI$>$0). We then calculate the normalised difference vegetation index (NDVI) which uses the infrared and red spectral bands and is widely used to assess vegetation coverage and

Table 4.1: A table summarising the case studies used, along with the years of eruption, forest type and climate type

Volcano	Eruptions studied (VEI)	Deposits studied	Forest	Climate
Sinabung	2013 (4), 2019 (4), 2020 (3)	Tephra, PDCs, Lava	Tropical and subtropical moist broadleaf forest	Tropical rainforest
Taal	2020 (4)	Tephra, PDCs	Tropical and subtropical moist broadleaf forest	Tropical savannah
Kuchineoerabujima	2015 (3), 2018 (3), 2020 (3)	Tephra, PDCs	Temperate broadleaf and mixed	Humid subtropical
Ulawun	2019 (4), 2000(4)	Tephra, PDCs, Lavas	Tropical and subtropical moist broadleaf forest	Tropical rainforest
Soputan	2015 (3), 2016 (3), 2018 (3)	PDCs, Lavas	Tropical and subtropical moist broadleaf forest	Tropical rainforest
Krakatau	2018 (3)	Tephra, PDCs, Lavas	Tropical and subtropical moist broadleaf	Tropical rainforest
Merapi	2010 (4), 2014 (3), 2018 (3)	PDCs	Tropical and subtropical moist broadleaf	Tropical monsoon
Agung	1963 (5), 2017(3)	Tephra, PDCs	Tropical and subtropical moist broadleaf forest	Tropical rainforest
Calbuco	2015 (4)	Tephra, PDCs	Temperate broadleaf and mixed forest	Temperate oceanic
Turrialba	2015 (3)	PDCs	Tropical and subtropical moist broadleaf forest	Tropical rainforest
Rabaul	1994 (4), 2006 (4), 2014 (3)	Tephra, PDCs, Lavas	Tropical and subtropical moist broadleaf forest	Tropical rainforest
Sangeang Api	2014 (3)	Tephra, PDCs, Lavas	tropical and subtropical dry broadleaf forest	Tropical monsoon
Semeru	2014 (3)	PDCs	tropical and subtropical moist broadleaf forest	Tropical rainforest
Kelud	1990 (4), 2014 (4)	Tephra, PDCs, Blast	tropical and subtropical moist broadleaf forest	Tropical monsoon
Chaitén	2008 (4)	Tephra, PDCs, Blast	Temperate broadleaf and mixed forest	Temperate oceanic
Puyehue-Cordon Caulle	2011 (5)	Tephra, PDCs	Temperate broadleaf and mixed forest	Temperate oceanic
El Chichon	1982 (5)	PDCs	Tropical and subtropical moist broadleaf forest	Tropical savanna
Mount St Helens	1980 (5)	PDCs, Blast	Temperate coniferous forest	Warm summer Mediterranean

health (Myneni et al. 1995; Goetz et al. 2006; Santin-Janin et al. 2009; Bai et al. 2008; Tian et al. 2015). NDVI ranges from -1 to 1 with strong positive values representing dense, healthy vegetation, while low values near zero typically represent bare rock or soil. The decrease in NDVI will depend on the pre-eruption NDVI and the severity of the damage. For example, damage due to fire can result in smaller reductions of around 0.15 or larger drops of up to 0.6 (Hislop et al. 2019; Cuevas-González et al. 2009). NDVI is the best metric for detecting the impacts of volcanic activity on forests as it is sensitive to changes in greenness indicating vegetation health or coverage. Compared to biomass or productivity metrics NDVI is simpler to compute, widely available at high spatial and temporal resolution and can be calculated from decades of historical satellite data, making it ideal to study both the long and short term changes in forests around volcanoes (Urbazaev et al. 2016; Vaglio Laurin et al. 2017).

4.2.2 Cluster Analysis

We perform k-means cluster analysis (Likas et al. 2003) on the NDVI time series as an initial tool to assess the forest damage at each volcano by grouping pixels that share common temporal trends. This has previously been shown to be effective at Calbuco with pixels sharing similar NDVI decreases and recovery times grouped into clusters, showing the different types of damage from different deposit types (Udy et al. 2024). We first downsample the NDVI images by a factor of 2 in both the azimuth and range directions and removing any images where >20% pixels are NaNs (this threshold is relaxed for islands and partially ice covered volcanoes). We handle the remaining NaNs by applying a 2D linear interpolation, which estimates missing values based on their spatial neighbours within the same time step. In regions where interpolation is unsuccessful, we apply zero-padding to fill the gaps. Whilst performing the cluster analysis, we set the number of clusters to 5 as a standard, based on an iterative approach that showed it to be the most appropriate value for the majority of our targets. However, in cases where this number is insufficient, particularly due to intense damage or large structural changes, we adjust accordingly. We performed cluster analysis separately for pre-, co-, and post-eruptive sections of the time series and the algorithm iterated 10 times with different

centroid seeds. In cases with multiple eruptions or extended eruption periods, we perform clustering throughout, either after each distinct eruption period or at regular intervals (e.g. every 5 or 10 years), depending on the length of time series. Supplementary Figures C.1 - C.18 show the most representative clustered image for each case study to assess the style and spatial extent of damage to surrounding vegetation.

4.2.3 Deposit Classification and Sampling Area Selection

We use our NDVI time series, k-means cluster analysis and a review of previous research or volcano observatory reports to identify locations affected by tephra deposits, volcanic blasts, PDCs and lava flows. Within each identified deposit area, we define multiple candidate sampling regions to evaluate which best represents the NDVI response of that deposit type at that target volcano. Size of the area taken varies by deposit type: for tephra deposits and blasts, we typically use 30 x 30 pixel boxes and for lava and pyroclastic flows, 20 x 20 pixels. However, these dimensions are adjusted based on extent and morphology of the specific deposit if required - large boxes are used for more extensive or heterogeneous areas, while smaller boxes are selected for narrower features such as confined flow channels. Using an area of pixels, rather than individual pixels, helps reduce the influence of outliers and provides a more robust estimate of NDVI recovery trends, whilst taking the whole area of a deposit type is challenging due to the potential influence of overlapping deposits or cloud cover.

4.2.4 Recovery Time Estimation

We estimate recovery times for each deposit type at the locations shown in Supplementary Figures C.1 - C.18. We define recovery as the point at which NDVI values return to within 1% of the pre-eruption median NDVI. While this does not necessarily indicate a complete return to the pre-eruption vegetation composition or structure, it is a practical and objective threshold that can be consistently applied using remote sensing data. The 1% buffer was selected to account for any small variations while ensuring the recovery estimate reflects near-complete regrowth. In cases where the pre-eruption NDVI time series is sparce, either due to it being an earlier eruption within the satellite

era or persistent cloud cover, we estimate the pre-eruption median NDVI by using a reference approach. At these locations (Soputan, El Chichón, Mount St Helens) we calculate a representative NDVI value by averaging the NDVI from 10 proximal reference sites that remained largely unaffected by volcanic disturbance, selected based on geographic proximity, comparable elevation and consistent land cover characteristics. This approach assumes that unaffected areas serve as a reasonable ecological proxy for the pre-disturbance state of the impacted site.

Our recovery times can be split into 2 categories, observed recovery times and predicted recovery times, depending on if the NDVI values reach the pre-eruption median within the span of our time series. If NDVI reaches the recovery threshold (1% of the pre-eruption median NDVI) within the observed time period, the recovery time is calculated as the interval between the eruption date and the first image where NDVI exceeds the pre-eruption threshold. At locations that do not reach the NDVI threshold within the time series, predominantly at flow deposit sites, we estimate a predicted recovery time using linear extrapolation. This is based on the observation that NDVI values at these flow deposit sites tend to exhibit a linear recovery trend (Figure 4.5 panel B). We calculate annual mean NDVI values for the post-eruption time series to smooth out any short-term fluctuations. We then calculate the average rate of NDVI increase from the most recent three years. This multi-year average helps mitigate short-term fluctuations caused by seasonal variability, cloud contamination, or other transient disturbances that may obscure long-term recovery trends. We then estimate how many years it would take, at that average annual rate of increase to reach the recovery threshold from the most recent observed annual NDVI value (2024). This yields a predicted year of recovery, from which we can get the predicted recovery time by subtracting the eruption year. This approach strikes a balance between filtering noise and maintaining sensitivity to recent recovery dynamics. We assume that recent vegetation recovery trends are a reasonable indicator of near-future recovery, though we acknowledge this is an oversimplification. It is, however, a justified compromise given the challenges of accounting for all potential variables, such as future disturbances or changes in the landscape.

This method appears effective at all PDC deposit locations which do not reach recovery within our observation window, with the exception of Krakatua and Semeru. These locations do not show any initial recovery, and so we cannot make a reliable estimate of recovery rate. Similarly, we are not able to make estimates at lava flow locations, again due to lack of initial detectable recovery following emplacement. We also attempt this method for the tephra deposit location at Puyehue-Cordón Caulle, the only tephra location that does not reach the threshold within our observation period. In Figure 4.2, the tephra time series plateaus in the last 5 years, resulting in no clear increase in the last 3 years and so we are unable to predict if or when the threshold would be reached. However, this stabilisation of NDVI may in fact mean it has recovered, but with new vegetation assemblages which have lower NDVI values.

4.3 Results

Figures 4.2 and 4.3 present the NDVI time series for each defined sampling area, corresponding to the identified deposits at each target volcano. The target volcanoes are grouped into categories reflecting the dominant focus of each case study: large scale impact, flow deposits or recovery. This highlights the range in NDVI decreases and subsequent recovery rates between different deposit types and locations.

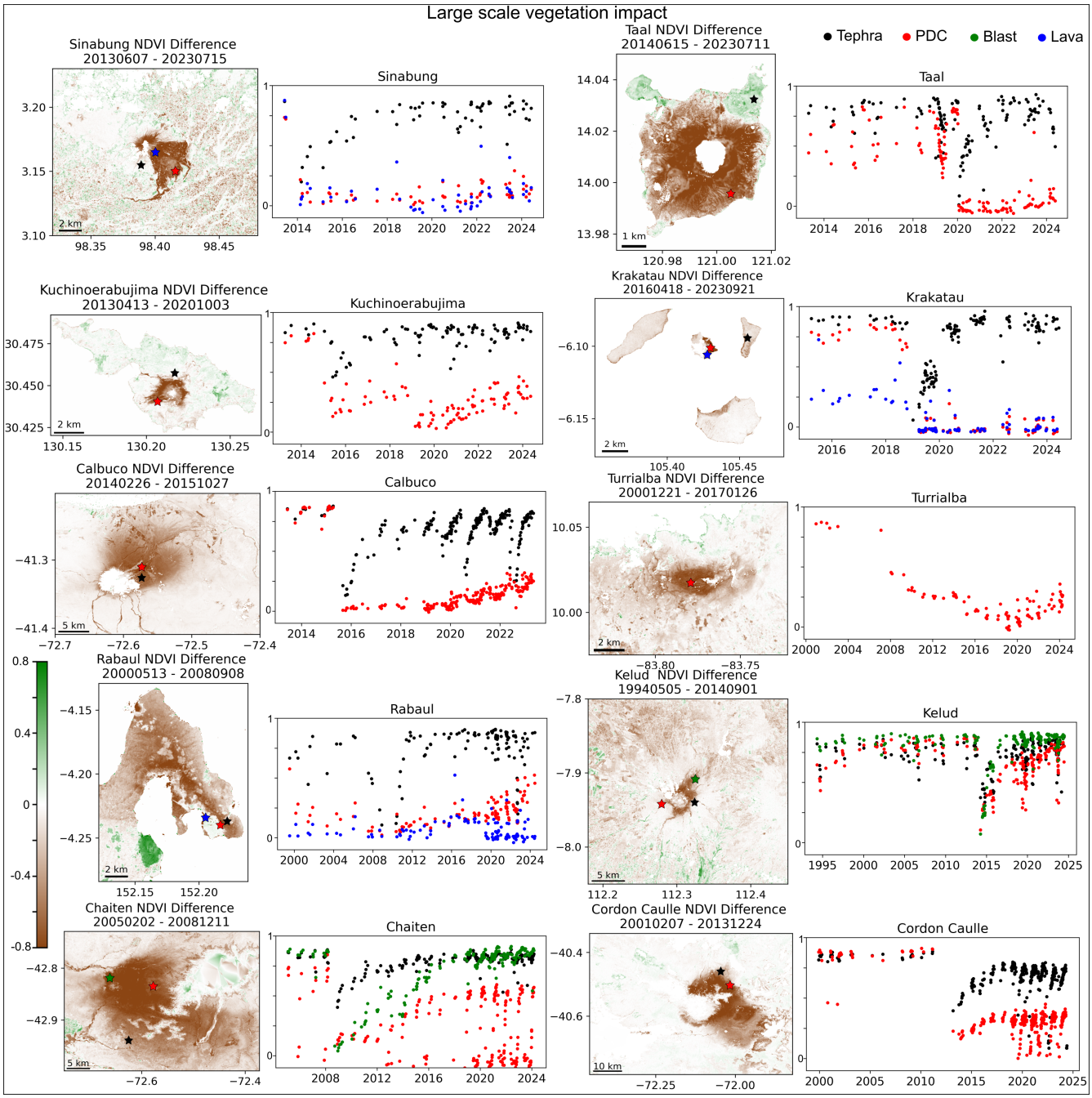

Figure 4.2: NDVI difference map and time series for each target volcano that illustrates large scale (spatially and in terms of NDVI decrease) vegetation impacts associated with different volcanic deposit types. The NDVI time series depict the measurable decrease in NDVI and subsequent recovery for each identifiable deposit at the respective volcano. The deposits are colour-coded as follows: Tephra (black), Pyroclastic Density Currents (PDC) (red), blast-affected areas (green), and lava flow (blue) in both the time series and the locations (stars) on the NDVI difference maps, which indicate the sites of the time series.

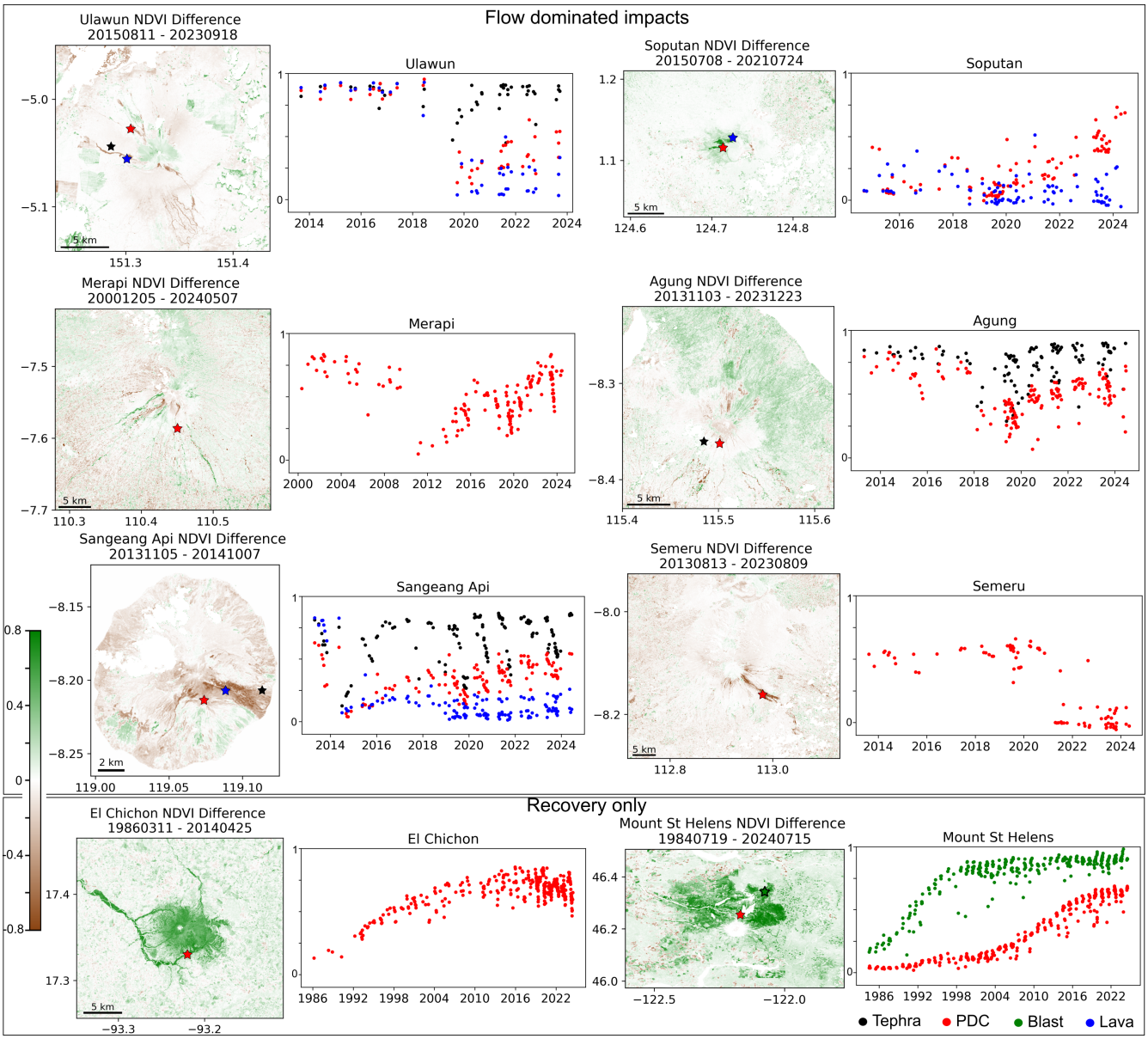

Figure 4.3: NDVI difference map and time series for each target volcano that is dominated by flow deposits (Ulawun - Semeru) and those only showing the recovery stage of the NDVI trajectory (El Chichón and Mount St Helens). The NDVI time series depict the measurable decrease in NDVI and subsequent recovery for each identifiable deposit at the respective volcano. The deposits are colour-coded as follows: Tephra (black), Pyroclastic Density Currents (PDC) (red), blast-affected areas (green), and lava flow (blue) in both the time series and the locations (stars) on the NDVI difference maps, which indicate the sites of the time series.

An example of the NDVI time series, NDVI and cluster analysis at a target volcano is shown in Figure 4.4 at Rabaul following a VEI 4 eruption that began in August 2006 and

continued until January 2010. Prior to this was a VEI 4 eruption from September 1994 - April 1995 and a VEI2 eruption from November 1995 - September 2001. These eruptions resulted in Tephra fall primarily to the NW of the vent, as well as lava flows and PDCs. We link clusters extracted from the NDVI time series to volcanic eruption impacts using independent data where possible (Global Volcanism Program 2025). At Rabaul, we attribute the damage represented by cluster 5 (shown in dark red in Figure 4.4) to lava and pyroclastic flow deposits. Clusters 3 and 4 represent the damage due to tephra deposits as the plume primarily travelled SE-NW (Global Volcanism Program 2025), with cluster 4 likely associated with thicker deposits. Panel D shows the time series for each cluster, primarily differentiated by the magnitude of NDVI drop and recovery rate. Panel E shows the NDVI time series for an area impacted by tephra deposits. Panel F is the NDVI time series for an area impacted by PDC deposits and panel G is impacted by lava flows. As these two areas share the same cluster we use optical imagery and the eruption reports (Global Volcanism Program 2025) to differentiate the flow deposits.

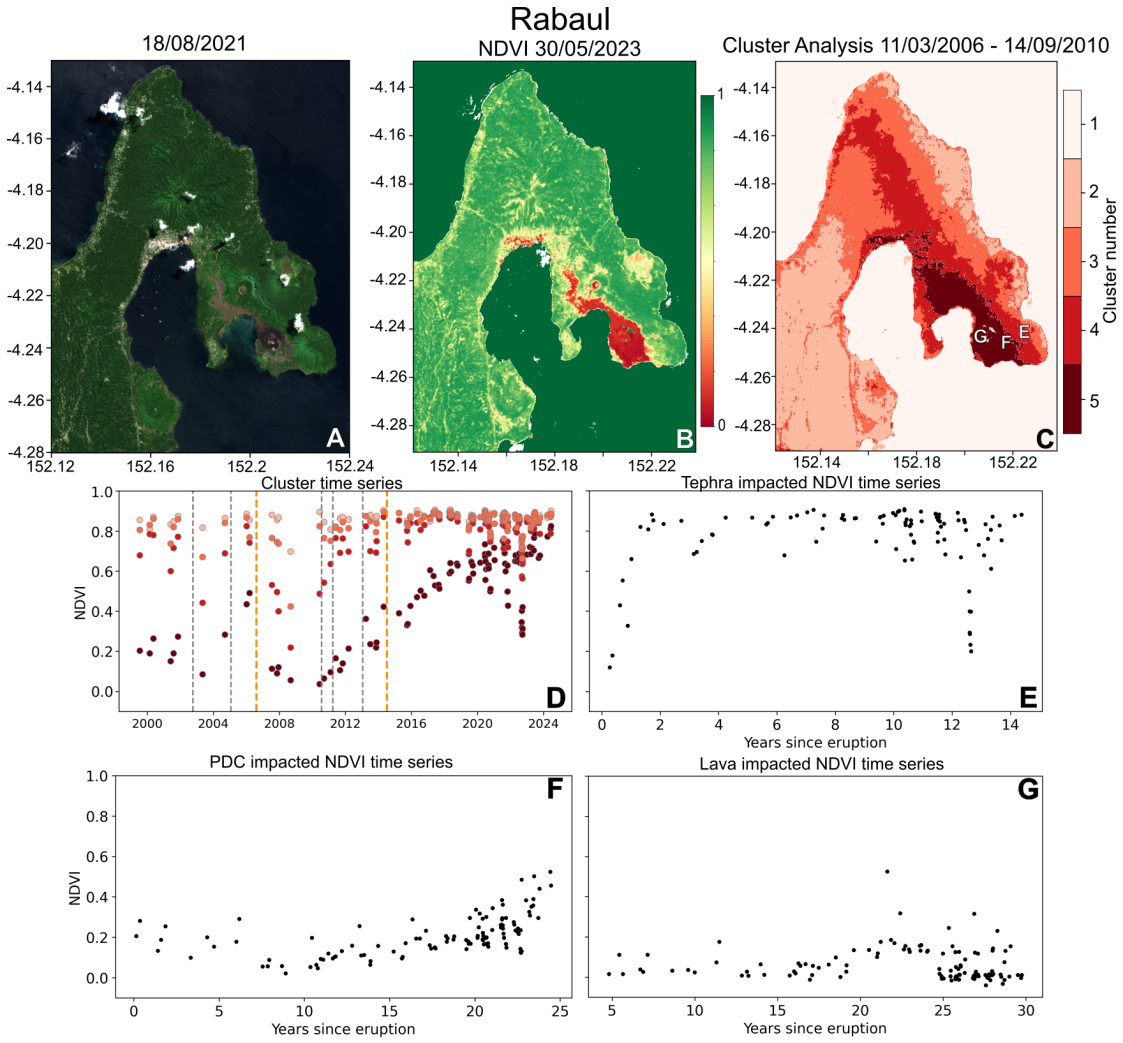

Figure 4.4: A) Sentinel-2 optical image of Rabaul on 18/08/2021. B) Sentinel-2 NDVI image of Rabaul on 30/05/2023. C) K-means cluster analysis of NDVI imagery over Rabaul from 11/03/2006 - 14/09/2010, also showing the location of the time series in panels E-G. D) Time series of the median pixel of each cluster identified in panel C over the whole NDVI time series with eruption onsets marked by dashed line (orange = VEI4, grey = <VEI3). E) NDVI time series for an area identified as impacted by tephra. F) NDVI time series for an area identified as impacted by PDCs. G) NDVI time series for an area identified as impacted by lava flows. Areas of impact identified from a combination of optical imagery, cluster analysis and activity reports (Global Volcanism Program 2025).

We compare the time series that we link to the locations of different volcanic impacts (tephra, PDCs, lavas) for all 18 volcanoes in order to characterise any similarities in vegetation recovery trajectory 4.5. We then consider the impact of factors such as latitude, distance from eruption centre, VEI, forest type, climate type and time since previous

eruption on patterns in forest regrowth. We find that forest type shows the clearest trends with more tropical forests showing quicker recovery (return to pre-eruption NDVI values) compared to more temperate forests. Panels A-C in Figure 4.5 show that darker green points (representing more tropical forest sites) tend to have quicker recovery rates (e.g. at Kelud). The more temperate forests have slower recovery rates and also show a seasonal signature (particularly Puyehue-Cordón Caulle), as to be expected for their forest type. However, seasonal patterns in NDVI only appear towards the end of the time series (Supplementary Figure C.16 panel D), likely due to recovery of the vegetation promoting the return of stronger seasonal changes (Udy et al. 2024), possibly due to less dense vegetation or different species assemblage demonstrating different seasonal signatures. Tephra deposits result in detectable NDVI changes at 12 of our case studies, and are characterised by a large drop in NDVI of up to ∼0.8 (e.g. at Krakatau in 2018, Figure 4.2), followed by a quick recovery time (considering the magnitude of NDVI drop), with an average recovery time of ∼2.8 years (Figure 4.5 panel A). We expect the primary mechanism of damage due to tephra deposits is leaf abrasion and leaf loss, with plant death in areas of thickest deposit. Spatial scales of identified tephra deposits range from 10s-1000s km^2. On average, tropical forests recovered from tephra deposits in approximately 2 years, compared to around 5 years for temperate locations.

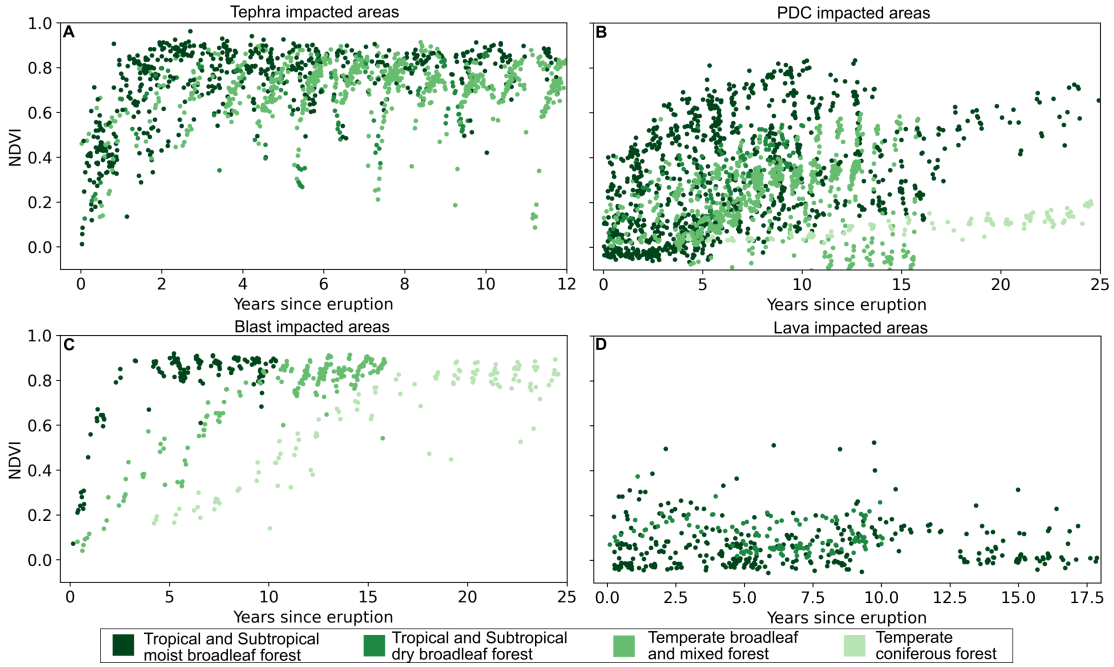

Figure 4.5: A. NDVI time series for the tephra impacted areas of the case studies. B) NDVI time series for the PDC impacted areas of the case studies. C) NDVI time series for the blast impacted areas of the case studies. D) NDVI time series for the lava impacted areas of the case studies. The time series are coloured by forest type. The location of each time series can be found in the Supplementary Figures C.1 - C.18 panel A, along with a table of which case studies are in each panel, with co-ordinates of each location noted (Table C.1).

We measure PDC deposit impacts at all 18 of our case studies (Figure 4.5 panel B). There is a large variety in time series shape here, and they can be inspected in Figures 4.2 and 4.3 as well as individually in Supplementary Figures C.1 - C.18. PDC emplacement causes a large drop in NDVI in all cases, followed by a steady, slower recovery (in comparison to the tephra NDVI time series) of 22 years on average, but this varied widely from ∼5 years (at Kelud in Tropical forest) to over 50 years (at Puyehue-Cordón Caulle and Mount St Helens). The primary mechanism of damage is likely plant death, although some remnants may remain in less severely impacted areas. Recovery from PDCs was faster in tropical regions, taking on average 31 years, compared to 38 years in temperate forests. While these average values offer a general indication of differences in recovery rates, direct comparisons are complicated by additional variables such as eruption magnitude, duration, and environmental factors like species composition. We

also note that the impact of individual PDC deposits are challenging to isolate, especially in channels likely to later be affected by additional flow deposits.

Three of our case studies capture volcanic blasts impacting vegetation (Kelud in 2014, Chaitén in 2008 and Mount St Helens in 1980, Supplementary Figures C.14 panel F, C.15 panel F and C.18 panel E). The gradient of the initial recovery appears to be more linear, like the flow deposits but on quicker time scales similar to the tephra deposits. Possibly due to the intensity of damage being more severe, like the flow deposits, but with more surviving legacies, like tephra damage. The average recovery time is ∼12.5 years, in the middle of the average recovery times of the tephra and flow deposit sites. Again the time series are coloured by forest type, with the quickest recovery time in tropical forest at Kelud (2.5 years) and the slowest is in the temperate coniferous forest at Mount St Helens (24.4 years). However, it is difficult to compare these recovery times due to the limited examples of blast impacts and the varying style and scale of eruptions, Mount St Helens, in particular, being exceptionally large. Given this range, there is also likely a range in damage mechanisms, although foliage loss and felling of trees is most likely, causing significant damage but leaving more remnant plant matter compared to flow deposit areas.

NDVI changes due to the emplacement of lava flows are detected at 6 of the case studies, all of which are in tropical forests (Figure 4.5 panel D). Lava flows completely destroy and remove vegetation and resurface the area. Lava flow surfaces are characterised by very low NDVI values (usually below 0.2) with little to no NDVI increase detected within our observation period, meaning we cannot estimate recovery times. This is to be expected as on average we have ∼10 years of data post-eruption to capture any initial stages of recovery, but lava flows are likely to take hundreds to thousands of years to recover (Grishin et al. 1996; Kitayama et al. 1995). As such we do not have adequate time series to estimate recovery times.

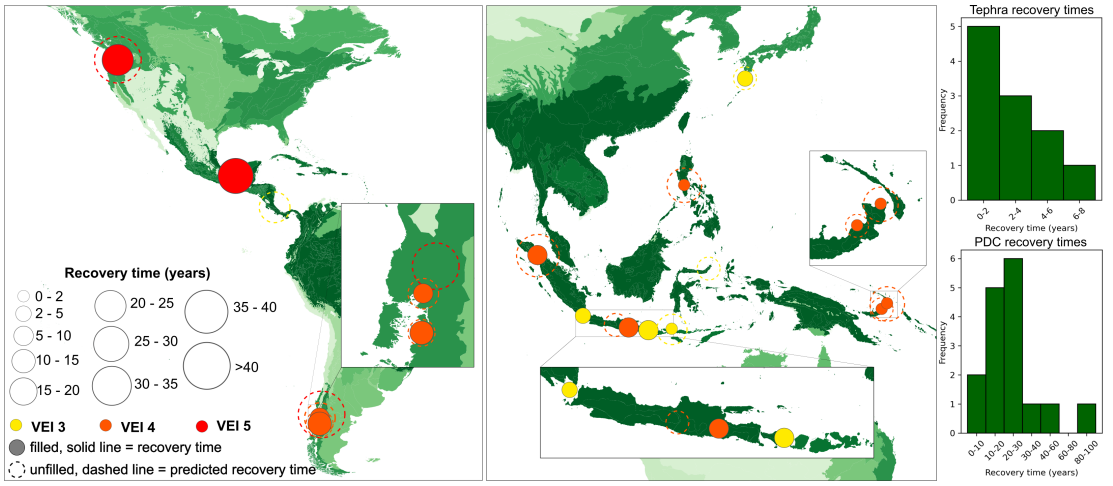

Figure 4.6: A map of the ecoregions of the world (Olson et al. 2001) with recovery times (solid circles) and predicted recovery times (dashed circles) for our case studies, coloured by VEI. The key of forest types can be found in Figure 4.1.

The recovery times for each deposit type at the locations shown in Supplementary Figures C.1 - C.18 is summarised in Figure 4.6. Solid circles represent estimated recovery times and dashed lines represent predicted recovery times. Where we have multiple deposit types that have either recovered, or have a predicted recovery we take the larger of these values, to visualise how long the footprint of the eruptive activity is likely to be present at each target volcano. Circles are also coloured by eruption VEI to detect any trend in the recovery time (size of circle) compared to the size of the eruption and also how this may change with distance from the equator (as forests get more temperate). We also show the difference in distribution of recovery times for tephra deposits compared to PDCs, which take much longer to recover.

4.4 Discussion

4.4.1 Link Between Eruption Style and Forest Recovery

Volcanic impacts on surrounding forests can vary in scale over orders of magnitude. While tephra deposits have spatial footprints that extend up to tens of thousands of kilometres, their satellite detectable impact being more on the order of 100s km^2 and usually lasting weeks-months (Figure 4.7). Lava flows, in contrast, cover areas up to

several km^2 but have an impact on the NDVI of vegetation that will last hundreds, if not thousands, of years, even over small areas (Del Moral et al. 1999; Grishin et al. 1996; Kitayama et al. 1995). The mechanism of damage, level of destruction, number and assemblage of remaining biological legacies, and the size and shape of deposit are all expected to contribute to the duration of damage to the vegetation.

Tephra causes the shortest duration of satellite-measurable damage. The thinnest deposits (mm thickness) cover large areas, but with very short impact times, as they will cause little damage to the vegetation, and little if any NDVI drop making them difficult to detect. Thicker deposits, which do generate a measurable drop in NDVI (e.g. deposits thicker than 15 cm generate a signal at Calbuco (Udy et al. 2024)), can take years to recover (an average of ∼2.8 years for our 18 study sites but a wide range from less than a year to over 6 years). Thicker tephra can abrade leaves and cause foliage damage and removal, but is unlikely to remove whole plants completely, resulting in a large amount of legacies even in regions of acute damage, facilitating easier regrowth and promoting quicker recovery (Foster et al. 1998; Dale, Delgado-Acevedo, et al. 2008). The impact of volcanic blasts on forests lasts from 2.5 years (Kelud) to 25 years (Mount St Helens). Although that can be highly destructive, felling trees across large areas, they leave behind large numbers of legacies due to their lower temperature and felled trees potentially protecting underlying plant matter. As such, recovery rates are quicker than within the smaller areas of buried by flow deposits, which can completely remove and burn vegetation (Dale, Delgado-Acevedo, et al. 2008).

Flow deposits are most damaging, being a linear shape they have more concentrated zones of damage with a greater level of destruction due to burial, burning and force of flows damaging the vegetation (Charbonnier et al. 2013). At our 18 case studies the largest drops in NDVI, with the longest recovery rates, occur from flow deposits. For example, at Sinabung, the pyroclastic and lava flows severely damage vegetation, carving out a strong NDVI decrease that lasts for years following the flow emplacement (Figure 4.2). From the NDVI data alone it is hard to differentiate the effects of lahar deposits from pyroclastic density current deposits as their spatial footprints overlap

within the same channels. In two cases (Chaitén and Mount St Helens) we can identify lahars from published deposit maps (Major and Lara 2013; Druitt 1992) allowing us to confidently differentiate lahars from PDCs. At these sites the recovery time is quicker than that of PDCs, this is to be expected as lahars are cooler than PDCs and so likely less damaging, leaving more legacies to aid recovery (Charbonnier et al. 2013). Linear flows also influence recovery, as the distance to healthy vegetation, which helps recovery and regrowth, is shorter at any point within the affected area (Foster et al. 1998). PDCs have an average recovery time of 22 years for our 18 case studies. This long recovery time is due to the level of damage as it will almost totally remove the vegetation in its path as well as singing neighbouring vegetation (Charbonnier et al. 2013). Finally, the impact of lava flows on forests has a significantly longer duration as these completely remove and resurface vegetated areas and require primary succession for a forest to re-establish itself, a process which can take hundreds to thousands of years even over a small area (Del Moral et al. 1999; Grishin et al. 1996; Kitayama et al. 1995).

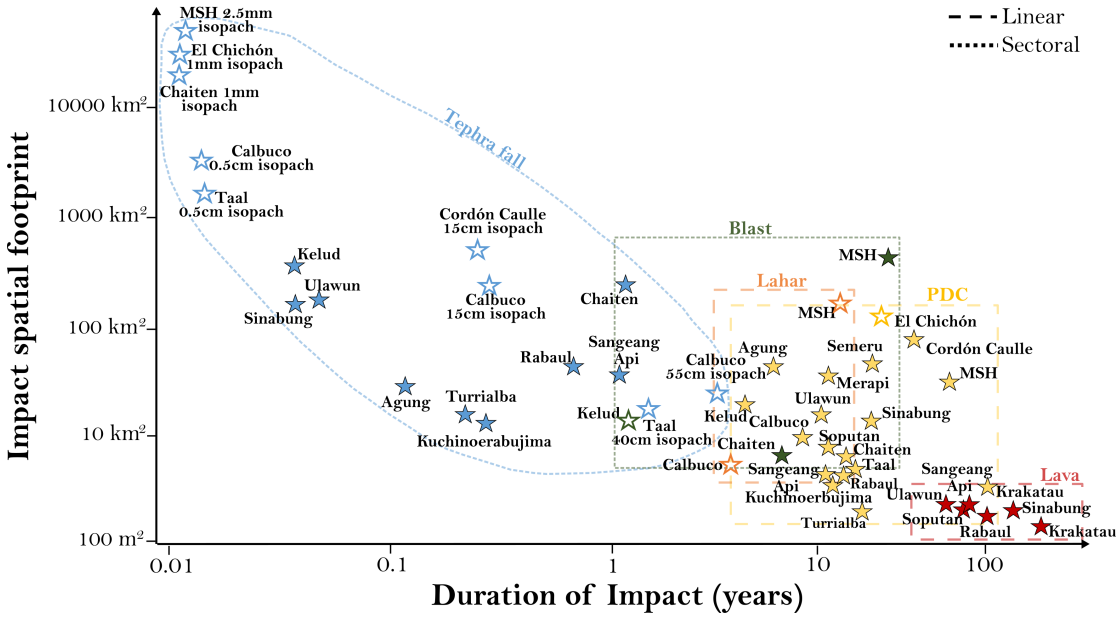

Figure 4.7: A schematic diagram of spatial extent vs impact selected for the identifiable deposits at each of our 18 case studies. The areas and duration of impact have primarily been taken from our optical imagery, but where possible have been combined with previous studies. Estimates taken from previous studies are shown as hollow markers (Major, Crisafulli, et al. 2020; Lagmay et al. 2021; Balangue-Tarriela et al. 2022; Udy et al. 2024; Varekamp et al. 1984; Pistolesi et al. 2015; Watt et al. 2009; Sigurdsson et al. 1984).

The size and explosivity of an eruption is also a factor in vegetation damage and recovery. More explosive eruptions are likely to damage more vegetation and result in fewer legacies, making it harder for areas to recover (Carey and Sigurdsson 1989; Self 2006). Forest damage over a larger area will also increase recovery times as the distance from the most acute damage zones, where biological legacies are limited, to healthy vegetation is larger, making regrowth from those sources more difficult, resulting in longer recovery times (Dale, Delgado-Acevedo, et al. 2008).

In Figure 4.6 we can see that VEI 3 eruptions (yellow) tend to have shorter recovery times. This is further highlighted in Figure 4.8 panel A, which shows the largest VEI 5 eruptions result in longer recovery times (average of around 50 years), VEI 4 eruptions have the intermediate recovery time (average 12 years) and VEI 3 eruptions have the shortest recovery times (average 9 years). We conducted statistical testing using ANOVA, pairwise t-tests and linear regression, which confirmed a statistically robust increasing trend in recovery time with increasing VEI. An exception to this overall trend is Anak Krakatau, for which we attempt to estimate the recovery time of the PDC area. The eruption completely removed all vegetation from the central island and as such there are no remaining legacies to aid recovery. There is no evidence of recovery in NDVI recorded in our time series (Figure C.6 panel E). The island location, and resulting large distance to healthy vegetation does make it possible that recovery will be exceptionally long and in the region of hundreds of years, as seen here previously and at other island volcanic systems (Tagawa 1992; Grishin 2011).

While there is a general relationship between eruption size and recovery time, it can be complicated by spatial variability in impact intensity. Large eruptions have high intensity impacts close to the vent but more moderate effects over broader, distal areas where vegetation may recover more quickly. This spatial heterogeneity highlights the limitations of using recovery time alone as a tool to measure the ecological impact of an eruption. Future work could explore metrics that integrate the magnitude, spatial extent and duration of NDVI decrease to better quantify the overall disturbance footprint and distinguish between short, intense impacts and longer, diffuse ones. Incorporating such

metrics would improve comparisons across eruption types, deposit areas and ecoregions.

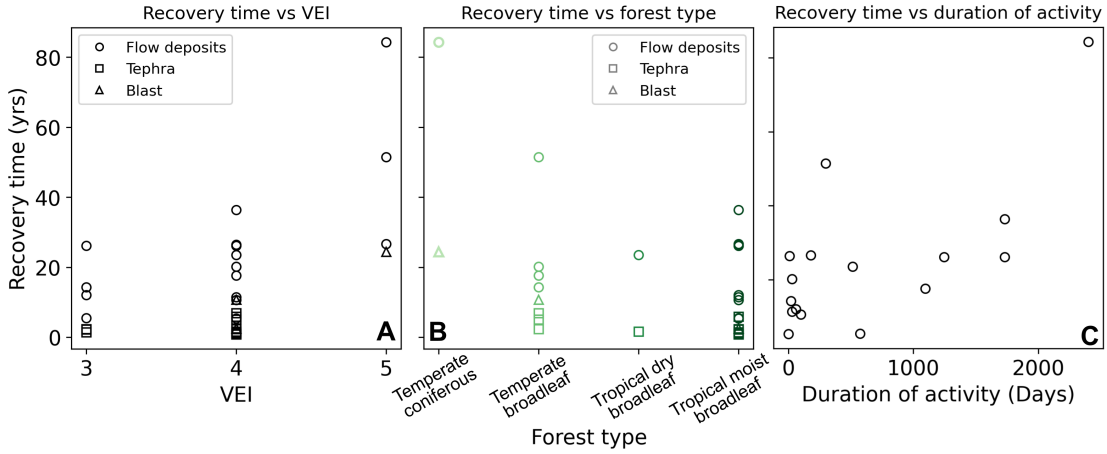

Figure 4.8: A. Recovery time vs VEI for our 18 target volcanoes. B. Recovery time vs forest type from more temperate (light) to more tropical (dark). C) Recovery time vs duration of continued activity for PDCs.

The duration of an eruption, or period of prolonged volcanic activity, clearly influences recovery time in flow deposit areas (Figure 4.8 panel C). Increasing activity duration is positively correlated with recovery time, as confirmed by Pearson correlation and linear regression, indicating a statistically significant and moderately strong relationship between the two. This effect is particularly evident for flow deposits, where material is often remobilised and channels may experience multiple lahar or pyroclastic flow events especially during prolonged or complex eruptions. Such secondary processes can extend the disturbance period well beyond the nominal eruption duration, resulting in sustained exposure, greater ecological damage, and delayed onset of recovery due to fewer surviving biological legacies (Foster et al. 1998; Pierson et al. 2014). For instance, the shortest duration eruption examined, Kelud (2 days,) showed recovery at the PDC site in just over 5 years. In contrast, Merapi, also in Indonesia with the same forest type and VEI 4 eruption classification, experienced month long activity and has a PDC recovery time of just over 11 years. While the relationship between eruption duration and recovery time is not strictly linear, likely due to the influence of other factors such as forest type, other deposits present and eruption style, a positive trend is still evident, with longer eruption durations generally resulting in longer recovery times.

4.4.2 Ecotype and Resilience to Volcanic Damage

Tropical forest has quicker recovery times than temperate forests (Figure 4.5), on average recovering 3 years quicker from tephra deposits and 7 years quicker from PDC deposits. This can be seen in Figure 4.6 with the larger circles (longer recovery times) tending to be further from the equator, in more temperate forest areas. We demonstrate this explicitly in Figure 4.8 panel B, as we plot the recovery time for each detectable impact from our case studies with forest type from more temperate (left, light green) to more tropical (right, dark green). In general, tropical recovery times are shorter in comparison to temperate forests. This is supported by ANOVA tests, which detected a significant difference in recovery time between the most temperate and most tropical forest types, and by linear regression, which confirmed a statistically significant decreasing trend in recovery time from temperate to tropical forests. This corroborates previous studies into primary productivity of forests in comparison with latitude, with lower latitude, more tropical forests having a faster regrowth and succession rate, and so a faster recovery following damage (Moral et al. 1993; Foster et al. 1998; Gillman et al. 2015).

Differences in forest type, influence by latitude and associated temperature and humidity conditions, contribute to variation in vegetation damage and recovery rates following volcanic eruptions. Our findings show tropical forests, with less seasonality, may be less vulnerable to eruption related damage during critical growing periods compared to temperate forests (Foster et al. 1998). This could partly explain the longer recovery times observed in temperate regions. However, the relationship is complex: eruptions occurring outside the growing season in temperate forests may reduce vegetation damage due to species dormancy or below ground seed sources (Dale, Delgado-Acevedo, et al. 2008). For instance, at Mount St Helens, the springtime eruption meant key plant elements required for growing, such as buds, remained protected underground (Dale, Crisafulli, et al. 2005). Additionally, the time of year of the eruption meant residual snow cover further protected vegetation, preserving more biological legacies to aid regrowth (Franklin 1990; Foster et al. 1998).

It is important to note that our dataset is dominated by tropical forest sites, limiting

direct comparisons with temperate forests. This imbalance is difficult to avoid given the density of active volcanoes in tropical and subtropical forests is more than twice that of other biomes (Crisafulli et al. 2015). Beyond broad forest types, species-specific traits likely also influence patterns of vegetation damage and recovery. Mature plants, with thicker cuticles and tougher cell walls, may be more resistant to eruption-related stressors (Han et al. 2022; Rankenberg et al. 2021), while juvenile plants may exhibit faster regrowth following disturbance (Rankenberg et al. 2021; Raihan et al. 2021). Structural factors such as tree height may further mediate damage: taller, mature trees may be positioned above certain deposit thicknesses, shielding both themselves and the understory from heavy deposits. Evidence from Valdivian forests supports the role of large trees in facilitating vegetation recovery (Hintz et al. 2021), though these interactions are dependent on species and context. Additionally, the legacy of previous disturbances, such as time since and severity of past eruptions, likely shapes current vegetation structure and resilience, influencing both the capacity to withstand damage and the speed of recovery.

4.4.3 Vegetation Recovery and Resilience

Vegetation resilience following volcanic eruptions appears to be strongly influenced by site specific factors including climate, historical disturbance and vegetation variability, making simple generalisations difficult. Vegetation resilience, defined as the ability of an ecosystem to resist and recover from external disturbances such as volcanic eruptions (Smith, Traxl, et al. 2022), is known to increase with water availability and vegetation variability, and is generally lower in regions with greater precipitation variability, such as temperate climates (Smith, Traxl, et al. 2022; Smith and Boers 2023; Wright 2002). These patterns may explain the faster recovery observed in tropical forests, as they are more inherently resilient. However, in volcanic landscapes, resilience may also be shaped by local factors and eruption history. Although we hypothesised that longer periods without eruptive activity would correlate with greater resilience, as vegetation would be more mature, our results did not reveal a clear relationship, likely due to the interplay of multiple factors. Given that resilience is closely tied to vegetation variability, site-specific histories of disturbance and recovery may play a critical role. Furthermore, while

intermediate disturbance levels have been associated with increased species diversity (Connell 1978; Molino et al. 2001), and thus potentially greater resilience, the complexity of volcanic disturbance regimes suggests that predicting resilience remains highly context dependent.

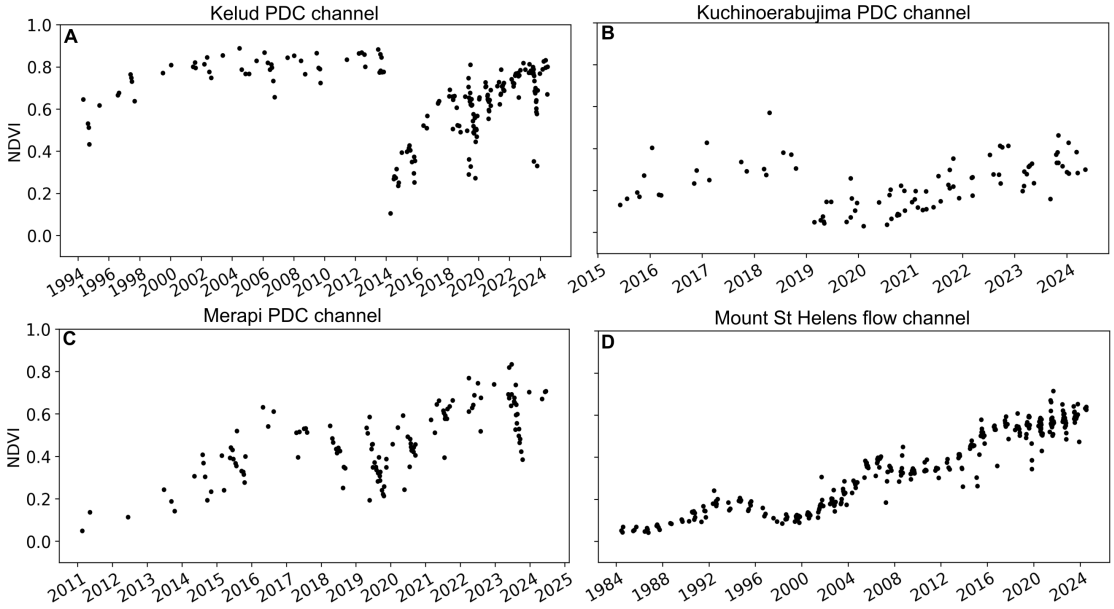

Figure 4.9: A. NDVI time series of PDC channel at Kelud (location E in Supplementary Figure C.14 panel A) B. NDVI time series of PDC channel at Kuchinoerabujima (location E in Supplementary Figure C.3 panel A) C. NDVI time series of PDC channel at Merapi (location D in Supplementary Figure C.7 panel A) D. NDVI time series of PDC and lahar channel at Mount St Helens (location F in Supplementary Figure C.18 panel A)

One possible example of increased resilience post eruption is at Kelud (Figure 4.9 panel A). This is in the same location as panel E in Supplementary Figure C.14 but extends back to 1994, to reveal a previous recovery trajectory following PDC and lahar deposits during the 1990 eruption (Thouret et al. 1998). The subsequent recovery following the 2014 eruption is much quicker, in comparison to this previous recovery, possibly due to increased resilience following the previous disturbance. In contrast is the PDC recovery at Kuchinoerabujima (Figure 4.9 panel B). Unlike at Kelud, the repeated disturbance happens during the recovery process, before full recovery is reached, and the second period of recovery is not quicker but follows a similar trajectory (maybe showing neither increased nor decreased resilience). While it is likely an important factor that

Kelud reached full recovery before repeated disturbance, Kelud is situated in tropical forest compared to Kuchinoerabujima in temperate forest, another factor contributing improved resilience at Kelud. The PDC channel at Merapi shows similarities to Kuchinoerabujima, as the recovery trajectory is interrupted by further deposits decreasing NDVI. However, the NDVI values do not decrease back to their initial low values (like they do at Kuchinoerabujima) and the recovery rate seems to continue at a similar rate as in the first 6 years of the post-eruption time. This could be due to some resilience from the previous disturbance or the difference compared to Kuchinoerabujima could be due to being tropical forest. Mount St Helens shows a final example of how repeated disturbance can change recovery trajectories (Figure 4.9 panel D). This channel was initially impacted by PDCs during the 1980 eruption and then repeated drops in NDVI can be detected years after the eruption, likely due to lahar or other channelised deposits interrupting the recovery. However, it sits somewhere between the previous examples as although the NDVI decreases are evident the general upward recovery trajectory continues, potentially showing the resilience in the regrowing vegetation, despite being in temperate forest. Resilience due to previous disturbance may not only be from previous eruptions. Shatto et al. 2024 demonstrated at La Palma that vegetation that had previously been impacted by wildfires recovered faster from volcanic activity. Simultaneously, they showed how distance was a controlling factor, with vegetation at an intermediate distance also recovering quicker, as it was close enough to have previously been impacted and have gained resilience but far enough that the damage was not severe.

Another factor to consider is the impact of multiple volcanic deposits or deposit types simultaneously or in short succession, and how the order of these deposits may impact the level of damage and subsequent recovery. Our study focuses on differentiating the different deposits to assess the differences in the damage and recovery so we try and avoid locations of multiple impacts. As seen at Kuchinoerabujima, Merapi and Mount St Helens in Figure 4.9, multiple disturbances during the recovery process will slow the recovery. Equally, multiple deposits at the same time during an eruption will likely lead to more damage, a more complex damage zone and fewer legacies, resulting in increased

recovery time (Foster et al. 1998). But this was not the case at Mount St Helens, where the initial blast felled trees, subsequently protecting the underlying vegetation from tephra and PDC deposits, resulting in more legacies post eruption and greater recovery as a result (Franklin 1990; Foster et al. 1998). While shown at Kelud and Mount St Helens that further disturbance during the recovery process can hinder recovery it can also aid it. It has been shown that ash deposits on lava flows can actually improve vegetation succession and lead to increased biomass as the vegetation recovers (Kitayama et al. 1995). Demonstrating that the relationship between volcanic impacts and vegetation recovery and resilience is complex and likely to change in different environmental settings, with different eruption dynamics and even at different times of year.

Volcanic eruptions can impact forests over thousands of square kilometres, with impacts detectable from optical satellite imagery over 10s-100s of square kilometres. The recovery time for these impacts is most commonly less than 7 years for tephra deposits and less than 30 years for PDC deposits (Figure 4.6). Particularly large, explosive eruptions in temperate forests can see lasting damage for multiple decades (Figure 4.6). This time period extends dramatically when considering lava flows which will remain unvegetated, or differ from the surrounding vegetation for 100s-1000s of years (Grishin et al. 1996; Kitayama et al. 1995; Cutler, Belyea, et al. 2008). This allows study of forest disturbance patterns as an insight into eruptions deposits and previous eruptions for decades following a sufficiently destructive eruptive event.

4.5 Conclusion

Using optical satellite data, we detected and analysed forest disturbance and recovery at 18 volcanoes, spanning 64 eruption periods, 4 forest biomes and different eruption styles. We found that tephra deposits, while covering the largest areas, were associated with the fastest recovery times ($\sim$2.8 years), followed by volcanic blast zones ($\sim$ 12.5 years), and pyroclastic density currents, which exhibited the longest recovery periods ($\sim$ 22 years). These patterns reflect the severity of vegetation damage and the amount of surviving plant matter following the disturbance. Recovery times were also

influenced by eruption size, duration, and forest type, with larger and longer eruptions resulting in greater forest damage and extended recovery periods. Tropical forests generally exhibited faster recovery, likely due to higher regrowth rates and greater vegetation resilience. Overall, most affected forest recover within approximately 30 years, although particularly large or severe eruptions, especially those involving lava flows, may extend recovery times substantially. Our findings offer new insights into post-volcanic forest disturbance dynamics and the timescales over which eruption impacts remain detectable in vegetation, providing valuable markers for reconstructing volcanic histories from forest characteristics.

Chapter 5

Discussion and Conclusions

This thesis has explored the use of remote sensing, particularly optical and radar satellite data, to monitor vegetation damage and recovery following volcanic eruptions. Through the previous three chapters I have demonstrated how remote sensing, primarily NDVI, backscatter and coherence, can effectively detect forest disturbances caused by volcanic activity including tephra deposition, flow deposits and volcanic gases at a range of environmental settings. I have also shown how the same techniques can track the post-eruption recovery, revealing insights into the controlling factors of vegetation recovery rate and influences on vegetation resilience.

In this chapter, I provide an overview of the findings of the previous three chapters and how it has advanced understanding of vegetation damage and recovery following volcanic eruptions. I then discuss how these outcomes may be applied in the future, either to non-volcanic hazards, such as wildfires or drought, or using upcoming missions to further advance remote sensing for monitoring vegetation damage at volcanoes

5.1 Remote Sensing of Vegetation Response to Volcanic Disturbance

5.1.1 Vegetation Damage from Volcanic Eruptions and Emissions

Monitoring volcanic eruptions is essential due to their wide-ranging environmental impacts, which can significantly affect surrounding ecosystems and local communities through a variety of damage mechanisms. These impacts include immediate physical damage from volcanic deposits such as tephra, pyroclastic density currents and lava flows, as well as more subtle and longer-term effects caused by volcanic gases. Understanding both the spatial extent and the different mechanisms of vegetation damage is crucial for assessing environmental impact and ecosystem resilience. This aids interpretation of past volcanic activity and deposits, which is essential for developing a complete eruption history to reveal eruption frequency, a key component for accurate risk assessment and preparedness for future events.

In this study, I presented observations of volcanic impacts on surrounding vegetation (primarily forests) using NDVI, backscatter, and coherence. These remote sensing measurements were sensitive and effective indicators of vegetation damage resulting from a variety of volcanic deposits, including explosive tephra fallout and pyroclastic flows. They were also effective at detecting the wide range of impacts due to volcanic gases (primarily SO_2). SO_2 can cause chlorophyll loss and photosynthesis inhibition, resulting in a range of damage from colour change in leaves through to total plant death. The combination of optical and radar measurements allowed the detection of this range of damage. The persistence and severity of gas-induced vegetation damage varied depending on emission duration, environmental and weather conditions, and ecosystem sensitivity. Some regions may experience relatively short term impacts lasting several months, while others suffer longer term disturbance spanning years or even decades. Recognising the range of damage is vital for interpreting remote sensing data and for developing comprehensive assessments of volcanic impacts on environment. Future work integrating gas emission monitoring with satellite observations could enhance our ability

to distinguish these effects and improve estimates of the impacts of volcanic gases on vegetation and predictions of vegetation recovery trajectories.

NDVI was the most sensitive to vegetation changes due to volcanic activity, with the most severe disturbances resulting in NDVI drops of up to 0.8, while more subtle damage was still detectable with changes as small as 0.1. Because NDVI captures changes in the red-edge region of the vegetation reflectance spectrum, it provides valuable information on vegetation health and coverage. However, it is limited in detecting structural changes or shifts in species composition, as it measures the greenness. To address these limitations, radar backscatter data offered additional insights. While it did respond to material emplacement and vegetation changes it was less sensitive compared to NDVI. At Calbuco, backscatter increased with the emplacement of volcanic material and later declined, although it did not return to pre-eruption levels. A notable observation was the change in backscatter variance, which I hypothesise reflects a more heterogenous post-eruption vegetation structure, resulting in a wider variety in scattering retrievals. Similar patterns emerged at Turrialba, where variance in backscatter differed depending on proximity to the vent as it recovered after SO_2 exposure. Areas closer to the vent, severely affected by SO_2 emissions, initially showed large increases in variance which do not begin to recover, possibly reflecting the new structure of the vegetation as it recovers. In contrast, areas further from the vent started to show a return to lower variance and more stable backscatter values, potentially indicating more dense vegetation and homogenous regrowth. Radar backscatter also proved useful in distinguishing between primary causes of damage, such as at Krakatau, where similar declines in NDVI could be attributed to predominantly tephra damage or SO_2 damage due to changes in, or lack of changes in backscatter. Finally, coherence analysis, particularly at Calbuco provided a valuable complementary perspective. Loss of coherence aligned well with areas of vegetation loss, especially over flow deposit areas and spatially correspond well with areas of large NDVI decrease. Importantly, coherence increased again in areas of regrowth, reinforcing the NDVI evidence of recovery. Compared to backscatter, coherence was often more directly interpretable in terms of vegetation presence or absence.

K-means cluster analysis proved to be useful additional tool to the time series analysis of the optical and radar data. At Calbuco, where deposit information was already known, clustering NDVI data successfully identifies and delineated volcanic deposits. Similar patterns emerged in the clustering of coherence, though NDVI produced more distinct and interpretable results. That said, coherence remained a useful alternative when optical data coverage is extremely limited. One of the key outcomes of the NDVI cluster analysis was the ability to estimate tephra isopachs, particularly in the proximal, severely damaged regions where field access was limited or impossible. While assigning absolute thickness values to these isopachs required field estimates from Romero, Morgavi, et al. (2016), this approach demonstrated how remote sensing could complement and extend field data. Although field measurements remain essential for calibration, NDVI-derived clusters allowed a re-estimation of tephra deposit volume, reinforcing the potential of this method for remote, hazardous, or otherwise inaccessible locations. The isopach maps generated from NDVI closely aligned with those produced from field measurements and fell between the field based maps of Romero, Morgavi, et al. (2016) and the modelled plume isopachs from Hayes et al. (2019), suggesting strong reliability. Encouraged by the success at Calbuco, I applied this clustering approach to 18 additional case studies, where it again proved useful to differentiate deposit types and delineate the extent of damage, especially when used alongside supporting datasets and imagery. A key limitation of this method is the threshold of detectability. At Calbuco, damage from ash deposits thinner than approximately 15 cm was difficult to reliably detect. This suggests a minimum thickness is needed to produce measurable NDVI declines. However, this threshold likely varies depending on factors such as forest type, leaf structure, and weather conditions. For instance, thinner deposits may still cause significant NDVI drops if ash persists on foliage due to a lack of rainfall. This warrants further investigation to refine the method's sensitivity and applicability across environments, but reinforces its ability in the areas of most intense damage and largest deposits.

Based on observed trends in remote sensing data, the following table provides a practical guide linking common changes in satellite measurements to likely vegetation responses

or disturbances following volcanic activity. This summary is intended to assist users in interpreting volcanic impacts on vegetation and in selecting appropriate remote sensing tools. It is not exhaustive, as vegetation responses can be highly variable depending on eruption characteristics, vegetation type, and local conditions.

Table 5.1: Interpretation of vegetation damage based on remote sensing data

NDVI	**Backscatter**	**Coherence**	**Spatial Extent**	**Duration**	**Interpretation**
Large decrease	Minimal or some change	Large increase	Linear or channelised	Years-decades	Vegetation removal by flow deposit
Moderate to large decrease	Decrease	Increase	Large, sectoral	Years	Canopy or plant removal due to volcanic deposits e.g. thick tephra or gas emission
Small to moderate decrease	Minimal to no change	Minimal to no change	Diffuse, sectoral	days - months	Vegetation damage due to ash deposits with likely quick recovery
Decrease	no change	-	Variable	Months	Vegetation damage due to volcanic gas causing photosynthesis inhibition and colour change with minimal leaf loss
Decrease	Decrease	-	Variable	Years-decades	Vegetation damage due to volcanic gas causing leaf loss and possible plant death
No or minimal change	No change	No change	Variable	Variable	Minimal or no vegetation impact
Increase	Increase	Decrease	Variable	Long term	Post-disturbance vegetation recovery

Overall, this analysis shows that remote sensing, both optical and radar, offers valuable, high-resolution (up to 10 m) insights into the spatial distribution and severity of volcanic disturbance. These tools are especially powerful when integrated with field data, enabling a more complete understanding of eruption processes and their ecological impacts.

5.1.2 Post-Eruption Vegetation Recovery Dynamics

In addition to detecting vegetation disturbance, optical and radar data also proved effective in quantifying recovery rates across a variety of environmental settings. Recovery

is defined as the return to pre-eruption satellite derived measurements, e.g. a return to the pre-eruption NDVI or radar values. Recovery rates primarily varied by deposit type, while this is expected, it has previously not been quantified using data from a range of eruptions and environmental settings. Tephra deposits demonstrated the fastest recovery, with an average of 2.8 years with a range spanning from a few months to six years. It was distinguished from other deposits by a rapid initial recovery rate, before a slower progression back to pre-eruption levels. Volcanic blasts, examined at Kelud, Chaitén, and Mount St Helens, showed more varied recovery patterns due to differences in eruption scale and intensity, but recovery took an average of 12.5 years. Blast zones generally exhibited recovery rates that were intermediate between tephra and PDC deposits. However, given the limited number of sites studied, broader generalisations about blast recovery dynamics remain tentative. PDC deposits were significantly more damaging, averaging over 20 years to recover, but with a wide range of recovery times ranging from just over five years to predictions exceeding 50 years. These areas experienced a sharp initial drop in NDVI followed by a slow and consistent recovery trend. This allowed extrapolation of recovery times even for areas that had not recovered by the end of the observation period studied. Lava flow deposits, observed at six volcanoes, showed no meaningful recovery within the available time series. Based on surface characteristics and biological succession rates, full recovery in these zones is expected to take hundreds to thousands of years, significantly greater than other deposit types. Volcanic gas impacts, observed at 5 volcanoes, showed a wide range of recovery time from as little as $\sim$ 4 months to multiple decades. This variability reflects both the duration and intensity of gas emissions, which can range from a few hours or days to persistent degassing lasting years. It also depends on environmental factors influencing gas exposure, such as where and how long the plume grounds, as well as environmental conditions like wind, temperature, and humidity. Because of this, defining a precise onset time and thus the subsequent recovery time is challenging; however, the wide range of recovery durations is clearly evident.

Recovery time generally increases with severity of disturbance. More explosive eruptions

with larger-volume deposits had longer recovery periods. Flow deposits, such as lava and PDCs, which physically remove or destroy vegetation, were associated with the slowest recovery. A key factor influencing this pattern is the presence, or absence, of remnant biological legacies. Tephra deposits typically leave more plant material intact, facilitating quicker regrowth. Blast zones, though destructive, often leave behind some biological material that can aid recovery, as demonstrated at Mount St Helens. In contrast, PDCs and lava flows tend to strip or bury vegetation entirely, sometimes creating new substrates that require full ecological succession. Possible future work could apply the techniques presented here to study ecological succession on new volcanic surfaces such as lava flows, as well as newly formed volcanic islands. This would help to understand how satellite data can inform early ecosystem development and successional processes in volcanic environments.

As biological legacies diminish, recovery times increase. However, recovery is influenced by a wide range of interacting factors, making it difficult to isolate the most controlling variables. In addition to eruption parameters like deposit type, VEI, and activity duration, environmental conditions play a crucial role. For example, the type of forest, particularly whether it is tropical or temperate, was a clear factor in the 18 case studies examined in Chapter 4. Other factors likely influence recovery as well. At Calbuco, for instance, areas with slower recovery appeared to correspond with steeper slopes or varying topography. While this thesis does not explore all these variables in depth, future studies could investigate how elevation, slope, and other site-specific conditions influence recovery. One possible direction would be to compare recovery times for eruptions of similar size within the same forest type, for example, several Indonesian volcanoes due to close proximity and similarity, examining whether differences can be attributed to elevation, slope, or broader ecological and social contexts, even within the same biome.

Overall, the majority of affected areas achieve significant recovery within approximately 30 years. However, this timeline is significantly extended in regions impacted by lava flows, and recovery may be further delayed in cases of continued volcanic activity.

5.1.3 Insights into Vegetation Resilience

Understanding vegetation resilience, the ability of an ecosystem to resist and recover from external disturbances such as volcanic eruptions, is key to assessing long-term environmental recovery and evaluating how volcanoes shape their surrounding ecosystem. While the primary focus of this thesis was on disturbance and recovery patterns, the patterns observed across multiple case studies offer valuable insights into the nature of resilience, whether it is inherent or acquired over time. Tropical forests are more resilient than temperate forests, due to water availability and species variety, and this is likely the cause of their quicker observed recovery times. Some species will be naturally more resilient to specific disturbances, such as by having thicker cuticles protecting from volcanic gases or being more mature, or taller, increasing resilience to deposits such as tephra or flow to a certain depth.

Vegetation at volcanoes may also gain resilience due to repeat exposure. This could be the explanation to increases in recovery rate at Kelud following previous disturbance or the ability for recovery at Turrialba despite long term SO_2 flux. It has previously been hypothesised that disturbance can improve resilience but only to a degree and with intermediate levels of disturbance. This is the foundation for the intermediate disturbance theory (Connell 1978; Molino et al. 2001), that vegetation experiencing intermediate disturbance levels results in maximum diversity which in turn results in resilience. This vegetation at an intermediate distance will have experienced previous disturbance, but been able to recover as damage was not too severe, and as a result it shows maximum diversity and is more resilient, and will have faster recovery rates post disturbance (Molino et al. 2001). This was explored at La Palma by Shatto et al. 2024, which found that vegetation at intermediate distances, which had experienced intermediate disturbance levels, had the quickest recovery rate. This theory could explain the observations at Calbuco, where a more proximal ash area recovered faster than an area further away, possibly the first location had more inherent resilience due to it being closer to the vent.

Investigating this pattern further would be a promising avenue for future research. A

targeted approach might involve selecting multiple case studies with stratified sampling at varying distances from the eruption centre, either using satellite data or field data, to assess the spatial gradient of recovery rates and resilience. This could help determine whether an optimal "intermediate zone" exists where biodiversity and recovery rates peak and potentially confirm how broadly applicable the intermediate disturbance theory is to volcanic eruptions. While Sentinel-2 NDVI data was shown effective at La Palma, successfully detecting recovery rates that peaked at intermediate distances from the volcano (Shatto et al. 2024), finer-scale resilience traits such as species turnover, structural heterogeneity, and legacy effects may require complementary ground-based data in some locations.

5.2 Future of Remote Sensing for Monitoring Vegetation Damage from Eruptions

While this thesis has advanced the use of satellite data to monitor vegetation disturbance, recovery, and resilience in volcanic settings, there remains substantial room for further progress. I believe this work lays important groundwork, particularly as upcoming satellite missions, particularly SAR missions at longer wavelengths, hold significant potential to enhance and expand this field.

5.2.1 Future Satellite Missions

Table 5.2 summarises upcoming and additional satellite missions that have the potential to enhance understanding of vegetation disturbance and recovery in volcanic environments. Among these, the forthcoming SAR missions, Biomass (2025), NISAR (2025), and ROSE-L (2028), are particularly promising due to their use of longer-wavelength radar, which is advantageous for studying vegetation. L-band (NISAR and ROSE-L) has a wavelength of 15-30 cm and will penetrate through the canopy, enabling retrievals of understory vegetation as well as the crown layer. P-band (Biomass) has a wavelength of 30-100 cm and again will penetrate through the canopy and to the ground and has high cross polarised returns. This sensitivity to biomass structure and volume could prove

Table 5.2: A summary of additional or upcoming satellite missions that may advance the field of measuring vegetation damage at volcanoes (Quegan et al. 2019; Roy, Huang, et al. 2021; Das et al. 2021)

Satellite	**Type**	**Launch date**	**Bands**	**Spatial resolution**	**Repeat time**
Biomass	Radar (P-band)	29th April 2025	Quad polarisation	up to 50 m	3-day
NISAR	Radar (L and S-band)	June 2025	up to quad polarisation	3-10 m	12 day
ROSE-L	Radar (L-band)	2028	up to quad polarisation	up to 50 m	3-6 day
PlanetScope	Optical	2014	8 spectral bands	up to 3 m	3-6 day
WorldView-3	Optical	2014	29 spectral bands	up to 0.31 m	1-4.5 day

particularly relevant in densely vegetated volcanic settings where C-band SAR may not be capturing the full vertical vegetation dynamics.

One area with significant potential for advancement is the monitoring of understory vegetation, which may serve as a more sensitive indicator of disturbance and early-stage recovery than taller canopy trees. This aspect was not fully explored in the current study due to sensor limitations but could be investigated more robustly using the P- and L-band SAR capabilities of these missions. These longer-wavelength systems, particularly when utilising cross-polarisation and frequent repeat cycles (up to every 3 days), will enable more detailed temporal monitoring of regrowth processes following eruptions.

In addition to radar, additional optical missions, such as those from PlanetScope and WorldView-3 offer higher spatial and temporal resolution. These could improve the detection of fine-scale features, including narrow or fragmented flow deposits and thin tephra layers that may not persist long enough or be spatially extensive enough to be captured at Sentinel-2 or Landsat resolutions. The shorter revisit times of these commercial optical constellations, though still affected by cloud cover, also increase the likelihood of capturing transient post-eruption changes shortly after deposition or disturbance events.

Together, these upcoming missions offer substantial opportunities to build on the work

Figure 5.1: World ecoregion map showing the locations of future possible target volcanoes to expand on this work with additional satellite data.

presented in this thesis. By incorporating higher-resolution observations, longer wavelength SAR, and more frequent temporal sampling, future studies will be better equipped to quantify complex vegetation responses to volcanic activity. With this in mind, I have considered potential future targets that could most effectively leverage these enhanced observational capacities (shown in Figure 5.1). These targets were not included in this study either due to excess cloud cover (e.g. Soufrière St. Vincent, Reventador), limited vegetation (e.g. Kilauea, Wolf, Ruang), smaller scale disturbances (e.g. Tinakula), or did not fit the criteria but may be a useful study site (e.g. Arenal), or a combination of these factors. I also include some targets with high SO_2 flux (e.g. Kilauea, Manam, Ambae, Miyakejima) to expand on the work in Chapter 3, and try to include targets in omitted regions (e.g. Shiveluch, Etna, Nyiragongo + Nyamuragira) to expand on the work in Chapter 4. As such these targets would potentially benefit from the higher spatial and temporal resolution optical data to increase cloud-free images or highlight smaller scale disturbance. Targets with particularly dense cloud cover would benefit from longer wavelength SAR to provide more detailed observations on potential vegetation damage without the use of optical. This would be useful at Ambae, for example, where there is high SO_2 flux (mean of 2870 t/d (Carn et al. 2017)) and recent eruptive activity. Notably, complementary work has been undertaken at a neighbouring island volcano, Ambrym, by Richard Harvey, a Master's student I am co-supervising, focusing on vegetation impacts due to SO_2 using backscatter as there are no cloud-free optical images. This study could provide useful comparative insights and demonstrates the potential of radar data in persistently cloudy regions, suggesting that the upcoming availability of longer-wavelength SAR sensors may yield even more effective observations of vegetation dynamics in such challenging environments.

5.2.2 Incorporation with Field Campaigns

Satellite remote sensing offers a powerful means of assessing vegetation disturbance and recovery over large spatial and temporal scales, often exceeding the coverage possible in field campaigns. However, it is not a replacement for field studies. Ground-based observations provide crucial context, such as assigning deposit thicknesses to tephra-

affected areas or confirming the presence of specific vegetation types, that cannot be derived solely from satellite data. Field campaigns, however, are not always feasible. Political instability, rugged terrain, dense vegetation, or limited funding can make ground surveys difficult or impossible. In such cases, the remote sensing approaches developed in this thesis are especially valuable. They can serve as a stand-alone tool to map and monitor change where field data is sparse or absent, and perhaps more importantly, they can be used to enhance and guide fieldwork by identifying priority areas, reducing the scope of campaigns, and filling observational gaps in inaccessible zones.

If I were to plan a field campaign to build on this work, it would focus on selected volcanoes in Indonesia, namely Kelud, Semeru and Merapi. Between them, all deposit types investigated as part of this study are represented and they all have eruptions of VEI4 and sit within the same forest and climate type. It would be an opportunity to better quantify how environmental conditions impact vegetation e.g. topography, distance from eruption centre, and what effects are site/eruption specific. I would assess vegetation coverage, health, density and height at multiple sites located at varying distances from the volcano to capture spatial variations in recovery patterns. Vegetation coverage and density would be quantified using standardised quadrants or transects, estimating percent ground cover and species composition to identify differences in community structure. Plant height would be measured directly on representative individuals to gauge structural complexity. Plant health could be assessed by measuring leaf chlorophyll content to estimate photosynthetic capacity and stress levels in dominant species. This would be particularly interesting at Semeru to assess the impacts of volcanic gas.

These ground-based measurements would complement satellite observations by providing detailed, site-specific data that clarify ecological mechanisms behind observed remote sensing trends, such as changes in backscatter variance. This approach would allow assessment of heterogeneity in recovering vegetation that may be undetectable from space or to detect differences in recovered vegetation assemblage which were not detected by optical and radar data. Additionally, sampling vegetation at increasing distances from the volcano could provide insights into how resilience varies with proximity to disturbance

sources and determine how applicable the intermediate distance theory is in relation to volcanic disturbances. If possible, the establishment of permanent monitoring plots at these sites would allow long term tracking of vegetation dynamics and resilience in response to ongoing volcanic disturbance. This integration of satellite data and fieldwork offers the most comprehensive approach for understanding volcanic impacts on ecosystems and represents a powerful path forward for future research.

5.2.3 Applicability to Other Disturbances

Although this study focuses on volcanic eruptions, the remote sensing methods and analytical approaches developed here have broader relevance for other types of landscape disturbance. In particular, events such as wildfires, landslides, floods and severe storms share key characteristics with volcanic activity: they often occur suddenly, can produce substantial ecological and geomorphological impacts, and are frequently difficult or dangerous to monitor on the ground. The ability to map disturbance extent, characterise severity, and track recovery using satellite data therefore offers significant advantages in these contexts.

Volcanic activity serves as a valuable testing ground for these approaches due to the diversity and intensity of the disturbances it produces, ranging from abrupt vegetation burial to prolonged gas exposure. However, many of the core principles, including the use of NDVI to quantify vegetation health and radar metrics (e.g. backscatter change, coherence loss) to assess structural changes, are directly transferable. For example, wildfires similarly cause abrupt vegetation loss and canopy thinning, producing sharp NDVI declines and coherence loss in interferometric SAR datasets. These similarities suggest that post-fire dynamics could be effectively studied using similar methods, with the potential to extract comparable metrics such as recovery times.

This is particularly relevant as wildfire frequency and intensity continue to rise globally, driven by climate change and land-use change. As noted in recent work by Shatto et al. (2024), understanding ecosystem resilience in the face of repeated disturbance is becoming increasingly important. Building on this, one promising direction is to inves-

tigate whether vegetation communities regularly exposed to volcanic activity, such as those near active vents or in frequently tephra-impacted zones, develop forms of adaptive resilience that influence their responses to other disturbance types. This could be particularly valuable in comparing multiple disturbance response: for instance, whether frequent ash exposure leads to increased tolerance to canopy damage or soil disruption from fire. It would be interesting to investigate whether this potential pattern holds across different types of volcanic eruptions, or if exposure to only specific deposit types enhances resilience to other forms of disturbance, and whether such effects are consistent across diverse ecosystems.

Nonetheless, the transferability of these methods is not without limitations. For example, wildfires are often concentrated near human settlements or in managed landscapes where post-disturbance trajectories may be heavily influenced by human intervention. These factors may obscure the natural recovery dynamics and complicate direct comparison with volcanic landscapes, which are often more remote and left to regenerate. Despite these considerations, the integration of optical and radar datasets, particularly coupled with clustering and time-series analysis, holds potential for multi-hazard disturbance mapping. These methods enable assessment of disturbance severity and distribution, recovery trajectories and the effects of ecosystem resilience. Expanding this framework to encompass a broader range of disturbance types could reveal key differences and commonalities in recovery processes, highlighting how ecosystems adapt, or fail to adapt, under varying intensities, frequencies, and combinations of environmental stressors.

5.3 Conclusion

This thesis has demonstrated the value of optical and radar satellite data in assessing vegetation disturbance caused by volcanic eruptions. Through a suite of global case studies across diverse ecosystems, I have shown the effectiveness of remote sensing in detecting, differentiating, and even mapping volcanic deposits. This method is widely applicable and particularly valuable in inaccessible regions, offering comprehensive spatial coverage. When combined with field data, it provides a robust and nuanced analysis of volcanic

impacts. The insights gained into vegetation recovery offer indicative timelines for how long volcanic disturbance may persist in the landscape, raising the possibility of using vegetation patterns to infer past eruptive activity. Furthermore, this study contributes to a better understanding of vegetation resilience in volcanic settings, including how ecosystems resist and recover from repeated disturbances. Overall, these findings present new opportunities for monitoring volcanic activity through the lens of vegetation change and suggest broader applications for mapping and assessing disturbance from other natural hazards.

Bibliography

Agilandeeswari, L., M. Prabukumar, V. Radhesyam, K. L. N. B. Phaneendra, and A. Farhan (Jan. 2022). "Crop Classification for Agricultural Applications in Hyperspectral Remote Sensing Images". en. In: *Applied Sciences* 12.3. Number: 3 Publisher: Multidisciplinary Digital Publishing Institute, p. 1670. ISSN: 2076-3417. DOI: 10.3390/app12031670.

Aiuppa, A., J. M. de Moor, S. Arellano, D. Coppola, V. Francofonte, B. Galle, G. Giudice, M. Liuzzo, E. Mendoza, A. Saballos, G. Tamburello, A. Battaglia, M. Bitetto, S. Gurrieri, M. Laiolo, A. Mastrolia, and R. Moretti (2018). "Tracking Formation of a Lava Lake From Ground and Space: Masaya Volcano (Nicaragua), 2014–2017". en. In: *Geochemistry, Geophysics, Geosystems* 19.2, pp. 496–515. ISSN: 1525-2027. DOI: 10.1002/2017GC007227.

Arnalds, O. (Jan. 2013). "Chapter Six - The Influence of Volcanic Tephra (Ash) on Ecosystems". In: *Advances in Agronomy*. Ed. by family=Sparks, familyi=S., given=Donald L., giveni=D. L. Vol. 121. Academic Press, pp. 331–380. DOI: 10.1016/B978-0-12-407685-3.00006-2.

Arnold, D. W. D., J. Biggs, G. Wadge, and P. Mothes (May 2018). "Using satellite radar amplitude imaging for monitoring syn-eruptive changes in surface morphology at an ice-capped stratovolcano". In: *Remote Sensing of Environment* 209, pp. 480–488. ISSN: 0034-4257. DOI: 10.1016/j.rse.2018.02.040.

Askne, J., P. Dammert, L. Ulander, and G. Smith (Jan. 1997). "C-band repeat-pass interferometric SAR observations of the forest". In: *IEEE Transactions on Geoscience and Remote Sensing* 35.1. Conference Name: IEEE Transactions on Geoscience and Remote Sensing, pp. 25–35. ISSN: 1558-0644. DOI: 10.1109/36.551931.

Ayris, P. M. and P. Delmelle (Nov. 2012). "The immediate environmental effects of tephra emission". en. In: *Bulletin of Volcanology* 74.9, pp. 1905–1936. ISSN: 1432-0819. DOI: 10.1007/s00445-012-0654-5.

Babu, A. and S. Kumar (2019). "InSAR Coherence and Backscatter Images Based Analysis for the Anak Krakatau Volcano Eruption". en. In: *Proceedings* 24.1. Number: 1 Publisher: Multidisciplinary Digital Publishing Institute, p. 21. ISSN: 2504-3900. DOI: 10.3390/IECG2019-06216.

Bai, Z. G., D. L. Dent, L. Olsson, and M. E. Schaepman (2008). "Proxy global assessment of land degradation". en. In: *Soil Use and Management* 24.3, pp. 223–234. ISSN: 1475-2743. DOI: 10.1111/j.1475-2743.2008.00169.x.

Balangue-Tarriela, M. I. R., A. M. F. Lagmay, D. M. Sarmiento, J. Vasquez, M. C. Baldago, R. Ybañez, A. A. Ybañez, J. R. Trinidad, S. Thivet, L. Gurioli, B. V. W. de Vries, M. Aurelio, D. J. Rafael, A. Bermas, and J. A. Escudero (Mar. 2022). "Analysis of the 2020 Taal Volcano tephra fall deposits from crowdsourced information and field data". en. In: *Bulletin of Volcanology* 84.3, p. 35. ISSN: 1432-0819. DOI: 10.1007/s00445-022-01534-y.

Balzter, H. (June 2001). "Forest mapping and monitoring with interferometric synthetic aperture radar (InSAR)". en. In: *Progress in Physical Geography: Earth and Environment* 25.2. Publisher: SAGE Publications Ltd, pp. 159–177. ISSN: 0309-1333. DOI: 10.1177/030913330102500201.

Ban, Y., P. Zhang, A. Nascetti, A. R. Bevington, and M. A. Wulder (Jan. 2020). "Near Real-Time Wildfire Progression Monitoring with Sentinel-1 SAR Time Series and Deep Learning". en. In: *Scientific Reports* 10.1. Number: 1 Publisher: Nature Publishing Group, p. 1322. ISSN: 2045-2322. DOI: 10.1038/s41598-019-56967-x.

Bastos, A., C. M. Gouveia, C. C. DaCamara, and R. M. Trigo (Dec. 2011). "Modelling post-fire vegetation recovery in Portugal". English. In: *Biogeosciences* 8.12. Publisher: Copernicus GmbH, pp. 3593–3607. ISSN: 1726-4170. DOI: 10.5194/bg-8-3593-2011.

Beekley, P. K. and G. R. Hoffman (1981). "Effects of Sulfur Dioxide Fumigation on Photosynthesis, Respiration, and Chlorophyll Content of Selected Lichens". In: *The Bryologist* 84.3. Publisher: American Bryological and Lichenological Society, pp. 379–389. ISSN: 0007-2745. DOI: 10.2307/3242857.

Beirle, S., C. Hörmann, M. Penning de Vries, S. Dörner, C. Kern, and T. Wagner (Aug. 2014). "Estimating the volcanic emission rate and atmospheric lifetime of SO_2 from space: a case study for Kīlauea volcano, Hawai'i". en. In: *Atmospheric Chemistry and Physics* 14.16, pp. 8309–8322. ISSN: 1680-7324. DOI: 10.5194/acp-14-8309-2014.

Bernard, O. and C. Bouvet de Maisonneuve (Nov. 2020). "Controls on eruption style at Rabaul, Papua New Guinea – Insights from microlites, porosity and permeability measurements". In: *Journal of Volcanology and Geothermal Research* 406, p. 107068. ISSN: 0377-0273. DOI: 10.1016/j.jvolgeores.2020.107068.

Biass, S., S. F. Jenkins, W. H. Aeberhard, P. Delmelle, and T. Wilson (Aug. 2022). "Insights into the vulnerability of vegetation to tephra fallouts from interpretable machine learning and big Earth observation data". English. In: *Natural Hazards and Earth System Sciences* 22.9. Publisher: Copernicus GmbH, pp. 2829–2855. ISSN: 1561-8633. DOI: 10.5194/nhess-22-2829-2022.

Biondi, F., I. G. Estrada, J. C. G. Ruiz, and A. E. Torres (May 2003). "Tree growth response to the 1913 eruption of Volcán de Fuego de Colima, Mexico". en. In: *Quaternary Research* 59.3, pp. 293–299. ISSN: 0033-5894, 1096-0287. DOI: 10.1016/S0033-5894(03)00034-6.

Blankenship, R. E. (July 2021). *Molecular Mechanisms of Photosynthesis*. en. John Wiley & Sons. ISBN: 978-1-119-80011-8.

Bonesmo, H. and A. O. Skjelvåg (Dec. 1999). "Regrowth Rates of Timothy and Meadow Fescue Cut at Five Phenological Stages". en. In: *Acta Agriculturae Scandinavica, Section B - Soil & Plant Science* 49.4, pp. 209–215. ISSN: 0906-4710, 1651-1913. DOI: 10.1080/713782028.

Briffa, K. R., P. D. Jones, F. H. Schweingruber, and T. J. Osborn (June 1998). "Influence of volcanic eruptions on Northern Hemisphere summer temperature over the past 600 years". en. In: *Nature* 393.6684. Publisher: Nature Publishing Group, pp. 450–455. ISSN: 1476-4687. DOI: 10.1038/30943.

Brown, S., A. J. R. Gillespie, and A. E. Lugo (Dec. 1989). "Biomass Estimation Methods for Tropical Forests with Applications to Forest Inventory Data". In: *Forest Science* 35.4, pp. 881–902. ISSN: 0015-749X. DOI: 10.1093/forestscience/35.4.881.

Brychkova, G., Z. Xia, G. Yang, Z. Yesbergenova, Z. Zhang, O. Davydov, R. Fluhr, and M. Sagi (2007). "Sulfite oxidase protects plants against sulfur dioxide toxicity". en. In: *The Plant Journal* 50.4. _eprint: https://onlinelibrary.wiley.com/doi/pdf/10.1111/j.1365-313X.2007.03080.x, pp. 696–709. ISSN: 1365-313X. DOI: 10.1111/j.1365-313X.2007.03080.x.

Buitenwerf, R., B. Sandel, S. Normand, A. Mimet, and J.-C. Svenning (2018). "Land surface greening suggests vigorous woody regrowth throughout European semi-natural vegetation". en. In: *Global Change Biology* 24.12, pp. 5789–5801. ISSN: 1365-2486. DOI: 10.1111/gcb.14451.

Burrows, K., R. J. Walters, D. Milledge, K. Spaans, and A. L. Densmore (Jan. 2019). "A New Method for Large-Scale Landslide Classification from Satellite Radar". en. In: *Remote Sensing* 11.3. Number: 3 Publisher: Multidisciplinary Digital Publishing Institute, p. 237. ISSN: 2072-4292. DOI: 10.3390/rs11030237.

Burton, M. R., C. Oppenheimer, L. A. Horrocks, and P. W. Francis (Oct. 2000). "Remote sensing of CO2 and H2O emission rates from Masaya volcano, Nicaragua". In: *Geology* 28.10, pp. 915–918. ISSN: 0091-7613. DOI: 10.1130/0091-7613(2000)28<915:RSOCAH>2.0.CO;2.

C3S (2018). *ERA5 hourly data on single levels from 1940 to present*. Type: dataset. DOI: 10.24381/CDS.ADBB2D47.

Cape, J. N. (Jan. 1993). "Direct damage to vegetation caused by acid rain and polluted cloud: Definition of critical levels for forest trees". In: *Environmental Pollution* 82.2, pp. 167–180. ISSN: 0269-7491. DOI: 10.1016/0269-7491(93)90114-4.

Cape, J. N., D. Fowler, and A. Davison (June 2003). "Ecological effects of sulfur dioxide, fluorides, and minor air pollutants: recent trends and research needs". In: *Environment International*. Future Directions in Air Quality Research : Ecological,Atmospheric,Regulatory/Policy/Economic, and Educational Issues 29.2, pp. 201–211. ISSN: 0160-4120. DOI: 10.1016/S0160-4120(02)00180-0.

Carey, S. and M. Bursik (Jan. 2015). "Chapter 32 - Volcanic Plumes". In: *The Encyclopedia of Volcanoes (Second Edition)*. Ed. by family=Sigurdsson, familyi=S., given=Haraldur, giveni=H. Amsterdam: Academic Press, pp. 571–585. ISBN: 978-0-12-385938-9. DOI: 10.1016/B978-0-12-385938-9.00032-8.

Carey, S. and H. Sigurdsson (Jan. 1989). "The intensity of plinian eruptions". en. In: *Bulletin of Volcanology* 51.1, pp. 28–40. ISSN: 1432-0819. DOI: 10.1007/BF01086759.

Carlón Allende, T., J. L. Macías, M. E. Mendoza, and J. V. Díaz (Aug. 2022). "Influence of volcanic ash deposits on the radial growth of trees in Central Mexico: the case of Parícutin volcano". en. In: *European Journal of Forest Research* 141.4, pp. 605–615. ISSN: 1612-4677. DOI: 10.1007/s10342-022-01463-7.

Carlón Allende, T., J. L. Macías, M. E. Mendoza, and J. Villanueva Díaz (Jan. 2020). "Evidence of volcanic activity in the growth rings of trees at the Tacaná volcano, Mexico–Guatemala border". In: *Canadian Journal of Forest Research* 50.1. Publisher: NRC Research Press, pp. 65–72. ISSN: 0045-5067. DOI: 10.1139/cjfr-2019-0214.

Carn, S. A., V. E. Fioletov, C. A. McLinden, C. Li, and N. A. Krotkov (Mar. 2017). "A decade of global volcanic SO2 emissions measured from space". en. In: *Scientific Reports* 7.1. Publisher: Nature Publishing Group, p. 44095. ISSN: 2045-2322. DOI: 10.1038/srep44095.

Castruccio, A. and J. Clavero (June 2015). "Lahar simulation at active volcanoes of the Southern Andes: implications for hazard assessment". en. In: *Natural Hazards* 77.2, pp. 693–716. ISSN: 1573-0840. DOI: 10.1007/s11069-015-1617-x.

Castruccio, A., J. Clavero, A. Segura, P. Samaniego, O. Roche, J.-L. Le Pennec, and B. Droguett (Aug. 2016). "Eruptive parameters and dynamics of the April 2015 sub-Plinian eruptions of Calbuco volcano (southern Chile)". en. In: *Bulletin of Volcanology* 78.9, p. 62. ISSN: 1432-0819. DOI: 10.1007/s00445-016-1058-8.

Charbonnier, S. J., A. Germa, C. B. Connor, R. Gertisser, K. Preece, J. .-. Komorowski, F. Lavigne, T. Dixon, and L. Connor (July 2013). "Evaluation of the impact of the 2010 pyroclastic density currents at Merapi volcano from high-resolution satellite imagery, field investigations and numerical simulations". en. In: *Journal of Volcanology and Geothermal Research*. Merapi eruption 261, pp. 295–315. ISSN: 0377-0273. DOI: 10.1016/j.jvolgeores.2012.12.021.

Chen, S.-W., Y.-Z. Li, X.-S. Wang, S.-P. Xiao, and M. Sato (July 2014). "Modeling and Interpretation of Scattering Mechanisms in Polarimetric Synthetic Aperture Radar: Advances and perspectives". In: *IEEE Signal Processing Magazine* 31.4. Conference Name: IEEE Signal Processing Magazine, pp. 79–89. ISSN: 1558-0792. DOI: 10.1109/MSP.2014.2312099.

Chen, X., J. E. Vogelmann, M. Rollins, D. Ohlen, C. H. Key, L. Yang, C. Huang, and H. Shi (Dec. 2011). "Detecting post-fire burn severity and vegetation recovery using multitemporal remote sensing spectral indices and field-collected composite burn index data in a ponderosa pine forest". en. In: *International Journal of Remote Sensing* 32.23, pp. 7905–7927. ISSN: 0143-1161, 1366-5901. DOI: 10.1080/01431161.2010.524678.

Chou, W.-C., W.-T. Lin, and C.-Y. Lin (May 2009). "Vegetation recovery patterns assessment at landslides caused by catastrophic earthquake: A case study in central Taiwan". en. In: *Environmental Monitoring and Assessment* 152.1, pp. 245–257. ISSN: 1573-2959. DOI: 10.1007/s10661-008-0312-8.

Clark, M. A., M. Douglas, and J. Choi (2018). *Biology 2e*. en. Google-Books-ID: HrEcEQAAQBAJ.

Clark, R. (1999). *Spectroscopy of rocks and minerals, and principles of spectroscopy.*

Connell, J. H. (Mar. 1978). "Diversity in Tropical Rain Forests and Coral Reefs". In: *Science* 199.4335. Publisher: American Association for the Advancement of Science, pp. 1302–1310. DOI: 10.1126/science.199.4335.1302.

Coppin, P. and M. Bauer (July 1994). "Processing of multitemporal Landsat TM imagery to optimize extraction of forest cover change features". In: *IEEE Transactions on Geoscience and Remote Sensing* 32.4. Conference Name: IEEE Transactions on Geoscience and Remote Sensing, pp. 918–927. ISSN: 1558-0644. DOI: 10.1109/36.298020.

Covshoff, S., ed. (2018). *Photosynthesis: Methods and Protocols*. en. Vol. 1770. Methods in Molecular Biology. New York, NY: Springer. ISBN: 978-1-4939-7785-7 978-1-4939-7786-4. DOI: 10.1007/978-1-4939-7786-4.

Crisafulli, C. M., F. J. Swanson, J. J. Halvorson, and B. D. Clarkson (Jan. 2015). "Chapter 73 - Volcano Ecology: Disturbance Characteristics and Assembly of Biological Communities". In: *The Encyclopedia of Volcanoes (Second Edition)*. Ed. by family=Sigurdsson, familyi=S., given=Haraldur, giveni=H. Amsterdam: Academic Press, pp. 1265–1284. ISBN: 978-0-12-385938-9. DOI: 10.1016/B978-0-12-385938-9.00073-0.

Crk, T., M. Uriarte, F. Corsi, and D. Flynn (May 2009). "Forest recovery in a tropical landscape: what is the relative importance of biophysical, socioeconomic, and landscape variables?" en. In: *Landscape Ecology* 24.5, pp. 629–642. ISSN: 0921-2973, 1572-9761. DOI: 10.1007/s10980-009-9338-8.

Cuevas-González, M., F. Gerard, H. Balzter, and D. Riaño (2009). "Analysing forest recovery after wildfire disturbance in boreal Siberia using remotely sensed vegetation indices". en. In: *Global Change Biol-*

ogy 15.3. _eprint: https://onlinelibrary.wiley.com/doi/pdf/10.1111/j.1365-2486.2008.01784.x, pp. 561–577. ISSN: 1365-2486. DOI: 10.1111/j.1365-2486.2008.01784.x.

Cutler, K. S., S. F. L. Watt, M. Cassidy, A. L. Madden-Nadeau, S. L. Engwell, M. Abdurrachman, M. E. M. Nurshal, D. R. Tappin, S. N. Carey, A. Novellino, C. Hayer, J. E. Hunt, S. J. Day, S. T. Grilli, I. A. Kurniawan, and N. Kartadinata (Jan. 2022). "Downward-propagating eruption following vent unloading implies no direct magmatic trigger for the 2018 lateral collapse of Anak Krakatau". In: *Earth and Planetary Science Letters* 578, p. 117332. ISSN: 0012-821X. DOI: 10.1016/j.epsl.2021.117332.

Cutler, N. A., L. R. Belyea, and A. J. Dugmore (2008). "The spatiotemporal dynamics of a primary succession". en. In: *Journal of Ecology* 96.2. _eprint: https://besjournals.onlinelibrary.wiley.com/doi/pdf/10.1111/j.1365-2745.2007.01344.x, pp. 231–246. ISSN: 1365-2745. DOI: 10.1111/j.1365-2745.2007.01344.x.

Dale, V. H., C. M. Crisafulli, and F. J. Swanson (May 2005). "25 Years of Ecological Change at Mount St. Helens". In: *Science* 308.5724. Publisher: American Association for the Advancement of Science, pp. 961–962. DOI: 10.1126/science.1109684.

Dale, V. H., J. Delgado-Acevedo, and J. Macmahon (2008). "Effects of modern volcanic eruptions on vegetation". In: *Volcanoes and the Environment*. Ed. by family=Marti, familyi=M., given=Joan, giveni=J.family=Ernst, familyi=E., given=Gerald G. J., giveni=G. G. J. Cambridge University Press.

Dale, V. H., F. J. Swanson, and C. M. Crisafulli (2005). "Disturbance, Survival, and Succession: Understanding Ecological Responses to the 1980 Eruption of Mount St. Helens". en. In: *Ecological Responses to the 1980 Eruption of Mount St. Helens*. Ed. by family=Dale, familyi=D., given=Virginia H., giveni=V. H.family=Swanson, familyi=S., given=Frederick J., giveni=F. J.family=Crisafulli, familyi=C., given=Charles M., giveni=C. M. New York, NY: Springer, pp. 3–11. ISBN: 978-0-387-28150-6. DOI: 10.1007/0-387-28150-9_1.

Das, A., R. Kumar, and P. Rosen (Dec. 2021). "Nisar Mission Overview and Updates on ISRO Science Plan". In: *2021 IEEE International India Geoscience and Remote Sensing Symposium (InGARSS)*, pp. 269–272. DOI: 10.1109/InGARSS51564.2021.9791979.

De Schutter, A., M. Kervyn, F. Canters, S. A. Bosshard-Stadlin, M. A. M. Songo, and H. B. Mattsson (May 2015). "Ash fall impact on vegetation: a remote sensing approach of the Oldoinyo Lengai 2007–08 eruption". en. In: *Journal of Applied Volcanology* 4.1, p. 15. ISSN: 2191-5040. DOI: 10.1186/s13617-015-0032-z.

Decker, K. L. and R. Boerner (Sept. 2003). "Elevation and vegetation influences on soil properties in Chilean Nothofagus forests". en. In: *Revista chilena de historia natural* 76.3. ISSN: 0716-078X. DOI: 10.4067/S0716-078X2003000300003.

Del Moral, R. and S. Grishin (1999). "Volcanic disturbances and ecosystem recovery." In: *Ecosystems of the Worls*, pp. 137–160.

Delmelle, P., J. Stix, P. Baxter, J. Garcia-Alvarez, and J. Barquero (Sept. 2002). "Atmospheric dispersion, environmental effects and potential health hazard associated with the low-altitude gas plume of Masaya volcano, Nicaragua". en. In: *Bulletin of Volcanology* 64.6, pp. 423–434. ISSN: 1432-0819. DOI: 10.1007/s00445-002-0221-6.

Delmelle, P. (Jan. 2003). "Environmental impacts of tropospheric volcanic gas plumes". In: *Geological Society, London, Special Publications* 213.1. Publisher: The Geological Society of London, pp. 381–399. DOI: 10.1144/GSL.SP.2003.213.01.23.

Dominguez, E., J. A. Heredia-Guerrero, and A. Heredia (Nov. 2017). "The plant cuticle: old challenges, new perspectives". In: *Journal of Experimental Botany* 68.19, pp. 5251–5255. ISSN: 0022-0957. DOI: 10.1093/jxb/erx389.

Dorigo, W. A., R. Zurita-Milla, A. J. W. de Wit, J. Brazile, R. Singh, and M. E. Schaepman (May 2007). "A review on reflective remote sensing and data assimilation techniques for enhanced agroecosystem modeling". en. In: *International Journal of Applied Earth Observation and Geoinformation*. Advances in airborne electromagnetics and remote sensing of agro-ecosystems 9.2, pp. 165–193. ISSN: 1569-8432. DOI: 10.1016/j.jag.2006.05.003.

Driesen, E., W. Van den Ende, M. De Proft, and W. Saeys (Dec. 2020). "Influence of Environmental Factors Light, CO2, Temperature, and Relative Humidity on Stomatal Opening and Development: A Review". en. In: *Agronomy* 10.12. Number: 12 Publisher: Multidisciplinary Digital Publishing Institute, p. 1975. ISSN: 2073-4395. DOI: 10.3390/agronomy10121975.

Druitt, T. H. (Sept. 1992). "Emplacement of the 18 May 1980 lateral blast deposit ENE of Mount St. Helens, Washington". en. In: *Bulletin of Volcanology* 54.7, pp. 554–572. ISSN: 1432-0819. DOI: 10.1007/BF00569940.

Drusch, M., U. Del Bello, S. Carlier, O. Colin, V. Fernandez, F. Gascon, B. Hoersch, C. Isola, P. Laberinti, P. Martimort, A. Meygret, F. Spoto, O. Sy, F. Marchese, and P. Bargellini (May 2012). "Sentinel-2: ESA's Optical High-Resolution Mission for GMES Operational Services". In: *Remote Sensing of Environment*. The Sentinel Missions - New Opportunities for Science 120, pp. 25–36. ISSN: 0034-4257. DOI: 10.1016/j.rse.2011.11.026.

Dualeh, E. W., S. K. Ebmeier, T. J. Wright, F. Albino, A. Naismith, J. Biggs, P. A. Ordoñez, R. M. Boogher, and A. Roca (2021). "Analyzing Explosive Volcanic Deposits From Satellite-Based Radar Backscatter, Volcán de Fuego, 2018". en. In: *Journal of Geophysical Research: Solid Earth* 126.9. _eprint: https://onlinelibrary.wiley.com/doi/pdf/10.1029/2021JB022250, e2021JB022250. ISSN: 2169-9356. DOI: 10.1029/2021JB022250.

Dualeh, E. W. (Sept. 2022). "Potential of Synthetic Aperture Radar backscatter for monitoring volcanic eruptions". en. phd. University of Leeds.

Duffell, H. J., C. Oppenheimer, D. M. Pyle, B. Galle, A. J. S. McGonigle, and M. R. Burton (Aug. 2003). "Changes in gas composition prior to a minor explosive eruption at Masaya volcano, Nicaragua". In: *Journal of Volcanology and Geothermal Research* 126.3, pp. 327–339. ISSN: 0377-0273. DOI: 10.1016/S0377-0273(03)00156-2.

Easdale, M. H. and O. Bruzzone (Mar. 2018). "Spatial distribution of volcanic ash deposits of 2011 Puyehue-Cordón Caulle eruption in Patagonia as measured by a perturbation in NDVI temporal dynamics". en. In: *Journal of Volcanology and Geothermal Research* 353, pp. 11–17. ISSN: 0377-0273. DOI: 10.1016/j.jvolgeores.2018.01.020.

Ebmeier, S. K., J. Biggs, T. A. Mather, J. R. Elliott, G. Wadge, and F. Amelung (June 2012). "Measuring large topographic change with InSAR: Lava thicknesses, extrusion rate and subsidence rate at Santiaguito volcano, Guatemala". In: *Earth and Planetary Science Letters* 335-336, pp. 216–225. ISSN: 0012-821X. DOI: 10.1016/j.epsl.2012.04.027.

Echeverria, C., D. Coomes, J. Salas, J. M. Rey-Benayas, A. Lara, and A. Newton (July 2006). "Rapid deforestation and fragmentation of Chilean Temperate Forests". en. In: *Biological Conservation* 130.4, pp. 481–494. ISSN: 0006-3207. DOI: 10.1016/j.biocon.2006.01.017.

ESA (2013). *Sentinel-1 User Handbook*. Tech. rep.

Evans, D., T. Farr, J. van Zyl, and H. Zebker (Nov. 1988). "Radar polarimetry: analysis tools and applications". In: *IEEE Transactions on Geoscience and Remote Sensing* 26.6. Conference Name: IEEE Transactions on Geoscience and Remote Sensing, pp. 774–789. ISSN: 1558-0644. DOI: 10.1109/36.7709.

Fiantis, D., F. I. Ginting, Seprianto, F. Halfero, A. P. Saputra, M. Nelson, E. Van Ranst, and B. Minasny (June 2021). "Geochemical and mineralogical composition of the 2018 volcanic deposits of Mt. Anak Krakatau". In: *Geoderma Regional* 25, e00393. ISSN: 2352-0094. DOI: 10.1016/j.geodrs.2021.e00393.

Fioletov, V., C. A. McLinden, D. Griffin, I. Abboud, N. Krotkov, P. J. T. Leonard, C. Li, J. Joiner, N. Theys, and S. Carn (2025). *Multi-Satellite Air Quality Sulfur Dioxide (SO2) Database Long-Term L4 Global V2, Edited by Peter Leonard, Greenbelt, MD, USA, Goddard Earth Science Data and Information Services Center (GES DISC), Accessed: 31/01/2025*. Edited by Peter Leonard, Greenbelt, MD, USA, Goddard Earth Science Data and Information Services Center (GES DISC). DOI: 10.5067/MEASURES/SO2/DATA406.

Foga, S., P. L. Scaramuzza, S. Guo, Z. Zhu, R. D. Dilley, T. Beckmann, G. L. Schmidt, J. L. Dwyer, M. Joseph Hughes, and B. Laue (June 2017). "Cloud detection algorithm comparison and validation for operational Landsat data products". In: *Remote Sensing of Environment* 194, pp. 379–390. ISSN: 0034-4257. DOI: 10.1016/j.rse.2017.03.026.

Foster, D. R., D. H. Knight, and J. F. Franklin (Nov. 1998). "Landscape Patterns and Legacies Resulting from Large, Infrequent Forest Disturbances". en. In: *Ecosystems* 1.6, pp. 497–510. ISSN: 1432-9840. DOI: 10.1007/s100219900046.

Franco-Ramos, O., M. Castillo, and E. Muñoz-Salinas (Dec. 2016). "Using tree-ring analysis to evaluate intra-eruptive lahar activity in the Nexpayantla Gorge, Popocatépetl volcano (central Mexico)". In: *CATENA* 147, pp. 205–215. ISSN: 0341-8162. DOI: 10.1016/j.catena.2016.06.045.

Franklin, J. F. (1990). "Biological Legacies: A Critical Management Concept from Mount St. Helens". en. In: *Trans. North American wildlands natural resource conference* 55, pp. 216–219.

Franklin, J. F., D. Lindenmayer, J. A. MacMahon, A. McKee, J. Magnuson, D. A. Perry, R. Waide, and D. Foster (2000). "There are immense differences between even-aged silvicultural disturbances (especially clearcutting) and natural disturbances, such as windthrow, wildfire, and even volcanic eruptions." en. In: *Conservation in Practice* 1.1, pp. 8–17. ISSN: 1552-5228. DOI: 10.1111/j.1526-4629.2000.tb00155.x.

Galle, B., C. Oppenheimer, A. Geyer, A. J. S. McGonigle, M. Edmonds, and L. Horrocks (Jan. 2003). "A miniaturised ultraviolet spectrometer for remote sensing of SO2 fluxes: a new tool for volcano surveillance". In: *Journal of Volcanology and Geothermal Research* 119.1, pp. 241–254. ISSN: 0377-0273. DOI: 10.1016/S0377-0273(02)00356-6.

Gautason, B. and D. Widory (Apr. 2015). "Assessing the Environmental Impact of Geothermal Power Utilization Using Isotope Ratios (C, N, S, Pb) in Moss (Rhacomitrium Lanuginosum)". en. In: *ResearchGate*.

Gerlach, T. M., M. P. Doukas, K. A. McGee, and R. Kessler (July 2001). "Soil efflux and total emission rates of magmatic CO2 at the Horseshoe Lake tree kill, Mammoth Mountain, California, 1995–1999". en. In: *Chemical Geology*. High CO2 Flux Measurements in Volanic and Geothermal Areas, Methodologies and Results 177.1, pp. 101–116. ISSN: 0009-2541. DOI: 10.1016/S0009-2541(00)00385-5.

Geshi, N. and J. Itoh (July 2018). "Pyroclastic density currents associated with the 2015 phreatomagmatic eruption of the Kuchinoerabujima volcano". en. In: *Earth, Planets and Space* 70.1, p. 119. ISSN: 1880-5981. DOI: 10.1186/s40623-018-0881-x.

Gillman, L. N., S. D. Wright, J. Cusens, P. D. McBride, Y. Malhi, and R. J. Whittaker (2015). "Latitude, productivity and species richness". en. In: *Global Ecology and Biogeography* 24.1, pp. 107–117. ISSN: 1466-8238. DOI: 10.1111/geb.12245.

Global Volcanism Program, . (2020). *Report on Krakatau (Indonesia) (Sennert, S, ed)*. Weekly Volcanic Activity Report, 8 April-14 April 2020. Smithsonian Institution and US Geological Survey.

– (2023). "Report on Masaya (Nicaragua) (Bennis, K.L., and Andrews, B., eds.)" In.

Global Volcanism Program, . (2025). *[Database] Volcanoes of the World (v. 5.2.6; 5 Feb 2025).* Tech. rep. Distributed by Smithsonian Institution, compiled by Venzke, E. https://doi.org/10.5479/si.GVP.VOTW5-2024.5.2.

Global Volcanism Programme, . (2015). "Report on Calbuco (Chile) (Venzke, E., ed.)." en. In: *Bulletin of the Global Volcanism Network, 40:6,* Smithsonian Institution. DOI: https://doi.org/10.5479/si.GVP.BGVN201506-358020.

Goetz, S. J., G. J. Fiske, and A. G. Bunn (Apr. 2006). "Using satellite time-series data sets to analyze fire disturbance and forest recovery across Canada". en. In: *Remote Sensing of Environment* 101.3, pp. 352–365. ISSN: 0034-4257. DOI: 10.1016/j.rse.2006.01.011.

Gouveia, C., C. C. DaCamara, and R. M. Trigo (Apr. 2010). "Post-fire vegetation recovery in Portugal based on spot/vegetation data". English. In: *Natural Hazards and Earth System Sciences* 10.4. Publisher: Copernicus GmbH, pp. 673–684. ISSN: 1561-8633. DOI: 10.5194/nhess-10-673-2010.

Gouveia, C., R. M. Trigo, and C. C. DaCamara (Feb. 2009). "Drought and vegetation stress monitoring in Portugal using satellite data". English. In: *Natural Hazards and Earth System Sciences* 9.1. Publisher: Copernicus GmbH, pp. 185–195. ISSN: 1561-8633. DOI: 10.5194/nhess-9-185-2009.

Grilli, S. T., C. Zhang, J. T. Kirby, A. R. Grilli, D. R. Tappin, S. F. L. Watt, J. E. Hunt, A. Novellino, S. Engwell, M. E. M. Nurshal, M. Abdurrachman, M. Cassidy, A. L. Madden-Nadeau, and S. Day (Oct. 2021). "Modeling of the Dec. 22nd 2018 Anak Krakatau volcano lateral collapse and tsunami based on recent field surveys: Comparison with observed tsunami impact". In: *Marine Geology* 440, p. 106566. ISSN: 0025-3227. DOI: 10.1016/j.margeo.2021.106566.

Grilli, S. T., D. R. Tappin, S. Carey, S. F. L. Watt, S. N. Ward, A. R. Grilli, S. L. Engwell, C. Zhang, J. T. Kirby, L. Schambach, and M. Muin (Aug. 2019). "Modelling of the tsunami from the December 22, 2018 lateral collapse of Anak Krakatau volcano in the Sunda Straits, Indonesia". en. In: *Scientific Reports* 9.1. Number: 1 Publisher: Nature Publishing Group, p. 11946. ISSN: 2045-2322. DOI: 10.1038/s41598-019-48327-6.

Grishin, S. Y. (Dec. 2011). "Environmental impact of the powerful eruption of Sarychev Peak volcano (Kuril Islands, 2009) according to satellite imagery". en. In: *Izvestiya, Atmospheric and Oceanic Physics* 47.9, pp. 1028–1031. ISSN: 1555-628X. DOI: 10.1134/S0001433811090064.

Grishin, S. Y., R. del Moral, P. V. Krestov, and V. P. Verkholat (Dec. 1996). "Succession following the catastrophic eruption of Ksudach volcano (Kamchatka, 1907)". en. In: *Vegetatio* 127.2, pp. 129–153. ISSN: 0042-3106. DOI: 10.1007/BF00044637.

Gunderson, L. H. (Nov. 2000). "Ecological Resilience—In Theory and Application". en. In: *Annual Review of Ecology and Systematics* 31.1. Publisher: Annual Reviews, pp. 425–439. ISSN: 0066-4162. DOI: 10.1146/annurev.ecolsys.31.1.425.

Hadač, E. (Dec. 1972). "Fell-field and heath communities of Reykjanes Peninsula, SW. Iceland (plant communities of Reykjanes Peninsula, Part 5)". en. In: *Folia Geobotanica et Phytotaxonomica* 7.4, pp. 349–380. ISSN: 1874-9348. DOI: 10.1007/BF02854766.

Han, A., Y. Bao, X. Liu, Z. Tong, S. Qing, Y. Bao, and J. Zhang (Jan. 2022). "Plant Ontogeny Strongly Influences SO2 Stress Resistance in Landscape Tree Species Leaf Functional Traits". en. In: *Remote Sensing* 14.8. Number: 8 Publisher: Multidisciplinary Digital Publishing Institute, p. 1857. ISSN: 2072-4292. DOI: 10.3390/rs14081857.

Hansell, A. and C. Oppenheimer (Dec. 2004). "Health Hazards from Volcanic Gases: A Systematic Literature Review". en. In: *Archives of Environmental Health: An International Journal* 59.12, pp. 628–639. ISSN: 0003-9896. DOI: 10.1080/00039890409602947.

Hanssen, R. F. (2001). *Radar Interferometry: Data Interpretation and Error Analysis*. Dordrecht, NETHERLANDS, THE: Springer Netherlands. ISBN: 978-0-306-47633-4.

Hawryło, P., B. Bednarz, P. Wężyk, and M. Szostak (Jan. 2018). "Estimating defoliation of Scots pine stands using machine learning methods and vegetation indices of Sentinel-2". In: *European Journal of Remote Sensing* 51.1. Publisher: Taylor & Francis, pp. 194–204. ISSN: null. DOI: 10.1080/22797254.2017.1417745.

Hayes, J., N. Deligne, L. Bertin, R. Calderon, J. Wardman, T. Wilson, G. Leonard, C. Stewart, K. Wallace, and P. Baxter (Mar. 2019). *Impacts of the 2015 eruption of Calbuco volcano on Chilean infrastructure, utilities, agriculture, and health*. Lower Hutt, New Zealand : GNS Science. DOI: 10.21420/02YC-VX66.

Head, E. M., A. L. Maclean, and S. A. Carn (June 2012). "Mapping lava flows from Nyamuragira volcano (1967–2011) with satellite data and automated classification methods". en. In: *Geomatics, Natural Hazards and Risk* 4.2, pp. 119–144. ISSN: 1947-5705, 1947-5713. DOI: 10.1080/19475705.2012.680503.

Hintz, L., D. Fischer, N. Ferrari, and C. M. Crisafulli (Aug. 2021). "Vegetation dynamics under residual large trees following a volcanic eruption in a Valdivian temperate rainforest". en. In: *Plant Ecology* 222.8, pp. 915–931. ISSN: 1573-5052. DOI: 10.1007/s11258-021-01151-3.

Hislop, S., S. Jones, M. Soto-Berelov, A. Skidmore, A. Haywood, and T. H. Nguyen (Feb. 2019). "A fusion approach to forest disturbance mapping using time series ensemble techniques". In: *Remote Sensing of Environment* 221, pp. 188–197. ISSN: 0034-4257. DOI: 10.1016/j.rse.2018.11.025.

Hoad, S. P., C. E. Jeffree, and J. Grace (Nov. 1992). "Effects of wind and abrasion on cuticular integrity in *Fagus sylvatica* L. and consequences for transfer of pollutants through leaf surfaces". In: *Agriculture, Ecosystems & Environment*. Physiology of Plant Responses to Pollutants 42.3, pp. 275–289. ISSN: 0167-8809. DOI: 10.1016/0167-8809(92)90004-U.

Holland, H. D. (Nov. 2002). "Volcanic gases, black smokers, and the great oxidation event". In: *Geochimica et Cosmochimica Acta* 66.21, pp. 3811–3826. ISSN: 0016-7037. DOI: 10.1016/S0016-7037(02)00950-X.

Holling, C. S. (1973). "RESILIENCE AND STABILITY OF ECOLOGICAL SYSTEMS". In: *Foundations of Socio-Environmental Research: Legacy Readings with Commentaries*. Cambridge: Cambridge University Press, pp. 460–482. ISBN: 978-1-00-917785-6. DOI: 10.1017/9781009177856.038.

Horler, D. N. H., M. Dockray, and J. Barber (Jan. 1983). "The red edge of plant leaf reflectance". In: *International Journal of Remote Sensing* 4.2. Publisher: Taylor & Francis, pp. 273–288. ISSN: 0143-1161. DOI: 10.1080/01431168308948546.

Huang, S., L. Tang, J. P. Hupy, Y. Wang, and G. Shao (Feb. 2021). "A commentary review on the use of normalized difference vegetation index (NDVI) in the era of popular remote sensing". en. In: *Journal of Forestry Research* 32.1, pp. 1–6. ISSN: 1993-0607. DOI: 10.1007/s11676-020-01155-1.

Huete, A., K. Didan, T. Miura, E. Rodriguez, X. Gao, and L. Ferreira (Nov. 2002). "Overview of the radiometric and biophysical performance of the MODIS vegetation indices". en. In: *Remote Sensing of Environment* 83.1-2. Publisher: Elsevier BV, pp. 195–213. ISSN: 0034-4257. DOI: 10.1016/s0034-4257(02)00096-2.

Hüve, K., S. Veljovic-Jovanovic, C. Wiese, and U. Heber (Apr. 2000). "Oxygen and Light Accelerate Recovery from SO2-induced Inhibition of Leaf Photosynthesis and from Cytoplasmic Acidification". In: *Journal of Plant Physiology* 156.4, pp. 537–544. ISSN: 0176-1617. DOI: 10.1016/S0176-1617(00)80170-4.

Imperatore, P., R. Azar, F. Calò, D. Stroppiana, P. A. Brivio, R. Lanari, and A. Pepe (Oct. 2017). "Effect of the Vegetation Fire on Backscattering: An Investigation Based on Sentinel-1 Observations". In: *IEEE Journal of Selected Topics in Applied Earth Observations and Remote Sensing* 10.10. Conference Name: IEEE Journal of Selected Topics in Applied Earth Observations and Remote Sensing, pp. 4478–4492. ISSN: 2151-1535. DOI: 10.1109/JSTARS.2017.2717039.

Inbar, M., M. Tamir, and L. Wittenberg (July 1998). "Runoff and erosion processes after a forest fire in Mount Carmel, a Mediterranean area". In: *Geomorphology* 24.1, pp. 17–33. ISSN: 0169-555X. DOI: 10.1016/S0169-555X(97)00098-6.

Ireland, G. and G. P. Petropoulos (Jan. 2015). "Exploring the relationships between post-fire vegetation regeneration dynamics, topography and burn severity: A case study from the Montane Cordillera Ecozones of Western Canada". en. In: *Applied Geography* 56, pp. 232–248. ISSN: 01436228. DOI: 10.1016/j.apgeog.2014.11.016.

Irons, J. R., J. L. Dwyer, and J. A. Barsi (July 2012). "The next Landsat satellite: The Landsat Data Continuity Mission". en. In: *Remote Sensing of Environment* 122, pp. 11–21. ISSN: 00344257. DOI: 10.1016/j.rse.2011.08.026.

Jacquemoud, S. and F. Baret (Nov. 1990). "PROSPECT: A model of leaf optical properties spectra". en. In: *Remote Sensing of Environment* 34.2, pp. 75–91. ISSN: 0034-4257. DOI: 10.1016/0034-4257(90)90100-Z.

Jepsen, J. U., S. B. Hagen, K. A. Høgda, R. A. Ims, S. R. Karlsen, H. Tømmervik, and N. G. Yoccoz (Sept. 2009). "Monitoring the spatio-temporal dynamics of geometrid moth outbreaks in birch forest using MODIS-NDVI data". In: *Remote Sensing of Environment* 113.9, pp. 1939–1947. ISSN: 0034-4257. DOI: 10.1016/j.rse.2009.05.006.

Jiang, Z., A. Huete, K. Didan, and T. Miura (Oct. 2008). "Development of a two-band enhanced vegetation index without a blue band". en. In: *Remote Sensing of Environment* 112.10, pp. 3833–3845. ISSN: 00344257. DOI: 10.1016/j.rse.2008.06.006.

Johnstone, J. F., E. J. B. McIntire, E. J. Pedersen, G. King, and M. J. F. Pisaric (2010). "A sensitive slope: estimating landscape patterns of forest resilience in a changing climate". en. In: *Ecosphere* 1.6, art14. ISSN: 2150-8925. DOI: 10.1890/ES10-00102.1.

Jong, R. de, J. Verbesselt, M. E. Schaepman, and S. de Bruin (2012). "Trend changes in global greening and browning: contribution of short-term trends to longer-term change". en. In: *Global Change Biology* 18.2, pp. 642–655. ISSN: 1365-2486. DOI: 10.1111/j.1365-2486.2011.02578.x.

Jung, J., D.-j. Kim, M. Lavalle, and S.-H. Yun (Oct. 2016). "Coherent Change Detection Using InSAR Temporal Decorrelation Model: A Case Study for Volcanic Ash Detection". In: *IEEE Transactions on Geoscience and Remote Sensing* 54.10. Conference Name: IEEE Transactions on Geoscience and Remote Sensing, pp. 5765–5775. ISSN: 1558-0644. DOI: 10.1109/TGRS.2016.2572166.

Just, D. and R. Bamler (July 1994). "Phase statistics of interferograms with applications to synthetic aperture radar". EN. In: *Applied Optics* 33.20. Publisher: Optica Publishing Group, pp. 4361–4368. ISSN: 2155-3165. DOI: 10.1364/AO.33.004361.

Kasting, J. F. (Feb. 1993). "Earth's Early Atmosphere". In: *Science* 259.5097. Publisher: American Association for the Advancement of Science, pp. 920–926. DOI: 10.1126/science.11536547.

Kharuk, V. I., K. J. Ranson, and S. T. Im (May 2009). "Siberian silkmoth outbreak pattern analysis based on SPOT VEGETATION data". In: *International Journal of Remote Sensing* 30.9. Publisher: Taylor & Francis _eprint: https://doi.org/10.1080/01431160802549419, pp. 2377–2388. ISSN: 0143-1161. DOI: 10.1080/01431160802549419.

Kim, Y., T. Jackson, R. Bindlish, H. Lee, and S. Hong (July 2012). "Radar Vegetation Index for Estimating the Vegetation Water Content of Rice and Soybean". In: *IEEE Geoscience and Remote*

Sensing Letters 9.4. Conference Name: IEEE Geoscience and Remote Sensing Letters, pp. 564–568. ISSN: 1558-0571. DOI: 10.1109/LGRS.2011.2174772.

Kitayama, K., D. Mueller-Dombois, and P. M. Vitousek (1995). "Primary succession of Hawaiian montane rain forest on a chronosequence of eight lava flows". en. In: *Journal of Vegetation Science* 6.2. _eprint: https://onlinelibrary.wiley.com/doi/pdf/10.2307/3236216, pp. 211–222. ISSN: 1654-1103. DOI: 10.2307/3236216.

Knabe, W. (1976). "Effects of Sulfur Dioxide on Terrestrial Vegetation". In: *Ambio* 5.5/6. Publisher: [Springer, Royal Swedish Academy of Sciences], pp. 213–218. ISSN: 0044-7447.

Kumar, L. and O. Mutanga (Sept. 2017). "Remote Sensing of Above-Ground Biomass". en. In: *Remote Sensing* 9.9. Number: 9 Publisher: Multidisciplinary Digital Publishing Institute, p. 935. ISSN: 2072-4292. DOI: 10.3390/rs9090935.

Kump, L. R. and M. E. Barley (Aug. 2007). "Increased subaerial volcanism and the rise of atmospheric oxygen 2.5 billion years ago". en. In: *Nature* 448.7157. Publisher: Nature Publishing Group, pp. 1033–1036. ISSN: 1476-4687. DOI: 10.1038/nature06058.

Lagmay, A. M. F., M. I. R. Balangue-Tarriela, M. Aurelio, R. Ybanez, A. Bonus-Ybanez, J. Sulapas, C. Baldago, D. M. Sarmiento, H. Cabria, R. Rodolfo, D. J. Rafael, J. R. Trinidad, E. Obille, and N. Rosell (Aug. 2021). "Hazardous base surges of Taal's 2020 eruption". en. In: *Scientific Reports* 11.1, p. 15703. ISSN: 2045-2322. DOI: 10.1038/s41598-021-94866-2.

Lai, R., T. Oguchi, and C. Zhong (Jan. 2022). "Evaluating Spatiotemporal Patterns of Post-Eruption Vegetation Recovery at Unzen Volcano, Japan, from Landsat Time Series". en. In: *Remote Sensing* 14.21. Number: 21 Publisher: Multidisciplinary Digital Publishing Institute, p. 5419. ISSN: 2072-4292. DOI: 10.3390/rs14215419.

Lara, L. E. (Jan. 2009). "The 2008 eruption of the Chaitén Volcano, Chile: a preliminary report". en. In: *Andean geology* 36.1. ISSN: 0718-7106. DOI: 10.4067/S0718-71062009000100009.

Lee, H. K., I. Khaine, M. J. Kwak, J. H. Jang, T. Y. Lee, J. K. Lee, I. R. Kim, W. I. Kim, K. S. Oh, and S. Y. Woo (Dec. 2017). "The relationship between SO2 exposure and plant physiology: A mini review". en. In: *Horticulture, Environment, and Biotechnology* 58.6, pp. 523–529. ISSN: 2211-3460. DOI: 10.1007/s13580-017-0053-0.

Lee, J. S., M. R. Grunes, and R. Kwok (July 1994). "Classification of multi-look polarimetric SAR imagery based on complex Wishart distribution". In: *International Journal of Remote Sensing* 15.11. Publisher: Taylor & Francis, pp. 2299–2311. ISSN: 0143-1161. DOI: 10.1080/01431169408954244.

Lewis, S. L., B. Sonké, T. Sunderland, S. K. Begne, G. Lopez-Gonzalez, G. M. F. van der Heijden, O. L. Phillips, K. Affum-Baffoe, T. R. Baker, L. Banin, J.-F. Bastin, H. Beeckman, P. Boeckx, J. Bogaert, C. De Cannière, E. Chezeaux, C. J. Clark, M. Collins, G. Djagbletey, M. N. K. Djuikouo,

V. Droissart, J.-L. Doucet, C. E. N. Ewango, S. Fauset, T. R. Feldpausch, E. G. Foli, J.-F. Gillet, A. C. Hamilton, D. J. Harris, T. B. Hart, T. de Haulleville, A. Hladik, K. Hufkens, D. Huygens, P. Jeanmart, K. J. Jeffery, E. Kearsley, M. E. Leal, J. Lloyd, J. C. Lovett, J.-R. Makana, Y. Malhi, A. R. Marshall, L. Ojo, K. S.-H. Peh, G. Pickavance, J. R. Poulsen, J. M. Reitsma, D. Sheil, M. Simo, K. Steppe, H. E. Taedoumg, J. Talbot, J. R. D. Taplin, D. Taylor, S. C. Thomas, B. Toirambe, H. Verbeeck, J. Vleminckx, L. J. T. White, S. Willcock, H. Woell, and L. Zemagho (Sept. 2013). "Above-ground biomass and structure of 260 African tropical forests". In: *Philosophical Transactions of the Royal Society B: Biological Sciences* 368.1625. Publisher: Royal Society, p. 20120295. DOI: 10.1098/rstb.2012.0295.

Li, L., L. Bakelants, C. Solana, F. Canters, and M. Kervyn (2018). "Dating lava flows of tropical volcanoes by means of spatial modeling of vegetation recovery". en. In: *Earth Surface Processes and Landforms* 43.4, pp. 840–856. ISSN: 1096-9837. DOI: 10.1002/esp.4284.

Liew, S. C., L. K. Kwoh, K. Padmanabhan, O. K. Lim, and H. Lim (1999). "Delineating land/forest fire burnt scars with ERS Interferometric Synthetic Aperture Radar". en. In: *Geophysical Research Letters* 26.16. _eprint: https://onlinelibrary.wiley.com/doi/pdf/10.1029/1999GL900189, pp. 2409–2412. ISSN: 1944-8007. DOI: 10.1029/1999GL900189.

Likas, A., N. Vlassis, and J. J. Verbeek (Feb. 2003). "The global k-means clustering algorithm". en. In: *Pattern Recognition* 36.2, pp. 451–461. ISSN: 00313203. DOI: 10.1016/S0031-3203(02)00060-2.

Likens, G. E., R. F. Wright, J. N. Galloway, and T. J. Butler (1979). "Acid Rain". In: *Scientific American* 241.4. Publisher: Scientific American, a division of Nature America, Inc., pp. 43–51. ISSN: 0036-8733.

Liu, H. Q. and A. Huete (Mar. 1995). "A feedback based modification of the NDVI to minimize canopy background and atmospheric noise". In: *IEEE Transactions on Geoscience and Remote Sensing* 33.2, pp. 457–465. ISSN: 1558-0644. DOI: 10.1109/TGRS.1995.8746027.

Lowenstern, J. B., H. Bleick, J. A. Vazquez, J. M. Castro, and P. B. Larson (Dec. 2012). "Degassing of Cl, F, Li, and Be during extrusion and crystallization of the rhyolite dome at Volcán Chaitén, Chile during 2008 and 2009". en. In: *Bulletin of Volcanology* 74.10, pp. 2303–2319. ISSN: 1432-0819. DOI: 10.1007/s00445-012-0663-4.

Lu, T., H. Zeng, Y. Luo, Q. Wang, F. Shi, G. Sun, Y. Wu, and N. Wu (2012). "Monitoring vegetation recovery after China's May 2008 Wenchuan earthquake using Landsat TM time-series data: a case study in Mao County". en. In: *Ecological Research* 27.5, pp. 955–966. ISSN: 1440-1703. DOI: 10.1007/s11284-012-0976-y.

Macias, J. L., M. F. Sheridan, and J. M. Espíndola (Apr. 1997). "Reappraisal of the 1982 eruptions of El Chichón Volcano, Chiapas, Mexico: new data from proximal deposits". en. In: *Bulletin of Volcanology* 58.6, pp. 459–471. ISSN: 1432-0819. DOI: 10.1007/s004450050155.

Macorps, E., M. Jo, B. Osmanoglu, and R. A. Albayrak (Apr. 2023). "MAPPING AREAS IMPACTED BY VOLCANIC FLOWS DURING AN ERUPTION USING SYNTHETIC APERTURE RADAR AND OPTICAL IMAGERY". English. In: *The International Archives of the Photogrammetry, Remote Sensing and Spatial Information Sciences* XLVIII-M-1-2023, pp. 175–182. ISSN: 1682-1750. DOI: 10.5194/isprs-archives-XLVIII-M-1-2023-175-2023.

Madamanchi, N. R. and R. G. Alscher (Sept. 1991). "Metabolic Bases for Differences in Sensitivity of Two Pea Cultivars to Sulfur Dioxide 1". In: *Plant Physiology* 97.1, pp. 88–93. ISSN: 0032-0889. DOI: 10.1104/pp.97.1.88.

Maeno, F., S. Nakada, M. Yoshimoto, T. Shimano, N. Hokanishi, A. Zaennudin, and M. Iguchi (Sept. 2019). "A sequence of a plinian eruption preceded by dome destruction at Kelud volcano, Indonesia, on February 13, 2014, revealed from tephra fallout and pyroclastic density current deposits". In: *Journal of Volcanology and Geothermal Research*. Lessons learned from the recent eruptions of Sinabung and Kelud Volcanoes, Indonesia 382, pp. 24–41. ISSN: 0377-0273. DOI: 10.1016/j.jvolgeores.2017.03.002.

Main-Knorn, M., B. Pflug, J. Louis, V. Debaecker, U. Müller-Wilm, and F. Gascon (Oct. 2017). "Sen2Cor for Sentinel-2". In: *Image and Signal Processing for Remote Sensing XXIII*. Vol. 10427. SPIE, pp. 37–48. DOI: 10.1117/12.2278218.

Major, J. J., C. M. Crisafulli, and F. J. Swanson (2020). "Lessons from a post-eruption landscape". en. In: *Eos, Earth and Space Science News* 101.5, pp. 34–40. DOI: 10.1029/2020EO143198.

Major, J. J. and L. E. Lara (Apr. 2013). "Overview of Chaitén Volcano, Chile, and its 2008-2009 eruption". es. In: *Andean Geology* 40.2. Number: 2, pp. 196–215. ISSN: 0718-7106. DOI: 10.5027/andgeoV40n2-a01.

Makbul, S., N. Guler, N. Durmus, and S. Guven (Jan. 2011). "Changes in anatomical and physiological parameters of soybean under drought stress". In: *Turkish Journal of Botany* 35.4, pp. 369–377. ISSN: 1300-008X. DOI: 10.3906/bot-1002-7.

Martin, R. S., S. F. L. Watt, D. M. Pyle, T. A. Mather, N. E. Matthews, R. B. Georg, J. A. Day, T. Fairhead, M. L. I. Witt, and B. M. Quayle (July 2009). "Environmental effects of ashfall in Argentina from the 2008 Chaitén volcanic eruption". en. In: *Journal of Volcanology and Geothermal Research* 184.3, pp. 462–472. ISSN: 0377-0273. DOI: 10.1016/j.jvolgeores.2009.04.010.

Martini, F., F. Tassi, O. Vaselli, R. Del Potro, M. Martinez, R. V. del Laat, and E. Fernandez (Dec. 2010). "Geophysical, geochemical and geodetical signals of reawakening at Turrialba volcano (Costa Rica) after almost 150 years of quiescence". In: *Journal of Volcanology and Geothermal Research* 198.3, pp. 416–432. ISSN: 0377-0273. DOI: 10.1016/j.jvolgeores.2010.09.021.

Marx, A. and B. Kleinschmit (2017). "Sensitivity analysis of RapidEye spectral bands and derived vegetation indices for insect defoliation detection in pure Scots pine stands". en. In: *iForest - Biogeosciences and Forestry* 10.4. Publisher: SISEF - Italian Society of Silviculture and Forest Ecology Section: Remote Sensing and Information System, p. 659. ISSN: 1971-7458. DOI: 10.3832/ifor1727-010.

Marzen, L. J., Z. Szantoi, L. M. Harrington, and J. A. Harrington (Aug. 2011). "Implications of management strategies and vegetation change in the Mount St. Helens blast zone". In: *Geocarto International* 26.5. Publisher: Taylor & Francis, pp. 359–376. ISSN: 1010-6049. DOI: 10.1080/10106049.2011.584977.

Masek, J. G., C. Huang, R. Wolfe, W. Cohen, F. Hall, J. Kutler, and P. Nelson (June 2008). "North American forest disturbance mapped from a decadal Landsat record". en. In: *Remote Sensing of Environment* 112.6, pp. 2914–2926. ISSN: 0034-4257. DOI: 10.1016/j.rse.2008.02.010.

Mather, T. A., J. R. McCabe, V. K. Rai, M. H. Thiemens, D. M. Pyle, T. H. E. Heaton, H. J. Sloane, and G. R. Fern (2006). "Oxygen and sulfur isotopic composition of volcanic sulfate aerosol at the point of emission". en. In: *Journal of Geophysical Research: Atmospheres* 111.D18. _eprint: https://onlinelibrary.wiley.com/doi/pdf/10.1029/2005JD006584. ISSN: 2156-2202. DOI: 10.1029/2005JD006584.

Mather, T. A., D. M. Pyle, and C. Oppenheimer (2003). "Tropospheric volcanic aerosol". en. In: *Geophysical Monograph Series*. Ed. by family=Robock, familyi=R., given=Alan, giveni=A.family=Oppenheimer, familyi=O., given=Clive, giveni=C. Vol. 139. Washington, D. C.: American Geophysical Union, pp. 189–212. ISBN: 978-0-87590-998-1. DOI: 10.1029/139GM12.

Mather, T. A., D. M. Pyle, V. I. Tsanev, A. J. S. McGonigle, C. Oppenheimer, and A. G. Allen (Jan. 2006). "A reassessment of current volcanic emissions from the Central American arc with specific examples from Nicaragua". In: *Journal of Volcanology and Geothermal Research* 149.3, pp. 297–311. ISSN: 0377-0273. DOI: 10.1016/j.jvolgeores.2005.07.021.

Mather, T. A. (Sept. 2008). "Volcanism and the atmosphere: the potential role of the atmosphere in unlocking the reactivity of volcanic emissions". In: *Philosophical Transactions of the Royal Society A: Mathematical, Physical and Engineering Sciences* 366.1885. Publisher: Royal Society, pp. 4581–4595. DOI: 10.1098/rsta.2008.0152.

– (Oct. 2015). "Volcanoes and the environment: Lessons for understanding Earth's past and future from studies of present-day volcanic emissions". In: *Journal of Volcanology and Geothermal Research* 304, pp. 160–179. ISSN: 0377-0273. DOI: 10.1016/j.jvolgeores.2015.08.016.

Mather, T. A., D. M. Pyle, and A. G. Allen (Oct. 2004). "Volcanic source for fixed nitrogen in the early Earth's atmosphere". In: *Geology* 32.10, pp. 905–908. ISSN: 0091-7613. DOI: 10.1130/G20679.1.

Matsushita, B., W. Yang, J. Chen, Y. Onda, and G. Qiu (Nov. 2007). "Sensitivity of the Enhanced Vegetation Index (EVI) and Normalized Difference Vegetation Index (NDVI) to Topographic Effects:

A Case Study in High-density Cypress Forest". en. In: *Sensors* 7.11. Number: 11 Publisher: Molecular Diversity Preservation International, pp. 2636–2651. ISSN: 1424-8220. DOI: 10.3390/s7112636.

McBirney, A. (1956). "The Nicaraguan volcano Masaya and its caldera". en. In: *Eos, Transactions American Geophysical Union* 37.1. _eprint: https://onlinelibrary.wiley.com/doi/pdf/10.1029/TR037i001p00083, pp. 83–96. ISSN: 2324-9250. DOI: 10.1029/TR037i001p00083.

Mella, M., H. Roa, A. Vergés, D. Quiroz, L. Bertin, D. Basualto, D. Bertin, and N. Garrido (Jan. 2015). "Productos volcánicos e impactos asociados al ciclo eruptivo del 2015 del volcán Calbuco". In.

Meyer, F. J., D. B. McAlpin, W. Gong, O. Ajadi, S. Arko, P. W. Webley, and J. Dehn (Feb. 2015). "Integrating SAR and derived products into operational volcano monitoring and decision support systems". en. In: *ISPRS Journal of Photogrammetry and Remote Sensing*. High-Resolution Earth Imaging for Geospatial Information 100, pp. 106–117. ISSN: 0924-2716. DOI: 10.1016/j.isprsjprs.2014.05.009.

Michener, W. K. and P. F. Houhoulis (1997). "Detection of Vegetation Changes Associated with Extensive Flooding in a Forested Ecosystem". en. In: *Photogrammetric Engineering and Remote Sensing*, p. 12.

Mitchard, E. T. A., S. S. Saatchi, I. H. Woodhouse, G. Nangendo, N. S. Ribeiro, M. Williams, C. M. Ryan, S. L. Lewis, T. R. Feldpausch, and P. Meir (2009). "Using satellite radar backscatter to predict above-ground woody biomass: A consistent relationship across four different African landscapes". en. In: *Geophysical Research Letters* 36.23. ISSN: 1944-8007. DOI: 10.1029/2009GL040692.

Molino, J.-F. and D. Sabatier (Nov. 2001). "Tree Diversity in Tropical Rain Forests: A Validation of the Intermediate Disturbance Hypothesis". en. In: *Science* 294.5547, pp. 1702–1704. ISSN: 0036-8075, 1095-9203. DOI: 10.1126/science.1060284.

Mora, J. L., C. M. Armas-Herrera, J. A. Guerra, C. D. Arbelo, A. Rodríguez-Rodríguez, and J. S. Notario del Pino (2016). "A Comparative Study of Long-Term Effects on Fire-Affected Volcanic Soils in Two Different Ecosystems in the Canary Islands". en. In: *Land Degradation & Development* 27.5. _eprint: https://onlinelibrary.wiley.com/doi/pdf/10.1002/ldr.2458, pp. 1489–1500. ISSN: 1099-145X. DOI: 10.1002/ldr.2458.

Morais, L. F. d., A. C. R. Cavalcante, D. d. N. Aquino, F. H. M. Nogueira, and M. J. D. Cândido (Sept. 2021). "Spectral responses in rangelands and land cover change by livestock in regions of the Caatinga biome, Brazil". en. In: *Scientific Reports* 11.1. Publisher: Nature Publishing Group, p. 18261. ISSN: 2045-2322. DOI: 10.1038/s41598-021-97784-5.

Moral, R. del and D. M. Wood (1993). "Early primary succession on the volcano Mount St. Helens". en. In: *Journal of Vegetation Science* 4.2, pp. 223–234. ISSN: 1654-1103. DOI: 10.2307/3236108.

Moran, M. S., Y. Inoue, and E. M. Barnes (Sept. 1997). "Opportunities and limitations for image-based remote sensing in precision crop management". en. In: *Remote Sensing of Environment* 61.3, pp. 319–346. ISSN: 0034-4257. DOI: 10.1016/S0034-4257(97)00045-X.

Myneni, R. B., F. G. Hall, P. J. Sellers, and A. L. Marshak (Mar. 1995). "The interpretation of spectral vegetation indexes". In: *IEEE Transactions on Geoscience and Remote Sensing* 33.2. Conference Name: IEEE Transactions on Geoscience and Remote Sensing, pp. 481–486. ISSN: 1558-0644. DOI: 10.1109/TGRS.1995.8746029.

Nadeau, P. A. and G. Williams-Jones (May 2009). "Apparent downwind depletion of volcanic SO2 flux—lessons from Masaya Volcano, Nicaragua". en. In: *Bulletin of Volcanology* 71.4, pp. 389–400. ISSN: 1432-0819. DOI: 10.1007/s00445-008-0251-9.

Olson, D. M., E. Dinerstein, E. D. Wikramanayake, N. D. Burgess, G. V. N. Powell, E. C. Underwood, J. A. D'amico, I. Itoua, H. E. Strand, J. C. Morrison, C. J. Loucks, T. F. Allnutt, T. H. Ricketts, Y. Kura, J. F. Lamoreux, W. W. Wettengel, P. Hedao, and K. R. Kassem (2001). "Terrestrial Ecoregions of the World: A New Map of Life on Earth". en. In: *BioScience* 51.11, p. 933. ISSN: 0006-3568. DOI: 10.1641/0006-3568(2001)051[0933:TEOTWA]2.0.CO;2.

Olszyk, D. M. and D. T. Tingey (Apr. 1984). "Phytotoxicity of Air Pollutants: Evidence for the Photodetoxification of SO2 but Not O3". In: *Plant Physiology* 74.4, pp. 999–1005. ISSN: 0032-0889. DOI: 10.1104/pp.74.4.999.

OpenTopography (2021). *Copernicus GLO-30 Digital Surface Model*. DOI: 10.5069/G9028PQB.

Oppenheimer, C., D. M. Pyle, and J. Barclay (2003). *Volcanic Degassing*. en. Geological Society of London. ISBN: 978-1-86239-136-9.

Orynbaikyzy, A., S. Plank, Y. Vetrita, S. Martinis, I. Santoso, R. Dwi Ismanto, F. Chusnayah, A. Tjahjaningsih, Suwarsono, N. Genzano, F. Marchese, M. Rokhis Khomarudin, and G. Strunz (Feb. 2023). "Joint use of Sentinel-2 and Sentinel-1 data for rapid mapping of volcanic eruption deposits in Southeast Asia". In: *International Journal of Applied Earth Observation and Geoinformation* 116, p. 103166. ISSN: 1569-8432. DOI: 10.1016/j.jag.2022.103166.

Pallister, J., R. Wessels, J. Griswold, W. McCausland, N. Kartadinata, H. Gunawan, A. Budianto, and S. Primulyana (Sept. 2019). "Monitoring, forecasting collapse events, and mapping pyroclastic deposits at Sinabung volcano with satellite imagery". In: *Journal of Volcanology and Geothermal Research*. Lessons learned from the recent eruptions of Sinabung and Kelud Volcanoes, Indonesia 382, pp. 149–163. ISSN: 0377-0273. DOI: 10.1016/j.jvolgeores.2018.05.012.

Patel, P., H. S. Srivastava, S. Panigrahy, and J. S. Parihar (Jan. 2006). "Comparative evaluation of the sensitivity of multi-polarized multi-frequency SAR backscatter to plant density". en. In: *Inter-*

national Journal of Remote Sensing 27.2, pp. 293–305. ISSN: 0143-1161, 1366-5901. DOI: 10.1080/01431160500214050.

Payne, R. J. and J. Egan (Jan. 2019). "Using palaeoecological techniques to understand the impacts of past volcanic eruptions". In: *Quaternary International*. Distal Effects of Volcanic Eruptions on Pre-Industrial Societies 499, pp. 278–289. ISSN: 1040-6182. DOI: 10.1016/j.quaint.2017.12.019.

Peel, M. C., B. L. Finlayson, and T. A. McMahon (2007). "Updated world map of the Ko¨ppen-Geiger climate classification". en. In: *Hydrol. Earth Syst. Sci.*, p. 12.

Pfeffer, M. A., S. Arellano, S. Barsotti, G. N. Petersen, T. Barnie, E. Ilyinskaya, T. Hjörvar, E. Bali, G. B. M. Pedersen, G. B. Guðmundsson, K. Vogfjorð, E. J. Ranta, B. A. Óladóttir, B. A. Edwards, Y. Moussallam, A. Stefánsson, S. W. Scott, J.-F. Smekens, M. Varnam, and M. Titos (May 2024). "SO2 emission rates and incorporation into the air pollution dispersion forecast during the 2021 eruption of Fagradalsfjall, Iceland". In: *Journal of Volcanology and Geothermal Research* 449, p. 108064. ISSN: 0377-0273. DOI: 10.1016/j.jvolgeores.2024.108064.

Picotte, J. J., K. M. Robertson, J. J. Picotte, and K. M. Robertson (May 2011). "Validation of remote sensing of burn severity in south-eastern US ecosystems". en. In: *International Journal of Wildland Fire* 20.3. Publisher: CSIRO PUBLISHING, pp. 453–464. ISSN: 1448-5516, 1448-5516. DOI: 10.1071/WF10013.

Pierson, T. C., N. J. Wood, and C. L. Driedger (Nov. 2014). "Reducing risk from lahar hazards: concepts, case studies, and roles for scientists". In: *Journal of Applied Volcanology* 3.1, p. 16. ISSN: 2191-5040. DOI: 10.1186/s13617-014-0016-4.

Pistolesi, M., R. Cioni, C. Bonadonna, M. Elissondo, V. Baumann, A. Bertagnini, L. Chiari, R. Gonzales, M. Rosi, and L. Francalanci (Jan. 2015). "Complex dynamics of small-moderate volcanic events: the example of the 2011 rhyolitic Cordón Caulle eruption, Chile". en. In: *Bulletin of Volcanology* 77.1, p. 3. ISSN: 1432-0819. DOI: 10.1007/s00445-014-0898-3.

Pyle, D. M. (Jan. 1989). "The thickness, volume and grainsize of tephra fall deposits". en. In: *Bulletin of Volcanology* 51.1, pp. 1–15. ISSN: 1432-0819. DOI: 10.1007/BF01086757.

– (Dec. 1995). "Assessment of the minimum volume of tephra fall deposits". In: *Journal of Volcanology and Geothermal Research* 69.3, pp. 379–382. ISSN: 0377-0273. DOI: 10.1016/0377-0273(95)00038-0.

Quegan, S., T. Le Toan, J. Chave, J. Dall, J.-F. Exbrayat, D. H. T. Minh, M. Lomas, M. M. D'Alessandro, P. Paillou, K. Papathanassiou, F. Rocca, S. Saatchi, K. Scipal, H. Shugart, T. L. Smallman, M. J. Soja, S. Tebaldini, L. Ulander, L. Villard, and M. Williams (June 2019). "The European Space Agency BIOMASS mission: Measuring forest above-ground biomass from space". In: *Remote Sensing of Environment* 227, pp. 44–60. ISSN: 0034-4257. DOI: 10.1016/j.rse.2019.03.032.

Raihan, T., R. L. Geneve, S. E. Perry, and C. M. Rodriguez Lopez (Dec. 2021). "The Regulation of Plant Vegetative Phase Transition and Rejuvenation: miRNAs, a Key Regulator". en. In: *Epigenomes* 5.4. Number: 4 Publisher: Multidisciplinary Digital Publishing Institute, p. 24. ISSN: 2075-4655. DOI: 10.3390/epigenomes5040024.

Rana, F., S. Siddiqui, and Z. ul-Haq (Aug. 2023). "Investigating the Spatiotemporal Distributions of NO2, SO2 and Their Association with NDVI in Lahore (Pakistan) and Its Adjoining Region of Punjab (India)". en. In: *Journal of the Indian Society of Remote Sensing* 51.8, pp. 1683–1696. ISSN: 0974-3006. DOI: 10.1007/s12524-023-01726-9.

Rankenberg, T., B. Geldhof, H. van Veen, K. Holsteens, B. Van de Poel, and R. Sasidharan (July 2021). "Age-Dependent Abiotic Stress Resilience in Plants". en. In: *Trends in Plant Science* 26.7, pp. 692–705. ISSN: 13601385. DOI: 10.1016/j.tplants.2020.12.016.

Refice, A., D. Capolongo, G. Pasquariello, A. D'Addabbo, F. Bovenga, R. Nutricato, F. P. Lovergine, and L. Pietranera (July 2014). "SAR and InSAR for Flood Monitoring: Examples With COSMO-SkyMed Data". In: *IEEE Journal of Selected Topics in Applied Earth Observations and Remote Sensing* 7.7. Conference Name: IEEE Journal of Selected Topics in Applied Earth Observations and Remote Sensing, pp. 2711–2722. ISSN: 2151-1535. DOI: 10.1109/JSTARS.2014.2305165.

Robock, A. (2000). "Volcanic eruptions and climate". en. In: *Reviews of Geophysics* 38.2. _eprint: https://onlinelibrary.wiley.com/doi/pdf/10.1029/1998RG000054, pp. 191–219. ISSN: 1944-9208. DOI: 10.1029/1998RG000054.

Romero, J. E., D. Morgavi, F. Arzilli, R. Daga, A. Caselli, F. Reckziegel, J. Viramonte, J. Díaz-Alvarado, M. Polacci, M. Burton, and D. Perugini (May 2016). "Eruption dynamics of the 22–23 April 2015 Calbuco Volcano (Southern Chile): Analyses of tephra fall deposits". en. In: *Journal of Volcanology and Geothermal Research* 317, pp. 15–29. ISSN: 0377-0273. DOI: 10.1016/j.jvolgeores.2016.02.027.

Romero, J. E., F. J. Swanson, J. A. Jones, D. Morgavi, G. Giordano, M. Trolese, F. Aguilera, T. Izquierdo, and D. Perugini (Sept. 2023). "The April 2015 Calbuco eruption pyroclastic density currents: deposition, impacts on woody vegetation, and cooling on the northern flank of the cone". en. In: *Andean Geology* 50.3. Number: 3, pp. 319–345. ISSN: 0718-7106. DOI: 10.5027/andgeoV50n3-3650.

Rosch, M. and S. Plank (Jan. 2022). "Detailed Mapping of Lava and Ash Deposits at Indonesian Volcanoes by Means of VHR PlanetScope Change Detection". en. In: *Remote Sensing* 14.5. Number: 5 Publisher: Multidisciplinary Digital Publishing Institute, p. 1168. ISSN: 2072-4292. DOI: 10.3390/rs14051168.

Roy, D., L. Boschetti, and S. Trigg (Jan. 2006). "Remote sensing of fire severity: assessing the performance of the normalized burn ratio". In: *IEEE Geoscience and Remote Sensing Letters* 3.1. Conference Name:

IEEE Geoscience and Remote Sensing Letters, pp. 112–116. ISSN: 1558-0571. DOI: 10.1109/LGRS.2005.858485.

Roy, D. P., H. Huang, R. Houborg, and V. S. Martins (Oct. 2021). "A global analysis of the temporal availability of PlanetScope high spatial resolution multi-spectral imagery". In: *Remote Sensing of Environment* 264, p. 112586. ISSN: 0034-4257. DOI: 10.1016/j.rse.2021.112586.

Rudorff, B. F. T., C. L. Mulchi, E. H. Lee, R. A. Rowland, and C. S. T. Daughtry (Sept. 1995). "Effects of O3 and SO2 on leaf characteristics in soybeans grown under ambient- and enriched-carbon dioxide atmosphere". In: *Air Toxics and Water Monitoring*. Vol. 2503. SPIE, pp. 89–100. DOI: 10.1117/12.221087.

Santin-Janin, H., M. Garel, J.-L. Chapuis, and D. Pontier (June 2009). "Assessing the performance of NDVI as a proxy for plant biomass using non-linear models: a case study on the Kerguelen archipelago". en. In: *Polar Biology* 32.6, pp. 861–871. ISSN: 1432-2056. DOI: 10.1007/s00300-009-0586-5.

Seiler, R., I. Hajdas, M. Saurer, N. Houlié, R. D'Arrigo, J. W. Kirchner, and P. Cherubini (2021). "Tree-ring stable isotopes and radiocarbon reveal pre- and post-eruption effects of volcanic processes on trees on Mt. Etna (Sicily, Italy)". en. In: *Ecohydrology* 14.8, e2340. ISSN: 1936-0592. DOI: 10.1002/eco.2340.

Self, S. (Aug. 2006). "The effects and consequences of very large explosive volcanic eruptions". In: *Philosophical Transactions of the Royal Society A: Mathematical, Physical and Engineering Sciences* 364.1845. Publisher: Royal Society, pp. 2073–2097. DOI: 10.1098/rsta.2006.1814.

Shatto, C., M. Kiene, P. Hofmann, A. Walentowitz, V. Wilkens, T. Heuser, and F. Weiser (Nov. 2024). "Assessing the recovery of *Pinus canariensis* stands after wildfires and volcanic eruption on La Palma, Canary Islands". In: *Forest Ecology and Management* 572, p. 122317. ISSN: 0378-1127. DOI: 10.1016/j.foreco.2024.122317.

Shimazaki, K.-i., T. Sakaki, N. Kondo, and K. Sugahara (Dec. 1980). "Active oxygen participation in chlorophyll destruction and lipid peroxidation in SO2-fumigated leaves of spinach". In: *Plant and Cell Physiology* 21.8, pp. 1193–1204. ISSN: 0032-0781. DOI: 10.1093/oxfordjournals.pcp.a076118.

Sigurdsson, H., S. N. Carey, and J. M. Espindola (Dec. 1984). "The 1982 eruptions of El Chichón Volcano, Mexico: Stratigraphy of pyroclastic deposits". In: *Journal of Volcanology and Geothermal Research* 23.1, pp. 11–37. ISSN: 0377-0273. DOI: 10.1016/0377-0273(84)90055-6.

Sigurdsson, H. (1982). "Volcanic pollution and climate: The 1783 Laki eruption". en. In: *Eos, Transactions American Geophysical Union* 63.32, pp. 601–602. ISSN: 2324-9250. DOI: 10.1029/EO063i032p00601.

Silva, C. R., A. E. Olthoff, J. A. D. de la Mata, and A. P. Alonso (2013). "Remote monitoring of forest insect defoliation. A review". In: *Forest Systems* 22.3. Publisher: Instituto Nacional de Investigación y Tecnología Agraria y Alimentaria (INIA), pp. 377–391.

Simkin, T. (Jan. 1983). "Krakatau, 1883: The Volcanic Eruption And Its Effects". In: *Books by Alumni*.

Slaton, M. R., E. Raymond Hunt Jr., and W. K. Smith (2001). "Estimating near-infrared leaf reflectance from leaf structural characteristics". en. In: *American Journal of Botany* 88.2. _eprint: https://onlinelibrary.wiley.com/doi/pdf/10.2307/2657019, pp. 278–284. ISSN: 1537-2197. DOI: 10.2307/2657019.

Small, D. (Aug. 2011). "Flattening Gamma: Radiometric Terrain Correction for SAR Imagery". In: *IEEE Transactions on Geoscience and Remote Sensing* 49.8. Conference Name: IEEE Transactions on Geoscience and Remote Sensing, pp. 3081–3093. ISSN: 1558-0644. DOI: 10.1109/TGRS.2011.2120616.

Smathers, G. A. and D. Mueller-Dombois (1972). *Invasion and Recovery of Vegetation After a Volcanic Eruption in Hawaii*. en. Google-Books-ID: 2c89AAAAIAAJ. Department of Botany, University of Hawaii.

Smith, S. J., H. Pitcher, and T. M. L. Wigley (May 2001). "Global and regional anthropogenic sulfur dioxide emissions". In: *Global and Planetary Change* 29.1, pp. 99–119. ISSN: 0921-8181. DOI: 10.1016/S0921-8181(00)00057-6.

Smith, T. and N. Boers (Jan. 2023). "Global vegetation resilience linked to water availability and variability". en. In: *Nature Communications* 14.1, p. 498. ISSN: 2041-1723. DOI: 10.1038/s41467-023-36207-7.

Smith, T., D. Traxl, and N. Boers (May 2022). "Empirical evidence for recent global shifts in vegetation resilience". en. In: *Nature Climate Change* 12.5. Publisher: Nature Publishing Group, pp. 477–484. ISSN: 1758-6798. DOI: 10.1038/s41558-022-01352-2.

Smith, W. H. (1981). *Air pollution and forests: interactions between air contaminants and forest ecosystems*. eng. Springer series on environmental management. New York: Springer-Verlag. ISBN: 978-0-387-90501-3.

Solikhin, A., J.-C. Thouret, S. C. Liew, A. Gupta, D. S. Sayudi, J.-F. Oehler, and Z. Kassouk (Feb. 2015). "High-spatial-resolution imagery helps map deposits of the large (VEI 4) 2010 Merapi Volcano eruption and their impact". en. In: *Bulletin of Volcanology* 77.3, p. 20. ISSN: 1432-0819. DOI: 10.1007/s00445-015-0908-0.

Song, C. (Feb. 2013). "Optical remote sensing of forest leaf area index and biomass". en. In: *Progress in Physical Geography: Earth and Environment* 37.1. Publisher: SAGE Publications Ltd, pp. 98–113. ISSN: 0309-1333. DOI: 10.1177/0309133312471367.

Spruce, J. P., S. Sader, R. E. Ryan, J. Smoot, P. Kuper, K. Ross, D. Prados, J. Russell, G. Gasser, R. McKellip, and W. Hargrove (Feb. 2011). "Assessment of MODIS NDVI time series data products for detecting forest defoliation by gypsy moth outbreaks". In: *Remote Sensing of Environment* 115.2, pp. 427–437. ISSN: 0034-4257. DOI: 10.1016/j.rse.2010.09.013.

Stoiber, R. E., S. N. Williams, and B. J. Huebert (1986). "Sulfur and halogen gases at Masaya Caldera Complex, Nicaragua: Total flux and variations with time". en. In: *Journal of Geophysical Research: Solid Earth* 91.B12, pp. 12215–12231. ISSN: 2156-2202. DOI: 10.1029/JB091iB12p12215.

Stothers, R. B. (Jan. 1996). "The great dry fog of 1783". en. In: *Climatic Change* 32.1, pp. 79–89. ISSN: 1573-1480. DOI: 10.1007/BF00141279.

Swanson, F. J., J. A. Jones, C. M. Crisafulli, and A. Lara (Apr. 2013). "Effects of volcanic and hydrologic processes on forest vegetation: Chaitén Volcano, Chile". en. In: *Andean Geology* 40.2. Number: 2, pp. 359–391. ISSN: 0718-7106. DOI: 10.5027/andgeoV40n2-a10.

Swanson, F. J. and J. J. Major (Jan. 2005). "Physical Events, Environments, and Geological—Ecological Interactions at Mount St. Helens: March 1980–2004". In: *Ecological Responses to the 1980 Eruption of Mount St. Helens*. Springer New York, NY, pp. 27–44. ISBN: 978-0-387-23868-5. DOI: 10.1007/0-387-28150-9_3.

Syahbana, D. K., K. Kasbani, G. Suantika, O. Prambada, A. S. Andreas, U. B. Saing, S. L. Kunrat, S. Andreastuti, M. Martanto, E. Kriswati, Y. Suparman, H. Humaida, S. Ogburn, P. J. Kelly, J. Wellik, H. M. N. Wright, J. D. Pesicek, R. Wessels, C. Kern, M. Lisowski, A. Diefenbach, M. Poland, F. Beauducel, J. Pallister, R. G. Vaughan, and J. B. Lowenstern (June 2019). "The 2017–19 activity at Mount Agung in Bali (Indonesia): Intense unrest, monitoring, crisis response, evacuation, and eruption". en. In: *Scientific Reports* 9.1, p. 8848. ISSN: 2045-2322. DOI: 10.1038/s41598-019-45295-9.

Symonds, R. B., W. I. Rose, G. J. S. Bluth, and T. M. Gerlach (Dec. 1994). "Chapter 1. VOLCANIC-GAS STUDIES: METHODS, RESULTS, AND APPLICATIONS". en. In: *Volatiles in Magmas*. Ed. by family=Carroll, familyi=C., given=Michael R., giveni=M. R.family=Holloway, familyi=H., given=John R., giveni=J. R. De Gruyter, pp. 1–66. ISBN: 978-1-5015-0967-4. DOI: 10.1515/9781501509674-007.

Tagawa, H. (Oct. 1992). "Primary succession and the effect of first arrivals on subsequent development of forest types". en. In: *GeoJournal* 28.2, pp. 175–183. ISSN: 1572-9893. DOI: 10.1007/BF00177231.

Tang, L., Q. Lei, W. Liu, X. Chen, Y. Zhang, X. Cai, and F. Chen (Feb. 2021). "Optimization of Multi-Ecosystem Model Ensembles to Simulate Vegetation Growth at the Global Scale". In: *IEEE Transactions on Geoscience and Remote Sensing* 59.2. Conference Name: IEEE Transactions on Geoscience and Remote Sensing, pp. 962–978. ISSN: 1558-0644. DOI: 10.1109/TGRS.2020.2993641.

Teltscher, K. and F. E. Fassnacht (Sept. 2018). "Using multispectral landsat and sentinel-2 satellite data to investigate vegetation change at Mount St. Helens since the great volcanic eruption in 1980". en. In: *Journal of Mountain Science* 15.9, pp. 1851–1867. ISSN: 1993-0321. DOI: 10.1007/s11629-018-4869-6.

Thiel, C. and C. Schmullius (Feb. 2016). "The potential of ALOS PALSAR backscatter and InSAR coherence for forest growing stock volume estimation in Central Siberia". en. In: *Remote Sensing of Environment* 173, pp. 258–273. ISSN: 0034-4257. DOI: 10.1016/j.rse.2015.10.030.

Thomas, M. D. and G. R. Hill (Apr. 1935). "ABSORPTION OF SULPHUR DIOXIDE BY ALFALFA AND ITS RELATION TO LEAF INJURY1". In: *Plant Physiology* 10.2, pp. 291–307. ISSN: 0032-0889.

Thordarson, T. and S. Self (2003). "Atmospheric and environmental effects of the 1783–1784 Laki eruption: A review and reassessment". en. In: *Journal of Geophysical Research: Atmospheres* 108.D1. _eprint: https://onlinelibrary.wiley.com/doi/pdf/10.1029/2001JD002042, AAC 7–1–AAC 7–29. ISSN: 2156-2202. DOI: 10.1029/2001JD002042.

Thouret, J.-C., K. E. Abdurachman, J.-L. Bourdier, and S. Bronto (June 1998). "Origin, characteristics, and behaviour of lahars following the 1990 eruption of Kelud volcano, eastern Java (Indonesia)". en. In: *Bulletin of Volcanology* 59.7, pp. 460–480. ISSN: 0258-8900, 1432-0819. DOI: 10.1007/s004450050204.

Tian, F., R. Fensholt, J. Verbesselt, K. Grogan, S. Horion, and Y. Wang (June 2015). "Evaluating temporal consistency of long-term global NDVI datasets for trend analysis". en. In: *Remote Sensing of Environment* 163, pp. 326–340. ISSN: 0034-4257. DOI: 10.1016/j.rse.2015.03.031.

Tomsche, L., A. Marsing, T. Jurkat-Witschas, J. Lucke, S. Kaufmann, K. Kaiser, J. Schneider, M. Scheibe, H. Schlager, L. Röder, H. Fischer, F. Obersteiner, A. Zahn, M. Zöger, J. Lelieveld, and C. Voigt (Nov. 2022). "Enhanced sulfur in the upper troposphere and lower stratosphere in spring 2020". English. In: *Atmospheric Chemistry and Physics* 22.22. Publisher: Copernicus GmbH, pp. 15135–15151. ISSN: 1680-7316. DOI: 10.5194/acp-22-15135-2022.

Torres, R., P. Snoeij, D. Geudtner, D. Bibby, M. Davidson, E. Attema, P. Potin, B. Rommen, N. Floury, M. Brown, I. N. Traver, P. Deghaye, B. Duesmann, B. Rosich, N. Miranda, C. Bruno, M. L'Abbate, R. Croci, A. Pietropaolo, M. Huchler, and F. Rostan (May 2012). "GMES Sentinel-1 mission". en. In: *Remote Sensing of Environment*. The Sentinel Missions - New Opportunities for Science 120, pp. 9–24. ISSN: 0034-4257. DOI: 10.1016/j.rse.2011.05.028.

Tortini, R., S. M. van Manen, B. R. B. Parkes, and S. A. Carn (July 2017). "The impact of persistent volcanic degassing on vegetation: A case study at Turrialba volcano, Costa Rica". In: *International Journal of Applied Earth Observation and Geoinformation* 59, pp. 92–103. ISSN: 1569-8432. DOI: 10.1016/j.jag.2017.03.002.

Trabaud, L. (1987). "Dynamics after fire of sclerophyllous plant communities in the mediterranean basin". eng. In: Publisher: Persée - Portail des revues scientifiques en SHS. DOI: 10.3406/ecmed.1987.1186.

Treuhaft, R. N., S. N. Madsen, M. Moghaddam, and J. J. v. Zyl (Nov. 1996). "Vegetation characteristics and underlying topography from interferometric radar". In: *Radio Science* 31.6. Conference Name: Radio Science, pp. 1449–1485. ISSN: 1944-799X. DOI: 10.1029/96RS01763.

Turner, M. G., V. H. Dale, and E. H. Everham (1997). "Fires, Hurricanes, and Volcanoes: Comparing Large Disturbances". In: *BioScience* 47.11. Publisher: [American Institute of Biological Sciences, Oxford University Press], pp. 758–768. ISSN: 0006-3568. DOI: 10.2307/1313098.

Udy, M. L., S. K. Ebmeier, S. F. L. Watt, A. Hooper, and A. Paredes (Nov. 2024). "Satellite measurement of forest disturbance, recovery and deposit distribution following explosive volcanic eruptions". In: *Journal of Volcanology and Geothermal Research* 455, p. 108204. ISSN: 0377-0273. DOI: 10.1016/j.jvolgeores.2024.108204.

Urbazaev, M., C. Thiel, M. Migliavacca, M. Reichstein, P. Rodriguez-Veiga, and C. Schmullius (Aug. 2016). "Improved Multi-Sensor Satellite-Based Aboveground Biomass Estimation by Selecting Temporally Stable Forest Inventory Plots Using NDVI Time Series". en. In: *Forests* 7.8. Number: 8 Publisher: Multidisciplinary Digital Publishing Institute, p. 169. ISSN: 1999-4907. DOI: 10.3390/f7080169.

Ustin, S. L. and S. Jacquemoud (2020). "How the Optical Properties of Leaves Modify the Absorption and Scattering of Energy and Enhance Leaf Functionality". en. In: *Remote Sensing of Plant Biodiversity*. Ed. by family=Cavender-Bares, familyi=C.-B., given=Jeannine, giveni=J.family=Gamon, familyi=G., given=John A., giveni=J. A.family=Townsend, familyi=T., given=Philip A., giveni=P. A. Cham: Springer International Publishing, pp. 349–384. ISBN: 978-3-030-33156-6 978-3-030-33157-3. DOI: 10.1007/978-3-030-33157-3_14.

Ustin, S. L. and E. M. Middleton (Jan. 2021). "Current and near-term advances in Earth observation for ecological applications". In: *Ecological Processes* 10.1, p. 1. ISSN: 2192-1709. DOI: 10.1186/s13717-020-00255-4.

Vaglio Laurin, G., F. Pirotti, M. Callegari, Q. Chen, G. Cuozzo, E. Lingua, C. Notarnicola, and D. Papale (Jan. 2017). "Potential of ALOS2 and NDVI to Estimate Forest Above-Ground Biomass, and Comparison with Lidar-Derived Estimates". en. In: *Remote Sensing* 9.1. Number: 1 Publisher: Multidisciplinary Digital Publishing Institute, p. 18. ISSN: 2072-4292. DOI: 10.3390/rs9010018.

Van Eaton, A. R., Á. Amigo, D. Bertin, L. G. Mastin, R. E. Giacosa, J. González, O. Valderrama, K. Fontijn, and S. A. Behnke (2016). "Volcanic lightning and plume behavior reveal evolving hazards during the April 2015 eruption of Calbuco volcano, Chile". en. In: *Geophysical Research Letters* 43.7, pp. 3563–3571. ISSN: 1944-8007. DOI: 10.1002/2016GL068076.

Varekamp, J. C., J. F. Luhr, and K. L. Prestegaard (Dec. 1984). "The 1982 eruptions of El Chichón Volcano (Chiapas, Mexico): Character of the eruptions, ash-fall deposits, and gasphase". In: *Journal of Volcanology and Geothermal Research* 23.1, pp. 39–68. ISSN: 0377-0273. DOI: 10.1016/0377-0273(84)90056-8.

Veloso, A., S. Mermoz, A. Bouvet, T. Le Toan, M. Planells, J.-F. Dejoux, and E. Ceschia (Sept. 2017). "Understanding the temporal behavior of crops using Sentinel-1 and Sentinel-2-like data for agricul-

tural applications". en. In: *Remote Sensing of Environment* 199, pp. 415–426. ISSN: 0034-4257. DOI: 10.1016/j.rse.2017.07.015.

Veraverbeke, S., I. Gitas, T. Katagis, A. Polychronaki, B. Somers, and R. Goossens (Mar. 2012). "Assessing post-fire vegetation recovery using red–near infrared vegetation indices: Accounting for background and vegetation variability". In: *ISPRS Journal of Photogrammetry and Remote Sensing* 68, pp. 28–39. ISSN: 0924-2716. DOI: 10.1016/j.isprsjprs.2011.12.007.

Vermote, E., C. Justice, M. Claverie, and B. Franch (Nov. 2016). "Preliminary analysis of the performance of the Landsat 8/OLI land surface reflectance product". en. In: *Remote Sensing of Environment*. Landsat 8 Science Results 185, pp. 46–56. ISSN: 0034-4257. DOI: 10.1016/j.rse.2016.04.008.

Viedma, O., J. Meliá, D. Segarra, and J. Garcia-Haro (Sept. 1997). "Modeling rates of ecosystem recovery after fires by using landsat TM data". In: *Remote Sensing of Environment* 61.3, pp. 383–398. ISSN: 0034-4257. DOI: 10.1016/S0034-4257(97)00048-5.

Watt, S. F. L., D. M. Pyle, T. A. Mather, R. S. Martin, and N. E. Matthews (2009). "Fallout and distribution of volcanic ash over Argentina following the May 2008 explosive eruption of Chaitén, Chile". en. In: *Journal of Geophysical Research: Solid Earth* 114.B4. ISSN: 2156-2202. DOI: 10.1029/2008JB006219.

Wegmuller, U. and C. Werner (Jan. 1997). "Retrieval of vegetation parameters with SAR interferometry". In: *IEEE Transactions on Geoscience and Remote Sensing* 35.1. Conference Name: IEEE Transactions on Geoscience and Remote Sensing, pp. 18–24. ISSN: 1558-0644. DOI: 10.1109/36.551930.

Weiser, F., E. Baumann, A. Jentsch, F. M. Medina, M. Lu, M. Nogales, and C. Beierkuhnlein (Feb. 2022). "Impact of Volcanic Sulfur Emissions on the Pine Forest of La Palma, Spain". en. In: *Forests* 13.2. Number: 2 Publisher: Multidisciplinary Digital Publishing Institute, p. 299. ISSN: 1999-4907. DOI: 10.3390/f13020299.

Werner, C., U. Wegmüller, T. Strozzi, and A. Wiesmann (2000). "GAMMA SAR AND INTERFEROMETRIC PROCESSING SOFTWARE". en. In.

Werner, C., M. Schmid, T. A. Ehlers, J. P. Fuentes-Espoz, J. Steinkamp, M. Forrest, J. Liakka, A. Maldonado, and T. Hickler (Oct. 2018). "Effect of changing vegetation and precipitation on denudation – Part 1: Predicted vegetation composition and cover over the last 21 thousand years along the Coastal Cordillera of Chile". English. In: *Earth Surface Dynamics* 6.4. Publisher: Copernicus GmbH, pp. 829–858. ISSN: 2196-6311. DOI: 10.5194/esurf-6-829-2018.

White, J. D., K. C. Ryan, C. C. Key, and S. W. Running (1996). "Remote Sensing of Forest Fire Severity and Vegetation Recovery". en. In: *International Journal of Wildland Fire* 6.3. Publisher: CSIRO PUBLISHING, pp. 125–136. ISSN: 1448-5516. DOI: 10.1071/wf9960125.

Whittaker, R. J., M. B. Bush, and K. Richards (1989). "Plant Recolonization and Vegetation Succession on the Krakatau Islands, Indonesia". en. In: *Ecological Monographs* 59.2, pp. 59–123. ISSN: 1557-7015. DOI: 10.2307/2937282.

Whitty, R. C. W., M. A. Pfeffer, E. Ilyinskaya, T. J. Roberts, A. Schmidt, S. Barsotti, W. Strauch, L. R. Crilley, F. D. Pope, H. Bellanger, E. Mendoza, T. A. Mather, E. J. Liu, N. Peters, I. A. Taylor, H. Francis, X. Hernández Leiva, D. Lynch, S. Norbert, and P. Baxter (Feb. 2022). "Effectiveness of low-cost air quality monitors for identifying volcanic SO and PM downwind from Masaya volcano, Nicaragua". en. In: *Volcanica* 5.1. Number: 1 Publisher: Volcanica, pp. 33–59.

Williams-Jones, G., H. Rymer, and D. A. Rothery (Apr. 2003). "Gravity changes and passive SO2 degassing at the Masaya caldera complex, Nicaragua". In: *Journal of Volcanology and Geothermal Research*. Volcanic hazards: Monitoring, prediction and mitigation 123.1, pp. 137–160. ISSN: 0377-0273. DOI: 10.1016/S0377-0273(03)00033-7.

Wilson, T. M., J. W. Cole, C. Stewart, S. J. Cronin, and D. M. Johnston (Apr. 2011). "Ash storms: impacts of wind-remobilised volcanic ash on rural communities and agriculture following the 1991 Hudson eruption, southern Patagonia, Chile". en. In: *Bulletin of Volcanology* 73.3, pp. 223–239. ISSN: 1432-0819. DOI: 10.1007/s00445-010-0396-1.

Wilson, T. M., S. Jenkins, and C. Stewart (Jan. 2015). "Chapter 3 - Impacts from Volcanic Ash Fall". en. In: *Volcanic Hazards, Risks and Disasters*. Ed. by family=Shroder, familyi=S., given=John F., giveni=J. F.family=Papale, familyi=P., given=Paolo, giveni=P. Hazards and Disasters Series. Boston: Elsevier, pp. 47–86. ISBN: 978-0-12-396453-3. DOI: 10.1016/B978-0-12-396453-3.00003-4.

Wilson, T. M., C. Stewart, H. Bickerton, P. Baxter, A. V. Outes, G. Villarosa, and E. Rovere (Jan. 2013). *Impacts of the June 2011 Puyehue-Cordón Caulle volcanic complex eruption on urban infrastructure, agriculture and public health*. eng. Accepted: 2019-06-12T19:27:36Z ISSN: 1177-2425. Institute of Geology and Nucelar Sciences. ISBN: 978-1-972192-02-3.

Winner, W. E. and C. J. Atkinson (July 1986). "Absorption of air pollution by plants, and consequences for growth". eng. In: *Trends in Ecology & Evolution* 1.1, pp. 15–18. ISSN: 0169-5347. DOI: 10.1016/0169-5347(86)90061-3.

Winner, W. E. and J. D. Bewley (Jan. 1978). "Terrestrial mosses as bioindicators of SO2 pollution stress". en. In: *Oecologia* 35.2, pp. 221–230. ISSN: 1432-1939. DOI: 10.1007/BF00344733.

Woodhouse, I. H., A. Marino, and I. Cameron (Dec. 2011). "A standard index of spatial resolution for distributed targets in synthetic aperture radar imagery". en. In: *International Journal of Remote Sensing* 32.23, pp. 7929–7938. ISSN: 0143-1161, 1366-5901. DOI: 10.1080/01431161.2010.502546.

Woodhouse, I. H. (Jan. 2017). *Introduction to Microwave Remote Sensing*. Boca Raton: CRC Press. ISBN: 978-1-315-27257-3. DOI: 10.1201/9781315272573.

Wright, J. S. (Jan. 2002). "Plant diversity in tropical forests: a review of mechanisms of species coexistence". en. In: *Oecologia* 130.1, pp. 1–14. ISSN: 0029-8549, 1432-1939. DOI: 10.1007/s004420100809.

Xi, X., M. S. Johnson, S. Jeong, M. Fladeland, D. Pieri, J. A. Diaz, and G. L. Bland (Oct. 2016). "Constraining the sulfur dioxide degassing flux from Turrialba volcano, Costa Rica using unmanned aerial system measurements". In: *Journal of Volcanology and Geothermal Research* 325, pp. 110–118. ISSN: 0377-0273. DOI: 10.1016/j.jvolgeores.2016.06.023.

Xu, H. (July 2006). "Modification of normalised difference water index (NDWI) to enhance open water features in remotely sensed imagery". In: *International Journal of Remote Sensing* 27.14. Publisher: Taylor & Francis, pp. 3025–3033. ISSN: 0143-1161. DOI: 10.1080/01431160600589179.

Yagüe-Martínez, N., P. Prats-Iraola, F. Rodríguez González, R. Brcic, R. Shau, D. Geudtner, M. Eineder, and R. Bamler (Apr. 2016). "Interferometric Processing of Sentinel-1 TOPS Data". In: *IEEE Transactions on Geoscience and Remote Sensing* 54.4. Conference Name: IEEE Transactions on Geoscience and Remote Sensing, pp. 2220–2234. ISSN: 1558-0644. DOI: 10.1109/TGRS.2015.2497902.

Yamaguchi, M., M. Watanabe, C. Tabe, J. Naba, H. Matsumura, Y. Kohno, and T. Izuta (Dec. 2012). "Effects of sulfur dioxide on growth and net photosynthesis of six Japanese forest tree species grown under different nitrogen loads". en. In: *Trees* 26.6, pp. 1859–1874. ISSN: 1432-2285. DOI: 10.1007/s00468-012-0755-y.

Yoo, J.-M., Y.-R. Lee, D. Kim, M.-J. Jeong, W. R. Stockwell, P. K. Kundu, S.-M. Oh, D.-B. Shin, and S.-J. Lee (Jan. 2014). "New indices for wet scavenging of air pollutants (O3, CO, NO2, SO2, and PM10) by summertime rain". In: *Atmospheric Environment* 82, pp. 226–237. ISSN: 1352-2310. DOI: 10.1016/j.atmosenv.2013.10.022.

Yun, S.-H., K. Hudnut, S. Owen, F. Webb, M. Simons, P. Sacco, E. Gurrola, G. Manipon, C. Liang, E. Fielding, P. Milillo, H. Hua, and A. Coletta (Nov. 2015). "Rapid Damage Mapping for the 2015 Mw 7.8 Gorkha Earthquake Using Synthetic Aperture Radar Data from COSMO–SkyMed and ALOS-2 Satellites". In: *Seismological Research Letters* 86.6, pp. 1549–1556. ISSN: 0895-0695. DOI: 10.1785/0220150152.

Zebker, H., a. J. Villasenor, H. A. Zebker, and H. A. Zebker (1992). *Decorrelation in Interferometric Radar Echoes*.

Zhang, J., C. Han, and Y. Li (Aug. 2010). "The effects of sulphur dioxide on the spectral curves and chlorophyll concentration of rice canopy". In: *International Journal of Remote Sensing* 31.16. Publisher: Taylor & Francis _eprint: https://doi.org/10.1080/01431160903232816, pp. 4257–4264. ISSN: 0143-1161. DOI: 10.1080/01431160903232816.

Zhao, Q., L. Yu, Z. Du, D. Peng, P. Hao, Y. Zhang, and P. Gong (Jan. 2022). "An Overview of the Applications of Earth Observation Satellite Data: Impacts and Future Trends". en. In: *Remote Sensing*

14.8. Number: 8 Publisher: Multidisciplinary Digital Publishing Institute, p. 1863. ISSN: 2072-4292. DOI: 10.3390/rs14081863.

Zhu, Z., C. E. Woodcock, and P. Olofsson (July 2012). "Continuous monitoring of forest disturbance using all available Landsat imagery". en. In: *Remote Sensing of Environment*. Landsat Legacy Special Issue 122, pp. 75–91. ISSN: 0034-4257. DOI: 10.1016/j.rse.2011.10.030.

Zobel, D. B. and J. A. Antos (1997). "A Decade of Recovery of Understory Vegetation Buried by Volcanic Tephra from Mount St. Helens". en. In: *Ecological Monographs* 67.3, pp. 317–344. ISSN: 1557-7015. DOI: 10.1890/0012-9615(1997)067[0317:ADOROU]2.0.CO;2.

Appendix A

Supplementary information: Chapter 2

A.1 SAR processing flow chart

A.2 Study areas

We use five sites around Calbuco to illustrate the impact of different volcanic deposits on vegetation and recovery rates, we selected 3 areas impacted by tephra fall, at increasing distances from the vent and decreasing tephra thickness. The most proximal tephra fall area, shown in light blue, is 3 km to the north east of the vent (83 by 134 pixels, 1.2 km^2), between the 30 cm and 60 cm isopach from SERNAGEOMIN in Hayes (2019). The medial tephra fall area, in dark blue, is 5 km to the north east of the vent (56 by 78 pixels, 0.5 km^2) going through the 30 cm isopach. The most distal tephra fall area, shown in purple, is 8 km away from the vent (56 by 78 pixels, 0.5 km^2) between the 20 cm and 30 cm isopach. We define an area impacted by channelised PDC deposition 3.7 km away from the vent (14 by 23 pixels, 0.04 km^2). Finally, we select an area not directly impacted by the eruption material, the 'unaffected area' situated in dense forest 12 km to the south east of the volcano (223 by 222 pixels, covering an area of approximately 4 km^2). We select the study areas using the optical imagery to assess for

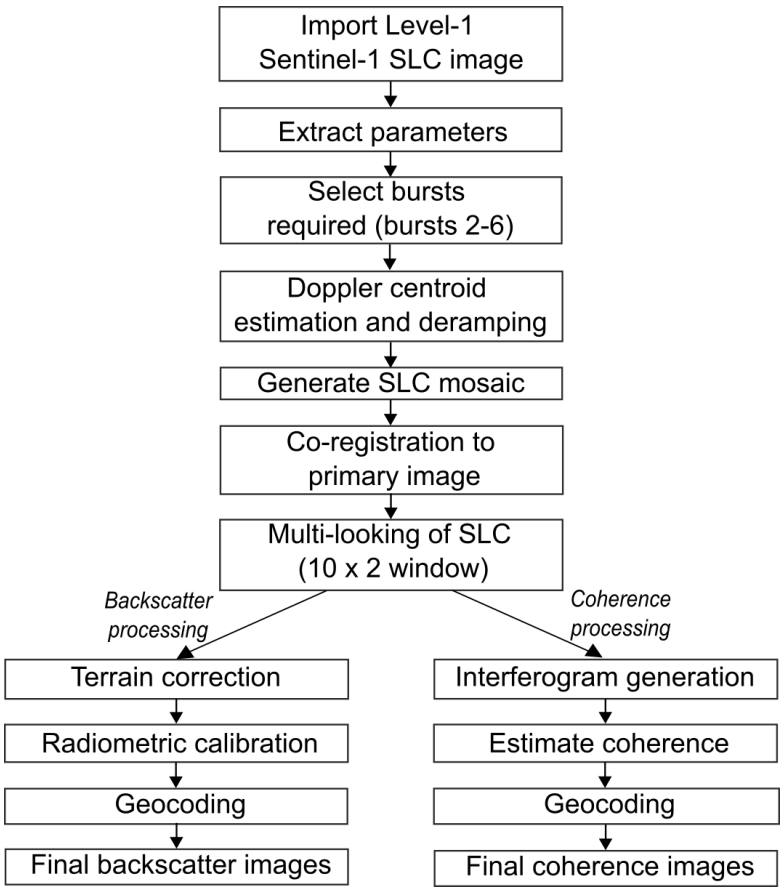

Figure A.1: A flow chart illustrating our SAR processing steps using GAMMA remote sensing software to produce backscatter and coherence images.

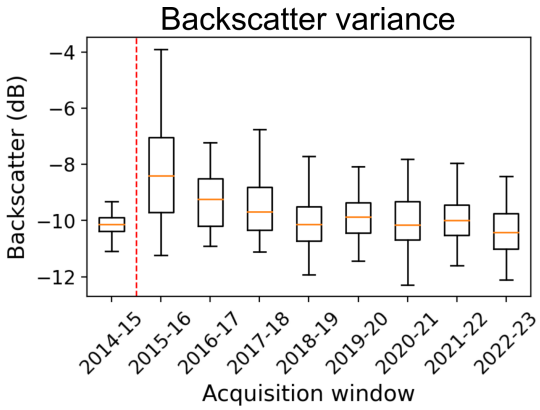

Figure A.2: Backscatter variance changes substantially from pre-eruption to post-eruption. Each box plot represents a year starting from April 2014 (due to the time of the eruption). The pre-eruption variance was 0.15, increasing to 3.18 post-eruption before decreasing with time to around 1.

uniform land surface and to only include pixels impacted by the specified deposit type. As such the PDC region is small to ensure only pixels impacted by the channelised PDC were included, and eliminating pixels at the boundary of the channel. We maximise the possible size of the study areas as we then take the mean value for all pixels within the region, reducing any potential influences from anomalous pixel values e.g. due to cloud cover in the NDVI dataset.

A.3 Backscatter variation

The variation in the backscatter values after the eruption onset (April 2015 - April 2016, variance 3.18) is greater than before the eruption (October 2014 - April 2015, variance 0.15), and although the variance decreases with recovery it does not reach pre-eruption values (April 2016 - June 2023, average variance of 0.89) (Figure A.2). This may be due to structural changes to the vegetation, and would be consistent with the vegetation coverage becoming less homogeneous post-eruption, a change that may not be apparent in the NDVI or the coherence. This increase in post-eruption variance also meant the cluster analysis struggled to form meaningful clusters for the backscatter time series (figure A.3).

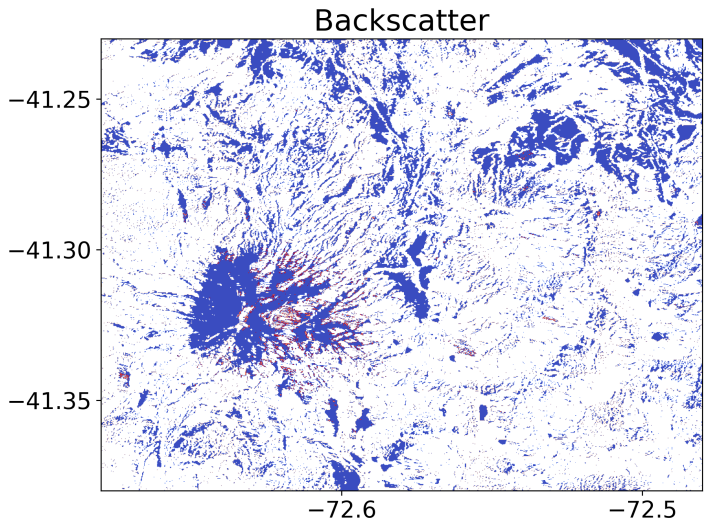

Figure A.3: Clustering of backscatter over the whole time series.

Enclosed isopach thickness (mm)	Thickness (m)	Area (km^2)	$Area^{0.5}$
550	0.55	32.25	5.6789
400	0.4	67.85	8.2371
300	0.3	98.61	9.9303
180	0.18	163.46	12.7851
150	0.15	208.11	14.4260
60	0.06	392.48	19.8111
5	0.005	3854.9	62.0878
4	0.004	14619	120.9091
2	0.002	23756	154.1298
1	0.001	45271	212.7698
0.5	0.0005	87959	296.5788
0.1	0.0001	150683	388.1791

Table A.1: Table of enclosed isopach thickness estimation and $area^{0.5}$.

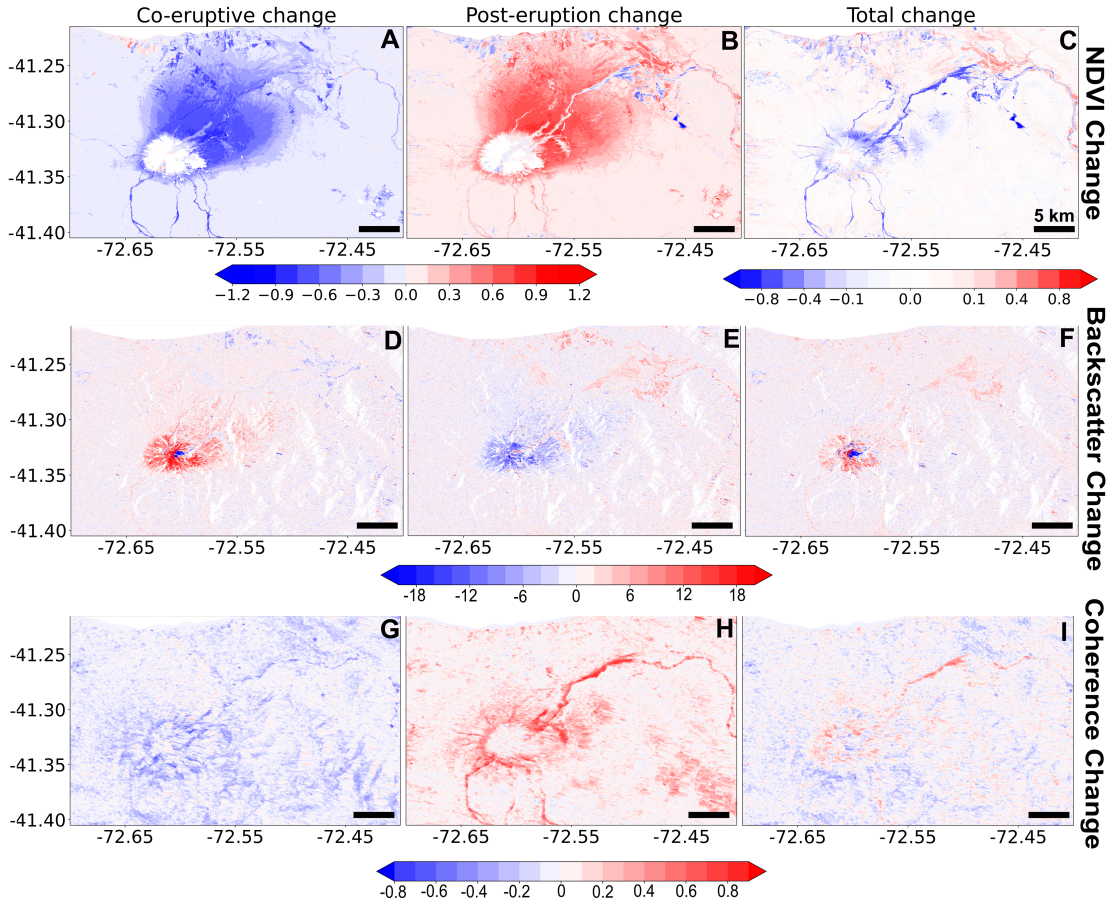

Figure A.4: The difference maps from NDVI, coherence and backscatter (figure 2, 4 and 5 panels E-G) A) NDVI co-eruptive change (26/02/2014 - 27/10/2015), B) NDVI post-eruption change (27/10/2015 - 17/02/2023), C) NDVI total change (26/02/2014 - 17/02/2023), D) co-eruptive backscatter change (23/10/2014 - 15/05/2015), E) post-eruption backscatter change (15/05/2015 - 02/06/2023), F) total backscatter change (23/10/2014 - 02/06/2023), G) co-eruptive 24-day coherence change (23/10/2014 - 08/06/2015), H) post-eruption coherence change (15/05/2015 - 25/05/2021), I) total coherence change (23/10/2014 - 21/01/2023), the dates show the first date of the first acquisition and the last date of the second acquisition, showing the span of time captured by the coherence change.

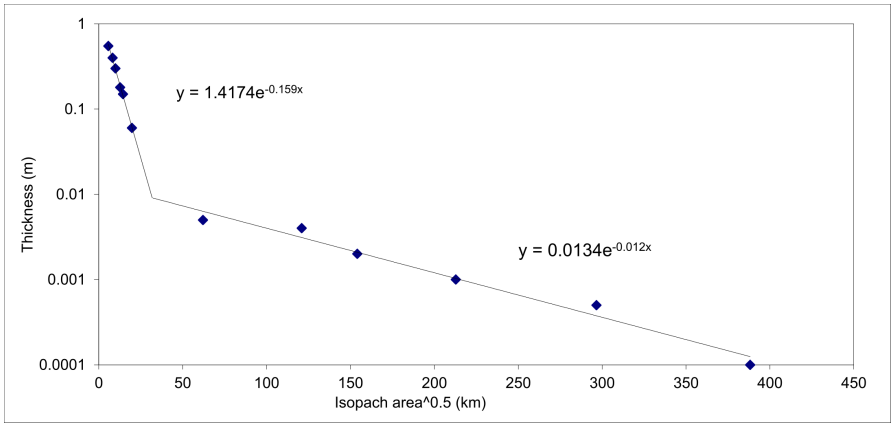

Figure A.5: Graph of thickness vs area for the re-estimated isopachs using the method from Pyle (1989) and Pyle (1995), and based on two exponential segments.

	Proximal segment	Distal segment
T_o	1.4174	0.0134
k	0.159	0.012
T_{last}	0.0091	0.0091
b_t	2.4595	32.5889
V (km^3)		0.1861
Correction base (Pyle 95)	0.1078	0.0108
Used Correction (Pyle 95)		0.0970

Table A.2: Data for proximal and distal segments for volume re-estimation

Final V (km^3)	0.2831
Mass (kg)	339691576742.17
Magnitude	4.5311

Table A.3: Table of resulting values of volume, mass (using nominal density of 1200 kg/m3) and magnitude

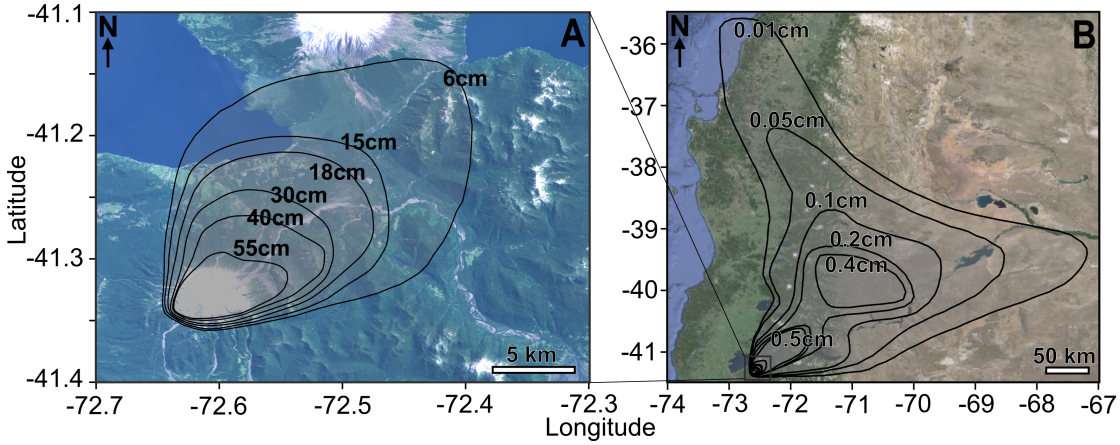

Figure A.6: Our estimated isopachs used to re-estimate the total eruption volume. Isopachs for thicknesses 15 cm and greater have been re-estimated using our cluster analysis, isopachs with thicknesses 6 cm and lower have been taken from (Romero, Morgavi, et al. 2016) A) The proximal isopachs, overlain on Sentinel-2 optical image of Calbuco. B) The distal isopachs from (Romero, Morgavi, et al. 2016), used to re-estimate the eruption volume, overlain on Sentinel-2 optical image.

Appendix B

Supplementary information: Chapter 3

B.1 Comparison to other vegetation indices

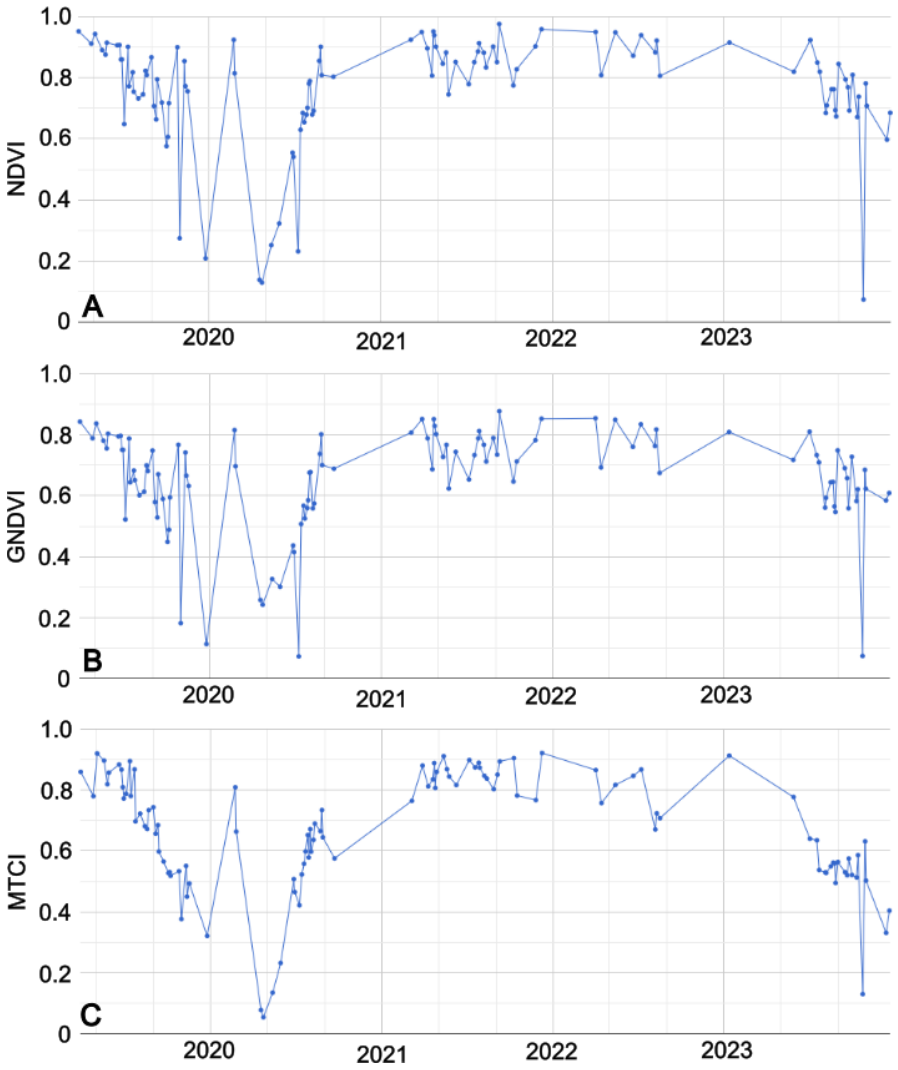

Figure B.1: A comparison of different vegetation indices reported to be beneficial to measure vegetation damage (Hawryło et al. 2018). The time series is for the same area as indicated in 3.3 (to the NE of Sertung island). Panel A) shows the time series for NDVI, B) is the time series for GNDVI, panel C) is the time series for the MTCI.

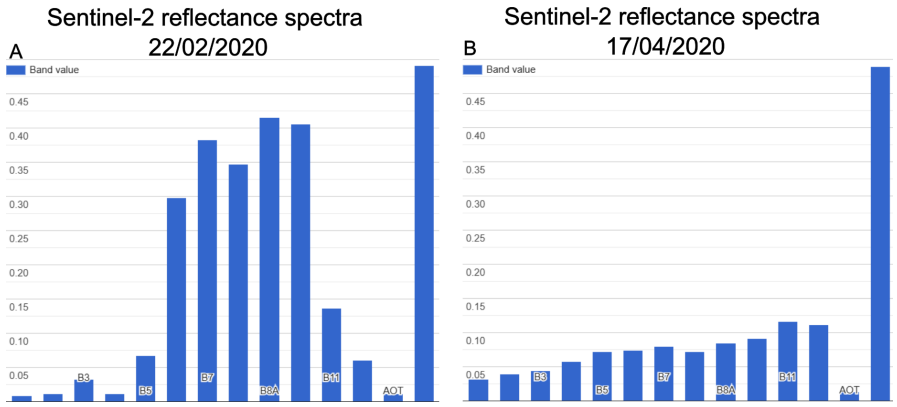

Figure B.2: A comparison of the Sentinel-2 reflectance spectra before (A. 22/02/2020) and after (B. 17/04/2020) the sulphur plume impact on the island of Sertung for bands 1-14.

B.2 Backscatter variance at Turrialba

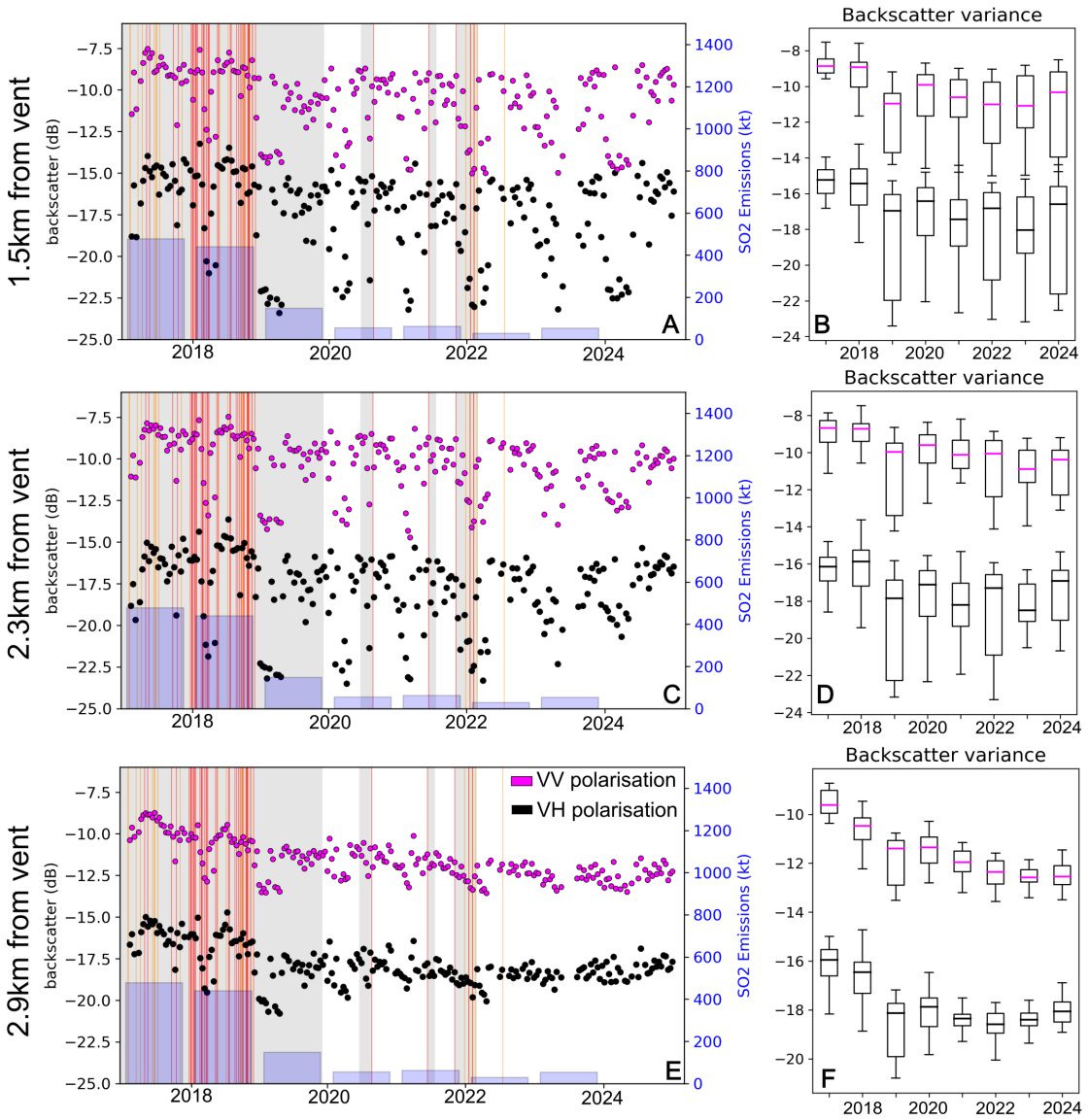

Figure B.3: A) Backscatter time series for VV and VH polarisation backscatter at a location 1.5 km from Turrialba's Crater. B) The backscatter variance for the time series in panel A. C) Backscatter time series for VV and VH polarisation backscatter at a location 2.3 km from Turrialba's Crater. D) The backscatter variance for the time series in panel C. E) Backscatter time series for VV and VH polarisation backscatter at a location 2.9km from Turrialba's Crater. F) The backscatter variance for the time series in panel E.

B.3 Masaya

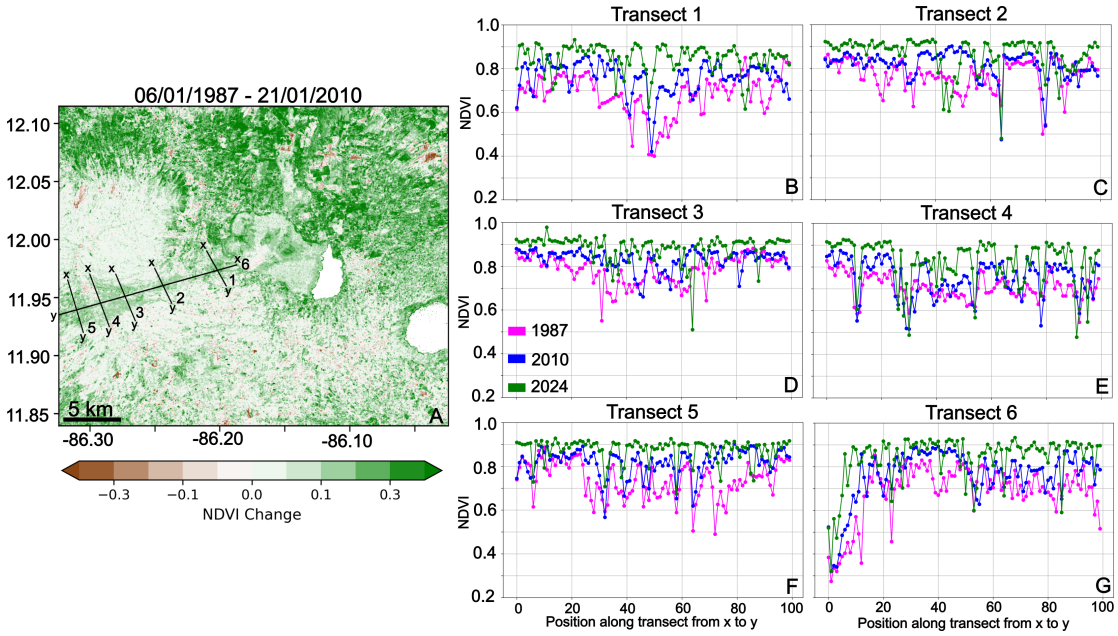

Figure B.4: A) NDVI difference image from 06/01/1987 until 21/01/2010 with locations of 6 transects along the downwind area of damage from Masaya. Panels B-G show the NDVI along transects 1-6, each from x to y showing the changes in NDVI along the transect from 1987, 2010 and 2024.

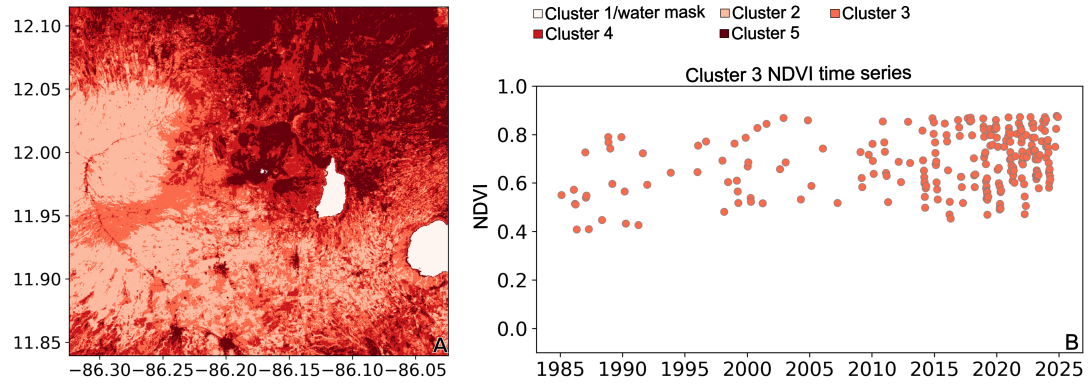

Figure B.5: A) A k-means clustered image over Masaya, all NDVI images are clustered into 5 clusters, of which, cluster 3 highlights the area downwind of Masaya to the SW. B) the NDVI time series for cluster 3.

B.4 Semeru

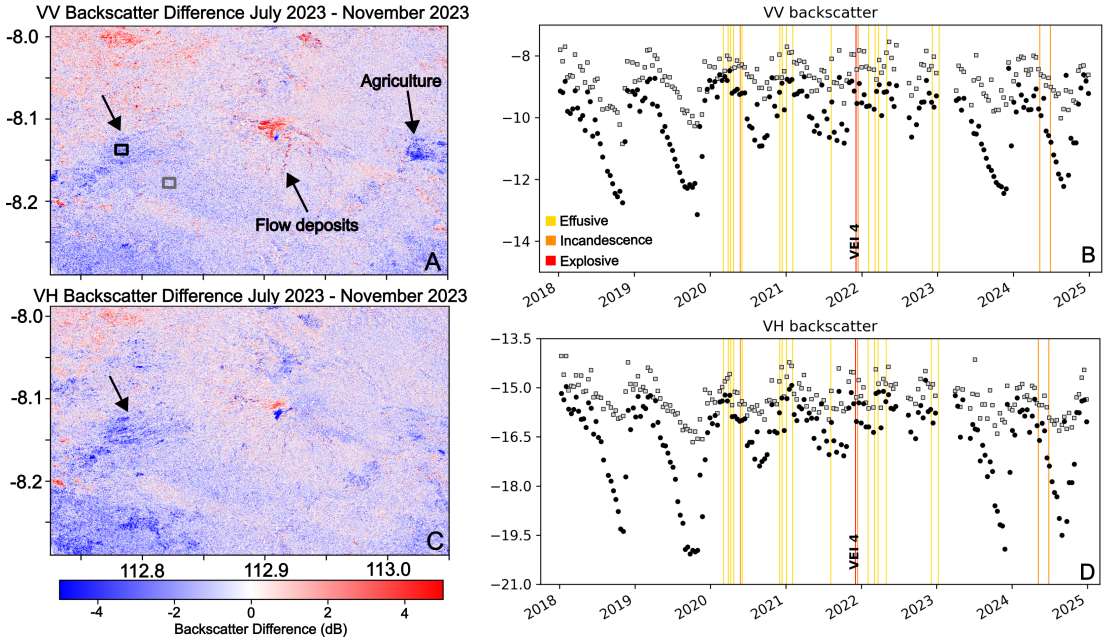

Figure B.6: A) Sentinel-1 VV Backscatter difference map from July to November 2023. B) VV backscatter timeseries for the 2 locations marked in panel A. C) Sentinel-1 VH Backscatter difference map from July to November 2023. D) VH backscatter time series for the 2 locations marked in panel A. The difference map is between a monthly backscatter composite for July 2023 which is subtracted from a November 2023 monthly backscatter composite to generate the difference map.

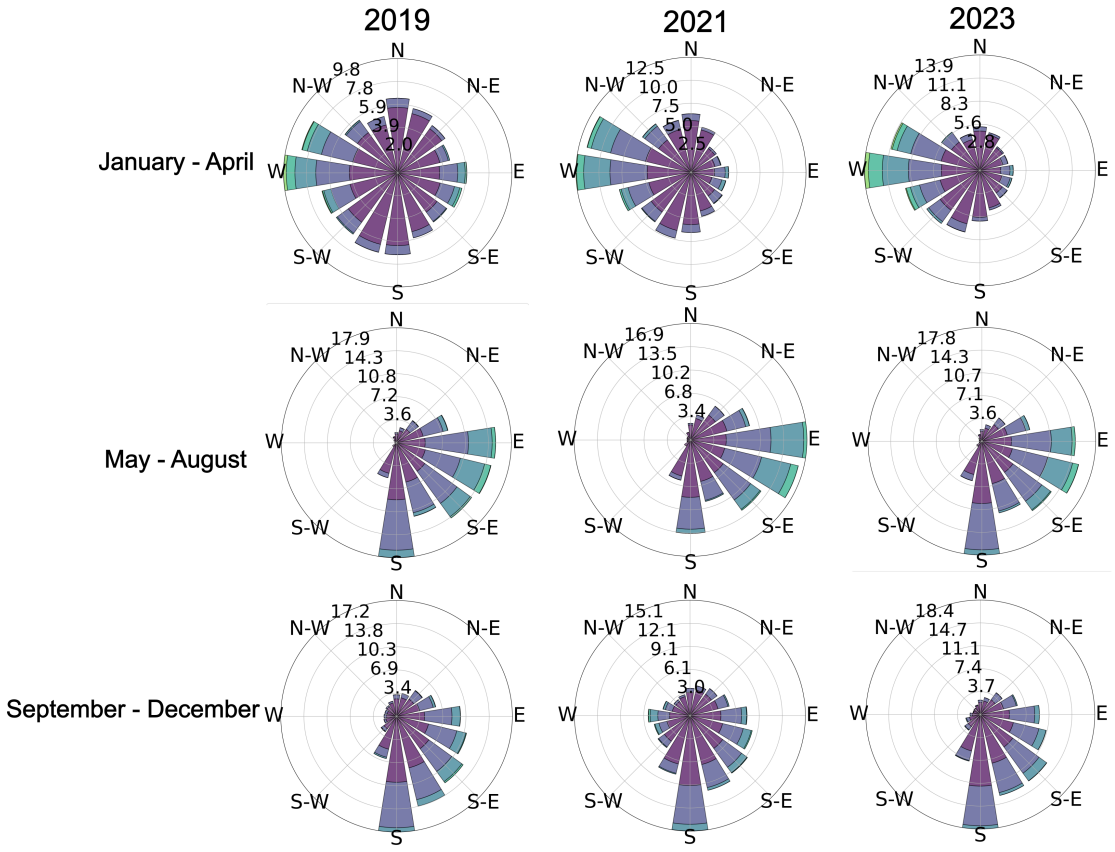

Figure B.7: Variations in wind direction at Semeru throughout the year for 2019, 2021 and 2023.

Appendix C

Supplementary information: Chapter 4

C.1 Case studies

C.1.1 Sinabung

A stratovolcano in Indonesia at 3.1'N with an elevation of 2460 m, Sinabung has a tropical and subtropical moist broadleaf forest cover in a tropical rainforest climate. From 2010 until present Sinabung has had 4 eruptions, all with VEI 3 or 4, in August - September 2010, September 2013 - June 2018, February - June 2019 and August 2020 - September 2021. Prior to this there had not been a confirmed eruption in at least 1000 years. The 2010 eruption was short-lived and consisted of ash fall, so we will be focusing on the eruptions from 2013 onwards which exhibited tephra, pyroclastic flows and lava flows, with flow deposits primarily down the S and SE flanks (supplementary figure C.1) (Pallister et al. 2019).

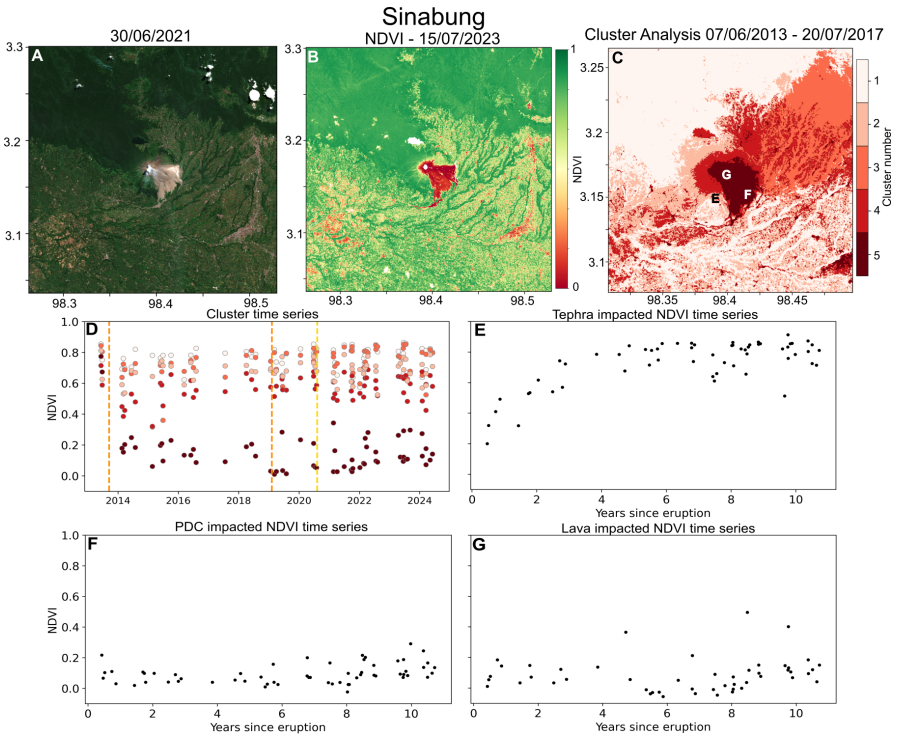

Figure C.1: A) Sentinel-2 optical image of Sinabung from 30/06/2021 B) Sentinel-2 NDVI image of Sinabung on 15/07/2023 after the eruption activity. C) K-means cluster analysis of NDVI imagery over Sinabung from 07/06/2013 - 20/07/2017, also showing the location of the time series in panels E-G. D) Time series of the median pixel of each cluster identified in panel C over the whole NDVI time series with eruption onsets marked by dashed line (orange = VEI4, yellow = VEI3). E) NDVI time series for an area identified as impacted by tephra. F) NDVI time series for an area identified as impacted by PDCs. G) NDVI time series for an area identified as impacted by a lava flow. Areas of impact identified from a combination of optical imagery, cluster analysis and deposit maps from Pallister et al. 2019.

C.1.2 Taal

A caldera volcano in the Philippines at 14'N and an elevation of 311 m, Taal sits within a tropical and subtropical moist broadleaf forest in a tropical savannah climate. A VEI 4 eruption began on the 12th of January 2020 and continued until the 22nd of January, with lava fountaining, tephra deposition, and a plume that reached 15 km high, primarily to the North West, and affecting most of the island (supplementary figure C.2). Tephra from the eruption covered an area of 8605 km^2 causing damage to crops, transport and houses (Balangue-Tarriela et al. 2022). Prior to this eruption was a period of activity consisting of 7 eruptions from 1965 until 1977 and then a period of quiescence until the

2020 eruption. Post-2020 Taal also had eruptions in 2021, 2022 and 2024 but only at VEI 1 and 2 (Global Volcanism Program 2025).

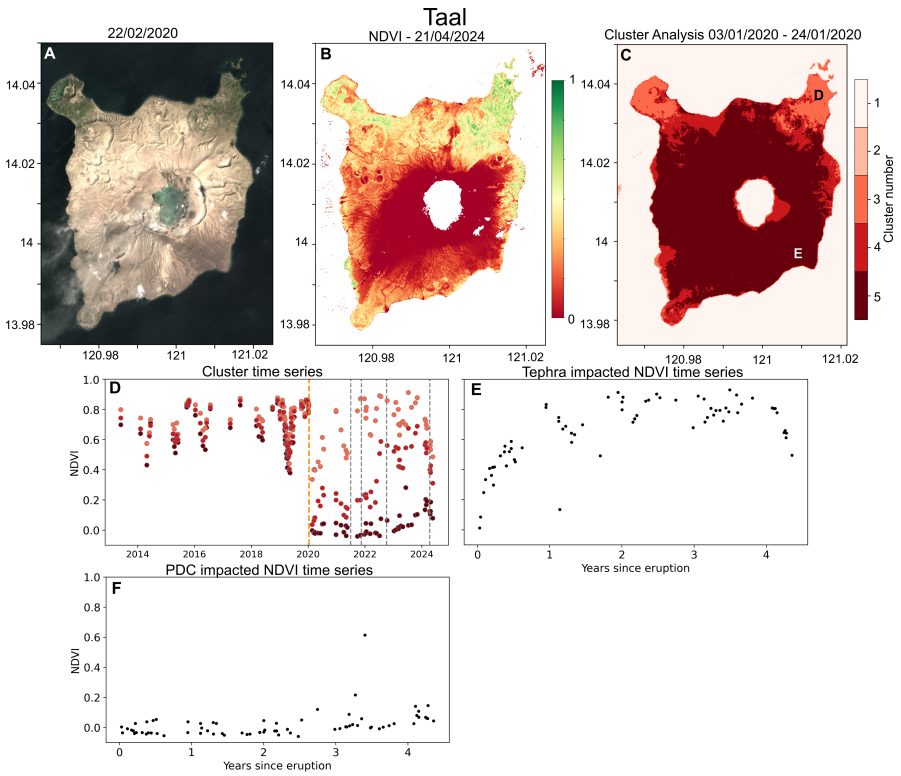

Figure C.2: A) Sentinel-2 image of Taal on 22/02/2020 B) Sentinel-2 NDVI image of Taal on 21/04/2024. C) K-means cluster analysis of NDVI imagery over Taal island from 03/01/2020 - 24/01/2020, also showing the location of the time series in panels E and F. D) Time series of the median pixel of each cluster identified in panel C over the whole NDVI time series with eruption onsets marked by dashed line (orange = VEI4, grey = <VEI3). E) NDVI time series for an area identified as impacted by tephra. F) NDVI time series for an area identified as impacted by PDCs. Areas of impact identified from a combination of optical imagery, cluster analysis and deposit maps from Balangue-Tarriela et al. 2022 and Lagmay et al. 2021.

C.1.3 Kuchinoerabujima

A group of stratovolcanoes in the northern Ryukyu Islands makes the island of Kuchinoerabujima, at 30'N on the southern tip of Japan with an elevation of 657 m. It sits in a region of humid subtropical climate with temperate broadleaf and mixed forest. An eruption began on the 29th of May 2015 and continued until the 19th of June, consisting of tephra, pyroclastic flows and sulphur dioxide emissions with a VEI of 3. Flow deposits primarily travelled to the west with PDCs damaging the forest (supplementary

figure C.3), whilst the plume drifted East (Geshi et al. 2018; Global Volcanism Program 2025). Prior to this eruption was an eruption in 2014 with VEI 1 and it was succeeded by eruptions in 2018 and 2020.

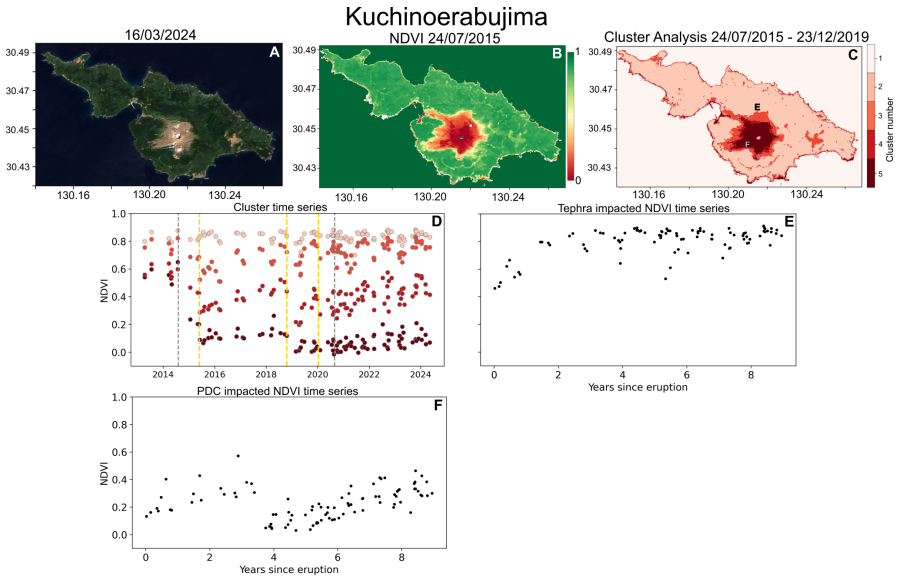

Figure C.3: A) Sentinel-2 image of Kuchinoerabujima on 16/03/2024 B) Landsat 8 NDVI image of Kuchinoerabujima on 24/07/2015. C) K-means cluster analysis of NDVI imagery over Kuchinoerabujima island from 24/07/2015 - 23/12/2019, also showing the location of the time series in panels E and F. D) Time series of the median pixel of each cluster identified in panel C over the whole NDVI time series with eruption onsets marked by dashed line (yellow = VEI3, grey = <VEI3). E) NDVI time series for an area identified as impacted by tephra. F) NDVI time series for an area identified as impacted by PDCs. Areas of impact identified from a combination of optical imagery, cluster analysis and deposit maps from Geshi et al. 2018.

C.1.4 Ulawun

Ulawun is a stratovolcano in the Bismarck arc of Papua New Guinea, at 5.05'S and 2,334 m elevation. It has 22 eruptive periods within the 21st century including a VEI 4 eruption in 2019 and VEI 3 eruption in 2023. Situated in tropical and subtropical moist broadleaf forests with a tropical rainforest climate. Here, we focus on the larger VEI 4 eruption which resulted in PDCs, lava flows and tephra deposition. Flow deposits primarily went on the N and NW flanks, but a new fissure also opened on the WSW flank towards the end of the eruption period (supplementary figure C.4) (Global Volcanism Program 2025). The plume reached 20 km high and frequently changed direction, but

mapping from Orynbaikyzy et al. 2023 showed deposits primarily to the west.

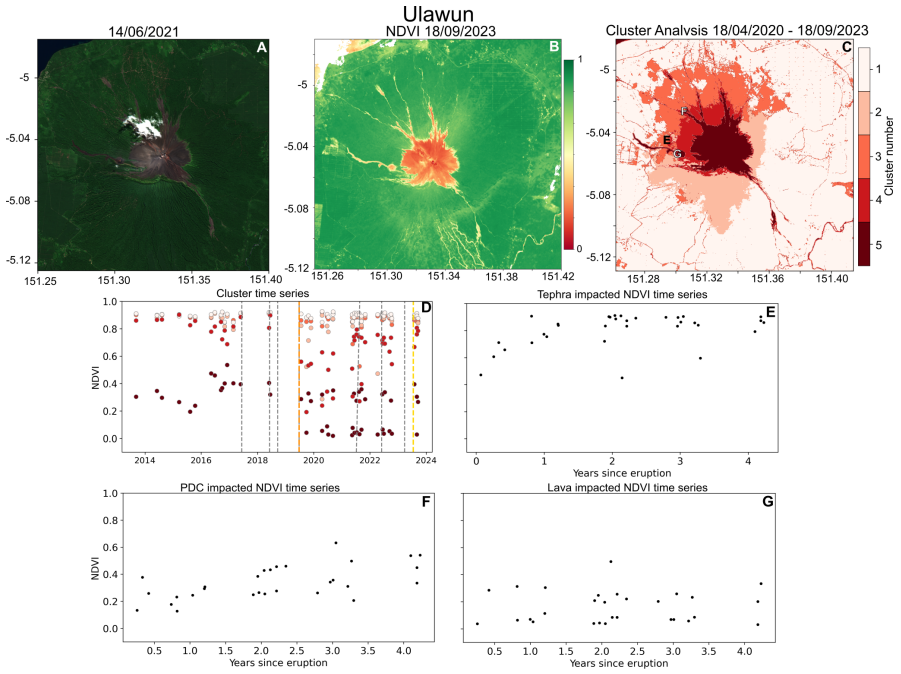

Figure C.4: A) Sentinel-2 image of Ulawun on 14/06/2021. B) Landsat 8 NDVI image of Ulawun on 18/09/2023. C) K-means cluster analysis of NDVI imagery over Ulawun from 18/04/2020 - 18/09/2023, also showing the location of the time series in panels E-G. D) Time series of the median pixel ofeach cluster identified in panel C over the whole NDVI time series with eruption onsets marked by dashed line (orange = VEI4, yellow = VEI3, grey = <VEI3). E) NDVI time series for an area identified as impacted by tephra. F) NDVI time series for an area identified as impacted by PDCs. G) NDVI time series for an area identified as impacted by a Lava flow. Areas of impact identified from a combination of optical imagery, cluster analysis and imagery from Orynbaikyzy et al. 2023.

C.1.5 Soputan

In a tropical and subtropical moist broadleaf forest within a region of tropical rainforest climate in Indonesia, Soputan is a stratovolcano at 1.1'N and 1785 m elevation. With relatively frequent and continuous activity Soputan has had 13 eruptive periods in the 21st century alone. We will be focusing on the period of activity from 2015-2018 which consisted of 3 eruptions all with VEI 3 and included tephra deposition, debris avalanches, lava flows and pyroclastic flows. Deposits often go down the W and SW flanks, but can also go to the N and E, likely affecting the dense surrounding forest (supplementary figure C.5) (Global Volcanism Program 2025).

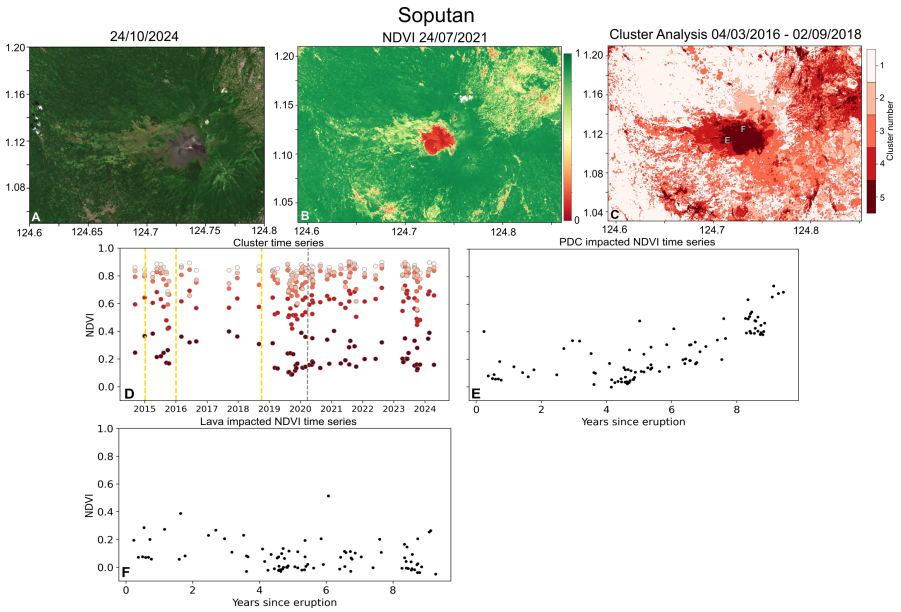

Figure C.5: A) Sentinel-2 optical image of Soputan on 24/10/2024. B) Landsat 8 NDVI image of Soputan on 24/07/2021. C) K-means cluster analysis of NDVI imagery over Soputan from 04/03/2016 - 02/09/2018, also showing the location of the time series in panels E and F. D) Time series of the median pixel of each cluster identified in panel C over the whole NDVI time series with eruption onsets marked by dashed line (yellow = VEI3, grey = <VEI3). E) NDVI time series for an area identified as impacted by PDCs. F) NDVI time series for an area identified as impacted by a Lava flow. Areas of impact identified from a combination of optical imagery, cluster analysis and activity reports (Global Volcanism Program 2025).

C.1.6 Krakatau

Krakatau is a caldera volcano in Indonesia at a latitude of 6'S and elevation of 285 m, in a tropical and subtropical moist broadleaf forest with a tropical rainforest climate, and is made up of 4 islands, Sertung, Panjang, Rakata and Anak Krakatau (supplementary figure C.6). A VEI 3 eruption began in June 2018, consisting of explosions, tephra fall affecting all islands and lava flows and PDCs affecting Anak Krakatau, culminating in a caldera collapse in December 2018 and a subsequent fatal tsunami (Grilli, Tappin, et al. 2019; Rosch et al. 2022). The eruptive activity continued until April 2020, before a period of inactivity until May 2021. In the 10 years prior to this there had been relatively frequent eruptions in 2017, 2014, 2013, 2010, 2009, 2007, however all had a VEI of 2 or less (Global Volcanism Program 2025).

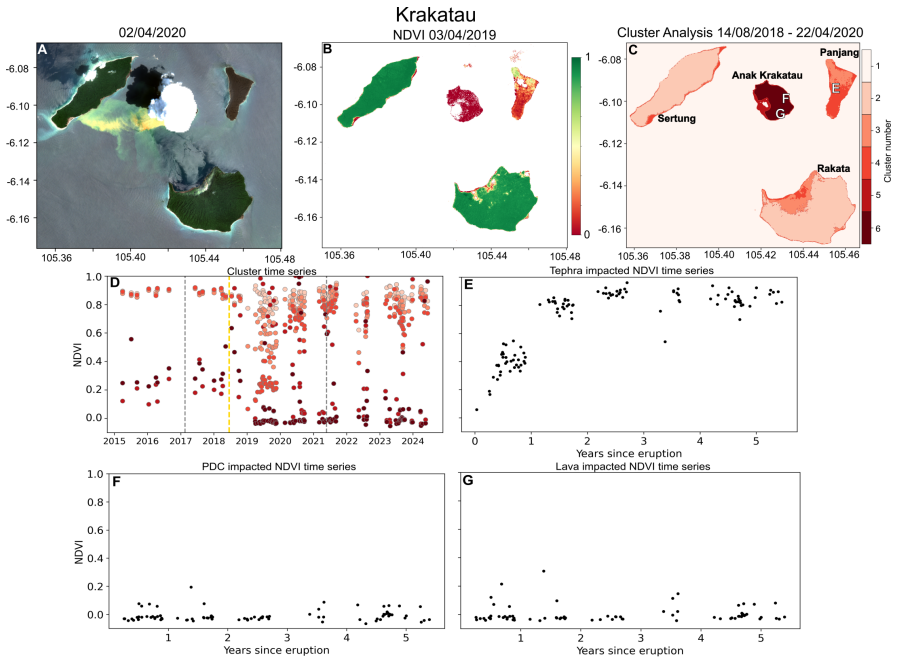

Figure C.6: A) Sentinel-2 image of Krakatau on 02/04/2020. B) Sentinel-2 NDVI image of Krakatau on 03/04/2019 C) K-means cluster analysis of NDVI imagery over Krakatau from 14/08/2018-22/04/2020, also showing the location of the time series in panels E-G. D) Time series of the median pixel of each cluster identified in panel C over the whole NDVI time series with eruption onsets marked by dashed line (yellow = VEI3, grey = <VEI3). E) NDVI time series for an area identified as impacted by tephra. F) NDVI time series for an area identified as impacted by PDCs. G) NDVI time series for an area identified as impacted by a Lava flow. Areas of impact identified from a combination of optical imagery, cluster analysis and imagery and deposit maps from Rosch et al. 2022, Grilli, Zhang, et al. 2021 and Fiantis et al. 2021.

C.1.7 Merapi

Located in Indonesia at 7.54'S and 2910 m elevation, Merapi is a stratovolcano surrounded by tropical and subtropical moist broadleaf forests with a tropical monsoon climate. Three VEI 3 eruptions occurred in 2013, 2014 and 2018-2020, prior to this Merapi had eruptions in 2013, 2011 and 2010. These eruptions resulted in tephra deposits and pyroclastic flows, the tephra deposits were minimal (max thickness 5.5 cm) and so harder to identify in comparison to the flow deposits primarily down the SE and SW flanks (supplementary figure C.7) (Solikhin et al. 2015).

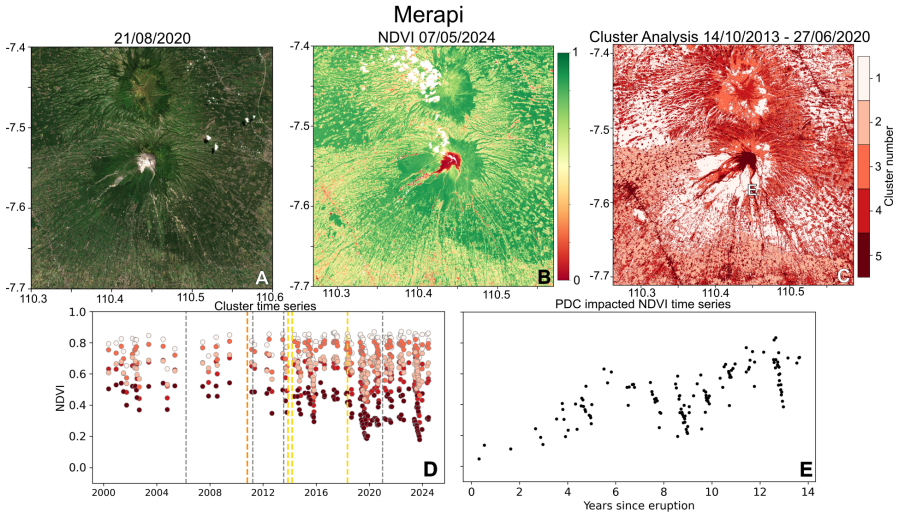

Figure C.7: A) Sentinel-2 image of Merapi on 21/08/2020. B) Sentinel-2 NDVI image of Merapi on 07/05/2024. C) K-means cluster analysis of NDVI imagery over Merapi from 14/10/2013 - 27/06/2020, also showing the location of the time series in panel E. D) Time series of the median pixel of each cluster identified in panel C over the whole NDVI time series with eruption onsets marked by dashed line (orange = VEI4, yellow = VEI3, grey = <VEI3). E) NDVI time series for an area identified as impacted by PDCs. Areas of impact identified from a combination of optical imagery, cluster analysis and imagery and deposit maps from Solikhin et al. 2015.

C.1.8 Agung

Agung is a stratovolcano in Indonesia at a latitude of 8.3'S and 2997 m elevation in an area of tropical and subtropical moist broadleaf forests with a tropical rainforest climate (supplementary figure C.8). A VEI 3 eruption began on the 21st of November 2017 and continued until June 2019, exhibiting ash, lava flows and lahars (Syahbana et al. 2019). The plume reached a height of 6 km and predominantly travelled W (Global Volcanism Program 2025). Prior to this was an eruption in 1963 which had a VEI of 5.

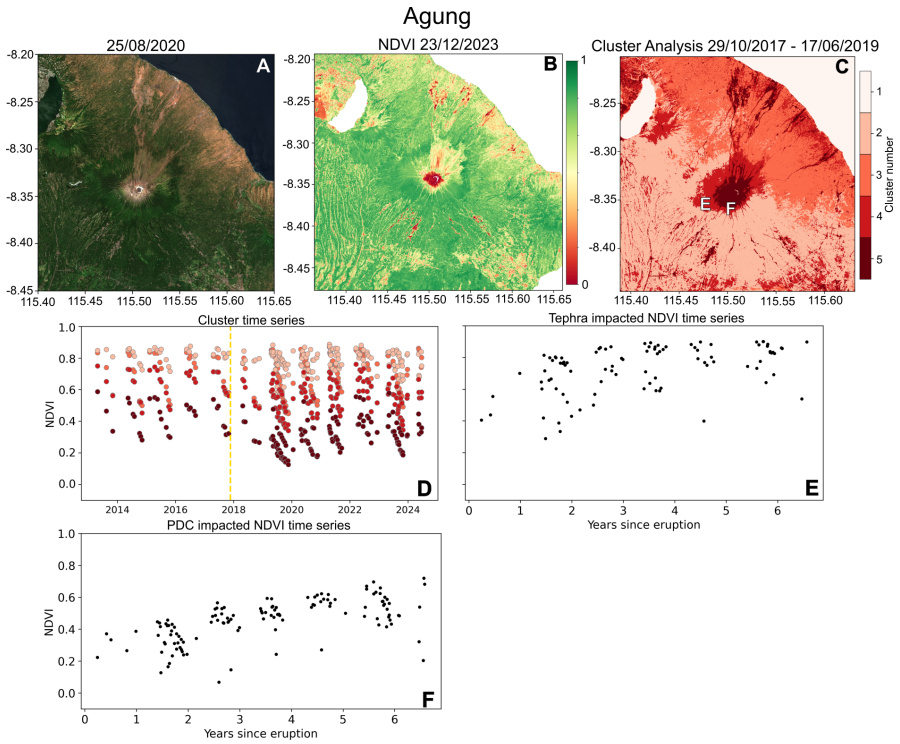

Figure C.8: A) Sentinel-2 optical image of Agung on 25/08/2020. B) Sentinel-2 NDVI image of Agung on 23/12/2023. C) K-means cluster analysis of NDVI imagery over Agung from 29/10/2017 - 17/06/2019, also showing the location of the time series in panels E and F. D) Time series of the median pixel of each cluster identified in panel C over the whole NDVI time series with eruption onsets marked by dashed line (yellow = VEI3). E) NDVI time series for an area identified as impacted by tephra. F) NDVI time series for an area identified as impacted by PDCs. Areas of impact identified from a combination of optical imagery, cluster analysis and imagery and maps from Rosch et al. 2022 and Syahbana et al. 2019.

C.1.9 Calbuco

Calbuco is located in the Southern Chilean Andes at a latitude of 41.3' South with an elevation of 1974 m. The volcano lies in an area of temperate oceanic climate in a temperate broadleaf and mixed forest. We focus on the 2015 eruption of Calbuco, which began on the 22nd of April and involved two main explosive pulses, on the 22nd and 23rd of April, the eruption ended on the 26th of May. The eruption produced tephra deposits up to 70 cm (predominantly to the NE), pyroclastic flows up to 8 km away and lahars extending down river channels reaching the coast (supplementary figure C.9) (Udy et al. 2024). The previous eruption to this was in 1972 which had a VEI 2 and

experienced tephra deposits, meaning the surrounding forest had not experienced recent disturbance.

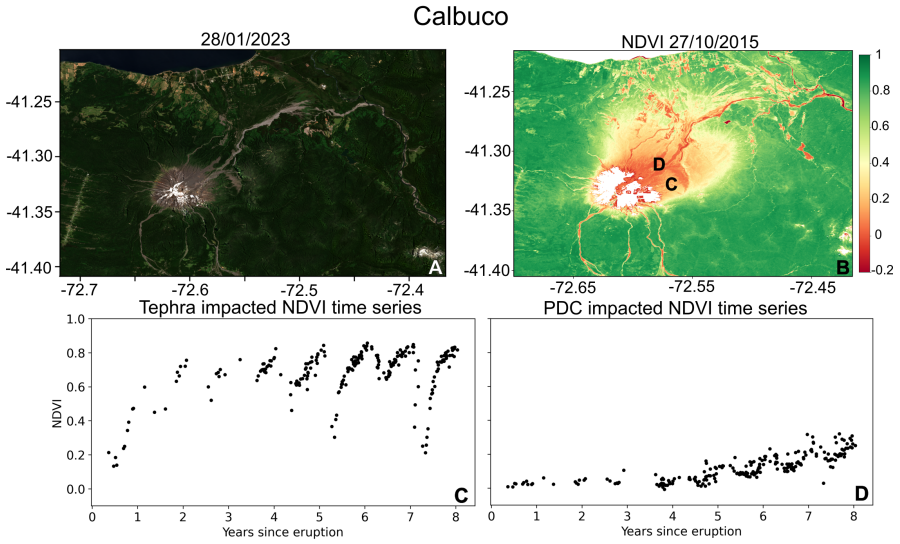

Figure C.9: A) Sentinel-2 optical image of Calbuco on 28/01/2023. B) Landsat-8 NDVI image of Calbuco on 27/10/2015. C) NDVI time series for an area identified as impacted by tephra. D) NDVI time series for an area identified as impacted by PDCs. Areas of impact identified from Udy et al. 2024.

C.1.10 Turrialba

Turrialba is a stratovolcano in Costa Rica located at 10.025'N with an elevation of 3,340 m. it has had 10 confirmed eruptive periods in the 21st century including a VEI 3 eruption on the 8th of March 2015 which lasted until December 2019 and resulted in tephra deposition and pyroclastic flows (Global Volcanism Program 2025). Turrialba has a tropical rainforest climate with Tropical and subtropical moist broadleaf forests. It is a large, persistent emitter of SO_2, significantly affecting the downwind (West) vegetation (supplementary figure C.10) (Tortini et al. 2017).

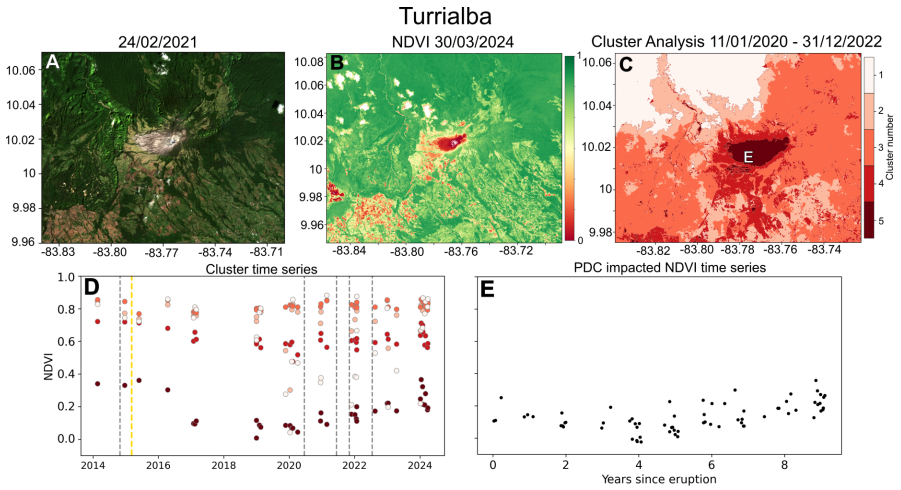

Figure C.10: A) Sentinel-2 optical image of Turrialba on 24/02/2021 B) Sentinel-2 NDVI image of Turrialba on 30/03/2024. C) K-means cluster analysis of NDVI imagery over Turrialba from 11/01/2020 - 31/12/2022, also showing the location of the time series in panel E. D) Time series of the median pixel of each cluster identified in panel A over the whole NDVI time series with eruption onsets marked by dashed line (yellow = VEI3, grey = <VEI3). E) NDVI time series for an area identified as impacted by PDCs. Areas of impact identified from a combination of optical imagery, cluster analysis and activity reports (Global Volcanism Program 2025).

C.1.11 Rabaul

Rabaul is a caldera volcano on the Bismarck volcanic arc in Papua New Guinea situated at 4.2'S with an elevation of 688 m. It has had 7 eruptive periods in the 21st century including VEI 4 eruptions in 2014 and 2006, with a previous VEI 4 eruption in 1994. Rabaul has a tropical rainforest climate with tropical and subtropical moist broadleaf forest. We focus on the 2006 eruption that resulted in tephra deposition, pyroclastic flows and lava flows (supplementary figure C.11). The plume reached 18 km high and and travelled SW then NW, with flow deposits concentrated near the vent and down the N and W flanks (Bernard et al. 2020; Global Volcanism Program 2025).

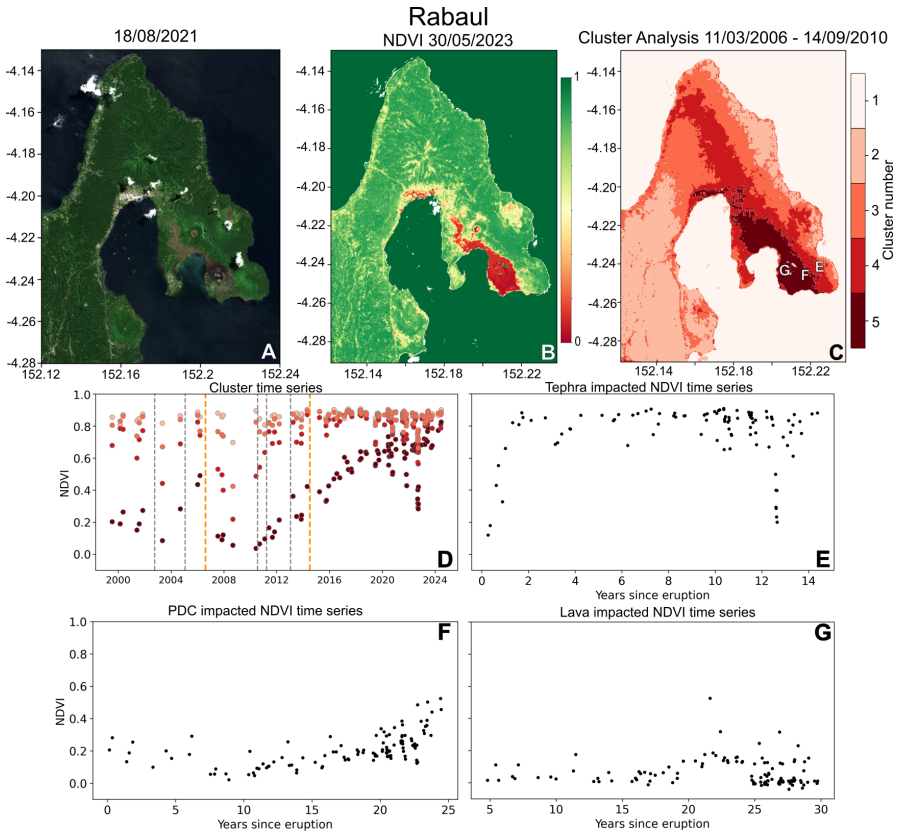

Figure C.11: A) Sentinel-2 optical image of Rabaul on 18/08/2021. B) Sentinel-2 NDVI image of Rabaul on 30/05/2023. C) K-means cluster analysis of NDVI imagery over Rabaul from 11/03/2006 - 14/09/2010, also showing the location of the time series in panels E-G. D) Time series of the median pixel of each cluster identified in panel C over the whole NDVI time series with eruption onsets marked by dashed line (orange = VEI4, grey = <VEI3). E) NDVI time series for an area identified as impacted by tephra. F) NDVI time series for an area identified as impacted by PDCs. G) NDVI time series for an area identified as impacted by lava flows. Areas of impact identified from a combination of optical imagery, cluster analysis and activity reports (Global Volcanism Program 2025).

C.1.12 Sangeang Api

A composite volcano in Indonesia at 8.2'S with an elevation of 1912 m. It has had 3 confirmed eruptive periods in the 21st century, of note is the VEI 4 eruption that occurred in May 2014 until November 2015, which resulted in tephra deposits, PDC deposits and lava flows primarily on the S and E flanks. Following this, it had 2 VEI 2 eruptions from 2017-2020 and 2022-2022 (supplementary figure C.12) (Global Volcanism Program 2025). It has a tropical monsoon climate with tropical and subtropical dry broadleaf

forests.

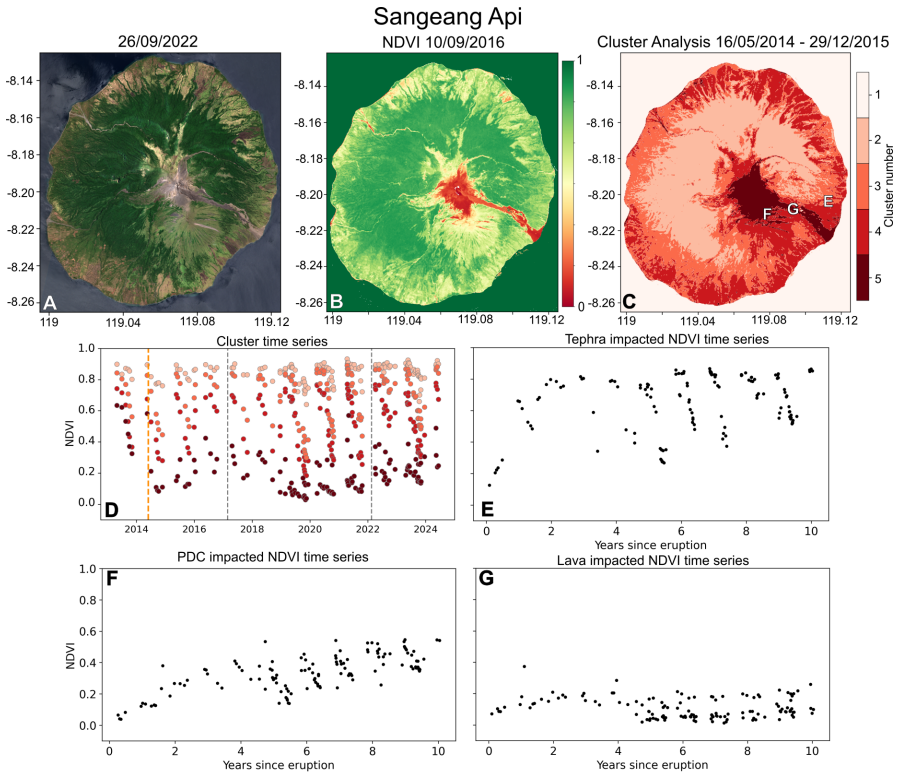

Figure C.12: A) Sentinel-2 optical image of Sangeang Api on 26/09/2022. B) Landsat 8 NDVI image of Sangeang Api on 10/09/2016. C) K-means cluster analysis of NDVI imagery over Sangeang Api from 16/05/2014 - 29/12/2015, also showing the location of the time series in panels F-G. D) Time series of the median pixel of each cluster identified in panel C over the whole NDVI time series with eruption onsets marked by dashed line (orange = VEI4, grey = <VEI3). E) NDVI time series for an area identified as impacted by tephra. F) NDVI time series for an area identified as impacted by PDCs. G) NDVI time series for an area identified as impacted by lava flows. Areas of impact identified from a combination of optical imagery, cluster analysis and activity reports (Global Volcanism Program 2025).

C.1.13 Semeru

Semeru is a stratovolcano in Indonesia, located on the island of Java with a latitude of 8.1'S and elevation of 3657 m in a tropical and subtropical moist broadleaf forests in a tropical rainforest climate (supplementary figure C.13). From April 2014, Semeru has had near continuous eruptive activity. Beginning April 1st 2014 until 9th January 2017 was an eruptive period with VEI 2, then starting 6th June 2017 until present there has been a period of explosive activity with VEI 4. This eruption resulted in tephra deposits

and Pyroclastic flows primarily down the S and SE flank (Global Volcanism Program 2020).

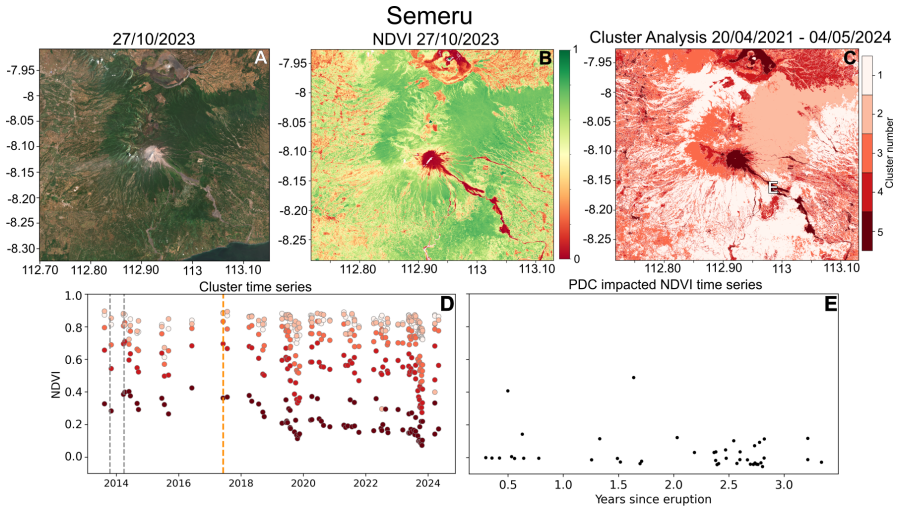

Figure C.13: A) Sentinel-2 optical image of Semeru on 27/10/2023. B) Sentinel-2 NDVI image of Semeru on 27/10/2023. C) K-means cluster analysis of NDVI imagery over Semeru from 20/04/2021 - 04/05/2024, also showing the location of the time series in panel E. D) Time series of the median pixel of each cluster identified in panel C over the whole NDVI time series with eruption onsets marked by dashed line (orange = VEI4, grey = <VEI3). E) NDVI time series for an area identified as impacted by PDCs. Areas of impact identified from a combination of optical imagery, cluster analysis and activity reports (Global Volcanism Program 2025).

C.1.14 Kelud

In Indonesia at a latitude of 7.9'S and 1730 m elevation, Kelud is a stratovolcano with surrounding tropical and subtropical moist broadleaf forest with a tropical monsoon climate (supplementary figure C.14). An eruption with VEI 4 began on the 13th of February 2014 and only lasted 2 days, producing a large plume reaching 26 km high and primarily to the west resulting in extensive tephra deposition along with pyroclastic flows and a blast damaging and blowing down surrounding vegetation (Maeno et al. 2019). Prior to this was a 2007 eruption with VEI 2 and a VEI 4 eruption in February 1990.

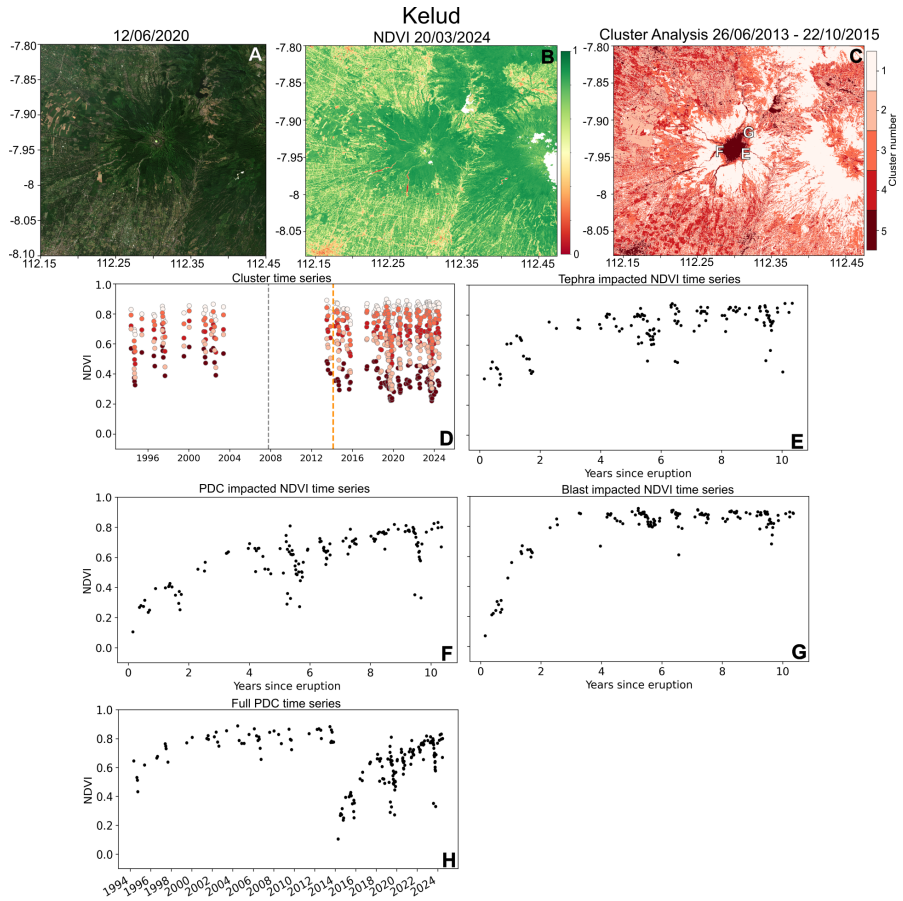

Figure C.14: A) Sentinel-2 optical image of Kelud on 12/06/2020. B) Landsat 8 NDVI image of Kelud on 20/03/2024. C) K-means cluster analysis of NDVI imagery over Kelud from 29/10/2017 - 17/06/2019, also showing the location of the time series in panels E-F. D) Time series of the median pixel of each cluster identified in panel C over the whole NDVI time series with eruption onsets marked by dashed line (orange = VEI4, grey = <VEI3). E) NDVI time series for an area identified as impacted by tephra. F) NDVI time series for an area identified as impacted by PDCs. G) NDVI time series for an area identified as impacted by a blast. H) The full time series for the PDC impacted area of panel F, including the pre-eruption time period. Areas of impact identified from a combination of optical imagery, cluster analysis and deposit maps and imagery from Maeno et al. 2019.

C.1.15 Chaitén

The 2008 eruption of Chaitén had a VEI of 4 and consisted of tephra deposits, pyroclastic flows and lahars and a blast resulting in blown down trees (Major and Lara 2013). The eruption began on the 2nd of May and continued until the 31st of May 2011. Chaitén is situated in Chile at 42.8'S with an elevation of 1122 m in a temperate and broadleaf

mixed forest with a temperate oceanic climate, next to the large glaciated Michinmahuida Volcano (supplementary figure C.15). Prior to this eruption there had been no eruptive activity since 1640, resulting in a likely almost pristine forest prior to the damage inflicted by the eruption. This eruption has been studied for its impacts on forests with tephra fall damaging trees through abrasion and canopy loading, resulting in bowing and breakage of trees over 480 km^2 (Swanson, Jones, et al. 2013). With previous studies producing maps of different levels of tree damage due to the eruption (Major and Lara 2013).

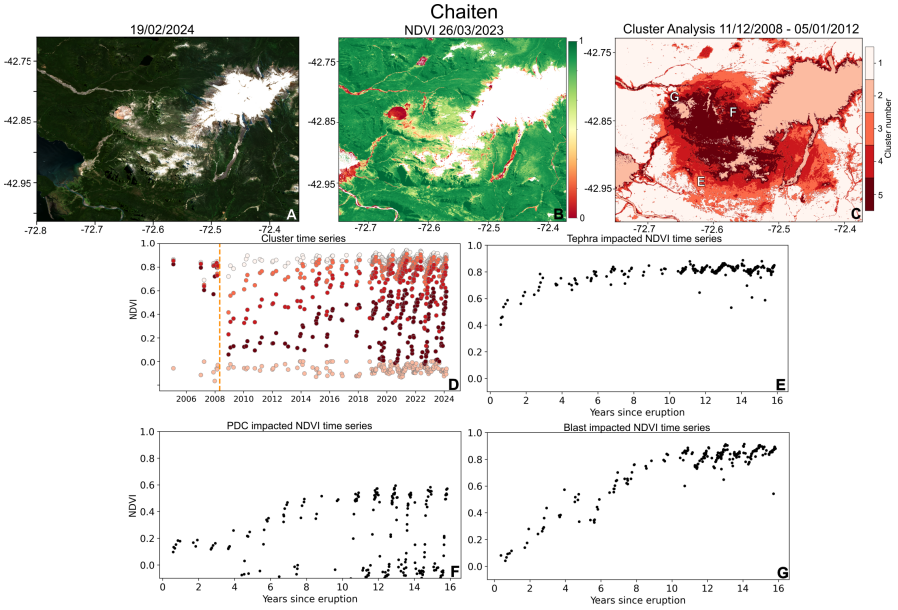

Figure C.15: A) Sentinel-2 optical image of Chaitén on 19/02/2024. B) Sentinel-2 NDVI image of Chaitén on 26/03/2023. C) K-means cluster analysis of NDVI imagery over Chaitén from 11/12/2008 - 05/01/2012, also showing the location of the time series in panels E-G. D) Time series of the median pixel of each cluster identified in panel C over the whole NDVI time series with eruption onsets marked by dashed line (orange = VEI4). E) NDVI time series for an area identified as impacted by tephra. F) NDVI time series for an area identified as impacted by PDCs. G) NDVI time series for an area identified as impacted by a blast. Areas of impact identified from a combination of optical imagery, cluster analysis and deposit maps and imagery from Lara 2009, Major and Lara 2013 and Watt et al. 2009.

C.1.16 Puyehue-Cordón Caulle

Puyehue-Cordón Caulle is a volcanic complex in Chile at 40.6'S with an elevation of 2236 m. Puyehue-Cordón Caulle is situated in Temperate broadleaf and mixed forests with a temperate oceanic climate. The only period of activity in the 21st century was

a VEI 5 eruption in June 2011 until April 2012. Which resulted in a large plume up to 12 km high and up to 178 km away, primarily moving to the East. There were also PDCs and lava flows, mostly concentrated near the summit (supplementary figure C.16) (Pistolesi et al. 2015; Global Volcanism Program 2025)

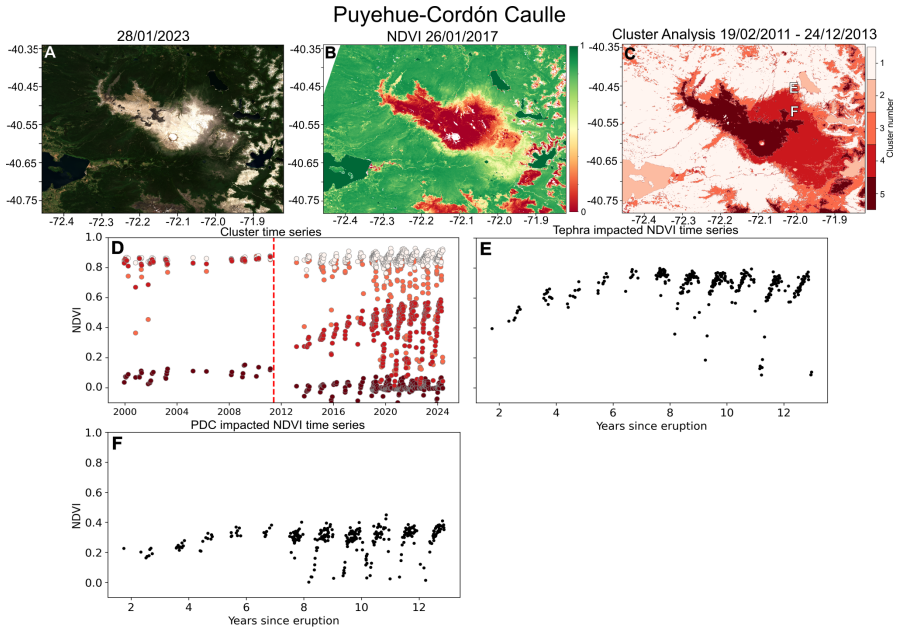

Figure C.16: A) Sentinel-2 optical image of Puyehue-Cordón Caulle. B) Landsat 8 NDVI image of Puyehue-Cordón Caulle on 26/01/2017. C) K-means cluster analysis of NDVI imagery over Puyehue-Cordón Caulle from 19/02/2011 - 24/12/2013, also showing the location of the time series in panels E and F. D) Time series of the median pixel of each cluster identified in panel C over the whole NDVI time series with eruption onsets marked by dashed line (red = VEI5). E) NDVI time series for an area identified as impacted by tephra. F) NDVI time series for an area identified as impacted by PDCs. Areas of impact identified from a combination of optical imagery, cluster analysis and deposit maps from Pistolesi et al. 2015.

C.1.17 El Chichón

El Chichón is a composite volcano in Mexico at 17.4'N with an elevation of 1150 m. It is situated in tropical and subtropical moist broadleaf forests with a tropical savanna climate. The only known eruption since the start of the 20th Century was a VEI 5 eruption from March 1982-September 1982. The eruption resulted in large tephra deposits, covering 45,000 km^2 within the 1 mm isopach (Varekamp et al. 1984), along with PDCs around the volcano and into nearby river drainages (supplementary figure C.17)

(Sigurdsson et al. 1984; Macias et al. 1997).

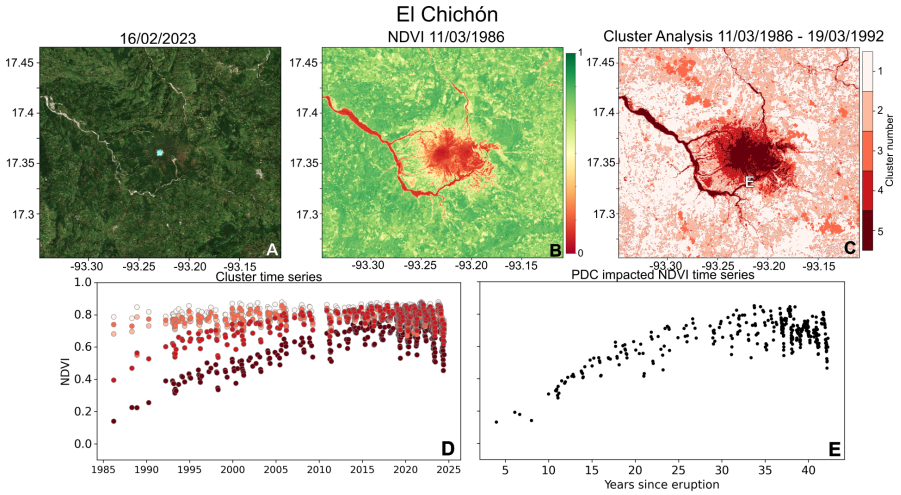

Figure C.17: A) Sentinel-2 optical image of El Chichón. B) Landsat 5 NDVI image of El Chichón on 11/03/1986. C) K-means cluster analysis of NDVI imagery over El Chichón from 11/03/1986 - 19/03/1992, also showing the location of the time series in panel E. D) Time series of the median pixel of each cluster identified in panel C over the whole NDVI time series. D) NDVI time series for an area identified as impacted by PDCs. Areas of impact identified from a combination of optical imagery, cluster analysis and deposit maps from Sigurdsson et al. 1984 and Macias et al. 1997.

C.1.18 Mount St Helens

A stratovolcano location in Washington, United states at 46.2'N with an elevation of 2549 m in temperate coniferous forests in a warm summer Mediterranean climate (supplementary figure C.18). It has had 4 confirmed eruptive periods since the start of the 20th century, including the VEI 5 eruption that began in March 1980. This eruption involved explosions, tephra fall, PDCs a blast and large landslide (Foster et al. 1998; Druitt 1992). It has been extensively studied, particularly in terms of the influence it had on the surrounding forest and how quickly it recovered following the eruption. The variety of deposit types and their interaction at different distances resulted in a range of damage severity, from completely destroying vegetation, to minor damage (Foster et al. 1998; Major and Lara 2013).

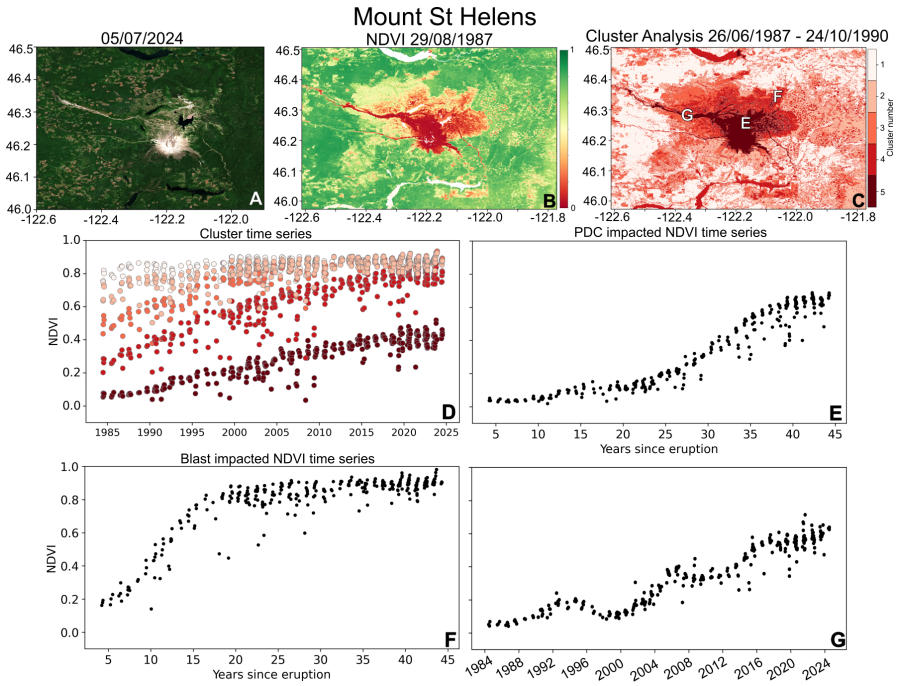

Figure C.18: A) Sentinel-2 optical image of Mount St Helens on 05/07/2024. B) Landsat 5 NDVI image of Mount St Helens on 29/08/1987. C) K-means cluster analysis of NDVI imagery over Mount St Helens from 26/06/1987 - 24/10/1990, also showing the location of the time series in panels E-G. D) Time series of the median pixel of each cluster identified in panel C over the whole NDVI time series. E) NDVI time series for an area identified as impacted by PDCs. F) NDVI time series for an area identified as impacted by a blast. G) NDVI time series for an area impacted by multiple flow deposits, impacting the recovery trajectory. Areas of impact identified from a combination of optical imagery, cluster analysis and deposit maps from Druitt 1992.

C.1.19 Table of time series locations

Table C.1: A table summarising the locations and distances of the time series used in figure 4.5

Volcano	Tephra locations	PDC locations	Blast locations	Lava locations
Sinabung	3.12N, 98.39E	3.15N, 98.42E		3.16N, 98.40E
Taal	14.03N, 121.01E	13.99N, 121.01E		
Kuchineoerabujima	30.46N, 130.22E	30.44N, 130.21E		
Ulawun	5.05S, 151.29E	5.03S, 151.31E		5.06S, 151.30E
Soputan		1.12N, 124.72E		1.13N, 124.73E
Krakatau	6.10S, 105.46E	6.10S, 105.43E		6.11S, 105.43E
Merapi		7.59S, 110.45E		
Agung	8.36S, 115.48E	8.36S, 115.50E		
Calbuco	41.32S, 72.57W	41.31S, 72.57W		
Turrialba		10.02N, 83.78W		
Rabaul	4.24S, 152.22E	4.24S, 152.21E		4.24S, 152.20E
Sangeang Api	8.21S, 119.11E	8.21S, 119.08E		8.21S, 119.09E
Semeru		8.16S, 113.03E		
Kelud	7.94S, 112.32E	7.94S, 112.28E	7.91S, 112.33E	
Chaitén	42.94S, 72.63W	42.84S, 72.57W	42.82S, 72.64W	
Puyehue-Cordon Caulle	40.46S, 72.05W	40.51S, 72.03W		
El Chichon		17.33N, 93.22W		
Mount St Helens		46.25N, 122.12W	46.34N, 122.07W	